INAUGURAL - DISSERTATION

zur
Erlangung der Doktorwürde
der
Naturwissenschaftlich-Mathematischen Gesamtfakultät
der
Ruprecht-Karls-Universität
Heidelberg

vorgelegt von
Sreejith Pulloor Kuttanikkad, M.S.
aus Elankur (Kerala), Indien

Tag der mündlichen Prüfung: 15.10.2009

Pore-Scale Direct Numerical Simulation of Flow and Transport in Porous Media

Gutachter: **Prof. Dr. Peter Bastian**

Prof. Dr. Kurt Roth

To my extended family . . .
especially to my parents, my grandparents, my brother, my sister and to my wife!

Zusammenfassung

Porenskalige direkte numerische Simulation von Strmung und Transport in porsen Medien

Diese Dissertation stellt Untersuchungen zur porenskaligen Simulation von Strömung und Transport in porösen Medien vor und beschreibt die Anwendung eines neuen numerischen Ansatzes zu porenskaliger Modellierung, basierend auf unstetigen Galerkin (DG) Finiten Elementen. In diesem Ansatz werden die partiellen Differentialgleichungen, die die Strömung auf der Porenskala bestimmen, direkt auf einer strukturierten Partitionierung des Rechengebiets gelöst. Der Hauptvorteil ist, dass auf das Erstellen einer konformen Triangulierung verzichtet werden kann. AuSSerdem ist dieser Ansatz lokal massenerhaltend, eine wünschenswerte Eigenschaft für Transportsimulationen. Dies erlaubt die effizientere Untersuchung von Prozessen auf der Porenskala und ihrem Einfluss auf makroskopische Phänomene. Es wurde die Stokes-Strömung in zwei- und dreidimensionalen undgeordneten Kugelpackungen berechnet und in einem random-walk Teilchenverfolgungsmodell zur Simulation von Transport durch die Kugelpackung benutzt. Die Permeabilitäten wurden berechnet und das asymptotische Dispersionsverhalten des gelösten Stoffes für einen weiten Bereich der Péclet-Zahl untersucht. Die Ergebnisse der Simulationen stimmen gut mit den Literaturdaten überein, was zeigt, dass der hier gewählte Ansatz gut für porenskalige Simulation geeignet ist.

Abstract

Pore-Scale Direct Numerical Simulation of Flow and Transport in Porous Media

This dissertation presents research on the pore-scale simulation of flow and transport in porous media and describes the application of a new numerical approach based on the discontinuous Galerkin (DG) finite elements to pore-scale modelling. In this approach, the partial differential equations governing the flow at the pore-scale are solved directly where the main advantage is that it does not require a body fitted grid and works on a structured partition of the domain. Furthermore this approach is locally mass conservative, a desirable property for transport simulation. This allows the investigation of pore-scale processes and their effect on macroscopic behaviour more efficiently. The Stokes flow in two and three dimensional disordered packing was solved and the flow field was used in a random-walk particle tracking model to simulate the transport through the packing. The permeabilities were computed and asymptotic behaviour of solute dispersion for a wide range of Péclet numbers was studied. The simulated results agree well with the data reported in the literature, which indicates that the approach chosen here is well suited for pore-scale simulation.

Acknowledgements

I would like to express my profound gratitude to my advisers **Prof. Dr. Peter Bastian** and **Prof. Dr. Kurt Roth** for the research opportunity that they provided me. I am grateful to them for suggesting this interesting topic and for their continuous guidance, support and keen interest in the progress of my work. I shall always cherish the academic freedom that I have enjoyed under their guidance. Their scientific knowledge and directions helped me to make this work possible.

I am most thankful to Dr. Olaf Ippisch and my colleagues Christian Engwer and Markus Blatt for their constant help and many fruitful discussions and I appreciate their scientific ideas. In particular, I am indebted to Christian for his work on UDG and for his programming efforts. I have learnt a lot from them and would like to show my deep respect for them. I extend my thanks to Thimo Neubaur for helping me during the initial stages of my research and to Jö and Felix for always being helpful.

I gratefully acknowledge the scholarship offered by the International Graduiertenkolleg IGK 710 *Complex Processes: Modeling, Simulation and Optimization* at the Interdisciplinary Center of Scientific Computing (IWR). I am grateful for the opportunities that the program offered and giving me a platform for the exchange of scientific knowledge.

Many thanks to my colleagues in the soil physics group and in IPVS Stuttgart: Dan, Sven, Ute, Holger, Dr. H.-J. Vogel, Klaus, Stefan, Fereidoun, Enkaledja and all my former and current colleagues for their support and friendliness.

Thanks are also to all DUNE developers for their excellent work, which helped me to develop the required simulation codes using DUNE.

Special thanks to my wife Manisha for her love, support, encouragement and understanding. I am grateful for her consistent support during some difficult times.

I shall always recall with great fondness many of my friends: Nixon, Pradeep, Jishy, Vinod, Shahi, Smitha, Lakshmi, Alex, Pauly, Beena, Badri, Adarsh, Prem, Ganesh. Thanks also to Sabine for her nice hospitality during my stay in Heidelberg.

I would also like to thank many other people not listed who made my last few years a memorable time of my life. Thank you, one and all.

Last but not least, I thank the God for always being with me and my parents, brother, my wife and other family members for their love, support and constant encouragement. You all have always been there for me, for that I am eternally grateful.

Sreejith Pulloor Kuttanikkad

Contents

List of Figures

List of Tables

List of Symbols and Abbreviations

Abbreviations

ADE	Advection-Dispersion Equation
BCC	Body Centred Cubic
CTRW	Continuous Time Random Walk
DG	Discontinuous Galerkin
DOF	Degree of Freedom
FCC	Face Centred Cubic
IIPG	Incomplete Interior Penalty Galerkin
IP	Interior Penalty
LBB	Ladyzhenskaya-Babuška-Brezzi
LDG	Local Discontinuous Galerkin
MRI	Magnetic Resonance Imaging
NAPL	Non-Aqueous Phase Liquid
NIPG	Non-Symmetric Interior Penalty Galerkin
NMR	Nuclear Magnetic Resonance
OBB	Oden-Babuška-Baumann
PDE	Partial Differential Equation
PDL	Porous Diffusion Layer
PEM	Proton Exchange Membrane
PLIF	Planar Laser-Induced Fluorescence
REV	Representative Elementary Volume
RK	Runge-Kutta
RWPT	Random Walk Particle Tracking
SC	Simple Cubic
SIPG	Symmetric Interior Penalty Galerkin
SPH	Smoothed Particle Hydrodynamics
TA	Taylor-Aris
UDG	Unfitted Discontinuous Galerkin

Greek Letters

$\Gamma = \partial\Omega$	Boundary of the domain Ω
μ	Coefficient of Dynamic Viscosity
ν	Coefficient of Kinematic Viscosity
Ω	Domain

ϕ	Porosity
ρ	Density
σ	DG Penalising Parameter
σ	Standard Deviation
$\underline{\boldsymbol{\kappa}}$	Intrinsic Permeability Tensor
ζ	Geometric shape factor in the Taylor-Aris dispersion formula

Latin Letters

$\boldsymbol{g}$	Acceleration due to gravity
$\underline{\boldsymbol{D}}$	Hydrodynamic Dispersion Tensor
$\underline{\boldsymbol{K}}$	Permeability Tensor
C	Solute Concentration
D_L	Longitudinal Dispersion Coefficient
D_m	Molecular Diffusion Coefficient
D_T	Transverse Dispersion Coefficient
Pe	Péclet Number
Re	Reynolds Number

Other Symbols

$\langle\cdot\rangle$	DG Average Operator
Δ	Laplace Operator
$[\cdot]$	DG Jump Operator
$\nabla\cdot$	Divergence Operator
∇	Gradient Operator
$\boldsymbol{u} : \boldsymbol{v}$	Component-wise inner product, $\boldsymbol{u} : \boldsymbol{v} = \sum_{ij} u_{ij} v_{ij}$

1 Introduction

1.1 Relevance

Some of the biggest challenges that the world is facing today are related to the environment and energy such as global warming, climate change and safe disposal of nuclear waste. Increasing greenhouse gases caused by human activities is often considered as one of the major causes of global warming. The carbon dioxide (CO_2) sequestration where industrially-produced CO_2 are stored using subsurface saline aquifers and reservoirs is considered as an intermediate technique to reduce greenhouse gases. The other important issues currently being addressed are the increasing demand for fresh water and oil. For instance finding fresh water aquifers, remediation of contaminated water sources for drinking and irrigation, prevention of salt water intrusion into fresh water bodies, locating new oil deposits and optimising recovery of hydrocarbons etc. are of utmost importance. Interestingly all these processes are related to the fluid flow and transport in natural porous media. Apart from that, porous media are used widely in many man made systems such as fuel cells (porous diffusion layer), packed columns, filtration, paper pulp drying, textiles etc. Besides their potential applications in environmental and industrial processes, they also find an important place in biological sciences. For example, flow of blood through human body and purification of blood in kidneys etc. involve flow through porous materials. Hence understanding the chemical and physical processes involved in the flow and transport through porous media is of utmost importance. However its simulation and predictions are very challenging because of the complexity involved in these processes. In short, modelling the processes in porous media therefore has wide theoretical and applied interest.

The physics of fluid flow (single and multiphase) and transport gives rise to complex, nonlinear and coupled equations. The difficulties imposed by these nonlinear equations along with the irregular geometries and transient behaviour associated with various practical problems make numerical simulation an essential tool in the study of flow and transport. Nevertheless, the mathematical models remain the same irrespective of the nature of the fluid, which can be either gas or any organic/inorganic liquid. As a result, though complex and challenging, the numerical simulations are considered as viable and an effective approach to solve the environmental, biological and industrial problems that involve the flow and transport in porous media.

1.2 Modelling Approaches and Scales

In porous media, complex physical phenomena often occur on widely varying scales. For instance, the length scale of major interest in porous media varies from a pore-level (in the order of few micro meters) to field level (in the order of kilometres). Hence, a continuing challenge in mathematical and computational modelling is to handle these relevant scales properly. In general, the modelling approach varies based on the scale at which the porous medium is being described. An illustration of pore-scale and continuum scale is shown in Figure (1.1). In the following Section, the various scales and associated modelling approaches are described.

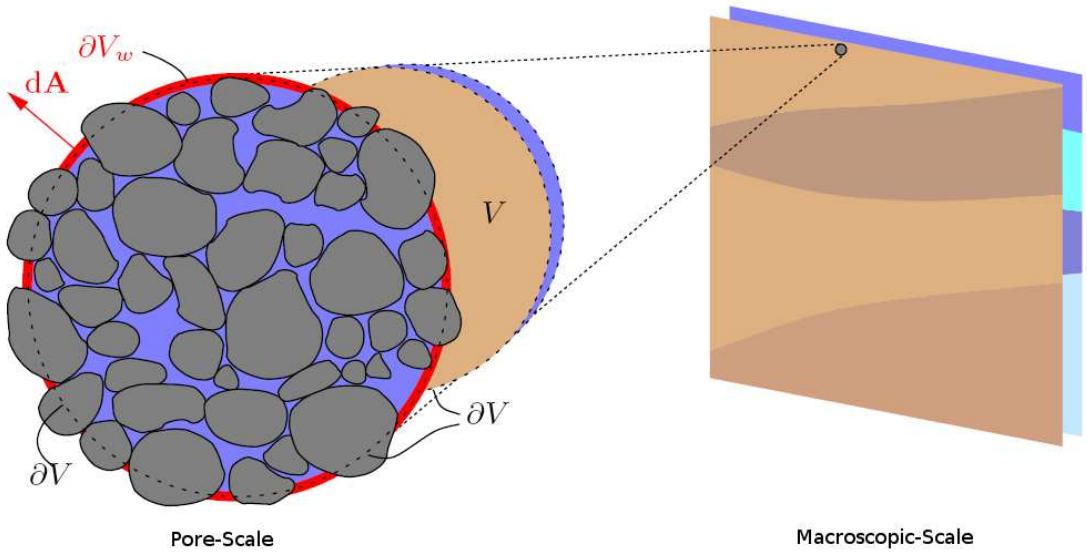

Figure. 1.1. Illustration of pore-scale and continuum scale (REV is marked) (adapted from Fig. 3.8 from Roth (2007))

1.2.1 Pore-Scale Modelling

The pore-scale or micro scale as the name suggests ranges from 10^{-6} to $10^{-3}m$, where individual pores enter the description. Flow at these scales is described by the specific geometry of the solid phase, which determines the boundary with the fluid phases and obeys the local conservation laws such as the Navier-Stokes equations. Given the appropriate boundary conditions for the surface of the solid grains (e.g. no-slip), the velocity and pressure field in the pore-space can be determined by solving the Navier–Stokes equation. Pore-scale modelling is more appealing as the approach is based on rigorous physics and it directly accounts for the fundamental physical processes that affect the fluid behaviour thus providing better understanding of flow and transport processes.In addition to that, pore-scale modelling offers ways to improve the prediction of macroscopic parameters which are difficult to measure experimentally. Despite its

attractiveness, the major difficulty involved in this approach is the presence of complex pore geometries. An accurate description of the pore geometries is essential for pore-scale modelling, which for intricate networks of pores is often very difficult.

1.2.2 Continuum-Scale Modelling

Typically continuum or macroscopic (or lab) scale is in the order of 10^{-2} to $10^{0}m$. In this scale, microscopic details in the pores are ignored and employs the volume averaged laws such as Darcy's law where the porous medium is considered as macroscopically uniform continuum. Owing to the difficulty to observe and characterise properties at the pore-scale, in this approach, a representative elementary volume (REV) (Bear 1972, Roth 2007) is considered and the effective macroscopic variables are defined by averaging the microscopic properties over this REV. Hence at the continuum scale, the concept of REV is very essential. Most of the laboratory experiments are conducted at this scale to obtain required parameters and hence it is widely used for modelling in porous media. The main difficulty with this approach is the requirement of accurate values of the macroscopic parameters (e.g. permeability, dispersion coefficients, capillary pressure, relative permeability etc.) which depend on the pore structure and pore-level physical processes. Furthermore, this approach does not take into account the pore geometries explicitly.

1.2.3 Field-Scale Modelling

Engineers and Hydrogeologists are concerned with practical problems involving flow and transport occurring at larger scales which is often referred to as field scale or regional scale in the order of kilometres. In this approach, large scale experiments are needed to characterise the highly varying heterogeneous porous system and they are often limited due to the expense and time. It is a common practise to apply the macroscopic continuum theory to field scale and use continuum parameters.

1.3 Motivation

The pore structure and the physical characteristics of a porous medium and the fluids that occupy the pore spaces determine several macroscopic or continuum parameters of the medium such as permeability and dispersion coefficients (Øren and Bakke 2003). Understanding the relation between the pore-scale properties and these continuum parameters is therefore a great interest both theoretically and practically in many fields. It is believed that the flow and transport processes depend strongly on the geometrical details of the porous media at the pore-scale while the physical properties of interest are observed at a larger scale. In this context, pore scale simulations can be used to

improve our understanding of the physical processes at the pore level and can provide a way to determine the macroscopic parameters. These parameters can in turn be used in continuum models which otherwise can only be found through expensive and time consuming laboratory or field scale experiments.

Recent advances in computational methodologies allow for the numerical simulation of flow and transport through arbitrarily complex geometries in three dimensions. Methods such as Lattice-Boltzmann, pore network models, discrete particle methods (smoothed particle hydrodynamics) and direct discretisation methods (standard finite element, finite volume, immersed boundary methods) have been developed and being improved over the years. However, at present none of these methods can fully satisfy the requirements for pore-scale simulations. For instance, pore network models use highly simplified geometries, Lattice Boltzmann method requires high computational power and is found inferior to finite element methods for low Reynolds number flows (Geller *et al.* 2006) and particle methods are often found very expensive. The direct discretisation methods like standard finite element and finite volume require highly refined grids to account for complex pore geometries while the structured grid approaches like immersed boundary and fictitious domain methods are yet to find wide interest in pore-scale simulations. Hence researchers are continuously looking for novel computational approaches suitable for pore-scale simulations. Moreover, new experimental technologies and high resolution imaging for porous media can provide three-dimensional structural details of porous materials with resolution approaching one micron. These techniques allow for direct observation of the pore space geometry and fluid configurations within the pores (Wildenschild *et al.* 2005, Kaestner *et al.* 2008). These advancements such as development of advanced numerical methods and high resolution imaging techniques are now helping researchers to make progress in the understanding of pore-scale processes and how they influence fluid transport at macroscopic scale.

1.4 Research Objectives

The main objective of this research is to simulate single phase flow and solute transport processes through porous media at the pore-scale and thereby improve the understanding of the influence of pore-scale properties on macroscopic flow and transport behaviour. In particular, the objective is to use a new numerical discretisation approach introduced by Engwer and Bastian (2005) for the solution of partial differential equations on complex domains to predict the macroscopic parameters of porous medium based on pore-scale simulations. The main advantage of this method compared to other direct discretisation approaches is that, it uses only a structured grid for the numerical discretisation and hence unstructured meshing of the complex pore geometries can be avoided. Among its benefits are the simplicity of a uniform structured grid and easy incorporation

of complex geometry via implicit function or level set methods. The method is also well adapted with the geometric description obtained from imaging techniques. These features are advantageous for fluid-flow problems in complex geometries. Moreover, this approach is locally mass conservative, a desirable property for transport simulation.

1.5 Thesis Outline

The rest of the thesis is organised as follows:

The second Chapter (2) briefly brush up the basic theory of fluid flow and transport where the governing equations of flow and transport in porous media and theory of hydrodynamic dispersion are discussed. In Chapter (3), a short description of various pore-scale modelling approaches is given. The fourth Chapter (4) presents the discontinuous Galerkin (DG) finite element methods in detail. DG discretisation of the model elliptic problem is given and its various formulations are described in this Chapter. In the fifth Chapter (5), discontinuous Galerkin discretisation of the steady Stokes equation is presented in detail. A brief discussion on previous works also given. The code development, implementation and verification using benchmark simulations are reported in this Chapter. The sixth Chapter (6) gives a background on numerical methods for complex domains and shortly describes the Unfitted Discontinuous Galerkin (UDG) method. Example numerical simulations using UDG are presented in this Chapter. It also contains the results of computation of permeabilities from pore-scale simulations and comparison with analytical and literature results. The seventh Chapter (7) describes the numerical simulation approaches for transport in porous media. The random walk particle tracking (RWPT) approach is described and code implementation, verification and test simulations are provided. The eighth Chapter (8) presents the results of pore-scale simulation of dispersion. Two and three dimensional simulations are presented and discussed in this Chapter. Finally in Chapter (9), summary and conclusions of the study are given.

2 Flow and Transport in Porous Media

As mentioned in the introductory Chapter (1), the problems involving porous media are enormous. Many of the natural, environmental and industrial problems are concerned with flow in porous media. Hence it is very important to understand the processes that take place inside a porous medium. This chapter is intended to provide the fundamentals of fluid flow and transport through porous media. The theory is explained very briefly and for details excellent lecture notes by Roth (2007), classic books by Bear (1972), Zheng and Bennett (2002) etc. are referred.

2.1 Porous Media

A porous medium consists of a solid matrix or skeleton with a large amount of tiny pores or voids in it. These microscopic pores within the matrix are typically connected, which allows various flow and transport processes to take place inside (Bear 1972). The interconnected network of pores is known as the *pore space*. Examples are natural substances such as soils, rocks, sandstone and industrial or artificial materials such as foam rubber, porous diffusion layer of a fuel cell, reactor beds etc. The Figure (2.1) shows an artificial and industrial porous medium. The porous materials are used in many areas of applied sciences and engineering such as soil mechanics, petroleum engineering, geosciences, biophysics, material science etc. and hence it is very important to study and understand the flow and transport through porous media. The pore structure of a porous medium and the physical characteristics of the matrix and the fluids that occupy the pore spaces influence the flow and transport processes. These processes are considered very complex in nature due to the intricacy found in the pore structure. The pores tend to have irregular surfaces, which is one of the reasons why fluid flow through them is so complex. Some of the pores make dead ends and influences the flow and transport behaviour significantly. The flow in porous media is referred to as *single phase flow* when only one fluid phase is flowing through the pores (for example in aquifers where the subsurface is saturated with water). When two or more phases flow through the pore spaces, it is referred to as *multiphase flow* or *two-phase flow* (if only two phases are present). Multiphase flow can occur in the unsaturated zone (for example in the case of spills of non-aqueous phase liquid (NAPL) resulting in NAPL and water phases), in petroleum recovery of hydro-carbons (system of oil, gas, water) and in many industrial contexts.

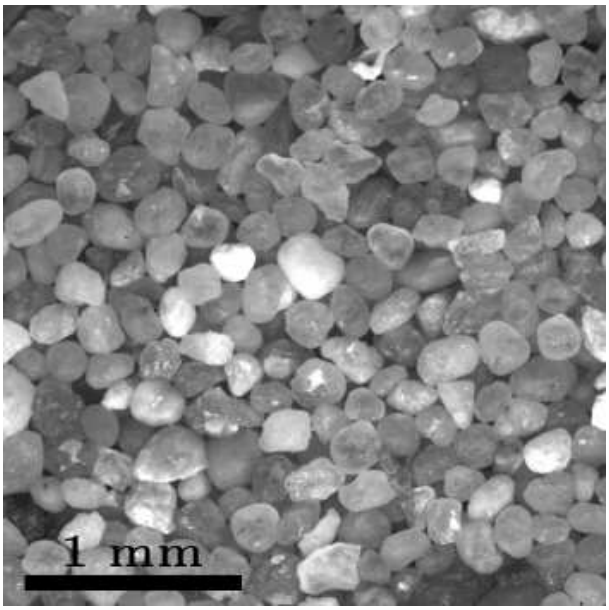

(a) Artificial porous medium created from sieved sand packed in a Hele-Shaw cell, a simple two-dimensional model (From Figure 3.1 of Roth (2007))

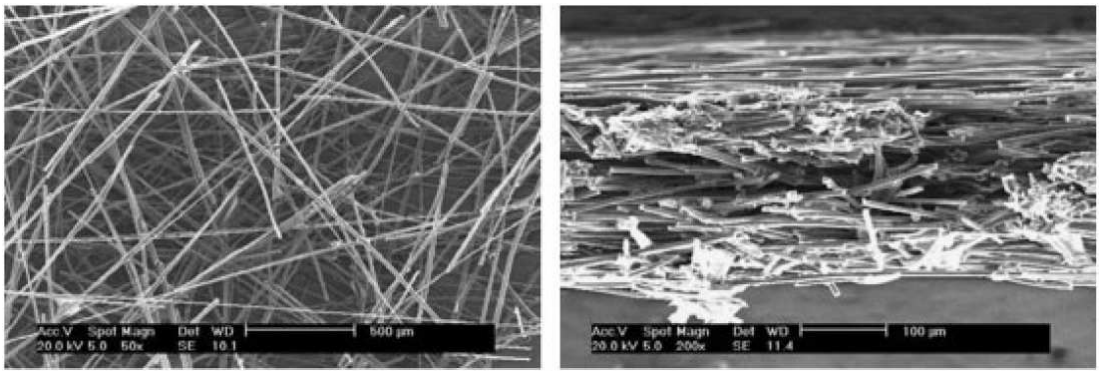

(b) Scanned electron microscopy micrograph of a porous gas diffusion layer in a PEM fuel cell (From Figure 3 of Van Doormaal and Pharoah (2008))

Figure. 2.1. Examples of porous media: an artificial and an industrial porous medium

2.2 Governing Equations of Fluid Flow in Porous Media

Fluid motion in a porous medium is governed by the conservation of mass, momentum, and energy. The simulation of flow in porous media is done widely using the momentum equation given in the form of Darcy's law (Darcy 1856), which is based on averaging (under the assumption of *continuum*). This macroscopically derived empirical law introduces the permeability parameter which must be obtained experimentally often with less accuracy. A more fundamental approach to porous media flow is to simulate the dynamics at the pore-scale described by Navier-Stokes equation. This is an important way to gain more insight into the fundamental processes and the macroscopic models.

However, this requires direct dealing with highly complex geometries of a porous medium. In this Section, we look at the governing equations of fluid flow in porous media.

2.2.1 Navier-Stokes Equations

In a porous medium, when a fluid starts moving (assuming single phase flow), friction develops at the fluid-solid interface and in fluid. The fundamental equation governing the motion of fluid in a porous medium at the pore-scale is described by the momentum balance equation. Together with the mass balance equation, the system of equations is known as Navier-Stokes equations. These are in fact the dynamical statement of the balance of forces acting at any region of fluid. For an incompressible Newtonian fluid with no other body forces than gravity, momentum balance equation is given by (Byron Bird *et al.* 1960, Roth 2007)

$$\rho\frac{\partial \boldsymbol{u}}{\partial t} + \rho(\boldsymbol{u}\cdot\nabla)\boldsymbol{u} = \rho\boldsymbol{g} - \nabla p + \mu\nabla^2\boldsymbol{u}. \tag{2.1}$$

where ρ is the density, $\boldsymbol{u}$ is the velocity, t is the time, p is the pressure, μ is the dynamic viscosity, and $\boldsymbol{g}$ is the gravitational acceleration. The mass balance equation is given by

$$\nabla\cdot(\rho\boldsymbol{u}) = 0; \tag{2.2}$$

which for incompressible flow becomes

$$\nabla\cdot\boldsymbol{u} = 0. \tag{2.3}$$

With appropriate initial and boundary conditions, the Equations (2.1) and (2.3) are well defined (Roth 2007). For a detailed derivation of the Navier-Stokes equations, we refer to standard text books of Batchelor (1970), Elman *et al.* (2005), Deville *et al.* (2002), Bear (1972) etc. The terms appearing in the Navier-Stokes equation (2.1) are explained in details below.

$$\overbrace{\rho\Big(\underbrace{\frac{\partial \mathbf{u}}{\partial t}}_{\substack{\text{Unsteady}\\ \text{acceleration}}} + \underbrace{\mathbf{u}\cdot\nabla\mathbf{u}}_{\substack{\text{Convective}\\ \text{acceleration}}}\Big)}^{\text{Inertia}} = \underbrace{-\nabla p}_{\substack{\text{Pressure}\\ \text{gradient}}} + \underbrace{\mu\nabla^2\mathbf{u}}_{\text{Viscosity}} + \underbrace{\rho\mathbf{g}}_{\substack{\text{Body}\\ \text{forces}}}$$

The term on the left of this equation represents the acceleration of the flow, while term on the right consists of the pressure force, the frictional force due to the viscosity and the body forces. The term $(\mathbf{u}\cdot\nabla\mathbf{u})$ is the convective acceleration term which can also be written as $(\mathbf{u}\cdot\nabla)\mathbf{u}$ and is often called the advection or convection term, while the term $\Delta\mathbf{u} = \nabla^2\mathbf{u}$ is called the diffusive or dissipation term. Note that the convection term is

nonlinear and the viscosity is represented by the vector Laplacian of the velocity field.

The kinematic form is obtained by dividing the Equation (2.1) by the constant fluid density ρ as

$$\frac{\partial \boldsymbol{u}}{\partial t} + (\boldsymbol{u} \cdot \nabla)\boldsymbol{u} = \boldsymbol{g} - \frac{1}{\rho}\nabla p + \nu \nabla^2 \boldsymbol{u}. \tag{2.4}$$

where $\nu = \left(\frac{\mu}{\rho}\right)$ is the kinematic viscosity of the fluid.

The Navier-Stokes equations describe the temporal and spatial evolution of an incompressible, Newtonian fluid movement in the void space of a medium at the pore-scale. At the pore-scale, given the geometry of the solid phase and surface properties and application of appropriate initial and boundary conditions, the equations can be solved to obtain the corresponding pressure and velocity field. This equation is a non-linear partial differential equation and the non-linear term $(\mathbf{u} \cdot \nabla)\mathbf{u}$ renders it difficult to solve analytically.

It is usually a convenient way to non-dimensionalise the variables by introducing scaling factors. Let the velocity $\mathbf{u}$ scales with the characteristic velocity U, ∇ scales with $1/L$ where L is a characteristic length, time t scales with L/U. Then, the dimensionless variables become

$$x' = \frac{x}{L}, \quad \mathbf{u}' = \frac{\mathbf{u}}{U}, \quad p' = \frac{p}{\rho U^2}$$

On substituting the primed variables into Equation (2.1) and rearranging the terms and dropping the primes, we obtain

$$\frac{\partial \mathbf{u}}{\partial t} + (\mathbf{u}.\nabla)\mathbf{u} = \frac{1}{\rho}(-\nabla p + \frac{1}{Re}\,\Delta \mathbf{u} + \mathbf{f}) \tag{2.5}$$

where Re is the Reynolds number,

$$Re = \frac{\rho L U}{\mu}. \tag{2.6}$$

In high-Reynolds-number flows, where typically $Re > 100$, the flow is dominated by the convective term and in low-Reynolds-number flows with $Re < 100$ the flow is dominated by viscous forces, i.e. the diffusion term. Looking at the Equation (2.5) we can observe that the Reynolds number represents a measure of the relative strength between the non-linear convective term and the viscous term. The higher the Re, the more important is the non-linear term in the dynamics of the flow. Since Navier-Stokes equations cannot be solved analytically (except in few simple cases), numerical approximation methods are necessary to solve them.

2.2.2 Stokes Equation

The flow of fluid in porous media under natural conditions (e.g. groundwater flow in the subsurface) is generally very slow, which allows to make important simplifications. The flow is assumed to be laminar and the Reynolds number is very small, i.e. much smaller than one ($Re \ll 1$). Flows at low Reynolds numbers are characterised by the fact that viscous effects dominate inertial ones. Hence the magnitude of $(\boldsymbol{u} \cdot \nabla)\boldsymbol{u}$ corresponding to inertial forces is small relative to that of the viscous forces $(\mu\nabla^2\boldsymbol{u})$ and the inertial term can be ignored. In addition, for many small-scale flow phenomena in porous media, external forcing varies slowly on the time scale of the internal dynamics (Roth 2007) making time irrelevant and hence the time dependent term $(\frac{\partial \boldsymbol{u}}{\partial t})$ in the equation of motion can also be neglected. Thus the combination of these assumptions leads to the simplification of the nonlinear, time-dependent Navier-Stokes equation (2.1) that govern general continuous fluid flows, to the linear incompressible stationary Stokes equations given as

$$-\nabla p + \mu\Delta\mathbf{u} + \rho\mathbf{g} = 0 \tag{2.7}$$

Such low Reynolds number flow is often called the *Stokes flow* or *creeping flow*. While still exhibiting the problem of the incompressibility, the Stokes problem is linear and does not contain a hyperbolic term. Hence it is the stationary linearised form of the Navier-Stokes equations and describes the creeping (low Reynolds number) flow of an incompressible Newtonian fluid.

The study of incompressible fluid flows in which viscous forces are either comparable with or dominate inertial forces has applications to many physical problems. Industrial, biological, and environmental processes often involve flows of low Reynolds number characterised by flow of slow viscous incompressible fluids. Sub-surface flows are often considered as creeping flows. At the pore-scale, when the flow is slow and laminar, the stationary Stokes equation can be used to describe the flow in porous media. The solution of Stokes equation is relatively easier to obtain than Navier-Stokes equations due to the absence of non-linear term.

2.2.3 Darcy's Law

Darcy's law is a phenomenologically derived constitutive equation that describes the flow of a fluid through porous media. This law was formulated by a French engineer, Henry Darcy (1856) based on the results of experiments on the flow of water through sand filters for a drinking water supply system for the city of Dijon, France. Through a series of experiments with sand-filled tubes, he was able to determine the factors that controlled the flow rate of water through the sand. He discovered one of the most important physical relationships in the science of porous media hydrodynamics, which

became known as Darcy's law:

$$q = -K\frac{\Delta p}{L} \tag{2.8}$$

where q is the specific discharge or volumetric flow rate per unit area of porous medium perpendicular to the direction of flow, and $\frac{\Delta p}{L}$ is the pressure gradient along the flow path. The proportionality constant K is the coefficient of permeability or hydraulic conductivity. By convention, the -ve sign implies that flow is along the direction of decreasing gradient. It should be noted that q has the dimension of velocity and is often called *Darcian velocity*.

Darcy's law is empirical, meaning that, it is not derived from first principles, rather the result of experimental observation. It is usually considered valid for creeping flow where the Reynolds number as defined for a porous medium is less than one. For instance, most subsurface flow (groundwater) cases fall in this category. Darcy's law is a macroscopic approach to the study of flow in porous media and in this equation, all the interaction between the fluid and the porous structure is lumped into a single parameter permeability tensor $\underline{\boldsymbol{K}}$. It should be noted that on a microscopic pore-scale level, there is no such thing as hydraulic conductivity or permeability.

Darcy's law is a vector relationship and can be extended to three dimensions. When the flow is three-dimensional, a Darcy's relation can be written for each of the directions For instance, in the case of a three dimensional isotropic medium, there are three equations:

$$q_x = -K\frac{\partial p}{\partial x} \tag{2.9}$$

$$q_y = -K\frac{\partial p}{\partial y} \tag{2.10}$$

$$q_z = -K\frac{\partial p}{\partial z} \tag{2.11}$$

In the case of anisotropic media, the permeability becomes a second order symmetrical tensor $\underline{\boldsymbol{K}}$ given as

$$\underline{\boldsymbol{K}} = \begin{bmatrix} K_{xx} & K_{xy} & K_{xz} \\ K_{yx} & K_{yy} & K_{yz} \\ K_{zx} & K_{zy} & K_{zz} \end{bmatrix} \tag{2.12}$$

Then the Darcy's law becomes

$$q_x = -K_{xx}\frac{\partial p}{\partial x} - K_{xy}\frac{\partial p}{\partial y} - K_{xz}\frac{\partial p}{\partial z} \tag{2.13}$$

$$q_y = -K_{xy}\frac{\partial p}{\partial x} - K_{yy}\frac{\partial p}{\partial y} - K_{yz}\frac{\partial p}{\partial z} \tag{2.14}$$

$$q_z = -K_{xz}\frac{\partial p}{\partial x} - K_{yz}\frac{\partial p}{\partial y} - K_{zz}\frac{\partial p}{\partial z}. \tag{2.15}$$

Notice that the potential gradients in one direction can yield flows in other directions. However, such situations are in practise not considered because it is not feasible to assess all permeability components in many cases.

It can be noted that the permeability K depends on the properties of the fluid as well as on the pore structure of the medium. We can write the permeability in terms of the so called *intrinsic permeability* κ (Roth 2007):

$$K = \frac{\kappa \rho g}{\mu} \tag{2.16}$$

where μ is the viscosity of the fluid, ρ is the density and $\mathbf{g}$ is the gravitational constant. The intrinsic permeability coefficient thus depends only on the micro-structural properties of the porous medium and is supposed to be independent of the properties of fluid. Now for the case of a single viscous fluid flowing through a porous medium and taking gravity into account, the Darcy's law can be written as

$$\boldsymbol{q} = -\frac{\underline{\boldsymbol{\kappa}}}{\mu}(\nabla p - \rho \mathbf{g}) \tag{2.17}$$

Darcy's law is well satisfied as long as the porous medium is sufficiently homogeneous and the flow velocity is sufficiently low such that the Reynold's number is always less than unity.

2.3 Theory of Solute Transport in Porous Media

In this section, the basic transport mechanisms of solute in porous media are discussed. In this study, the transport of ideal and inert (passive) solute that do not undergo decay is considered and hence reactive effects are not taken into account. Basically the transport of dissolved chemicals or solute is generally considered to be controlled by one or more of the following physical processes:

- Advection or Convection
- Molecular Diffusion
- Mechanical Dispersion

A brief explanation of these processes are given in the next Sections.

2.3.1 Advection

Advection (also called convection) is mass transport caused by the bulk movement of flowing fluid. If no other process acts, then the solute particles are simply moved at

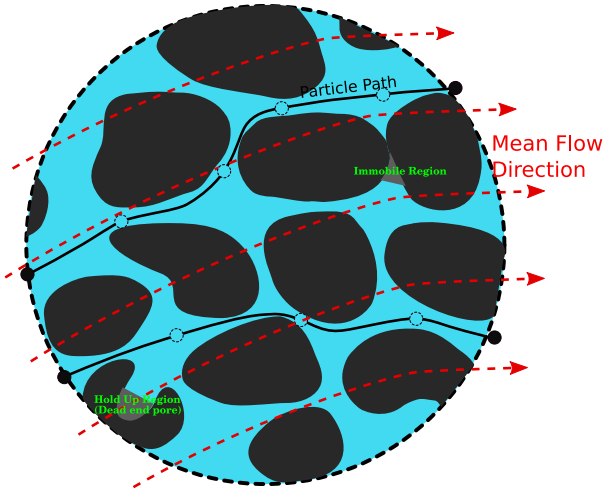

Figure 2.2: Advection (also called convection) is the transport due to average fluid velocity in a porous medium. Advective transport follows the streamlines.

average fluid velocity (Darcy's velocity). A schematic representation of advection process is shown in Figure (2.2). In this case, dead-end pores and recirculation zones are not accessible for particle path.

2.3.2 Molecular Diffusion

The transport of a solute from a region of higher concentration to a region of lower concentration is known as molecular diffusion. Diffusion is caused due to random molecular motion (Brownian motion) and will occur as long as a concentration gradient exists, even if the fluid is at rest. That is, it is independent of fluid velocity. The molecular diffusion is isotropic and acts very slowly. A schematic representation of diffusion process is shown in Figure (2.3). When spatial concentration gradients exist, diffusion is the net flux of solutes from zones of higher concentration to zones of lower concentration and the diffusive solute mass flux can be described by Fick's first law of diffusion. Under steady-state conditions the diffusive flux $\boldsymbol{J_m}$ is described by Fick's law as

$$\boldsymbol{J_m} = -D_m \nabla C \tag{2.18}$$

where D_m is the diffusion coefficient. For diffusion in water, D_m ranges from 1×10^{-9} to $2 \times 10^{-9} m^2/s$. The change of concentration over time inside a control volume subject to diffusion flux is given by Fick's second law:

$$\frac{\partial C}{\partial t} = D_m \nabla^2 C \tag{2.19}$$

Figure 2.3: Molecular diffusion: Primarily due to Brownian motion. When a concentration gradient exists, solute particles move in the direction of decreasing concentration.

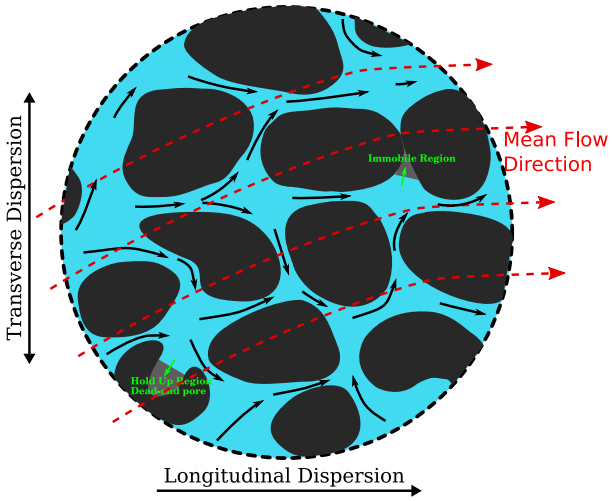

Figure 2.4: Dispersion: Dispersion is the spreading of the solute plume that occurs along and across the main flow direction due to advection, pore-scale mixing and diffusion.

2.3.3 Mechanical Dispersion

Mechanical dispersion in porous media refers to the spreading of a solute as it flows through the porous medium and is caused entirely by differential microscopic velocities in the pore spaces, for example, due to non-uniform velocity profile within a pore and variations in pore sizes (diameter and length).

On a microscopic scale, it is called pore-scale dispersion and is the result of deviations of microscopic velocity from the average flow velocity. Various factors contribute to these velocity variations at pore-scale such as:

- Fluid particles in the centre of a pore space travel faster than those near the pore walls (due to the parabolic velocity profile), see Figure (2.5(a)) and mixing occurs in individual pores due to viscous effects.
- Diversion of flow paths around individual grains of porous medium causes variation in average velocity among different pore spaces (see Figure 2.5(b)). The flow velocity is larger in smaller pores than in larger ones.

- The natural porous media render the flow paths in *sinuous* forms. Due to the *sinuousness* of individual flow channels, some pathways are longer than others (tortuous) (see Figure 2.5(c)).

Mathematically, mechanical dispersion is described the same way as diffusion (see Equation 2.18), i.e, the mass flux is assumed to be proportional to the concentration gradient.

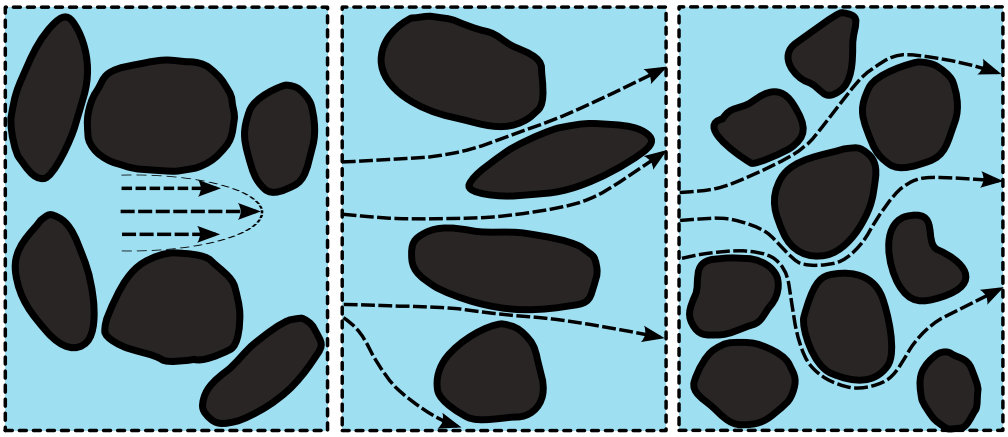

(a) Non-uniform velocity distribution in a pore cross-section (b) Different pore channel velocities (c) Changes in flow direction due to tortuous paths

Figure. 2.5. Mechanisms that cause velocity variations at pore-scale

2.3.4 Hydrodynamic Dispersion

Dispersion is considered to be the net result of (1) molecular diffusion (2) local velocity gradients within given pores (3) locally heterogeneous velocities and (4) mechanical mixing in pore bodies. In practise, it is almost impossible to separate the effects of mechanical dispersion and molecular diffusion. Hence the collective spreading due to both mechanical dispersion and molecular diffusion is usually referred to as hydrodynamic dispersion. The spreading is caused by both microscopic (pore-scale) and macroscopic effects. As explained previously, dispersion originates from the combined effects of pore tortuosity and differential velocities at the pore-scale. The porous medium is composed of tortuous pores in which fluid flows and transports. The transported quantities are then locally moved at velocities different than the average velocity. Due to the geometrical obstructions and interconnectedness of pore networks, the flow streams would split and rejoin at various pore junctions. These local flow and transport phenomena then result in a macroscopic mixing effect, which is called hydrodynamic dispersion.

The spreading along the direction of flow is called longitudinal dispersion and the spreading in directions normal to the flow is called transverse dispersion. For example,

in a three dimensional setting, solute introduced into a porous sample would move in the main flow direction, say x, and will undergo spreading parallel to the main flow (longitudinal dispersion) and dispersion parallel to other two directions y and z (transverse dispersion). Mechanical dispersion in transverse direction is much weaker process than in the longitudinal direction. At REV scale, dispersion can be described by equation analogous to Fick's law. The molecular diffusion coefficient D_m would be replaced by a dispersion coefficient D_L or D_T that becomes a phenomenological coefficient, which combines the effects of diffusion and mechanical dispersion. D_L and D_T respectively refer to longitudinal and transverse hydrodynamic dispersion coefficient.

In addition to mechanical dispersion and molecular diffusion, there are other pore-scale phenomena that can increase the hydrodynamic dispersion process such as re-circulation zones and eddy effects. Various mechanisms that can cause hydrodynamic dispersion or macroscopic mixing are listed below.

- Molecular diffusion

  If time scales are sufficiently long and flow is very slow, dispersion results from molecular diffusion.

- Mixing due to obstructions

  Tortuous flow channels due to the presence of grains or obstructions in a porous medium cause spreading and mixing of particles

- Dead-end pores

  The stagnant fluid regions introduced by dead ends in the porous matrix often can induce dispersion which is called holdup dispersion (see Figure 2.6(a)). Dead end pore volumes cause mixing because, as a solute front passes the pore, solute particles enter into the pore "pockets" by molecular diffusion. After the front passes, these solute particles will diffuse back into the channel flow and disperse.

- Recirculation zones

  Recirculation arising from flow restrictions (see Figure 2.6(b)) can cause dispersion effects.

- Boundary layer dispersion

  Solute particles may enter the boundary layer near the grain boundaries where fluid velocities are very small. Advection and diffusion may cause the particles to move into these layers, but due to very small velocities, diffusion can only allow them to escape from these regions.

- Eddies

  When the flow in the individual flow channels of the porous medium becomes turbulent, the resulting eddies cause mixing.

- Adsorption

Adsorption is the process where solute particles may deposit or remove material on the pore walls. This process often tends to flatten the concentration profiles.

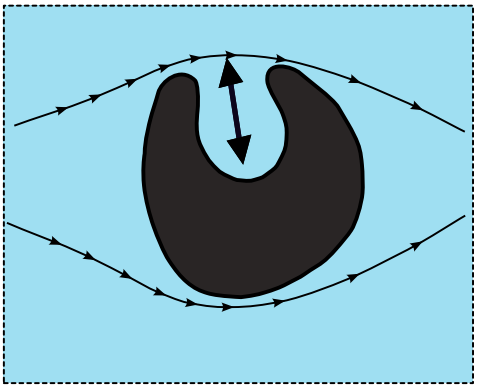

(a) Dead end pores induce holdup dispersion where solute particle diffuse into immobile fluid regions

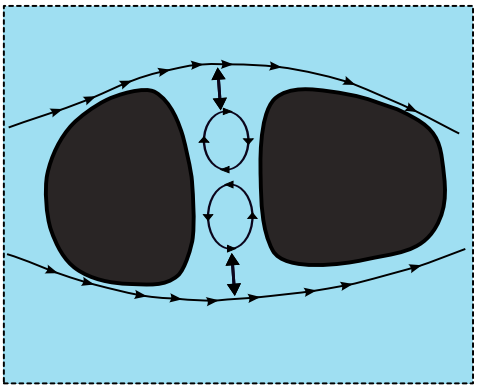

(b) Recirculation zones created by flow restriction

Figure. 2.6. Mechanisms that increase hydrodynamic dispersion: Dead end pores (holdup dispersion) and recirculation zones (Figure modified from Stöhr (2003)).

2.3.4.1 Péclet Number

The relative contribution of advection and dispersion (or diffusion) to solute transport is represented using a dimensionless number known as Péclet number (Pe). Pe can relate the effectiveness of mass transport by advection to the effectiveness of mass transport by either dispersion or diffusion, which is the ratio between typical time for dispersion (or diffusion) L^2/D and typical time for advection $L/\langle \mathbf{u} \rangle$. The Péclet number is thus given by

$$Pe = \frac{\langle \mathbf{u} \rangle L}{D} \tag{2.20}$$

where $\langle \mathbf{u} \rangle$ is the average velocity of the carrier fluid, L is the characteristic length and D is the hydrodynamic dispersion coefficient. At the pore-scale, D is the molecular diffusion coefficient D_m.

The nature of dispersion is controlled by the competition between advection, dispersion and molecular diffusion. Different regimes of dispersion can be identified according to the Péclet number (see Figure (2.7) taken from Batu (2006)). From Figure (2.7) it can be observed that the dispersion coefficient is strongly dependent on the average fluid velocity $\langle \mathbf{u} \rangle$ as well as on the geometrical properties of the porous medium, represented by the characteristic length L. For small Péclet number regime, at vanishing flow rates, the transport of solute is dominated by molecular diffusion. So as $Pe \to 0$, the dispersion coefficient approaches molecular diffusion coefficient, $D \to D_m$. For large

Pe regime, the transport is controlled by the advective effects. Here the solute velocity is approximately equal to carrier fluid velocity and molecular diffusion plays only a little role. In the intermediate range, both diffusion and mechanical mixing acts in the dispersion process.

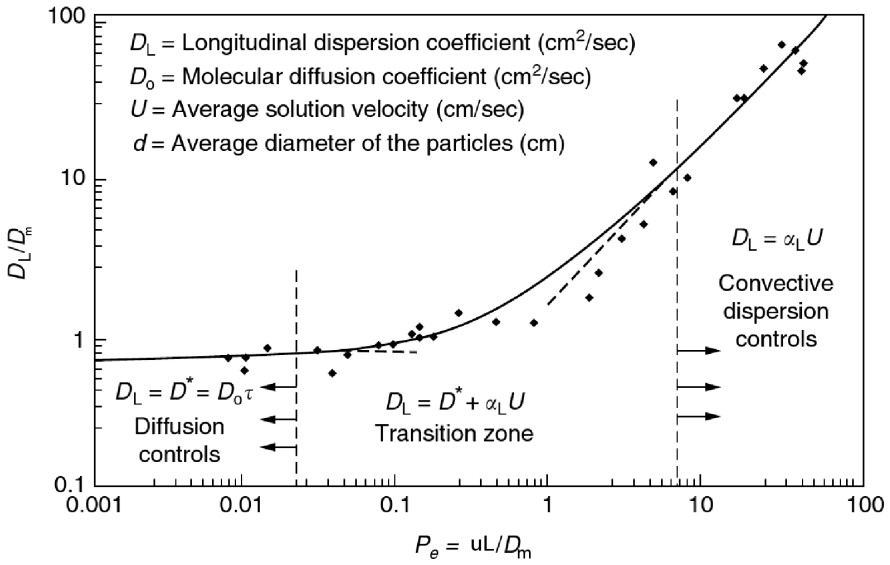

Figure. 2.7. Dimensionless longitudinal dispersion coefficient, D_L/D_m vs. Péclet number $Pe = \langle \mathbf{u} \rangle L/D_m$ (Figure 3-7 from Batu (2006)).

Notes:

- Molecular diffusion is an isotropic process whereas dispersion shows anisotropic behaviour even in simple isotropic medium. For example, in Taylor dispersion process longitudinal dispersion being always greater than the transverse dispersion.
- In general the dispersion coefficient is orders of magnitude larger than the coefficient of molecular diffusion.
- The coefficient of molecular diffusion is independent of the scale of observation, whereas the dispersion coefficient is scale dependent. Dispersion is observed to be increasing with the scale of observation.
- It is molecular diffusion which really causes the mixing process and dispersion mainly tries to increase its effect to larger area.

2.4 Advection-Dispersion Equation (ADE)

In general, the transport of a conservative solute in a rigid porous medium is described by the advection-dispersion equation (Bear 1972). Assuming a macroscopically homogeneous porous medium, the advection–dispersion equation on a representative

elementary volume (REV) is derived by combining a mass balance equation with an expression for the gradient of the mass flux (Bear (1972)). Here the key assumption is that dispersion can be represented by an expression analogous to Fick's second law of diffusion. Combining advective, diffusive and dispersive fluxes leads to

$$\frac{\partial C}{\partial t} = -\boldsymbol{u} \cdot \nabla C + \underline{\boldsymbol{D}} \nabla^2 C \tag{2.21}$$

which is called advection-dispersion equation (ADE). This is usually referred to as the classical or Fickian model of solute transport in porous media. Here effects of diffusion and dispersion are combined into a single tensor called hydrodynamic dispersion coefficient. In this equation, $\boldsymbol{u}$ is the velocity (of bulk motion of fluid) vector and $\underline{\boldsymbol{D}}$ is the macroscopic dispersion coefficient tensor with the form as shown below.

$$\underline{\boldsymbol{D}} = \begin{bmatrix} D_{xx} & D_{xy} & D_{xz} \\ D_{yx} & D_{yy} & D_{yz} \\ D_{zx} & D_{zy} & D_{zz} \end{bmatrix} \tag{2.22}$$

In one dimension, the advection–dispersion equation is given by (Bear 1972, Roth 2007)

$$\frac{\partial C}{\partial t} = -u \frac{\partial C}{\partial x} + D_L \frac{\partial^2 C}{\partial x^2} \tag{2.23}$$

where D_L denote the longitudinal dispersion coefficient. The solution of Equation (2.23) subject to the following initial and boundary conditions:

$$C(x, 0) = 0 \quad x \geq 0 \tag{2.24}$$

$$C(0, t) = C_0 \quad t \geq 0 \tag{2.25}$$

$$C(\infty, t) = 0 \quad t \geq 0 \tag{2.26}$$

is given by

$$C(x, t) = \frac{C_0}{2} \left[erfc\left(\frac{x - ut}{2\sqrt{D_L t}} \right) + exp\left(\frac{ux}{D_L} \right) erfc\left(\frac{x + ut}{2\sqrt{D_L t}} \right) \right] \tag{2.27}$$

where x is the distance from the injection point. The argument of the exponential term is the Péclet number ($Pe = ux/D_L$), which is the measure of the ratio of the rate of transport by advection to the rate of transport by diffusion as described in the previous Section. For large Péclet numbers ($Pe > 100$), the advection dominates and the second term in the right-hand side becomes negligible and the approximate solution becomes

$$C(x, t) = \frac{C_0}{2} \left[erfc\left(\frac{x - ut}{2\sqrt{D_L t}} \right) \right] \tag{2.28}$$

2.5 Hydrodynamic Dispersion Coefficients and Péclet Number

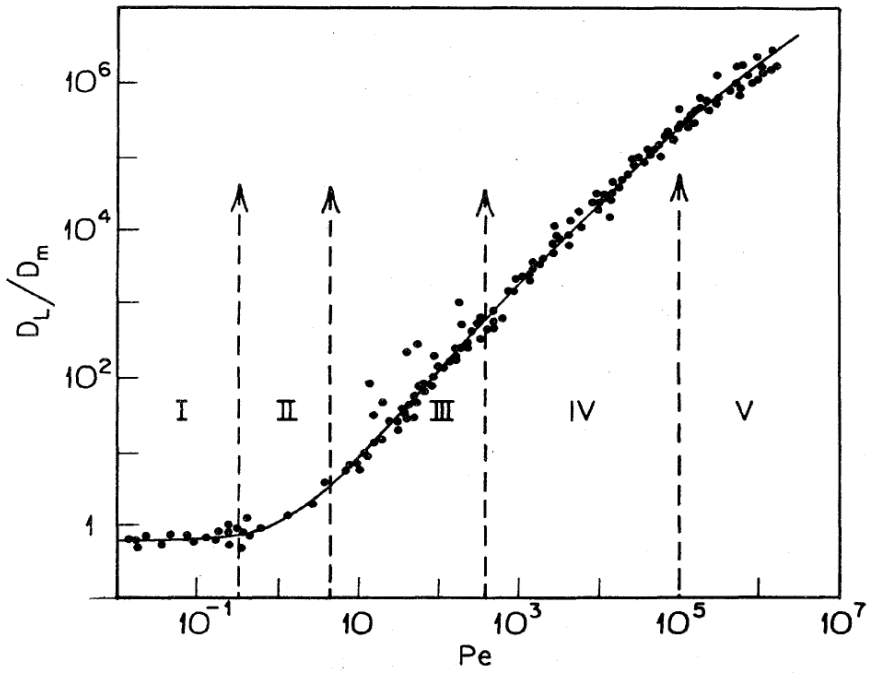

Figure. 2.8. Dependence of the dimensionless longitudinal dispersion coefficient $\frac{D_L}{D_m}$ on the Péclet number Pe with different Pe regimes marked (Fig. 36 from Sahimi (1993)).

The Figure (2.8) taken from Sahimi (1993), shows a compilation of measurements from several authors showing the dependence of the dimensionless longitudinal dispersion coefficient $\frac{D_L}{D_m}$ on the Péclet number Pe. Sahimi (1993) has classified the dependence of $\frac{D_L}{D_m}$ on Pe into different Pe regimes as marked in the Figure (2.8). In the following, the important laminar flow regimes are described.

$Pe \ll 1$

In this regime velocity is so slow that advective effects are negligible and dispersion is controlled almost completely by diffusion. The dispersion is isotropic and is given by

$$\frac{D_{L,T}}{D_m} = \frac{1}{F\phi}, \qquad Pe \ll 1 \tag{2.29}$$

where F is the formation resistivity factor, ϕ the porosity of the porous medium and subscripts L and T represent longitudinal and transverse dispersion respectively. For $Pe \to 0$, $\frac{D_L}{D_m}$ approaches the tortuosity factor (τ) which represents the long time diffusion coefficient in the pore-space. The tortuosity represents the resistance to diffusion through a porous medium due to the influence of the pore structure and account for the fact that the flow path is in general not straight. According to Bear

(1972), it is given by

$$\tau = \left(\frac{L}{L_e}\right)^2 = \frac{1}{F\phi} \tag{2.30}$$

$1 < Pe < 300$

This is the so called power law regime where dispersion due to diffusion from boundary layers are taken into account. The dispersion coefficients are described by the empirical relation

$$\frac{D_{L,T}}{D_m} = \beta Pe^{\delta}, \qquad 1 < Pe < 300. \tag{2.31}$$

It should be noted that another model sometimes found to be used in the literature is different where a logarithmic dependence of the form:

$$\frac{D_{L,T}}{D_m} = \beta Pe \ln Pe, \qquad 1 < Pe < 300 \tag{2.32}$$

is assumed.

$Pe > 300$

This is the mechanical dispersion regime where transport is dominated by convection and a linear dependence on Péclet number is assumed:

$$\frac{D_{L,T}}{D_m} = \alpha Pe, \qquad Pe > 300 \tag{2.33}$$

According to Sahimi (1993), there is another dispersion regime due to the hold-up dispersion. In this case, the solute is trapped in dead-end pores or low velocity regions, from which it can escape only by molecular diffusion giving a quadratic dependence on Pe:

$$\frac{D_{L,T}}{D_m} = \gamma Pe^2, \qquad \text{hold-up dispersion regime.} \tag{2.34}$$

Considering all these regimes, the scaling of asymptotic dispersion as a function of Péclet number in the laminar flow regime can be represented by (Sahimi 1993):

$$\frac{D_L}{D_m} = \frac{1}{F\phi} + \alpha Pe + \beta Pe^{\delta} + \gamma Pe^2 \tag{2.35}$$

or

$$\frac{D_L}{D_m} = \frac{1}{F\phi} + \alpha Pe + \beta Pe \ln Pe + \gamma Pe^2 \tag{2.36}$$

where the terms on the right are successively the molecular diffusion contribution, mechanical dispersion, dispersion due to diffusion from boundary layers and the hold-up dispersion. The first term $\frac{1}{F\phi}$ describes diffusion at very low Péclet numbers and depends on the formation resistivity factor F and the porosity ϕ of a porous medium.

In this Chapter, the basic concepts of flow and transport through porous media were introduced. Solute dispersion is one of the most important transport processes responsible for the spreading of contaminants in the subsurface because dispersion causes the solute to spread over a greater volume of porous medium than it would do simply based on the average flow (advection). The macroscopic parameters that quantify the solute dispersion in a porous medium are the hydrodynamic dispersion coefficients (longitudinal and transverse). Hence accurate values of these dispersion coefficients have to be estimated and is crucial for successful application of macroscopic models for practical problems. For instance, in order to obtain reliable results from contaminant risk assessment studies using advection–dispersion models, accurate values of dispersion coefficients have to be used in the numerical simulation codes.

3 Pore-Scale Modelling

3.1 Introduction

Pore-scale modelling is the fundamental approach to flow in porous media. In this approach, the physical processes acting on the pores also have been taken into account while modelling. That is, in contrast to macroscopic modelling where the real pore structure and the associated length scales are neglected and replaced by effective parameters, the pore-scale modelling directly account for pore geometries. Recently many studies of flow and transport in porous media are motivated by the central question of how does microscopic geometric structure of the medium influences the effective macroscopic transport parameters (Acharya 2004)? Hence in order to understand the dependence of complex pore geometry on macroscopic parameters, it is necessary to study the flow and transport processes at the pore-scale and to describe their overall influence on the macroscopic scale. Furthermore, pore-scale modelling provides a way for the parametrisation of macro-scale constitutive relationships that in effect govern the success of many flow and transport models. The quality of these constitutive relationships is a controlling factor in the accuracy of the results obtained by the continuum-scale model. Since these constitutive relationships are the result of averaging the pore-scale processes to obtain continuum scale relationships, pore-scale modelling can be used to obtain these relationships. The prediction of macroscopic transport properties from their microscopic origins requires in general two main steps (Øren and Bakke 2003): 1. Geometric description of the complex pore structure of the porous medium. 2. Exact or approximate solutions of the equations that govern the flow and transport behaviour. However, due to the tortuous nature of the pore-scale geometry, modelling processes at this scale is a difficult task which requires techniques for obtaining quantitative description of the complex pore geometries and numerical methods capable of handling it.

Since hydrogeologists and engineers are typically interested in flow and transport at scales much larger than that of a single pore, for most practical applications a continuum scale is preferred. At the continuum scale flow is described by an equation based on Darcy's law and mass transport by the advection–dispersion equation where both equations are satisfied by bulk averaged fluxes. However, flow and transport mechanisms at the pore-scale is often essential for better understanding of phenomena observed at larger scales. For instance, the presence of stagnant zones may affect the transport and

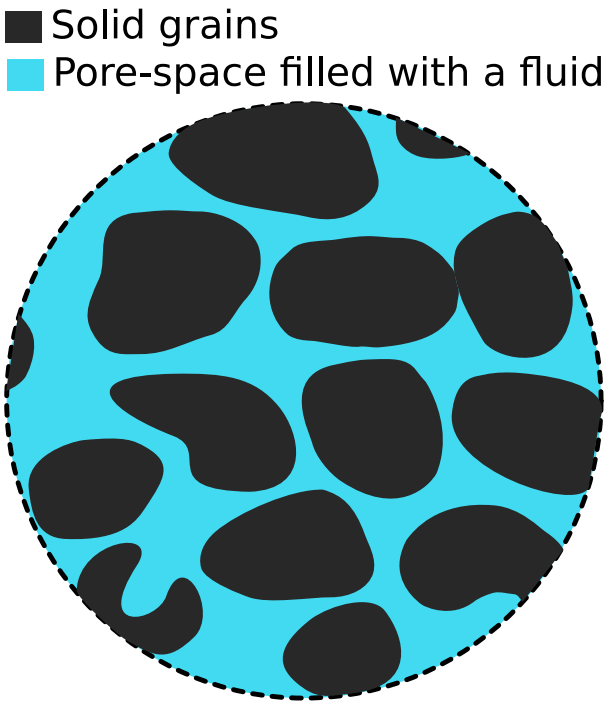

Figure 3.1: Schematic representation of a porous medium geometry at the pore-scale. In this scale, at each point either a solid phase or a fluid phase exists with distinct phase boundaries.

dispersive mixing. Pore-scale modelling can be used to observe these processes and their impact on macroscopic hydrodynamic dispersion. However, the geometry of actual porous media is very complex and the solution of Navier–Stokes or Stokes equations on such complex geometry is indeed a difficult task. Hence numerical methods capable of handling complex pore geometries are needed to make pore-scale simulations.

3.2 Pore-Scale Geometry

The pore-scale is characterised by the solid grains of the porous medium and the void space filled with fluid (see Figure (3.1)). The fluid occupying the pore-space can be described with fundamental quantities such as density, viscosity etc. On the pore-scale, since the features of the pore boundaries are available it is possible to directly take the known pore space geometry and combine with the appropriate boundary conditions to describe the flow (solution of mass and momentum balance equations) of fluids in the pore space.

3.3 Current Approaches To Pore-scale Modelling

Pore-scale modelling approach has been increasing for past few years. Advancements in high performance computing, development of new efficient numerical schemes and high resolution imaging to obtain accurate description of porous media are few reasons for the increased interest. Once the pore geometry is determined, numerous methods

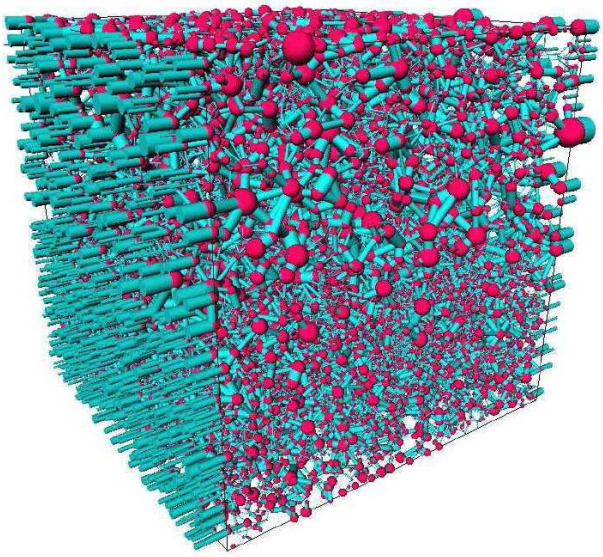

Figure 3.2: Graphical illustration of a pore network model showing pore bodies and pore throats (from Figure 4 of Aarnes *et al.* (2007)).

for modelling are available such as pore network modelling, Lattice-Boltzmann method, smoothed particle hydrodynamics (SPH) and traditional finite element methods. In the following Section, some of these methods are shortly explained.

3.3.1 Pore-Network Modelling

Pore network models are generally based on the attempts to idealise pore geometry into a hydraulically similar but much simpler geometries (i.e., spheres, cylinders, etc.) in a regular network. It uses simple flow models such as Poiseuille flow for governing the dynamics in the pore-spaces which are collection of tubes or similar geometric shapes. In the beginning, the network models used only spheres and cylindrical throats but recently much more realistic geometries have been used (Pan *et al.* 2001, Vogel *et al.* 2005). An illustration of the pore network representation (taken from Aarnes *et al.* (2007)) showing pores and pore bodies is given in Figure (3.2). In this method, the processes of interest are simulated in individual pores, and information at the pore scale is summed up and averaged to the continuum scale. Hence by applying rules that govern the flow and transport of fluids in pores and throats, macroscopic properties are estimated across the network, which typically consists of several thousand pores and throats representing a porous sample. Pore network models typically require less computational resources compared to other pore-scale approaches. The main disadvantage of this approach is that it assumes the pore geometry can be idealised as a network, which does not hold in general. Moreover, the surface processes cannot be properly taken into account as the surface is not accurately represented.

3.3.2 Lattice-Boltzmann Modelling

Lattice-Boltzmann (LB) methods have become very popular in the simulation of flow and transport for last two decades. Many authors have demonstrated the use of the LB methods for simulating flows in complex geometries and in particular for flow and transport in porous media (Spaid and Phelan 1997, Maier *et al.* 1998, Pan *et al.* 2001, Manwart *et al.* 2002, Pan *et al.* 2004, Vogel *et al.* 2005, Pan *et al.* 2006). It is a space discrete particle model where the governing PDEs are not solved directly instead movement and collision of a number of fictitious particles in a lattice is tracked. The fundamental idea behind the LB method is the construction of simplified kinetic models that incorporate the essential physics of pore-scale processes. The advantages of LB method are that it can account for complex geometry and implementation of boundary condition is easy due to the simplicity of the bounce back boundary condition. The method also allows easy parallelisation to speed up the computation. However, the scheme is found to be unstable for advection dominated problems (Zhang and Lv 2007). Traditionally LB methods only allow structured meshes and hence high resolution lattice are needed to handle real complex geometries which in turn increases computational and memory requirements.

3.3.3 Particle Based Methods

Particle based methods such as smoothed particle hydrodynamics (SPH) involve the discretisation of the Navier-Stokes equations spatially, leading to a set of ordinary differential equations (ODEs) with respect to time, which are solved via time integration (Zhu and Fox 2002, Tartakovsky *et al.* 2007). SPH is a mesh-free particle method that is Lagrangian in nature. The particle nature of SPH models allows multiphase interface problems to be modelled through simple particle-particle interactions, which allows for simulations of surface tension and well defined contact angles under both static and dynamic conditions. However, SPH is computationally intensive and implementation of prescribed boundary condition is considered difficult.

3.3.4 Direct Numerical Simulation

Traditional numerical methods such as finite difference, finite element and finite volume methods which directly discretise the governing partial differential equation on a computational domain may also be used for pore-scale simulation. However, they are not widely used for pore-scale simulation. The main reason for the lack of interest in applying such methods is that these classical numerical methods require a computational grid resolving the complicated boundaries of the porous medium at pore-scale. Generating such a boundary fitted or conforming grid is a highly involved process especially if coarse grids (to reduce the number of unknowns) and high quality solution are required

in three dimensions. The quality of triangulation affect the quality of solution. Geller *et al.* (2006) reported a comparison of the accuracy and computational efficiency of the Lattice–Boltzmann and the finite element method for incompressible laminar flows in two-dimension. In their study, the Lattice–Boltzmann methods perform equally well for incompressible unsteady problems, but for stationary laminar flows in complex geometries, finite element method is faster in solving Navier-Stokes equation than the Lattice Boltzmann Method. This is indeed the case for porous media flows where most often the flow is slow and laminar.

Recently Engwer and Bastian (2005) introduced a new approach called Unfitted Discontinuous Galerkin (UDG) to solve partial differential equations in complex geometries. The method is based on a structured grid and a discontinuous Galerkin discretisation of the governing PDEs. This scheme is attractive for pore-scale simulations because it is able to handle the complex geometry relatively easier than the standard finite element and with minimum number of unknowns (Engwer *et al.* 2008). In this thesis, this method has been used for the solution of the Stokes system at the pore-scale. The UDG approach is described briefly in Section (6.5.1).

4 Discontinuous Galerkin Finite Element Methods

The mathematical models are invaluable tool for engineers and scientists to study complex systems involving physical, chemical and biological processes and are being used extensively in science and engineering. These models are mostly described by partial differential equations (PDEs). The PDEs which represents practical problems arising in the field of science and engineering are often coupled and nonlinear and obtaining analytical solutions to such equations are very difficult or even impossible. Therefore, in practise, approximate solutions are sought and are obtained by use of numerical techniques. There are various numerical techniques to obtain the approximate solution of PDEs and the method is chosen based on the physical behaviour of the given problem i.e., on the type of PDE such as parabolic, elliptic and hyperbolic that models the system under study. Since PDEs are central to any mathematical model, an efficient numerical solution of PDEs plays an ever increasing role in the field of modelling and simulation. The numerical methods for obtaining approximate solutions to PDEs are generally based on the discretisation of the continuous problem. Some of the well known numerical schemes are finite difference methods, finite volume methods and finite element methods. A brief description of these methods is given in the next Section. For an elaborate reading on PDEs and numerical methods one can refer to standard text books by Grossmann *et al.* (2007), Braess and Schumaker (2007), Knabner and Angerman (2003), Schäfer (2006) etc.

4.1 Numerical Methods for Solving PDEs

Historically, finite difference (FD) methods were the first to be developed and applied (Thomée 2001). In finite difference methods, the solution is approximated by appropriate grid function on a uniform mesh. The function is defined only at a finite number of grid points on the domain and its boundary. The derivatives in the equations are approximated by Taylor series expansion, which results in an algebraic equation for each grid point. The finite difference method is the most simplest among all numerical methods and is very effective for simple geometries. The main drawback of this method is the difficulty of adapting the mesh to a complex domain.

The finite volume (FV) methods are a class of discretisation schemes for the approximation of conservation equations and was originally developed as a special finite difference formulation (Versteeg and Malalasekera 2007). The finite volume method consists of discretising the whole domain into small control volumes and differential equations are integrated over these individual volumes. The terms in the equations are approximated to get algebraic equation for each control volume. One advantage of the finite volume method over finite difference method is that it does not require a structured mesh to define the control volumes and hence effective for complex domains. However, finite volume method has low order of accuracy as it uses a piecewise constant approximation.

The finite element (FE) method is at present the most popular method to solve PDEs. In this approach, the domain is divided into finite number of elements, which can be structured or unstructured. It is based on the variational formulation of the differential equations and it uses simple piecewise functions such as linear or quadratic on the elements to describe the local variations of unknown variables. The substitution of the piecewise approximating functions into the equation will not hold exactly and will result in a residual. This residual and hence the errors are minimised by multiplying them by appropriate weighting function and integrating over the domain. This procedure results in a set of algebraic equations for the unknown coefficients of the approximating functions. The finite element method is well suited for complex domains. One of the reasons for its well acceptance is that it rests upon rigorous mathematical foundation (Ciarlet and Lions 1991).

The discontinuous Galerkin (DG) methods in general refer to finite element approaches that allow for discontinuities in the approximating spaces. Although the DG method was introduced by Reed and Hill (1973) for hyperbolic equations, over the years, these methods have emerged as a powerful tool for solving wide variety of problems. The main reason attributed to this explosion of interest in DG method is that allowing discontinuities in the finite element approximation gives tremendous flexibility (Dawson 2006). DG methods combine the features of finite element and finite volume methods and have been successfully applied to all class of PDEs arising from variety of application areas. Unlike the standard finite elements, DG methods do not require continuity of the approximating functions across the inter-element boundaries, instead, the continuity is enforced weakly. This makes it possible to use spaces of discontinuous piecewise polynomials and facilitates the development of higher order accurate methods using structured, unstructured and non-conforming grids.

All the numerical approximation methods produce a linear system of equations for the unknowns and these equations are then solved by using appropriate numerical techniques such as Gaussian elimination or iterative procedures. The number of equations in this system is as large as the number of degrees of freedom in the discretisation. The

system can be written algebraically as

$$A\boldsymbol{x} = \boldsymbol{b}$$

where A is the coefficient (stiffness) matrix, $\boldsymbol{b}$ is the given right-hand side vector and $\boldsymbol{x}$ is the vector of unknowns. It should be noted that the numerical solution of a linear system of the form $A\boldsymbol{x} = \boldsymbol{b}$ is, thus, an essential part of the numerical solution of PDEs.

This Chapter describes the discontinuous Galerkin finite element method in detail and gives a brief literature review highlighting its developments over the years. The DG discretisation of the model elliptic equation is also given and formulation of various interior penalty (IP) methods are shown. At the end, a brief comparison between standard (continuous) and discontinuous Galerkin finite element method is given.

4.2 Literature Review on Discontinuous Galerkin (DG) Methods

Ever since Reed and Hill (1973) introduced the discontinuous Galerkin (DG) method for hyperbolic equations in 1973, it has been growing steadily in various areas of application and a substantial quantity of literature on DG methods is available for reference. For a detailed history one can look up the paper from Cockburn *et al.* (2000). They have given extensive historical review of DG methods appeared until year 2000. A short description is given here.

In 1973, Reed and Hill (1973) introduced the discontinuous Galerkin method for first order hyperbolic problems and used it for solving the neutron transport equation. The DG methods have been developing ever since then. In 1974, LeSaint and Raviart (1974) performed the first numerical analysis of DG methods for a linear advection equation and derived *a priori* error estimates for DG methods applied to linear hyperbolic problems in 2D. Independent of this, in the 1970s the first version of the discontinuous Galerkin method for elliptic problems appeared (Wheeler 1978, Arnold 1982), using discontinuous ansatz functions and non-conforming meshes (Arnold *et al.* 2000; 2001). The idea of DG methods for elliptic equations originated from Nitsche's work in 1971 (Nitsche 1971). Instead of enforcing the Dirichlet boundary conditions strongly in standard finite elements, Nitsche applied it weakly by using *penalty terms*. In 1973, Babuška and Zlamal (1973) proposed an application of the penalty term for imposing the boundary conditions weakly for finite element methods. Motivated by Nitsche's work, Wheeler (1978) proposed penalty term for the enforcement of inter-element continuity for second order elliptic equations. These methods are often referred to as *interior penalty* (IP) methods. The IP method was then considered by Arnold (1982) to solve parabolic equations and nonlinear elliptic equations.

DG methods were not used extensively in the 1980s and early 1990s due to various reasons such as lack of computational power and efficient solvers (Arnold *et al.* 2000). Since mid 1990s and later 1990s DG methods have been gaining attention to a variety of problems. In the late 1990s, Baumann (1997) and Oden *et al.* (1998) introduced a non-symmetric DG method for solving convection-diffusion problems. In 1997, Baumann (1997) in his PhD thesis introduced a discontinuous Galerkin method especially suitable for elliptic problems, which is non-symmetric and does not require a penalty term. Their method was later known as *Oden-Babuška-Baumann* (OBB) method. Baumann and Oden (1999b;a; 2000) further enhanced this method and applied to various problems. Since the formulation of OBB results in a positive definite stiffness matrix, it is more stable and robust than the symmetric DG formulation. Also it exhibits a property of local mass conservation at element level, which is very important for solving convection–diffusion problems. Rivière *et al.* (1999) and Rivière (2000) introduced a variation of the OBB method with interior penalties, the so-called non-symmetric interior penalty Galerkin (NIPG) method, which contains an additional penalty term. In the study of compatibility condition of algorithms for coupled flow and transport, a new discontinuous Galerkin method called Incomplete Interior Penalty Galerkin (IIPG) was proposed by Dawson *et al.* (2004). This method was analysed for the solution of flow and chemical transport processes in porous media by Sun (2003).

In 1997, Bassi and Rebay (1997) proposed a DG formulation for the compressible Navier-Stokes equations. Based on this work, Cockburn and Shu (1998; 2001) introduced the local discontinuous Galerkin method (LDG). The idea of the LDG method was to introduce new auxiliary variables and rewrite the original equation into several first order equations. That is, in the LDG, besides the primary variable, the flux also appears as unknown. The LDG method is locally mass conservative.

Arnold *et al.* (2001) provided a unified analysis of several discontinuous Galerkin methods for the numerical treatment of elliptic problems with a common theoretical framework. The relationship between various DG schemes such as LDG, OBB, SIPG etc. was studied in their analysis. They obtained optimal error estimates for all existing DG methods. Castillo (2002) followed Arnold *et al.* (2001) and analysed the methods from a practical point of view. They compared the performance of several discontinuous Galerkin (DG) methods for elliptic partial differential equations (PDEs) on a model problem.

The discontinuous Galerkin method (DG) is an attractive scheme for problems dealing with fluid flow and transport through porous media because of its local mass conservation property. In addition, DG methods allow higher order approximation. Plenty of literature is available on DG methods and its application to flow and transport problems. Bastian and Reichenberger (2000) presented a higher order discontinuous Galerkin finite element approach to the groundwater flow equation and applied multigrid methods in two and three dimensions for the solution of the arising linear systems. They

have shown that the approximation using DG is considerably more accurate than a vertex centered finite volumes and it is even competitive with the mixed finite element methods. Bastian (2003) applied higher order discontinuous Galerkin methods based on the method of Oden *et al.* (1998) (OBB) for elliptic, hyperbolic and parabolic equations which describes single-phase and two-phase flow in porous media. In the work by Bastian and Rivière (2003), a post-processing method for the discontinuous Galerkin (DG) velocity approximations that preserves the local mass conservation property was proposed. The projected velocities have additional property of continuous normal component and numerical experiments have shown that the accuracy of the DG velocity field is maintained. Bastian and Rivière (2004) have introduced DG methods for the incompressible two-phase flow problem and applied to a total pressure-saturation formulation for two-phase flows.

In the last decades, several researchers have been working with the development of discontinuous Galerkin (DG) methods for the numerical approximation of incompressible fluid flow problems. One of the difficulties in obtaining numerical approximation of the Stokes system is the enforcement of the incompressibility condition on the velocity. This numerical difficulty is called *locking* and is the result of violating certain conditions when continuous approximations of the velocity is used. The point-wise enforcement could yield an over-constrained velocity and the only divergence-free function might then be zero (Cockburn *et al.* 2002).

In the 1990s, Baker *et al.* (1990) and Karakashian and Jureidini (1998) studied piecewise solenoidal discontinuous Galerkin method for the Stokes and Navier–Stokes equations and showed how to enforce the incompressibility condition point-wise inside each element and obtain optimal error estimates. They achieved this by using interior penalty approximation with discontinuous piecewise divergence–free velocities. However, their approach required to use continuous pressure approximation. Moreover, this method required different computational meshes to be considered for velocity and pressure to ensure stability. Recently Karakashian and Katsaounis (2006) extended this method to the incompressible Navier–Stokes equations in which velocity field is approximated using piecewise polynomial functions that are totally discontinuous across inter-element boundaries and which are point-wise divergence-free on each element (locally solenoidal). The pressure is approximated by standard continuous piecewise polynomial functions and a special weak formulation is designed to account for the inter element jumps.

Hansbo and Larson (2002) introduced an interior penalty DG method and studied the h-approximation for incompressible and nearly incompressible elasticity. They used the interior penalty (IP) method for the viscous term and approximating spaces of polynomial degrees k and $k-1$ for the velocity and the pressure respectively. That is, the approximation degree for the pressure is of one order less than that of the velocity. They derived the optimal error estimates in h, which remain valid in the incompressible

limit.

Filippini and Toselli (2002) proposed and analysed a domain decomposition method on non-matching grids for hp finite element approximations of the Stokes problem in two-dimensions. They proved an *inf-sup* stability result for a DG approximation of Stokes equations on non-matching grids.

Toselli (2002) proposed DG approximation together with suitable finite element spaces consisting of discontinuous velocities and pressures for the Stokes problem. The bilinear form was non-symmetric in this formulation and showed better stability properties than the continuous Galerkin approximation and uniform divergence stability was proved when velocity was approximated one or two degrees higher than pressure. With equal order approximation, there were no spurious pressure modes but no uniform stability properties were proven.

Cockburn *et al.* (2002) studied a local DG approximation of the Stokes problem in mixed form where the Stokes equation was rewritten as collection of conservation laws. Instead of imposing the incompressibility condition point wise inside the elements this condition was imposed weakly as in standard mixed methods. The fluxes were introduced as additional unknowns and appeared to have stabilising effect. They proved optimal error estimates for h approximation and showed that the local DG methods can easily handle meshes with hanging nodes and elements of general shapes. In addition to that they proved an *inf-sup* condition for equal approximating polynomial degree for the velocity and pressure by adding a stabilisation term to the discretised divergence-free constraint.

Schötzau *et al.* (2003), presented an unifying abstract framework for the analysis of mixed hp discontinuous Galerkin finite element approximation of the Stokes problem by employing the equal-order formulation with an interior penalty (IP) discretisation of the Laplacian.

Shahbazi *et al.* (2007) proposed the first DG approach to unsteady incompressible Navier–Stokes equations. Their approach was based on a semi-explicit temporal discretisation in which the convective term was treated explicitly while the Stokes operator was treated implicitly. The method employed a high-order DG spatial discretisation on triangular and tetrahedral elements in two and three dimensions respectively. They have used the IP method for the viscous term and used both equal and mixed order formulation.

Lazarov and Ye (2007) derived and studied discontinuous Galerkin approximation of the Stokes and linear elasticity (in the incompressible limit) equations as stabilisation schemes for certain saddle point problems. They studied two type of discretisations, one that leads to a symmetric problem and other that produces a non-symmetric linear system. Optimal error estimates were obtained and both methods were found to have the same advantage of LDG methods by using discontinuous functions. An additional

advantage was that their method had less number of unknowns compared to LDG as they did not introduce additional variables.

For the steady state Navier-Stokes equations, a totally discontinuous finite element method was formulated in (Girault *et al.* 2005a). They established optimal *a priori* estimates for totally discontinuous family of approximations of the steady incompressible Stokes and Navier Stokes equations in two-dimensions. Both non-symmetric and symmetric formulations were considered and discontinuities were balanced by inserting suitable jump terms. In a follow up paper, Rivière and Girault (2006) derived an improved *inf-sup* condition for a class of discontinuous Galerkin methods for solving the steady-state incompressible Stokes and Navier-Stokes equations. In their study, the computational domain was subdivided into sub-domains with non-matching meshes at the interfaces. Optimal error estimates were obtained and Numerical experiments including two benchmark problems were presented. They also compared several numerical schemes (symmetric versus non-symmetric) and obtained numerical convergence rates.

As we can see from the literature review, the discontinuous Galerkin (DG) methods have a long history and have become more and more popular recently. Further improvements are being introduced and are being applied to various types of problems. The main idea of DG methods is in the choice of approximation spaces consisting of piecewise polynomial functions with no inter-element continuity constraints. Consistency and well-posedness are achieved by introducing suitable bilinear forms defined on the interface. DG methods are closely related to finite volume methods as they rely on the definition of numerical fluxes. Similar to conforming finite element approximations, the corresponding discrete problem is given in terms of finite dimensional subspaces and bilinear forms (Schötzau *et al.* 2003). Hence they combine the advantages of both finite element and finite volume approximation.

4.3 Model Problem

In this Section, the continuous and discontinuous Galerkin discretisation of a standard model elliptic problem are presented. For most of the information in this Section, we referred to Brenner and Scott (2002), Morton and Mayers (2005) and Elman *et al.* (2005).

Consider the Poisson equation, which is the standard model problem for elliptic boundary value problems. For simplicity we consider the problem in two dimensions (2D) with homogeneous Dirichlet boundary condition. Let $\Omega \subset \mathbb{R}^2$ be an open, bounded and connected Lipschitz domain with a smooth boundary $\partial\Omega$. Let $f : \Omega \to \mathbb{R}$ be a given function. We seek a twice differentiable function u that satisfies the elliptic boundary

value problem given as

$$\begin{aligned} -\Delta u &= f \quad \text{in} \quad \Omega \\ u &= 0 \quad \text{on} \quad \partial\Omega. \end{aligned} \tag{4.1}$$

The Δ is known as the *Laplacian operator* and is the sum of second derivatives as given below

$$\Delta = \nabla^2 = \frac{\partial^2}{\partial x^2} + \frac{\partial^2}{\partial y^2}$$

4.3.1 Standard Finite Element Discretisation

Let us first consider the standard Galerkin finite element discretisation of the model problem (4.1). The first step in the finite element discretisation is the reformulation of the differential form (4.1) to the so called *variational form* and use this as a basis for the discretisation. The variational form is obtained using *Green's formula or Greens Identity*, a generalisation of the *integration by parts formula* to higher dimensions.

The Green's formula in its standard form is given as

$$\int_\Omega \nabla v \cdot \nabla u \, d\Omega = -\int_\Omega v \Delta u \, d\Omega + \int_{\partial\Omega} v \frac{\partial u}{\partial n} ds \tag{4.2}$$

Let v be a smooth function from $\bar{\Omega} = \Omega \cup \partial\Omega$ to $\mathbb{R}$ such that $v(x) = 0$ for each $x \in \partial\Omega$. To derive a variational equation, multiply both sides of equation (4.1) by the continuous function v, integrate over Ω and apply Green's formula (4.2) to obtain

$$\begin{aligned} \int_\Omega v f d\Omega &= -\int_\Omega v \Delta u \, d\Omega \\ &= -\underbrace{\int_{\partial\Omega} v \frac{\partial u}{\partial n} ds}_{=0} + \int_\Omega \nabla v \cdot \nabla u \, d\Omega \\ &= \int_\Omega \nabla v \cdot \nabla u \, d\Omega \end{aligned} \tag{4.3}$$

where v vanishes on the boundary has been used in the first term of equation (4.3).

Theorem 1 *If u is a classical solution to the Poisson problem (4.1), then u satisfies*

$$\int_\Omega \nabla v \cdot \nabla u \, d\Omega = \int_\Omega v f d\Omega, \tag{4.4}$$

for each smooth function v vanishing on the boundary.

The equation (4.4) is called the *variational form* of the Poisson equation.

The variational formulation of the Poisson equation (4.1) is formally written as
Find $u \in V$ *such that*

$$\int_\Omega \nabla v \cdot \nabla u \, d\Omega = \int_\Omega v f d\Omega \qquad \forall v \in V. \tag{4.5}$$

Solutions to the variational problem (4.5) are called *weak solutions* of the PDE.

In order to make a Galerkin finite element approximation, we start from the variational problem of the given PDE (4.5). To that end, we also introduce a *triangulation* of the domain Ω and define $V_h \subset V$ as the space of all functions that are *continuous* on $\bar{\Omega}$ and vanishing on the boundary $\partial\Omega$. We can then define the *finite element discretisation* of the Poisson problem as
Find $u_h \in V_h$ such that

$$\int_\Omega \nabla v_h \cdot \nabla u_h \, d\Omega = \int_\Omega v_h f d\Omega \qquad \forall v_h \in V_h \tag{4.6}$$

The construction of V_h is achieved by ensuring that specific choice of trial functions coincide with the choice of test functions. This way of discretising is called *Galerkin approximation* (Elman *et al.* 2005). Thus we have derived the standard Galerkin finite element discretisation of the model elliptic problem (4.1) and is given by equation (4.6).

4.3.2 Discontinuous Galerkin Discretisation

The *interior penalty* (IP) version of the discontinuous Galerkin discretisation of the model problem is formulated next. First of all, some notations and definition unique to the DG formulation is introduced.

4.3.2.1 Discretisation and Notation

The following notations are used throughout in this thesis. Let $\Omega \subset \mathbb{R}^d$, where d the dimension, be a Lipschitz domain in $\mathbb{R}^d$. We denote the boundary of Ω by $\Gamma = \partial\Omega$. In each point $x \in \partial\Omega$, $\mathbf{n} = \mathbf{n}(x)$ denotes the outward unit normal vector. Let $\mathcal{T}_h = \{E\} \subset \mathbb{R}^d$ be a family of triangulation (consisting of shape regular, non-overlapping polygonal sub-domains E_i) of $\bar{\Omega}$ that is possibly non-conforming. We denote the boundary of some generic element E by ∂E and $\mathcal{E}_h$ denotes the set of all edges/faces e of $\mathcal{T}_h$, *i.e.* the set of all edges in the domain $\bar{\Omega}$. Let $\mathcal{E}^I$ denotes the set of all interior edges of the discretisation and $\mathcal{E}^B$ be the set of boundary edges. Let e denotes a generic inter-element edge (*i.e.* edge shared by two generic elements). Let the elements of $\mathcal{T}_h$ be numbered sequentially, then for each $e \in \mathcal{E}^I$ there exist indices l and k such that $l > k$ and $e = \bar{E}_l \cap \bar{E}_k$. Let e_{lk} represent a segment of $\mathcal{E}_h$ shared by two elements E_l and E_k of $\mathcal{T}_h$ (see Figure (4.1)). Let $\mathbf{n}_l$ and $\mathbf{n}_k$ be the unit outer normal to element E_l and E_k on e_{lk}. Let us associate a unique normal vector $\mathbf{n}_e$ with face e_{lk} as the normal *out of* element E_l and *in to* element

E_k. That is the normal vector is directed from E_l to E_k (see Figure (4.1)). Then, $\mathbf{n}_l$ = $\mathbf{n}_e$ = -$\mathbf{n}_k$. Let $|e_{lk}|$ denote the measure of the edge/face e_{lk}. Consider a function φ for an

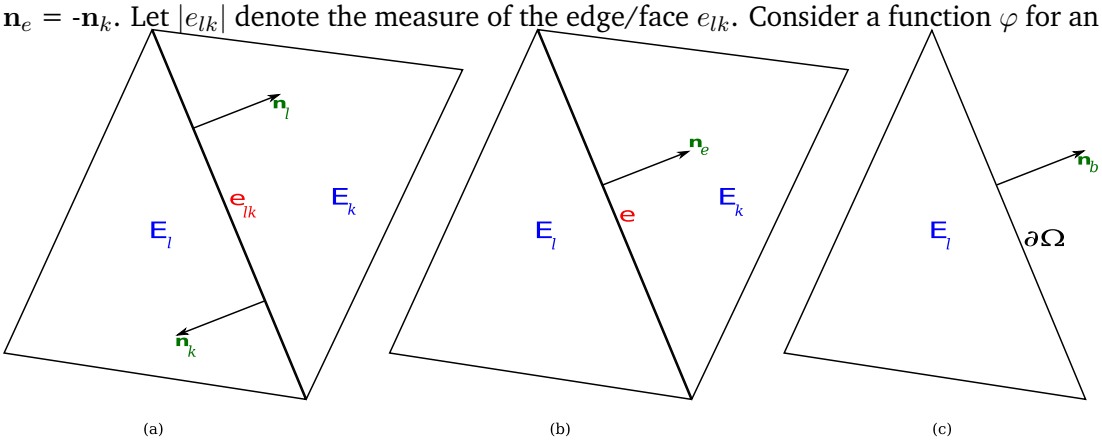

Figure. 4.1. Neighbouring elements in DG schemes: (a) Notation for two arbitrary elements (b) Generic notation for inter element face and unique normal associated with it (c) Notation for element on the boundary

arbitrary element $E \in \mathcal{T}_h$. Let l, k be two adjacent elements of $\mathcal{T}_h$ and x be an arbitrary point on the interior edge $e = e_{lk} = \partial E_l \cap \partial E_k$, $\varphi_k^{\pm}$ denote the trace of φ taken from within the interior of l and k, respectively. We associate a unique normal $\mathbf{n}_e$ such that $\mathbf{n}_e$ = $\mathbf{n}_l$ = -$\mathbf{n}_k$. Now let us define the *jump* and *average* of the function φ on e as follows:

Definition 1 (Jump:) *Let e be the interior face shared by the elements E_l and E_k. Let $e_b \subset \partial\Omega$ be the boundary face. For a function φ, the jump of φ on a face is defined as*

$$[\varphi]_{lk} = \begin{cases} \varphi|_l \mathbf{n}_l + \varphi|_k \mathbf{n}_k & on\ e \\ g\mathbf{n_b} & on\ e_b \end{cases} \tag{4.7}$$

The *jump* in φ across the face e_{lk} is written with the *square bracket* notation

$$\begin{aligned} [\varphi]_{lk} &= \varphi|_l \mathbf{n}_l + \varphi|_k \mathbf{n}_k \\ &= \varphi|_l - \varphi|_k \\ &= (\varphi|_{E^l})|_e - (\varphi|_{E^k})|_e \end{aligned}$$

Definition 2 (Average:) *Let e be the interior face shared by the elements E_l and E_k. Let $e_b \subset \partial\Omega$ be the boundary face. For a function φ, the jump of φ on a face is defined as*

$$\langle\varphi\rangle_{lk} = \begin{cases} \frac{1}{2}(\varphi|_l + \varphi|_k) & on\ e \\ g & on\ e_b \end{cases} \tag{4.8}$$

The discontinuity of the function, which is formally called *jump* is denoted with the square bracket $[\cdot]$. The orientation for each jump term is chosen according to the

direction of unit normal at each internal face. That is, the unit vector $\mathbf{n}_l$ points *out of* element E_l. The average operator is denoted with the angle bracket notation $\langle\cdot\rangle$. According to the definitions, if e belongs to the boundary $\partial\Omega$, i.e. $e = e_b$ then $\mathbf{n}_e$ is the unit normal exterior to Ω ($\mathbf{n}_e = \mathbf{n_b}$) and the jump and average are defined to be equal to the trace of φ (see Figure 4.1(c)). For $x \in \partial E \cup \partial\Omega$ if the outer trace is set to be $\varphi|_l = g$, where g denotes an appropriate boundary function and φ_l is the trace of function φ for element E_l. If we are on a face along the boundary of the domain, $e_b \in \partial E_b \cap \partial\Omega \neq \emptyset$, then we define $\langle\varphi\rangle = [\varphi] = g$. Now note the following identity or definition:

Definition 3 *Let φ, ψ be two functions, then for any internal face*

$$[\varphi\psi] = [\varphi]\langle\psi\rangle + [\psi]\langle\varphi\rangle \tag{4.9}$$

4.3.2.2 Weak formulation

We consider the model elliptic problem in 2D (4.1) and want to formulate the discretisation in a discontinuous Galerkin (DG) way. The variational problem of the Poisson problem is given in Equation (4.5). This can be written using the following bilinear form:
Find $u \in H^1(\Omega)$ with $u = 0$ on $\partial\Omega$ such that

$$a(u, v) := (\nabla u, \nabla v) = (f, v) \quad \forall v \in H_0^1(\Omega)$$

Let us recall our notations from Section 4.3.2.1. Let $\mathcal{T}_h$ be shape-regular mesh and $\mathcal{E}_h$ be set of all edges and $\mathcal{E}_h^I$ and $\mathcal{E}_h^B$ sets of all interior and boundary edges respectively.

Since discontinuous Galerkin methods are non-conforming methods, it is necessary to introduce Sobolev spaces defined on a subdivision T_h of the domain Ω. Such piecewise Sobolev spaces are called *broken Sobolev spaces* in literature. The DG method approximates weak solutions in finite-dimensional subspaces of the broken Sobolev space

$$H^m(\mathcal{T}_h) = \{v \in L^2(\Omega) : v|_E \in H^m(E) \; \forall \; E \in \mathcal{T}_h\}$$

with $m \geq 1$, *i.e.* functions may be discontinuous at element boundaries. In the discrete scheme the spaces $H^m(E)$ will be replaced by polynomials $P_r(E)$ of degree r on element E. These polynomials are generated from the polynomials on the reference element $\hat{E}$ via

$$P_r(E) = \{\varphi \mid \varphi = \hat{\varphi} \circ T_E^{-1}, \hat{\varphi} \in \hat{P} = P_r(\hat{E})\},$$

where $T_E : \hat{E} \to E$ is the mapping from the reference element to the transformed element. The degree r may vary from element to element.

The interior penalty version of the discontinuous Galerkin discretisation is considered and for that first obtain the weak formulation by multiplying equation (4.1) by a test function $v \in H^m(\mathcal{T}_h)$ and integrating over Ω. Applying Greens formula, we obtain the weak formulation of the Poisson problem given by equation (4.5). Weak form is given below:

$$\int_\Omega \nabla u \cdot \nabla v \; dx - \int_{\partial\Omega} \nabla u \cdot \mathbf{n}_e \; v \; ds = \int_\Omega f \; v \; dx \tag{4.10}$$

Next we decompose the integrals of the weak formulation into element contributions. Integrating over the discretised domain is the same as integrating over each of the discrete elements and summing the results. Hence sum over all elements gives:

$$\sum_{E\in\mathcal{T}_h} \int_E \nabla u \cdot \nabla v \; dx - \sum_{\partial E\in\mathcal{E}_h} \int_{\partial E} \nabla u \cdot \mathbf{n}_e \; v \; ds = \sum_{E\in\mathcal{T}_h} \int_E f \; v \; dx \tag{4.11}$$

Next step is to split the boundary integrals into external and internal boundaries as shown symbolically:

$$\sum_{\partial E\in\mathcal{E}_h} \int_{\partial E} \cdots = \sum_{\mathcal{E}_h^I\in\mathcal{E}_h} \int_{\mathcal{E}_h^I} \cdots + \sum_{\mathcal{E}_h^B\in\mathcal{E}_h} \int_{\mathcal{E}_h^B} \cdots$$

as a results, the second term in the Equation (4.11) becomes

$$\sum_{\partial E\in\mathcal{E}_h} \int_{\partial E} \nabla u \cdot \mathbf{n}_e \; v \; dx = \sum_{\mathcal{E}_h^I\in\mathcal{E}_h} \int_{\mathcal{E}_h^I} [\nabla u \cdot v \; \mathbf{n}_e] ds + \sum_{\mathcal{E}_h^B\in\mathcal{E}_h} \int_{\mathcal{E}_h^B} \nabla u \cdot v \; \mathbf{n}_b ds \tag{4.12}$$

Using the identity (4.9), the first term in the right-hand side of equation (4.12) can be written as

$$\sum_{\mathcal{E}_h^I\in\mathcal{E}_h} \int_{\mathcal{E}_h^I} [\nabla u \cdot v \; \mathbf{n}_e] ds = \sum_{\mathcal{E}_h^I\in\mathcal{E}_h} \int_{\mathcal{E}_h^I} \underbrace{[\nabla u \cdot \mathbf{n}_e]}_{=0} \langle v \rangle \; ds + \sum_{\mathcal{E}_h^I\in\mathcal{E}_h} \int_{\mathcal{E}_h^I} \langle \nabla u \cdot \mathbf{n}_e \rangle [v] \; ds \tag{4.13}$$

Now on substituting (4.13) in (4.12), we get

$$\sum_{\partial E\in\mathcal{E}_h} \int_{\partial E} \nabla u \cdot \mathbf{n}_e \; v \; dx = \sum_{\mathcal{E}_h^I\in\mathcal{E}_h} \int_{\mathcal{E}_h^I} \langle \nabla u \cdot \mathbf{n}_e \rangle [v] \; ds + \sum_{\mathcal{E}_h^B\in\mathcal{E}_h} \int_{\mathcal{E}_h^B} \nabla u \cdot v \; \mathbf{n}_b \; ds \tag{4.14}$$

and finally when substituting (4.14) in (4.11), we get

$$\begin{aligned} \sum_{E\in\mathcal{T}_h} \int_E \nabla u \cdot \nabla v \; dx - \sum_{\mathcal{E}_h^I\in\mathcal{E}_h} \int_{\mathcal{E}_h^I} \langle \nabla u \cdot \mathbf{n}_e \rangle [v] \; ds \\ - \sum_{\mathcal{E}_h^B\in\mathcal{E}_h} \int_{\mathcal{E}_h^B} \nabla u \cdot v \; \mathbf{n}_b \; ds = \sum_{E\in\mathcal{T}_h} \int_E f \; v \; dx \end{aligned} \tag{4.15}$$

Let us now define:

$$
\begin{aligned}
A(u,v) &= \sum_{E\in\mathcal{T}_h} \int_E \nabla u \cdot \nabla v \; dx \\
F(v) &= \sum_{E\in\mathcal{T}_h} \int_E f \; v \; dx \\
J(u,v) &= \int_{\mathcal{E}_h^I} \langle \nabla u \cdot \mathbf{n}_e \rangle [v] \; ds + \int_{\mathcal{E}_h^B} \nabla u \cdot v \; \mathbf{n}_b \; ds
\end{aligned} \tag{4.16}
$$

Then the primal formulation of the discontinuous Galerkin discretisation of the Poisson problem with interior penalties reads:
Find $u_h \in H^m(\mathcal{T}_h)$ such that

$$
A(u_h, v_h) - J(u_h, v_h) = F(v_h) \quad \forall v_h \in H^m(\mathcal{T}_h) \tag{4.17}
$$

The equation (4.15) is the basic interior penalty Galerkin formulation of the model problem (4.1).

The left-hand side of equation (4.15) has no symmetry and no positivity. One can make some modifications to the basic formulation (4.15) in order to provide the bilinear form with certain desirable properties such as symmetry and coercivity. Depending on the way the modifications are introduced, we obtain various interior penalty versions of DG methods such as Symmetric Interior Penalty Galerkin (SIPG), Non-Symmetric Interior Penalty Galerkin (NIPG), Incomplete Interior Penalty Galerkin (IIPG) and Oden-Babuška-Baumann (OBB) methods. In the following section we describe in detail the above variants of DG.

4.3.3 Various IP Discontinuous Galerkin Formulations

The interior penalty versions of discontinuous Galerkin methods are based on the idea that inter-element continuity could be achieved by following Nitsche's (Nitsche 1971) concept of imposing Dirichlet boundary conditions weakly rather than in the finite element space. Arnold (1982) and Wheeler (1978) introduced interior penalty terms to the DG formulation to enforce stability of the method for elliptic problems. It should be noted that the DG methods are usually defined by means of the so called numerical fluxes between neighbouring elements, but for most of the interior penalty methods for second order elliptic problems, it is possible to relate the expression of the numerical fluxes with a corresponding set of local interface condition that are weakly enforced on each inter-element boundary (Zunino 2008). There are many variants of primal DG formulations with interior penalties introduced over the years. As we can see from literature about those methods given in the Section (4.2), they differ in their properties such as convergence and stability from each other. In this Section we will see how to obtain different DG schemes from the basic formulation (4.15).

4.3.3.1 Symmetric Interior Penalty Galerkin (SIPG)

Consider the integral $J(u, v)$ given in (4.16). Then

$$J(v,u) = \int_{\mathcal{E}_h^I} \langle \nabla v \cdot \mathbf{n}_e \rangle [u] \, ds + \int_{\mathcal{E}_h^B} \nabla v \cdot u \, \mathbf{n}_b \, ds \tag{4.18}$$

Noting that $J(v, u) = 0$ for smooth u, we can add or subtract $J(v, u)$ to the left-hand side of equation (4.17) keeping the resulting equation still equivalent to (4.17). Now if we subtract, we will get the symmetric version of discontinuous Galerkin method called Symmetric Interior Penalty Galerkin (SIPG) as given below:

$A(u, v) - J(u, v) - J(v, u) = F(v)$ results in

$$\begin{aligned}\sum_{E\in\mathcal{T}_h} \int_E \nabla u \cdot \nabla v \, dx &- \sum_{\mathcal{E}_h^I \in \mathcal{E}_h} \int_{\mathcal{E}_h^I} \langle \nabla u \cdot \mathbf{n}_e \rangle [v] \, ds \\ &- \sum_{\mathcal{E}_h^I \in \mathcal{E}_h} \int_{\mathcal{E}_h^I} \langle \nabla v \cdot \mathbf{n}_e \rangle [u] \, ds \\ &- \sum_{\mathcal{E}_h^B \in \mathcal{E}_h} \int_{\mathcal{E}_h^B} \nabla u \cdot \mathbf{n}_b \, v \, ds \\ &- \sum_{\mathcal{E}_h^B \in \mathcal{E}_h} \int_{\mathcal{E}_h^B} \nabla v \cdot \mathbf{n}_b \, u \, ds = \sum_{E\in\mathcal{T}_h} \int_E f \, v \, dx \end{aligned} \tag{4.19}$$

Although the left-hand side of (4.19) is symmetric, there is no reason to be positive (Girault and Wheeler 2008). To enforce the coercivity one can penalise the jump terms. Let $\sigma > 0$ be a penalising parameter. Noting that the integrals involving a jump in u are zero for smooth u, the jump term $J_0(u, v)$ can be defined as given below:

$$J_0(u,v) = \frac{\sigma}{|\mathcal{E}_h^I|^\beta} \sum_{\mathcal{E}_h^I \in \mathcal{E}_h} \int_{\mathcal{E}_h^I} \sigma [u][v] \, ds + \frac{\sigma}{|\mathcal{E}_h^B|^\beta} \sum_{\mathcal{E}_h^B \in \mathcal{E}_h} \int_{\mathcal{E}_h^B} \sigma u \, v \, ds \tag{4.20}$$

Where $|e|$ denotes the measure of the edge, $\sigma > 0$ a suitable positive parameter and β is a user defined parameter.

The SIPG formulation then reads

$$A(u,v) - J(u,v) - J(v,u) + J_0(u,v) = F(v) \tag{4.21}$$

The interior penalty term $\frac{\sigma}{|e|^\beta}$ depends on the size of the interior interface. The penalisation term helps in controlling the magnitude of discontinuity to a certain extent, thus making this formulation more stable. It should be noted that as the $penalty \to \infty$, the method converge to a standard finite element method.

The SIPG formulation for the model problem looks as below:

$$\begin{aligned}\sum_{E\in\mathcal{T}_h}\int_E \nabla u\cdot\nabla v\,dx &- \sum_{\mathcal{E}_h^I\in\mathcal{E}_h}\int_{\mathcal{E}_h^I}\langle\nabla u\cdot\mathbf{n}_e\rangle[v]\,ds\\ &- \sum_{\mathcal{E}_h^I\in\mathcal{E}_h}\int_{\mathcal{E}_h^I}\langle\nabla v\cdot\mathbf{n}_e\rangle[u]\,ds\\ &- \sum_{\mathcal{E}_h^B\in\mathcal{E}_h}\int_{\mathcal{E}_h^B}\nabla u\cdot\mathbf{n}_b\,v\,ds\\ &- \sum_{\mathcal{E}_h^B\in\mathcal{E}_h}\int_{\mathcal{E}_h^B}\nabla v\cdot\mathbf{n}_b\,u\,ds\\ &+ \frac{\sigma}{|\mathcal{E}_h^I|^\beta}\sum_{\mathcal{E}_h^I\in\mathcal{E}_h}\int_{\mathcal{E}_h^I}\sigma[u][v]\,ds\\ &+ \frac{\sigma}{|\mathcal{E}_h^B|^\beta}\sum_{\mathcal{E}_h^B\in\mathcal{E}_h}\int_{\mathcal{E}_h^B}\sigma\,u\,v\,ds = \sum_{E\in\mathcal{T}_h}\int_E f\,v\,dx\end{aligned} \tag{4.22}$$

The stiffness matrix obtained by this formulation is symmetric. The method is symmetric, consistent and stable provided that the penalty is large enough. Because of the symmetric advantage of the stiffness matrix, SIPG is often applied to problems that do not have strict requirements on the stability.

4.3.3.2 Oden-Babuška-Baumann (OBB)

In 1998, Oden *et al.* (1998) introduced a new DG formulation later known as Oden-Babuška-Baumann (OBB) method obtained by dropping the penalty term in the SIPG formulation and switching the sign of certain integral terms. The OBB formulation is obtained when the term $J(v,u)$ is added to the left-hand side of equation (4.17). Although a minor difference, the change in sign has striking effects that it results in a positive definite bilinear form. The OBB formulation for the model problem is as follows:

$$\begin{aligned}\sum_{E\in\mathcal{T}_h}\int_E \nabla u\cdot\nabla v\,dx &- \sum_{\mathcal{E}_h^I\in\mathcal{E}_h}\int_{\mathcal{E}_h^I}\langle\nabla u\cdot\mathbf{n}_e\rangle[v]\,ds\\ &+ \sum_{\mathcal{E}_h^I\in\mathcal{E}_h}\int_{\mathcal{E}_h^I}\langle\nabla v\cdot\mathbf{n}_e\rangle[u]\,ds\\ &- \sum_{\mathcal{E}_h^B\in\mathcal{E}_h}\int_{\mathcal{E}_h^B}\nabla u\cdot\mathbf{n}_b\,v\,ds\\ &+ \sum_{\mathcal{E}_h^B\in\mathcal{E}_h}\int_{\mathcal{E}_h^B}\nabla v\cdot\mathbf{n}_b\,u\,ds = \sum_{E\in\mathcal{T}_h}\int_E f\,v\,dx\end{aligned} \tag{4.23}$$

Since the formulation of OBB results in a positive definite stiffness matrix, the method is more stable and robust than the symmetric DG formulation. Also, it exhibits local conservation properties at the element level. For polynomial approximation with minimum order of 2 ($p \geq 2$), OBB appears to be unconditionally stable (Oden *et al.* 1998, Castillo 2002, Romkes *et al.* 2006). The stiffness matrix obtained is still non-symmetric. This formulation has been used in solving variety of problems such as diffusion, convection-diffusion, Euler and Navier-Stokes (Babuška *et al.* 1999, Baumann and Oden 1999b, Oden and Baumann 2000).

4.3.3.3 Non-Symmetric Interior Penalty Galerkin (NIPG)

This method was introduced by Rivière (2000) based on both SIPG and OBB as an extension to the OBB by including a penalty term on the jump of the solution across the element interfaces. Like in SIPG, NIPG formulation also uses interior penalty terms that are mesh dependent and signs of certain integrals are kept same as that in OBB. On adding the term $J(v,u)$ to the left-hand side of Equation (4.17) and followed by the application of penalty, one can obtain the NIPG formulation. The NIPG formulation for the model problem is given below:

$$\begin{aligned}\sum_{E\in\mathcal{T}_h}\int_E \nabla u\cdot\nabla v\,dx &- \sum_{\mathcal{E}_h^I\in\mathcal{E}_h}\int_{\mathcal{E}_h^I}\langle\nabla u\cdot\mathbf{n}_e\rangle[v]\,ds \\ &+ \sum_{\mathcal{E}_h^I\in\mathcal{E}_h}\int_{\mathcal{E}_h^I}\langle\nabla v\cdot\mathbf{n}_e\rangle[u]\,ds \\ &- \sum_{\mathcal{E}_h^B\in\mathcal{E}_h}\int_{\mathcal{E}_h^B}\nabla u\cdot\mathbf{n}_b\,v\,ds \\ &+ \sum_{\mathcal{E}_h^B\in\mathcal{E}_h}\int_{\mathcal{E}_h^B}\nabla v\cdot\mathbf{n}_b\,u\,ds \\ &+ \frac{\sigma}{|\mathcal{E}_h^I|^\beta}\sum_{\mathcal{E}_h^I\in\mathcal{E}_h}\int_{\mathcal{E}_h^I}\sigma[u][v]\,ds \\ &+ \frac{\sigma}{|\mathcal{E}_h^B|^\beta}\sum_{\mathcal{E}_h^B\in\mathcal{E}_h}\int_{\mathcal{E}_h^B}\sigma\,u\,v\,ds = \sum_{E\in\mathcal{T}_h}\int_E f\,v\,dx \end{aligned} \tag{4.24}$$

This formulation results in a non-symmetric stiffness matrix and with sufficiently large penalties NIPG is found to be stable ((Rivière *et al.* 1999; 2000)). It exhibits more stable and robust behaviour than SIPG and in comparison to OBB, NIPG allows one to adjust penalty parameters to achieve more accurate results.

4.3.3.4 Incomplete Interior Penalty Galerkin (IIPG)

The Incomplete Interior Penalty Galerkin (IIPG) method was proposed by Dawson *et al.* (2004) in order to improve the performance of DG methods. They can be obtained by adding the penalty term (4.20) to the basic IP form (4.15) of the model problem. The IIPG formulation for the model problem is as follows:

$$\begin{aligned}\sum_{E\in\mathcal{T}_h}\int_E \nabla u\cdot\nabla v\,dx &- \sum_{\mathcal{E}_h^I\in\mathcal{E}_h}\int_{\mathcal{E}_h^I}\langle\nabla u\cdot\mathbf{n}_e\rangle[v]\,ds\\ &- \sum_{\mathcal{E}_h^B\in\mathcal{E}_h}\int_{\mathcal{E}_h^B}\nabla u\cdot\mathbf{n}_b\,v\,ds\\ &+ \frac{\sigma}{|\mathcal{E}_h^I|^\beta}\sum_{\mathcal{E}_h^I\in\mathcal{E}_h}\int_{\mathcal{E}_h^I}\sigma[u][v]\,ds\\ &+ \frac{\sigma}{|\mathcal{E}_h^B|^\beta}\sum_{\mathcal{E}_h^B\in\mathcal{E}_h}\int_{\mathcal{E}_h^B}\sigma\,u\,v\,ds = \sum_{E\in\mathcal{T}_h}\int_E f\,v\,dx\end{aligned} \tag{4.25}$$

The IIPG formulation differs from SIPG and NIPG in the fact that the symmetrising and stabilising terms are not enforced and only penalty term appears. It uses the regularity of the normal derivative of u (Girault and Wheeler 2008).

4.3.3.5 General Formulation

A general formulation for the interior penalty discontinuous Galerkin method for the model elliptic problem can be written as follows:

$$\begin{aligned}\sum_{E\in\mathcal{T}_h}\int_E \nabla u\cdot\nabla v\,dx &- \sum_{\mathcal{E}_h^I\in\mathcal{E}_h}\int_{\mathcal{E}_h^I}\langle\nabla u\cdot\mathbf{n}_e\rangle[v]\,ds\\ &- \epsilon\sum_{\mathcal{E}_h^I\in\mathcal{E}_h}\int_{\mathcal{E}_h^I}\langle\nabla v\cdot\mathbf{n}_e\rangle[u]\,ds\\ &- \sum_{\mathcal{E}_h^B\in\mathcal{E}_h}\int_{\mathcal{E}_h^B}\nabla u\cdot\mathbf{n}_b\,v\,ds\\ &- \epsilon\sum_{\mathcal{E}_h^B\in\mathcal{E}_h}\int_{\mathcal{E}_h^B}\nabla v\cdot\mathbf{n}_b\,u\,ds\\ &+ \frac{\sigma}{|\mathcal{E}_h^I|^\beta}\sum_{\mathcal{E}_h^I\in\mathcal{E}_h}\int_{\mathcal{E}_h^I}\sigma[u][v]\,ds\\ &+ \frac{\sigma}{|\mathcal{E}_h^B|^\beta}\sum_{\mathcal{E}_h^B\in\mathcal{E}_h}\int_{\mathcal{E}_h^B}\sigma\,u\,v\,ds = \sum_{E\in\mathcal{T}_h}\int_E f\,v\,dx\end{aligned} \tag{4.26}$$

Depending on the choices of the parameters ϵ and σ we obtain different variants of the DG methods that are developed for elliptic problems. For $\epsilon = 0$, we get IIPG, $\epsilon = 1$ for SIPG, $\epsilon = -1$ for NIPG and $\epsilon = -1$ and $\sigma = 0$ for OBB. The NIPG and OBB formulations differ only in the presence or absence of jump terms. In the case of non-homogeneous Dirichlet boundary condition with a given Dirichlet function g, the Dirichlet boundary conditions are imposed weakly and results in the appearance of extra integrals in the formulation. The general formulation then becomes:

$$\begin{aligned}
\sum_{E\in\mathcal{T}_h}\int_E \nabla u\cdot\nabla v\,dx &- \sum_{\mathcal{E}_h^I\in\mathcal{E}_h}\int_{\mathcal{E}_h^I}\langle\nabla u\cdot\mathbf{n}_e\rangle[v]\,ds \\
&- \epsilon\sum_{\mathcal{E}_h^I\in\mathcal{E}_h}\int_{\mathcal{E}_h^I}\langle\nabla v\cdot\mathbf{n}_e\rangle[u]\,ds \\
&- \sum_{\mathcal{E}_h^B\in\mathcal{E}_h}\int_{\mathcal{E}_h^B}\nabla u\cdot\mathbf{n}_b\,v\,ds \\
&- \epsilon\sum_{\mathcal{E}_h^B\in\mathcal{E}_h}\int_{\mathcal{E}_h^B}\nabla v\cdot\mathbf{n}_b\,u\,ds \\
&+ \frac{\sigma}{|\mathcal{E}_h^I|^\beta}\sum_{\mathcal{E}_h^I\in\mathcal{E}_h}\int_{\mathcal{E}_h^I}\sigma[u][v]\,ds \\
&+ \frac{\sigma}{|\mathcal{E}_h^B|^\beta}\sum_{\mathcal{E}_h^B\in\mathcal{E}_h}\int_{\mathcal{E}_h^B}\sigma\,u\,v\,ds \\
&= \sum_{E\in\mathcal{T}_h}\int_E f\,v\,dx \\
&- \sum_{\mathcal{E}_h^D\in\mathcal{E}_h}\int_{\mathcal{E}_h^D}\langle\nabla v\cdot\mathbf{n}_b\rangle\,g\,ds \\
&+ \frac{\sigma}{|\mathcal{E}_h^D|^\beta}\sum_{\mathcal{E}_h^D\in\mathcal{E}_h}\int_{\mathcal{E}_h^D}\sigma\,g\,v\,ds
\end{aligned} \tag{4.27}$$

where $\mathcal{E}_h^D$ represents the set of Dirichlet boundary faces.

4.3.3.6 Remarks on IP methods

The interior penalty discontinuous Galerkin method for elliptic partial differential equations is getting very popular. The IP methods facilitate hp adaptivity and give symmetric, locally conservative and small-stencil discretisation, which allows efficient parallelisation in large scale computation. However, one difficulty with IP scheme is that it requires the specification of a penalty term which is mesh dependent. It has been shown that if the value of the penalty parameter is not sufficiently large, the approximation is unstable due to the non-coercivity of the associated bilinear form (Castillo 2002, Shahbazi 2005). On the other hand, large penalty parameter causes

performance loss in the iterative solvers. Hence it is critical to know the optimal value of the penalty parameter for stable approximation. Except the OBB scheme, all other interior penalty DG schemes require the specification of penalty parameter.

Both the OBB and NIPG methods are non-symmetric even for symmetric continuous problem. The OBB method is stable for polynomial order $k \geq 2$ and for the NIPG method $k \geq 1$ is sufficient. Both methods are locally mass conservative. If the solution satisfies sufficient regularity, the OBB method exhibits optimal order of convergence in the H^1 norm ($\mathcal{O}(h^k)$) for polynomials of degree k. For odd degree polynomial OBB method shows optimal convergence in L^2 norm ($\mathcal{O}(h^{k+1})$) and for even degree polynomial the convergence is suboptimal ($\mathcal{O}(h^k)$). NIPG method, however is optimal in the L^2 norm for both odd and even degree polynomials. The suboptimal convergence of the OBB method is attributed to the absence of penalty terms. One of the advantage of the OBB method is that it does not require any user supplied parameters and is computationally cheaper due to the absence of penalty integral terms. Advantage of NIPG over SIPG is that the penalty parameter σ can be kept small and need not to be fine tuned.

4.3.4 Local Discontinuous Galerkin (LDG)

In order to complete the discussion, we also briefly mention another family of DG methods the so called Local Discontinuous Galerkin (LDG). All the previously mentioned IP methods fall into the category of primal methods and LDG is one another method in which flux also appear as variable as a result of rewriting the equation to first order. The LDG method was introduced by Cockburn and Shu (1998; 2001) as a generalisation of the DG method proposed by Bassi and Rebay (1997) and is very popular like IP methods. Compared to IP schemes, the LDG scheme introduces large-stencil discretisation.

4.4 Continuous and Discontinuous Galerkin

Having shown the derivation of both the standard and DG formulation of the model problem, in this section, we briefly compare standard and discontinuous Galerkin finite element methods. Like all numerical methods, discontinuous Galerkin finite element formulations have both advantages and disadvantages. It is important to understand these issues for developing specific applications. The discontinuous Galerkin finite element methods combine the advantages of both finite element and finite volume methods. For instance, the DG method has the flexibility of finite element methods and it uses the finite volume approach for the approximation of conservation equations. Standard finite elements require that the discrete solution is continuous over the interior boundaries or inter-element boundaries (such as edges in 2D or faces in 3D). In DG methods, for adjacent elements in the computational mesh, the approximate solution computed in the interior of elements does not have to match on the element interfaces.

Figure (4.2) shows a schematic representation of function variation across an element interface in 1D. In standard FEM, the function is continuous across the interface. In DG, the function is allowed to be discontinuous and the continuity is only weakly enforced and hence the jump is not zero. The degrees of freedom in DG methods are the coefficients in the expansion of the solution with respect to the chosen basis function. Hence in order to find the DG solution at a point, one has to compute the expansion by evaluating the basis function and multiplying by the coefficients.

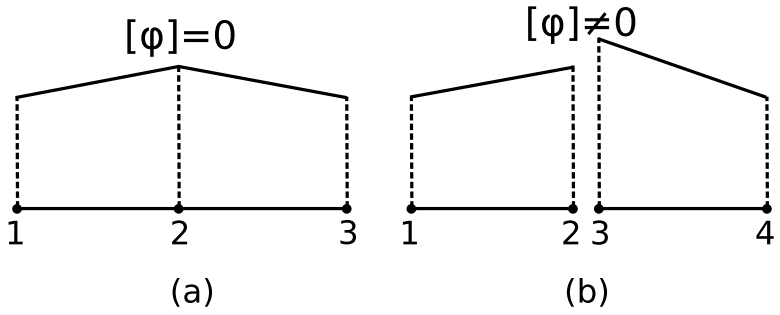

Figure. 4.2. (a) C^0 continuity in standard finite elements (b) Weak enforcement of continuity in discontinuous Galerkin methods.

Some of the appealing properties of discontinuous Galerkin finite element methods in comparison to standard continuous finite element methods, which made DG methods popular among the researchers (Arnold *et al.* 2001, Bastian 2003, Bastian and Rivière 2004) are listed below. They are:

- *Uniform applicability to hyperbolic, elliptic and parabolic problems*

  The DG methods are devised for all types of partial differential equations. Although originally developed for hyperbolic problems, DG methods found their way to efficient discretisation of elliptic and parabolic equations.

- *DG methods can handle problems in complex geometries to obtain high order accurate solutions*

  The DG methods are based on discontinuous basis function unlike standard finite elements. That is, the DG methods approximate the solution within each element by a function whereas in standard finite elements the function is not local to an element. DG methods are attractive since the element-wise discontinuous representation of the solution helps in achieving higher-order accuracy on arbitrary meshes in a natural way. It is well suited for complex geometries as it can handle non-conforming grids with hanging nodes. Hence it is easier to construct locally refined meshes. It should be noted that hanging nodes require no special treatment in DG methods but they do need particular attention in continuous FE methods.

- *Local (element-wise) conservation of physical properties*

The DG method conserves the appropriate physical quantities (e.g., mass, momentum, and energy) at the element level whereas the standard finite element method satisfies only a global mass balance over the whole computational domain. Similar to finite volume approach when conservation equations are integrated by parts over each element, certain terms yield integrals over the boundaries of the element. Since this natural coupling of boundary fluxes are included in the discretisation, conservations laws are guaranteed to hold locally also for the discrete problem. Since DG methods satisfy the local conservation property they are attractive for solving convection–diffusion problems.

- *DG methods allow easy parallelisation*

  In the DG method, the inter-element communications are minimal because each element only communicates to its neighbours through the edge/face integrals. This simple communication pattern to elements sharing a common face simplifies parallel computation. Since this discretisation produces a set of equations within each element that are only weakly coupled to its nearest neighbours, the discretisation is highly compact.

- *Easy hp adaptivity*

  Relaxing the continuity of approximation functions across element interfaces (which is required in standard FEM) gives the discontinuous Galerkin method more localisation and flexibility which in turn provide easier and more natural hp mesh adaptation. It can easily handle adaptive strategies, since refining or coarsening the mesh can be achieved without considering the continuity restrictions typical to conforming elements. Similarly, for p-adaptivity inter-element continuity is not required.

- *Use of arbitrary shaped elements*

  Unlike continuous finite element method where shape function is dependent on the shape of the elements, the DG methods can have arbitrary shaped elements in the discretisation.

- *Easy implementation of boundary conditions*

  Implementation of various boundary conditions is more natural in the DG method due to its compact formulation. This in turn greatly increases the robustness and accuracy of any boundary condition implementation.

- *Rigorous mathematical foundation*

  From theoretical point of view, it has several useful mathematical properties like continuous FEM with regards to stability and convergence.

Like all other numerical schemes, DG methods also have some disadvantages. Some of the problems when dealing with DG methods are the following:

- *Increase in degrees of freedom*

  The drawback of all discontinuous Galerkin approximations is that with discontinuous basis, the DG methods introduce more unknowns for a given order of accuracy on a mesh than the traditional finite element or finite volume methods, which increases the computational requirement. In continuous finite elements, the degrees of freedom of neighbouring elements are coupled directly, which effectively reduces the total number of degrees of freedom. On the other hand, in DG discretisation the degrees of freedom between neighbouring elements are coupled in an indirect fashion realised by inter-element edge/face terms such as numerical flux functions or interior penalty terms. This effectively increases the number of degrees of freedom in the system.

- *Method is more expensive*

  Referring to the continuous (4.6) and discontinuous (4.22) formulation of the model elliptic problem, one can see that DG approximation has some extra edge integral terms, which adds more computational burden. Also as previously mentioned, the DG approximation introduce a substantial increase in the number of degrees of freedom, which leads to a much larger algebraic system. Hence the method has been recognised as expensive in terms of both computational and storage requirements.

- *Integral evaluation demands simpler elements*

  Theoretically speaking, the DG method can be applied to an element of any shape because DG basis functions are independent of the shape of the elements. However, the evaluation of the integrals in the formulation (during the matrix assembly) requires the use of numerical quadrature approach, which in general restricts the applications to simpler elements.

- *Lack of specialised efficient solvers*

  Discontinuous Galerkin discretisation yields individual dense block matrices due to their locality in the approximation. For time dependent problems, since the interpolation functions are defined independently in each element the mass matrix has a block-diagonal structure and may be inverted directly. In order to exploit such compact discretisation of DG methods and matrix structure, more sophisticated solvers are necessary.

In this Chapter, discontinuous Galerkin finite element method was described in detail. In particular, interior penalty discretisation of the model elliptic problem was presented and various IP schemes were discussed. Finally, a brief comparison of continuous and discontinuous finite element methods was given.

5 Discontinuous Galerkin Discretisation of The Stokes Equation

The flow of an incompressible fluid through a porous medium can be described by a set of partial differential equations known as Navier–Stokes equations. These equations model the behaviour of a fluid under some external forces and govern the velocity and pressure fields. Navier–Stokes equations can be solved given appropriate boundary and initial conditions. In general, these equations do not have analytical solutions and hence a numerical approximation to the solution is necessary. The flow in porous media is generally laminar in nature and in the limit of very small flow velocities, the effect of inertia can be neglected and time may be irrelevant. Such flows are governed by the incompressible stationary Stokes equations. This Chapter deals with the numerical approximation to the solution of the stationary Stokes problem and in particular the discontinuous Galerkin (DG) formulation of the stationary Stokes equation. The last Chapter (4) gave an elaborate description of discontinuous Galerkin finite element methods in general and this Chapter deals with the theory and formulation specific to the Stokes equations.

5.1 The Stokes Problem

As described in the Section (2.2) of Chapter (2), the stationary Stokes equations (2.7) can be used to describe the flow of fluid through porous media at the pore-scale. For small values of Reynolds number, i.e. much smaller than one ($Re \ll 1$), viscous forces dominate the flow, the inertial and external forces are negligible and time may be irrelevant. This leads to the simplification of the nonlinear, time-dependent Navier-Stokes equation (2.1) that govern general continuous fluid flows, to the linear incompressible Stokes equations given as

$$\begin{aligned} -\nabla p + \mu\, \Delta \mathbf{u} + \mathbf{f} &= 0 \\ \nabla \cdot \mathbf{u} &= 0. \end{aligned} \tag{5.1}$$

where $\mathbf{f} = \rho \mathbf{g}$ is the body force. For small Reynolds numbers the flow is generally called *Stokes flow* and it characterise the flow of fluid at the pore-scale in a porous medium. The Stokes problem can be described formally as given below:

Let $\Omega \subset \mathbb{R}^d$ be a bounded, open and connected Lipschitz domain. The steady flow of a viscous incompressible fluid in a bounded sub-domain Ω of $\mathbb{R}^d$ is in general described by the inhomogeneous Stokes equations. The Stokes problem reads:

Find velocity and pressure $(\mathbf{u},p) \in (H^1(\Omega))^d \times L^2(\Omega)$ *such that*

$$\begin{aligned} -\mu\Delta\mathbf{u} + \nabla p &= \mathbf{f} \quad \text{in} \quad \Omega \\ \nabla \cdot \mathbf{u} &= 0 \quad \text{in} \quad \Omega \end{aligned} \tag{5.2}$$

$$\mathbf{u} = \mathbf{g} \quad \text{on} \quad \partial\Omega_D \tag{5.3}$$

$$\mu\frac{\partial \mathbf{u}}{\partial \mathbf{n}} - p\mathbf{n} = p_0 \quad \text{on} \quad \partial\Omega_N \tag{5.4}$$

Here, $\mathbf{u} = (u_1, u_2, \ldots, u_d) : \Omega \to \mathbb{R}^d$ is the velocity field, $p : \Omega \to \mathbb{R}$ is the pressure field, $\mathbf{f}$ represents applied or body forces, $\mathbf{n}$ is the unit normal vector pointing out of $\partial\Omega_N$ and $\mu > 0$ is the coefficient of viscosity of the fluid. The boundary $\partial\Omega = \partial\Omega_D \cup \partial\Omega_N$, where $\partial\Omega_D$ and $\partial\Omega_N$ are parts with essential (Dirichlet) and natural (Neumann) boundary conditions, respectively. Also $g \in H^{\frac{1}{2}}(\partial\Omega_D)$ describes the Dirichlet data and $p_0 \in L^2(\partial\Omega_N)$ represents the Neumann boundary condition data (Heywood *et al.* 1996). If Neumann/Outflow boundary condition is not applied, additionally it requires that

$$\int_\Omega p \, d\Omega = 0 \qquad \text{and} \qquad \int_{\partial\Omega} \mathbf{g} \cdot n \, ds = 0.$$

5.2 DG Discretisation of The Stokes Equation

In this Section, the discontinuous Galerkin discretisation of the Stokes equation is described. Over the past several years, many researchers have been working on the discontinuous Galerkin methods for Stokes and Navier–Stokes equations. For a detailed account of the development of discontinuous Galerkin methods for incompressible flows refer Baker *et al.* (1990), Karakashian and Jureidini (1998), Hansbo and Larson (2002), Toselli (2002), Filippini and Toselli (2002), Cockburn *et al.* (2002), Schötzau *et al.* (2003), Girault *et al.* (2005a), Rivière and Girault (2006), Karakashian and Katsaounis (2006), Shahbazi *et al.* (2007). In this thesis, the discretisation given by Girault *et al.* (2005a;b) and Rivière and Girault (2006) is followed. There are several variants of discontinuous Galerkin methods (cf. Section (4.2)) for the solution of elliptic partial differential equations and we have chosen to use the interior penalty (IP) version. The IP versions with symmetric and non-symmetric variant of stabilisation with interior and boundary penalties are referred to as SIPG (see Section (4.3.3.1)) and NIPG (see Section (4.3.3.3)) respectively. The non-symmetric version without penalties is called OBB (see Section (4.3.3.2)) method. Before proceeding further, the notations introduced in the Section (4.3.2.1) for DG discretisation are recalled.

5.2.1 Weak Formulation

The weak form of the Stokes problem is derived here. On multiplying the Equation (5.2) by an arbitrary chosen test function $\mathbf{v}$ and q respectively and integrating over a domain Ω, we obtain

$$\int_{\Omega} (-\mu\Delta\mathbf{u} + \nabla p)\ \mathbf{v}\ d\Omega = \int_{\Omega} \mathbf{f}\ \mathbf{v}\ d\Omega \tag{5.5}$$

$$\int_{\Omega} (\nabla\cdot\mathbf{u})\ q = 0 \tag{5.6}$$

Using the *Greens formula or Greens identity*, the first term in the left-hand side of the equation (5.5) can be written as

$$\int_{\Omega} -\mu\Delta\mathbf{u}\ \mathbf{v}\ d\Omega = \mu\left(\int_{\Omega} \nabla\mathbf{u} : \nabla\mathbf{v}\ d\Omega - \int_{\partial\Omega} (\nabla\mathbf{u}\cdot\mathbf{n})\ \mathbf{v}\ ds\right) \tag{5.7}$$

and applying the *integration by parts* formula, the second term can be written as

$$\int_{\Omega} \nabla p\ \mathbf{v}\ d\Omega = -\int_{\Omega} p\ \nabla\cdot\mathbf{v}\ d\Omega + \int_{\partial\Omega} p\mathbf{v}\cdot\mathbf{n}\ ds \tag{5.8}$$

where $(\nabla\mathbf{u} : \nabla\mathbf{v})$ represents the component-wise scalar product. For example, in 2D, it is $(\nabla u_x \cdot \nabla v_x + \nabla u_y \cdot \nabla v_y)$. Similarly *following the integration by parts formula or divergence theorem*, left-hand side of (5.6) can be written as

$$\int_{\Omega} (\nabla\cdot\mathbf{u})\ q\ d\Omega = -\int_{\Omega} q\nabla\cdot\mathbf{u}\ d\Omega + \int_{\partial\Omega} q\mathbf{u}\cdot\mathbf{n}\ ds$$

Combining together Equations (5.7) and (5.8) we get,

$$\begin{aligned}\int_{\Omega} (-\mu\Delta\mathbf{u} + \nabla p)\ \mathbf{v}\ d\Omega = &\int_{\Omega} \mu\nabla\mathbf{u} : \nabla\mathbf{v}\ \ d\Omega \\ &- \int_{\partial\Omega} \mu(\nabla\mathbf{u}\cdot\mathbf{n})\ \mathbf{v}\ ds \\ &- \int_{\Omega} p\nabla\cdot\mathbf{v}\ d\Omega \\ &+ \int_{\partial\Omega} p\mathbf{v}\cdot\mathbf{n}\ ds = \int_{\Omega} \mathbf{f}\ \mathbf{v}\ dx\end{aligned} \tag{5.9}$$

$$\begin{aligned}\int_{\Omega} (\nabla\cdot\mathbf{u})\ q\ d\Omega &= -\int_{\Omega} q\ \nabla\cdot\mathbf{u}\ d\Omega + \int_{\partial\Omega} q\mathbf{u}\cdot\mathbf{n}\ ds \\ &= 0\end{aligned} \tag{5.10}$$

The equations (5.9) and (5.10) are the weak formulation of the stationary Stokes problem. The integrals of the weak formulation are now decomposed into element

contributions as shown below:

$$\begin{aligned}\sum_{E\in\mathcal{T}_h}\int_E(-\mu\Delta\mathbf{u}+\nabla p)\ \mathbf{v}\ dx &= \sum_{E\in\mathcal{T}_h}\int_E \mu\nabla\mathbf{u}:\nabla\mathbf{v}\ dx\\ &\quad-\sum_{\partial E\in\mathcal{E}_h}\int_{\partial E}\mu(\nabla\mathbf{u}\cdot\mathbf{n}_e)\ \mathbf{v}\ ds\\ &\quad-\sum_{E\in\mathcal{T}_h}\int_E p\nabla\cdot\mathbf{v}\ dx\\ &\quad+\sum_{\partial E\in\mathcal{E}_h}\int_{\partial E}p\mathbf{v}\cdot\mathbf{n}_e\ ds\\ &= \sum_{E\in\mathcal{T}_h}\int_E \mathbf{f}\ \mathbf{v}\ dx\end{aligned}$$

$$\begin{aligned}\sum_{E\in\mathcal{T}_h}\int_E(\nabla\cdot\mathbf{u})\ q\ dx &= -\sum_{E\in\mathcal{T}_h}\int_E q\nabla\cdot\mathbf{u}\ dx\\ &\quad+\sum_{\partial E\in\mathcal{E}_h}\int_{\partial E}q\mathbf{u}\cdot\mathbf{n}_e\ ds\\ &= 0\end{aligned}$$

Splitting the edge integrals into external and inter-element boundary integrals gives

$$\begin{aligned}\sum_{\partial E\in\mathcal{E}_h}\int_{\partial E}\mu(\nabla\mathbf{u}\cdot\mathbf{n}_e)\ \mathbf{v}\ ds &= \sum_{\mathcal{E}\in\mathcal{E}_h^I}\int_{\mathcal{E}}[\mu(\nabla\mathbf{u}\cdot\mathbf{n}_e)\ \mathbf{v}]\ ds\\ &\quad+\sum_{\mathcal{E}\in\mathcal{E}_h^B}\int_{\mathcal{E}}\mu(\nabla\mathbf{u}\cdot\mathbf{n}_b)\ \mathbf{v}\ ds\\ \sum_{\partial E\in\mathcal{E}_h}\int_{\partial E}p\mathbf{v}\cdot\mathbf{n}_e\ ds &= \sum_{\mathcal{E}\in\mathcal{E}_h^I}\int_{\mathcal{E}}[p\mathbf{v}\cdot\mathbf{n}_e]\ ds+\sum_{\mathcal{E}\in\mathcal{E}_h^B}\int_{\mathcal{E}}p\mathbf{v}\cdot\mathbf{n}_b\ ds\\ \sum_{\partial E\in\mathcal{E}_h}\int_{\partial E}q\mathbf{u}\cdot\mathbf{n}_e\ ds &= \sum_{\mathcal{E}\in\mathcal{E}_h^I}\int_{\mathcal{E}}[q\mathbf{u}\cdot\mathbf{n}_e]\ ds+\sum_{\mathcal{E}\in\mathcal{E}_h^B}\int_{\mathcal{E}}q\mathbf{u}\cdot\mathbf{n}_b\ ds\end{aligned}$$

where $\mathcal{E}_h=\mathcal{E}_h^I\cup\mathcal{E}_h^B$, $\mathbf{n}_e$ is the normal to the interior boundary, $\mathbf{n}_b$ is the unit outward pointing normal to the domain boundary and $[\cdot]$ is the discontinuity or jump in the function. Upon applying the identity (4.9) and since p is continuous ($p|_{\mathcal{E}}=\langle p\rangle|_{\mathcal{E}}$), we obtain

$$\begin{aligned}\sum_{\mathcal{E}\in\mathcal{E}_h^I}\int_{\mathcal{E}}[\mu(\nabla\mathbf{u}\cdot\mathbf{n}_e)\ \mathbf{v}]\ ds &= \sum_{\mathcal{E}\in\mathcal{E}_h^I}\int_{\mathcal{E}}\mu\langle(\nabla\mathbf{u}\cdot\mathbf{n}_e)\rangle[\mathbf{v}]\ ds\\ &\quad+\sum_{\mathcal{E}\in\mathcal{E}_h^I}\int_{\mathcal{E}}\mu\underbrace{[(\nabla\mathbf{u}\cdot\mathbf{n}_e)]}_{=0}\langle\mathbf{v}\rangle\ ds\end{aligned}$$

$$\sum_{\mathcal{E}\in\mathcal{E}_h^I}\int_{\mathcal{E}}[p\mathbf{v}\cdot\mathbf{n}_e]\,ds=\sum_{\mathcal{E}\in\mathcal{E}_h^I}\int_{\mathcal{E}}\langle p\rangle[\mathbf{v}\cdot\mathbf{n}_e]ds$$
$$\sum_{\mathcal{E}\in\mathcal{E}_h^I}\int_{\mathcal{E}}[q\mathbf{u}\cdot\mathbf{n}_e]\,ds=\sum_{\mathcal{E}\in\mathcal{E}_h^I}\int_{\mathcal{E}}\langle q\rangle[(\mathbf{u}\cdot\mathbf{n}_e)]\,ds$$

Substituting the above expression into the corresponding jump terms, we get

$$\begin{aligned}
&\mu\sum_{E\in\mathcal{T}_h}\int_E\nabla\mathbf{u}:\nabla\mathbf{v}\,dx\\
&-\sum_{\mathcal{E}\in\mathcal{E}_h^I}\int_{\mathcal{E}}\mu\langle(\nabla\mathbf{u}\cdot\mathbf{n}_e)\rangle[\mathbf{v}]\,ds\\
&-\sum_{\mathcal{E}\in\mathcal{E}_h^B}\int_{\mathcal{E}}\mu(\nabla\mathbf{u}\cdot\mathbf{n}_b)\,\mathbf{v}\,ds\\
&-\sum_{E\in\mathcal{T}_h}\int_E p\nabla\cdot\mathbf{v}\,dx\\
&+\sum_{\mathcal{E}\in\mathcal{E}_h^I}\int_{\mathcal{E}}\langle p\rangle[\mathbf{v}\mathbf{n}_e]ds=\sum_{E\in\mathcal{T}_h}\int_E\mathbf{f}\,\mathbf{v}\,dx
\end{aligned}$$

and

$$-\sum_{E\in\mathcal{T}_h}\int_E q\nabla\cdot\mathbf{u}\,dx+\sum_{\mathcal{E}\in\mathcal{E}_h^I}\int_{\mathcal{E}}\langle q\rangle[(\mathbf{u}\cdot\mathbf{n}_e)]\,ds+\sum_{\mathcal{E}\in\mathcal{E}_h^B}\int_{\mathcal{E}}q\mathbf{u}\cdot\mathbf{n}_b\,ds=0 \tag{5.11}$$

Now referring to the general formulation of the model elliptic problem (4.26) described in the Section (4.3.2.2), we add the terms corresponding to consistency, symmetry and stabilisation as explained and additionally the Dirichlet boundary conditions are applied weakly.

In order to have symmetry the following term is added.

$$\epsilon\sum_{\mathcal{E}\in\mathcal{E}_h^I}\int_{\mathcal{E}}\mu\langle(\nabla\mathbf{v}\cdot\mathbf{n}_e)\rangle[\mathbf{u}]\,ds$$

and for stability, following penalty/jump term is applied:

$$J_0(\mathbf{u},\mathbf{v})=\sum_{\mathcal{E}\in\mathcal{E}_h^I}\frac{\sigma}{|e|}\int_{\mathcal{E}}[\mathbf{u}]\cdot[\mathbf{v}]\,ds \tag{5.12}$$

Note that both the above terms vanish for smooth solution. Now apply Dirichlet BCs weakly:

$$\epsilon\sum_{\mathcal{E}\in\mathcal{E}_h^D}\int_{\mathcal{E}}\mu(\nabla\mathbf{v}\cdot\mathbf{n}_b)(\mathbf{u}-\mathbf{g})\,ds$$

and

$$\sum_{\mathcal{E}\in\mathcal{E}_h^D} \frac{\sigma}{|e|} \int_{\mathcal{E}} [\mathbf{v}] \cdot (\mathbf{u} - \mathbf{g})\, ds$$

5.2.2 General Formulation

The primal formulation of the interior penalty version of DG discretisation of the Stokes problem (5.2) can be written as follows:

Find $(\mathbf{u}_h, p_h) \in \mathbf{V}_h \times Q_h$ such that

$$\begin{cases} \mu\,(A(\mathbf{u}_h, \mathbf{v}_h) + J_0(\mathbf{u}_h, \mathbf{v}_h)) + B(\mathbf{v}_h, p_h) = F(\mathbf{v}_h) & \forall \mathbf{v}_h \in \mathbf{V}_h \\ B(\mathbf{u}_h, q_h) = G(q_h) & \forall q_h \in Q_h \end{cases} \tag{5.13}$$

where

$$\begin{aligned} A(\mathbf{u}_h, \mathbf{v}_h) = &\sum_{E\in\mathcal{T}_h} \int_E \nabla\mathbf{u}_h : \nabla\mathbf{v}_h\, dx \\ &- \sum_{\mathcal{E}\in\mathcal{E}_h^I} \int_{\mathcal{E}} \langle \nabla\mathbf{u}_h \cdot \mathbf{n}_e \rangle [\mathbf{v}_h]\, ds \\ &+ \epsilon \sum_{\mathcal{E}\in\mathcal{E}_h^I} \int_{\mathcal{E}} \langle \nabla\mathbf{v}_h \cdot \mathbf{n}_e \rangle [\mathbf{u}_h]\, ds \\ &- \sum_{\mathcal{E}\in\mathcal{E}_h^B} \int_{\mathcal{E}} (\nabla\mathbf{u}_h \cdot \mathbf{n}_b)\, \mathbf{v}_h\, ds \\ &+ \epsilon \sum_{\mathcal{E}\in\mathcal{E}_h^B} \int_{\mathcal{E}} (\nabla\mathbf{v}_h \cdot \mathbf{n}_b) \mathbf{u}_h\, ds \end{aligned}$$

$$\begin{aligned} J_0(\mathbf{u}_h, \mathbf{v}_h) = &\sum_{\mathcal{E}\in\mathcal{E}_h^I} \frac{\sigma}{|e|} \int_{\mathcal{E}} [\mathbf{u}_h] \cdot [\mathbf{v}_h]\, ds \\ &+ \sum_{\mathcal{E}\in\mathcal{E}_h^B} \frac{\sigma}{|e|} \int_{\mathcal{E}} \mathbf{u}_h \cdot \mathbf{v}\, ds \end{aligned}$$

$$\begin{aligned} B(\mathbf{v}_h, p_h) = &- \sum_{E} \int_E p_h \nabla \cdot \mathbf{v}_h\, dx \\ &+ \sum_{\mathcal{E}\in\mathcal{E}_h^I} \int_{\mathcal{E}} \langle p_h \rangle [\mathbf{v}_h \cdot \mathbf{n}_e]\, ds \\ &+ \sum_{\mathcal{E}\in\mathcal{E}_h^B} \int_{\mathcal{E}} p_h\, \mathbf{v}_h \cdot \mathbf{n}_b\, ds \end{aligned}$$

$$B(\mathbf{u}_h, q_h) = -\sum_{\in\mathcal{T}_h} \int_E q_h \nabla \cdot \mathbf{u}_h \, dx + \sum_{\mathcal{E}\in\mathcal{E}_h^I} \int_{\mathcal{E}} \langle q_h \rangle [\mathbf{u}_h \cdot \mathbf{n}_e] \, ds + \sum_{\mathcal{E}\in\mathcal{E}_h^{DP}} \int_{\mathcal{E}} q_h \, \mathbf{u}_h \cdot \mathbf{n}_b \, ds$$

$$F(\mathbf{v}_h) = \sum_{E\in\mathcal{T}_h} \int_E \mathbf{f} \cdot \mathbf{v}_h \, dx + \mu \, \epsilon \sum_{\mathcal{E}\in\mathcal{E}_D} \int_{\mathcal{E}} (\nabla \mathbf{v}_h \cdot \mathbf{n}_b) \, \mathbf{g} \, ds + \mu \sum_{\mathcal{E}\in\mathcal{E}_\mathrm{D}} \frac{\sigma}{|e|} \int_{\mathcal{E}} \mathbf{g} \cdot \mathbf{v}_h \, ds - \sum_{\mathcal{E}\in\mathcal{E}_\mathrm{DP}} \int_{\mathcal{E}} p_0 \, \mathbf{v}_h \cdot \mathbf{n}_b \, ds$$

$$G(q) = -\sum_{\mathcal{E}\in\mathcal{E}_\mathrm{D}} \int_{\mathcal{E}} q_h \, \mathbf{g} \cdot \mathbf{n}_b \, ds.$$

Here $|e|$ denotes the measure of the edge and β is a user defined parameter. The user supplied parameters ϵ and $\sigma >= 0$ are defined as before for the model elliptic problem. We get SIPG for $\epsilon = 1$, IIPG for $\epsilon = 0$, NIPG for $\epsilon = -1$ and OBB for $\epsilon = -1$ and $\sigma = 0$.

Notes:

1. $\mathcal{E}_D \subset \mathcal{E}^B$ is the set of edges where Dirichlet boundary conditions for velocity is applied (e.g. no-slip, prescribed velocity profile)
2. $\mathcal{E}_{DP} \subset \mathcal{E}^B$ is the set of edges where Dirichlet boundary conditions for pressure is applied (e.g. prescribed pressure)

5.3 Local Mass Conservation

The local mass conservation, i.e. conservation of mass on each element, is natural in the DG discretisation. Since the continuity requirement between the elements is relaxed, we can take a test function that is different on each element. Within the Stokes problem, the local mass balance is the consequence of the discretisation of the incompressibility equation $\nabla \cdot \boldsymbol{u} = 0$. Let us take an arbitrary element E belongs to $\mathcal{E}_h$, and let q=1 on E

and 0 elsewhere. Then the Equation (5.11) becomes

$$-\int_E \nabla \cdot \mathbf{u}\, dx + \sum_{\mathcal{E}\in\partial E\setminus\partial\Omega}\int_{\mathcal{E}}[\mathbf{u}\cdot\mathbf{n}_e]\, ds + \sum_{\mathcal{E}\in\partial E\cap\Omega}\int_{\mathcal{E}}\mathbf{u}\cdot\mathbf{n}_b\, ds = 0 \tag{5.14}$$

Now using the *divergence theorem* (or Gauss' theorem) which states that the integral of a vector field divergence over a domain is equal to the integral of the normal component of the field along the boundaries, the first term in the Equation (5.14) can be written as

$$-\int_E \nabla \cdot \mathbf{u}\, dx = -\int_{\partial E}\mathbf{u}\cdot\mathbf{n}_E\, ds$$

where n_E denotes the outward normal to E. Upon substitution, the Equation (5.14) changes to

$$-\int_{\partial E}\mathbf{u}\cdot\mathbf{n}_E\, ds + \sum_{\mathcal{E}\in\partial E\setminus\partial\Omega}\int_{\mathcal{E}}[\mathbf{u}\cdot\mathbf{n}_e]\, ds + \sum_{\mathcal{E}\in\partial E\cap\Omega}\int_{\mathcal{E}}\mathbf{u}\cdot\mathbf{n}_b\, ds = 0 \tag{5.15}$$

The property of local mass conservation is important for flow and transport problems in porous media.

5.4 Saddle Point Stokes Problem

The primitive variable formulation with both velocity and pressure as unknowns is known as *mixed finite element* formulation. Such formulation present numerical difficulties related to the treatment of the saddle point problem which arises from the variational formulation of the incompressible flow equation with pressure acting as a Lagrangian multiplier of the incompressibility constraint (Elman *et al.* 2005). The resulting algebraic system for the velocity and pressure in a Galerkin framework can be expressed as a system of linear equations:

$$\begin{bmatrix}\mathbf{A} & B^T\\ B & \mathbf{0}\end{bmatrix}\begin{bmatrix}\mathbf{u}\\ p\end{bmatrix} = \begin{bmatrix}\mathbf{f}\\ g\end{bmatrix} \tag{5.16}$$

where the block matrix has a null sub-matrix on the diagonal (large block of zeros at the main diagonal giving rise to saddle point structure). In the discrete case, this block matrix will be symmetric but *indefinite*. The matrix $\mathbf{A}$ is called the *vector-Laplacian matrix* (viscous part) and the matrix B is called the *divergence matrix*. It is well known that the finite element spaces for velocity and pressure need to be chosen carefully satisfying the *inf-sup* condition or LBB condition to obtain a stable Galerkin formulation (Girault and Raviart 1979) such that the discrete problem is solvable.

The equal order basis for velocity and pressure does not satisfy the *inf-sup* condition and hence the discretisation is not stable. Usually the approximating polynomials

are taken *one degree higher* for velocity than for pressure and hence in all numerical computations presented in this thesis, the approximation basis for velocity is always taken one order higher than the pressure basis to satisfy LBB condition.

5.5 Boundary Conditions

The boundary conditions are the physical constraints associated with the fluid flow system and are important part of the mathematical model of fluid flows as boundaries direct motion of flow. Mathematically speaking, in order to yield a well-posed problem, partial differential equations have to be supplied with suitable boundary and initial conditions (in the case of transient problems). That is, to ensure the existence of a unique solution to the governing equations, appropriate boundary and initial conditions have to be imposed at the boundary $\partial\Omega$ of Ω. Mainly two types of boundary conditions are being used for the solution of Stokes equation: Dirichlet and Neumann boundary conditions. When using a Dirichlet boundary condition, one prescribes the value of the variable at the boundary, e.g. $\mathbf{u} = g$. The so called *no-slip* boundary condition is a Dirichlet type. In viscous flows, at the solid boundaries such as grains, obstacles and solid walls we apply the *no-slip* boundary condition in which tangential fluid velocity and normal velocity component are set to zero. When using a Neumann boundary condition, one prescribes the gradient normal to the boundary of a variable, e.g., $\partial_n u(x) = constant$.

The following boundary setups are considered for the solution of stationary Stokes equation:

- Inflow–outflow type

  When the velocity profile is known at inlet, it is specified at the inlet boundary. At the outlet, outflow boundary condition is used. Outflow condition models *flow exits* where the details of the flow velocity and pressure are not known prior to the solution of the flow problem. The outflow boundary condition assumes a zero normal gradient for all flow variables except pressure.

  Since outflow boundaries are caused by the need to limit the computational domain than any physically reasonable boundary, neither essential nor natural boundary data is available there. Hence outflow boundary conditions are considered a particular challenge in numerical simulations. In this thesis, the popular '*do nothing*' boundary condition by Heywood *et al.* (1996) is used at the outflow boundary, which implies the assumption of a zero Neumann boundary condition.

- Pressure drop

  A pressure boundary condition is required as the pressure is determined by the incompressible Navier-Stokes equations up to a constant. For pure flow problems the pressure constant is usually fixed implicitly by a Neumann boundary condition

or directly at a particular point. Alternatively the mean value of the pressure can be fixed. Pressure drop boundary conditions prescribe pressure both at the inlet and outlet and flow is driven by the imposed pressure difference. Pressure outlet must always be used when model is set up with a pressure inlet.

5.6 Prescribed Pressure Formulation

When using the *pressure drop* boundary condition as mentioned before, the following prescribed formulation is used (Heywood *et al.* 1996). Let $\Omega \subset \mathbb{R}^d$ be a bounded, open and connected Lipschitz domain. For any prescribed constants p_0, find velocity and pressure $\big((\mathbf{u},p) \in H^1(\Omega)^d \times L^2(\Omega)\big)$ such that

$$\begin{aligned} -\mu\Delta\mathbf{u} + \nabla p &= \mathbf{f} \quad \text{in} \quad \Omega \subset \mathbb{R}^3 \\ \nabla\cdot\mathbf{u} &= 0 \quad \text{in} \quad \Omega \\ \mathbf{u} &= 0 \quad \text{on} \quad \Gamma_0 \subseteq \partial\Omega \\ \partial_n\mathbf{u} - p &= p_0 \quad \text{on} \quad \Gamma_P. \end{aligned} \tag{5.17}$$

where $\mu > 0$ is the coefficient of viscosity of the fluid.

Finally, the DG discretisation of the Stokes equation using the non-symmetric scheme introduced by Oden-Babuška-Baumann with prescribed pressure formulation reads: *Find* $\mathbf{u} \in \mathbf{V}$, $p \in Q$ *such that*

$$\begin{aligned} \mu a(\mathbf{u},\mathbf{v}) + b(\mathbf{v},p) &= l(\mathbf{v}) \qquad \forall\, \mathbf{v} \in \mathbf{V} \quad , \\ b(\mathbf{u},q) &= 0 \qquad \forall\, q \in Q \quad . \end{aligned} \tag{5.18}$$

where

$$\begin{aligned} a(\mathbf{u},\mathbf{v}) &= \sum_E \int_\Omega \nabla\mathbf{u} : \nabla\mathbf{v} - \sum_{\gamma_{\text{ef}}\in\Gamma_{\text{int}}} \int_{\gamma_{\text{ef}}} \langle\nabla\mathbf{u}\cdot n\rangle[\mathbf{v}] + \sum_{\gamma_{\text{ef}}\in\Gamma_{\text{int}}} \int_{\gamma_{\text{ef}}} \langle\nabla\mathbf{v}\cdot n\rangle[\mathbf{u}] \\ b(\mathbf{u},q) &= -\sum \int_\Omega q\nabla\cdot\mathbf{u} + \sum_{\gamma_{\text{ef}}\in\Gamma_{\text{int}}} \int_{\gamma_{\text{ef}}} \langle q\rangle[\mathbf{u}\cdot n] \\ l(\mathbf{v}) &= -\sum_{\gamma_{\text{p}}\in\Gamma_{\text{P}}} p_0 \int_{\gamma_p} \mathbf{v}\cdot\mathbf{n}ds \end{aligned}$$

5.7 Implementation and Testing

The mathematical models that are represented by PDEs are solved using numerical techniques such as finite element methods. The numerical implementation of such methods is not an easy process especially for large and complex models. The numerical implementation of finite element based methods usually require the following:

1. *The spatial discretisation of the problem domain (representative mesh or grid)*

   The spatial discretisation which is called mesh generation or grid generation refers to the process of subdividing the domain to generate a polygonal or polyhedral mesh that approximates the given geometric domain. The mathematical entities and basis functions are defined on this elements. The mesh generation itself is an active research area involving mathematicians, computer scientists and engineers. The realistic mesh generation in 3D for complex objects is still considered a formidable task.

2. *The mathematical framework of the finite element method (basis, shape function, degrees of freedom)*

   Setting up of the finite element base for the problem where the basis functions are chosen to discretise the function space.

3. *Assembling of the stiffness matrix*

   Consists of assembling the entries of element stiffness matrices and right-hand side vectors into a global system of equation ($\mathbb{A}\mathbf{x} = \mathbf{b}$). This is mostly problem specific part in which boundary conditions are also to be considered.

4. *Solution of the system of equations*

   The numerical methods in general approximate the PDEs and generate the matrix and vector for the unknowns in the equation. The resulting algebraic system needs to be solved for the unknown coefficients.

5. *Post-processing of the results*

   The visualisation of the results, computation of errors and analysis are part of post-processing.

In general grid generation, finite element framework and solver parts can be implemented as a general purpose modules as they are independent of a particular application and there is no need to re-implement them. The assembling part is the only part which is problem specific to obtain the global system of equations for the corresponding differential equation. Such numerical tools must provide the problem independent components with a flexibility that ease incorporation of the problem specific parts. This requires data structures, which allow an easy and efficient implementation of the problem dependent parts. It should also have a linear algebra module with an efficient implementation of matrices, vectors and solvers for linear equations or access to other solver library routines. DUNE is such a general purpose and unified framework for the numerical solution of PDEs.

5.7.1 DUNE

In this section we briefly describe the concepts and important aspects of the DUNE software framework within which the discontinuous Galerkin discretisation of Stokes equation is realised. For a detailed understanding of the underlying concept of DUNE, refer to Bastian *et al.* (2004; 2008b;a). The DUNE website[a] provides all the documentation, implementation and development details on-line.

DUNE is a modular toolbox for solving partial differential equations (PDEs) with grid-based methods, which is available as a software package written in C++ that has a collection of abstract interfaces. One of the major goals of such an interface based numeric environment is the separation of data structures and algorithms (Bastian *et al.* 2004) . DUNE enables design and implementation of numerical algorithms independent of the type of grid (structured, unstructured, parallel) used. The DUNE framework uses generic C++ techniques to allow for efficiency, flexibility and code reuse (Bastian *et al.* 2004). The algorithms are written based on the abstract interface and users can access grids, finite element functionality, solvers, visualisation etc. through the abstract interface. The abstract interface with fine granularity use static (or compile-time) polymorphism to achieve high performance. Within the DUNE framework it is possible to use existing codes (e.g. UG. ALBERTA). One of the advantages with it's uniform interface is that, the user has the option to try out different implementations of grids and solvers without any extra effort.

The central to DUNE is its grid interface, which describes structured, unstructured and parallel grids of arbitrary dimensions and currently supports different grid implementations such as *SGrid* ,*YaspGrid*, *UG*, etc.

One of the important components in the numerical solution of PDEs is the linear algebra module, which solves the resulting system of linear equations arising from numerical discretisation. The solver module in the DUNE is called Iterative Solver Template Library (ISTL). The ISTL is designed to handle the natural sparse block structure of the matrices obtained when discretising PDEs using, for example, finite element methods (Blatt and Bastian 2007). Using generic programming techniques, ISTL exploits the matrix structure which is known at compile time to efficiently solve the system of linear equations. Currently ISTL has various direct (SuperLU) and iterative solvers (CG, BICG-Stab, etc.) available for the solution of large linear systems.

5.7.2 Assembling The Stiffness Matrix

Since the finite element methods are always based on the integral formulation, one important step in the implementation of finite element based codes is the assembling routine, which is the most problem specific part and it consists of evaluating certain

[a] http://www.dune-project.org/index.html

integrals over elements and boundaries. For example, implementation of the assembling routine for the DG discretisation of the Stokes equation using the formula given in Equation (5.13) consists of a sum over elements and faces like:

$$\sum_{E\in\mathcal{T}_h}\left(\int_E \cdots + \int_{\partial E} \cdots\right) = \sum_{E\in\mathcal{T}_h}\int_E \cdots + \sum_{\mathcal{E}\in\mathcal{E}_h^I}\int_{\mathcal{E}} \cdots + \sum_{\mathcal{E}\in\mathcal{E}_h^B}\int_{\mathcal{E}} \cdots \tag{5.19}$$

As we can see, such formulation allows to split the assembling into separate loops: one for volume, one for internal edges/faces and one for boundary faces. In general, the integrals as shown symbolically in the Equation (5.19) are not computed directly because in most cases the integrals are not simple analytical forms. They are often approximated using numerical integration techniques as the weighted sum of integrand evaluations on set of quadrature points in the reference geometry as (for e.g. in one dimension)

$$I = \int_a^b f(\xi)d\xi \approx \sum_{i=1}^{N} W_i f(\xi_i),$$

where W_i and (ξ_i) are the weights and chosen evaluation points, respectively. The approximation developed for one-dimensional integration can be easily extended to higher dimensions. However, as the dimension increases, the number of quadrature points grows geometrically. It should be noted that since basis functions are given in natural or local coordinates[b], we also need to map our real coordinates to the natural coordinates to perform the integration. There are various integration schemes such as Trapezoidal, Simpsons' and Gaussian rules. The Gaussian quadrature methods are widely being used due to its high-order accuracy with less number of sampling points. Using N quadrature points it can accurately evaluate the integral of a polynomial P of degree up to $2N-1$. In DUNE, implementation of Gaussian weights and quadrature points are available for various element geometries.

Because of the local nature of the discontinuous formulation, generally there is no need for a global assembly procedure and assembling can be done element-wise. The matrix arising from the DG discretisation has a block structure where the diagonal blocks represent inner element operation, while the off-diagonal blocks are the result of inter-element fluxes which couple adjacent elements. The block can be inverted at very low computational cost (where the inverse of the matrix can be calculated block-by-block instead of calculating the inverse of the whole matrix) when solving for the solution. The ISTL module in DUNE is designed to handle such block structured matrices very efficiently.

Another point to be considered when evaluating the face integrals is that one would

[b] Natural coordinates are dimensionless coordinates expressed with reference to the element than with reference to the global/real coordinate system.

also need the values of the adjacent elements' basis functions on the quadrature points. Due to the nested loop in the assembling, when iterating over the faces of each element, a face would be reached from both the elements that share the face. In order to assemble face terms only once, a simple conditional rule based on the index of the elements was introduced that decides from which element the face should be accessed.

5.7.3 Solver

An iterative solver based on the stabilised bi-conjugate gradient method (BICG-STAB) with ILU preconditioner was used to solve the Stokes equations. This solver is one of the many solvers available in the ISTL module of DUNE.

5.7.4 Visualisation of The Results

Visualisation of the results presented in this thesis was mostly done by ParaView[c] (Hendersen 2007) and gnuplot[d]. ParaView is an open-source visualisation application integrating many VTK features. DUNE has a VTK writer interface to write data in the VTK format and ParaView can be used to display the data. gnuplot is another widely used open source program to plot and visualise data and it has been used for some of the plots and graphs in this thesis.

5.7.5 Numerical Test Problems

The discontinuous Galerkin discretisation of the Stokes equation is implemented within the DUNE framework. In this Section, to verify the implementation, several numerical tests including benchmarking test are presented. The following problems are considered:

1. Mass conservation test
2. Problem with analytical solution, 2D
3. Poiseuille flow problem in channel, 2D
4. Driven cavity problem, 2D

5.7.5.1 Mass Conservation Test

One measure of the accuracy of any numerical discretisation scheme is to check how well the method conserves mass. This can be measured by comparing the net fluxes

[c] http://paraview.org/
[d] http://www.gnuplot.info/

in the domain (e.g, inflow, outflow). The continuity equation or mass conservation equation is given in the differential form as

$$\frac{\partial \rho}{\partial t} + \nabla \cdot (\rho \mathbf{u}) = 0$$

where ρ is the density of fluid, t is time, and $\mathbf{u}$ is fluid velocity. In the case of incompressible flow, density ρ is assumed to be constant and hence the mass conservation equation simplifies to a volume conservation equation:

$$\nabla \cdot \mathbf{u} = 0 \tag{5.20}$$

which means that the divergence of velocity field is zero everywhere. Hence the test for mass balance consists of checking if the velocity field satisfies the Equation (5.20). Alternatively the Equation (5.20) can be written as the derivative of the net flow of the velocity field across a very small surface ds. The amount of fluid passing through ds per unit time is then given by

$$\mathcal{F} = \mathbf{u} \cdot \mathbf{n}\, ds$$

and the total flux across a surface is given by

$$\int \mathcal{F} = \mathbf{u} \cdot \mathbf{n}\, ds$$

Since the DG based numerical schemes are locally and globally mass conservative (see Section (5.3)), both local and global mass balance were checked. The local mass balance test evaluates the integral

$$\int_{\partial E} \mathbf{u} \cdot \mathbf{n}_E\, ds \qquad \forall E \in \mathcal{E}_h$$

where E denotes an element or cell in the triangulation $\mathcal{E}_h$ of the domain, ∂E represents the edge or face of E and $\boldsymbol{n_E}$ is the outward normal to the element E. Similarly, the global mass balance check evaluates the following integral

$$\int_{\partial \Omega} \mathbf{u} \cdot \mathbf{n}\, ds$$

where the integration is over the domain boundary $\partial\Omega$. The domain considered for the mass balance test is shown in the Figure (5.1(a)) and the Stokes velocity field is given in Figure (5.1(b)). The computed errors in the global mass balance for various grid refinement levels are plotted in the Figure (5.2) where it is observed that the errors are in the order of the machine precision. Similarly local mass balance errors were computed and plotted in Figure (5.3) and again the errors are in the order of the machine precision. Hence the method is successfully implemented with respect to

the mass balance and is able to conserve mass locally and globally up to the machine precision.

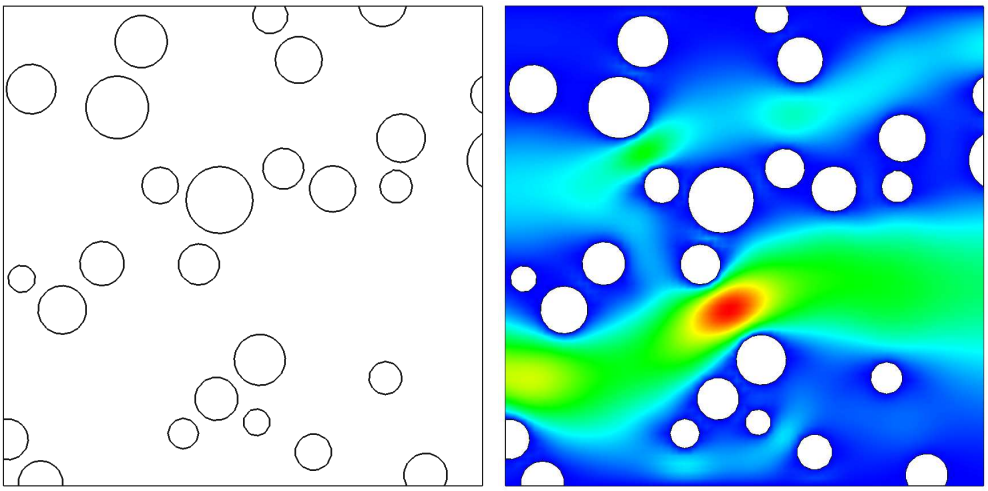

(a) Computational domain (b) Magnitude of the velocity field

Figure. 5.1. Computational domain for mass balance test is shown in the left (a). The domain consists of a unit square with some random holes in it. Velocity field was computed by solving the Stokes equation on the domain and its magnitude is shown in the right (b).

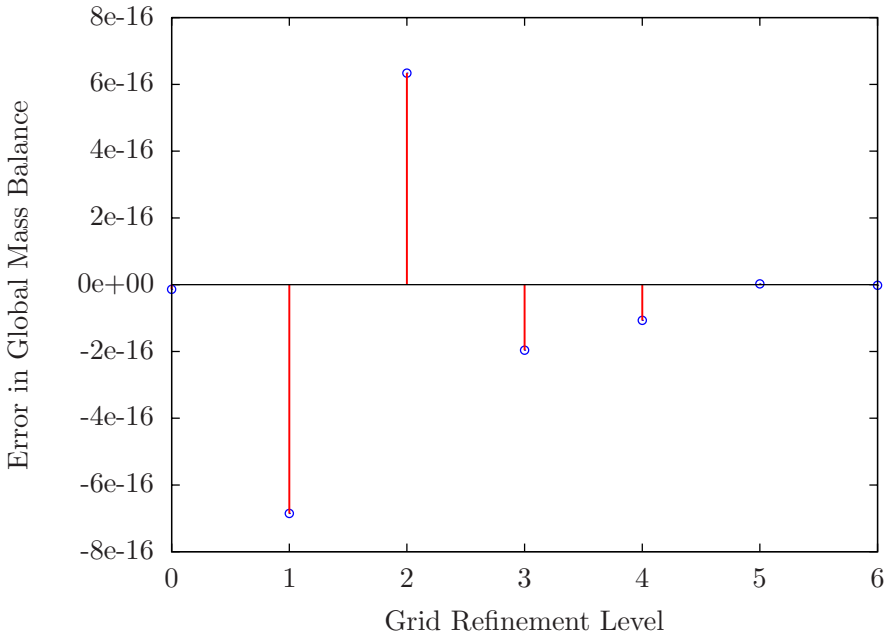

Figure. 5.2. Global mass balance error for various grid refinement level.

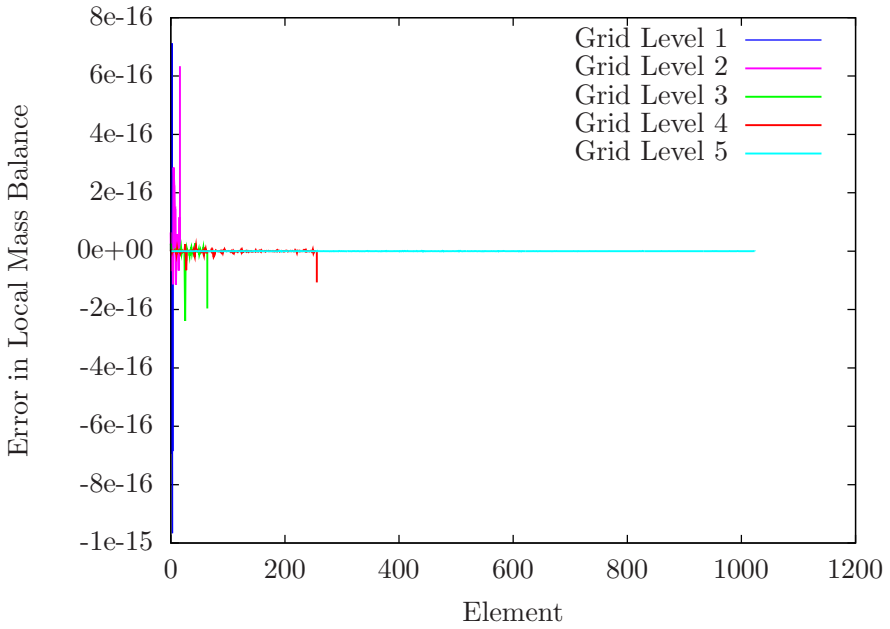

Figure. 5.3. Local mass balance error on each element of the grid for various grid refinement levels.

5.7.5.2 Stokes Flow With Analytical Solution (2D)

The Stokes problems with analytical solution are available for verifying the code and validating the numerical methods. In order to obtain an analytical solution, we need to find a velocity field such as $\nabla \cdot \mathbf{u} = 0$, the incompressibility condition. We refer to the example problem given in (Rivière and Girault 2006) which fulfills the above condition. Let $\mathbf{u}(u, v)$ be the velocity field with x-component u and y-component v. Then,

$$\begin{aligned} u(x,y) &= x^2(1-x)^2(2y - 6y^2 + 4y^3) \\ v(x,y) &= -y^2(1-y)^2(2x - 6x^2 + 4x^3) \end{aligned} \tag{5.21}$$

In addition, the constant of viscosity is taken as $\mu = 1$. The pressure field can be chosen randomly because only needed is its gradient. In this case, it has been chosen as

$$p(x,y) = x + y$$

as given in (Rivière and Girault 2006). Then, according to Equation (5.2), the applied forces match

$$\begin{aligned} f_x &= -(24y - 12)(x^4 - 2x^3 + x^2) + (4y^3 - 6y^2 + 2y)(12x^2 - 12x + 2) + 1 \\ f_y &= (24x - 12)(y^4 - 2y^3 + y^2) + (4x^3 - 6x^2 + 2x)(12y^2 - 12y + 2) + 1 \end{aligned}$$

The problem is solved in a square domain of unit sides, $\Omega = [0, 1] \times [0, 1]$. The analytical velocity is shown in Figure (5.4).

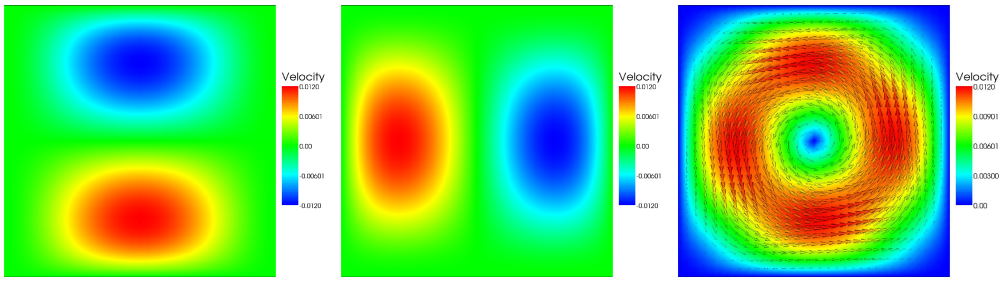

Figure. 5.4. Stokes velocity field for the analytical test problem

A uniform grid refinement study was performed to test the error convergence of the discretisation. In the following, we present the results of the convergent study on the analytical problem (5.21). Different variants of DG schemes were tested: OBB scheme, SIPG scheme with $\sigma = 1$ (SIPG1) and $\sigma = 10$ (SIPG10), NIPG scheme with $\sigma = 1$ (NIPG1) and $\sigma = 10$ (NIPG10). In all the tests, the velocity approximation was always taken one degree higher than pressure basis and the polynomial degree k and parameter σ were varied. The order of convergence was computed as described below.

Order of Convergence

Let u be the exact analytical solution and u_h be the approximate solution obtained with the discretisation size h. Then the discretisation error $e_h = u - u_h$ and the order of convergence p is defined as $\|e_h\| = \mathcal{O}(h^p)$. The order p can be evaluated by comparing the two discretisation errors obtained with two different sizes h_1 and h_2 respectively as

$$p = \frac{ln\ \|e_{h_1}\| - ln\ \|e_{h_2}\|}{ln\left(\frac{h_1}{h_2}\right)} \tag{5.22}$$

The Equation (5.22) can be further simplified when the mesh is refined uniformly and successively. Then the numerical convergence rate is calculated by

$$p = \frac{ln\left(\frac{e_h}{e_{\frac{h}{2}}}\right)}{ln(2)}$$

The results of the convergent study for $k = 1$, where linear approximation for velocity and piecewise constant approximation for pressure ($P_1 - P_0$) are given in the Table (5.1). As predicted by the theory, we observe that the error of $\mathbf{u}$ in the H^1 norm is $\mathcal{O}(h)$. We obtain optimal convergence rates for velocity in L^2 and H^1 norm and pressure in L^2 norm. The OBB method was not convergent in this case as it is stable only when $k \geq 2$ and hence the results are not given for OBB. We can also observe that SIPG1 is not converging possibly due to small value of σ. However, SIPG10 is converging optimally

Table 5.1. Numerical errors and convergence rates for $P_1 - P_0$ approximation of the Stokes problem

Method	h	Velocity				Pressure	
		L^2 Error	L^2 Rate	H^1 Error	H^1 Rate	L^2 Error	L^2 Rate
NIPG1	1						
	1/2	4.792e-02	2.38	1.222e-01	1.06	5.046e-01	1.09
	1/4	1.520e-02	1.65	5.351e-02	1.19	3.212e-01	0.65
	1/8	4.248e-03	1.83	2.048e-02	1.38	1.773e-01	0.85
	1/16	1.117e-03	1.92	8.130e-03	1.33	9.366e-02	0.92
	1/32	2.860e-04	1.96	3.531e-03	1.20	4.824e-02	0.95
	1/64	7.231e-05	1.98	1.651e-03	1.09	2.448e-02	0.97
NIPG10	1						
	1/2	1.073e-02	1.23	4.731e-02	0.03	5.843e-01	0.88
	1/4	3.285e-03	1.70	2.647e-02	0.83	3.019e-01	0.95
	1/8	1.015e-03	1.69	1.347e-02	0.97	1.551e-01	0.96
	1/16	2.918e-04	1.79	6.513e-03	1.04	7.852e-02	0.98
	1/32	7.744e-05	1.91	3.186e-03	1.03	3.950e-02	0.99
	1/64	1.975e-05	1.97	1.580e-03	1.01	1.981e-02	0.99
SIPG 1	1						
	1/2	1.021e+00	-1.98	3.074e+00	-3.22	5.178e+00	-2.26
	1/4	2.618e-01	1.93	2.154e+00	0.51	2.371e+00	1.12
	1/8	1.503e-02	4.12	2.531e-01	3.08	1.729e-01	3.77
	1/16	1.887e+01	-10.29	7.963e+02	-11.61	6.021e+02	-11.76
SIPG10	1						
	1/2	1.188e-02	1.09	4.747e-02	0.04	6.949e-01	0.63
	1/4	3.947e-03	1.59	2.837e-02	0.74	3.591e-01	0.95
	1/8	1.320e-03	1.58	1.458e-02	0.95	1.841e-01	0.96
	1/16	3.994e-04	1.72	6.798e-03	1.10	9.318e-02	0.98
	1/32	1.080e-04	1.88	3.233e-03	1.07	4.687e-02	0.99
	1/64	2.796e-05	1.95	1.587e-03	1.02	2.351e-02	0.99

and it means that in the case of SIPG1, σ=1 was not large enough. We can see that the NIPG method works well with small values of σ whereas SIPG needs large values of σ to be stable. The results presented here matches well with that reported in Rivière and Girault (2006).

The results for cases $k = 2$ and $k = 3$ are presented in Table (5.2) and (5.3) respectively. When velocities are approximated by piecewise quadratics and the pressure by piecewise linear all methods converge optimally in H^1 norm for velocity and L^2 norm for pressure. But in L^2 norm for velocity, NIPG methods and OBB are sub-optimal and exhibit only of the order $\mathcal{O}(h^k), k = 2$. These results confirm the previously reported results in literature that for elliptic problems optimal results are only observed when degree of polynomial is odd. Optimal convergence can be observed in the results presented in Table (5.3).

Table 5.2. Numerical errors and convergence rates for $P_2 - P_1$ approximation of the Stokes problem

Method	h	Velocity				P	
		L^2 Error	L^2 Rate	H^1 Error	H^1 Rate	L^2 Error	L^2 Rate
NIPG1	1						
	1/2	1.846e-03	2.22	2.756e-02	1.06	1.572e-02	
	1/4	4.878e-04	1.92	9.092e-03	1.60	6.703e-03	1.23
	1/8	8.743e-05	2.48	2.275e-03	1.99	1.098e-03	2.60
	1/16	1.870e-05	2.22	5.504e-04	2.04	1.618e-04	2.76
	1/32	4.409e-06	2.08	1.353e-04	2.02	3.094e-05	2.38
	1/64	1.082e-06	2.02	3.359e-05	2.01	7.389e-06	2.06
NIPG10	1						
	1/2	1.709e-03	1.27	2.485e-02	0.74	2.357e-03	
	1/4	2.998e-04	2.51	7.244e-03	1.77	5.627e-03	-1.25
	1/8	4.079e-05	2.87	1.941e-03	1.89	9.530e-04	2.56
	1/16	5.484e-06	2.89	4.892e-04	1.98	1.438e-04	2.72
	1/32	1.063e-06	2.36	1.222e-04	2.00	2.254e-05	2.67
	1/64	1.458e-07	2.86	3.055e-05	1.99	5.163e-06	2.12
OBB	1						
	1/2	2.590e-03	2.61	3.111e-02	1.35	2.091e-02	
	1/4	8.197-04	1.66	1.230e-02	1.33	1.194e-02	0.80
	1/8	1.674e-04	2.29	3.037e-03	2.01	2.177e-03	2.45
	1/16	3.817e-05	2.13	7.070e-04	2.10	3.257e-04	2.74
	1/32	8.998e-06	2.08	1.699e-04	2.05	6.158e-05	2.40
	1/64	2.175e-06	2.04	4.172e-05	2.02	1.463e-05	2.07
SIPG10	1						
	1/2	1.927e-03	1.03	2.720e-02	0.63		
	1/4	4.325e-04	2.15	7.886e-03	1.78	9.267e-03	-2.42
	1/8	5.795e-05	2.89	2.004e-03	1.97	1.726e-03	2.42
	1/16	6.176e-06	3.23	4.943e-04	2.02	2.395e-04	2.84
	1/32	7.052e-07	3.13	1.226e-04	2.01	3.341e-05	2.84

5.7.5.3 Channel Problem

The second problem considered is the simulation of Stokes flow in a two dimensional channel. The problem configuration is shown in the Figure (5.5). The classical Poiseuille flow is characterised by a parabolic velocity profile over the cross-section of the channel. Problem here is of finding a velocity vector field $\mathbf{u}$ and a pressure scalar field p. In this case, if we specify a parabolic inflow then the same velocity profile is maintained through the channel and it can be seen that the pressure drops in a linear fashion. The flow is driven by a constant pressure gradient along the channel, which acts as a body

Table 5.3. Numerical errors and convergence rates for $P_3 - P_2$ approximation of the Stokes problem

Method	h	Velocity				Pressure	
		L^2 Error	L^2 Rate	H^1 Error	H^1 Rate	L^2 Error	L^2 Rate
NIPG1	1						
	1/2	4.372e-04	2.65	8.899e-03	1.90	3.918e-03	
	1/4	8.097e-05	2.43	2.019e-03	2.13	7.695e-04	2.34
	1/8	5.373e-06	3.91	2.763e-04	2.86	8.863e-05	3.11
	1/16	3.279e-07	4.03	3.480-05	2.98	8.830e-06	3.32
	1/32	2.073e-08	3.98	4.317e-06	3.01	8.166e-07	3.43
NIPG10	1						
	1/2	3.420e-04	2.48	7.221e-03	1.83	2.891e-03	
	1/4	5.132e-05	2.73	1.766e-03	2.03	9.405e-04	1.62
	1/8	3.199e-06	4.00	2.435e-04	2.85	1.207e-04	2.96
	1/16	1.859e-07	4.10	3.096e-05	2.97	1.257e-05	3.26
OBB	1						
	1/2	6.437e-04	2.37	1.072e-02	1.79	5.603e-03	
	1/4	1.149e-04	2.48	2.400e-03	2.15	1.182e-03	2.24
	1/8	8.639e-06	3.73	3.373e-04	2.83	1.33e-04	3.14
	1/16	5.696e-07	3.92	4.320e-05	2.96	1.33e-05	3.31
	1/32	4.169e-08	3.77	5.387e-06	3.00	1.27e-06	3.39
SIPG10	1						
	1/2	1.194e-03	1.82	1.689e-02	1.73	2.024e-02	
	1/4	2.863e-04	2.06	3.772e-03	2.16	7.775e-03	1.38
	1/8	1.791e-05	3.99	3.411e-04	3.46	6.484e-04	3.58
	1/16	8.801e-07	4.34	3.379e-05	3.33	4.324e-05	3.90
	1/32	1.927e-07	2.19	4.168e-06	3.01	3.408e-06	3.66

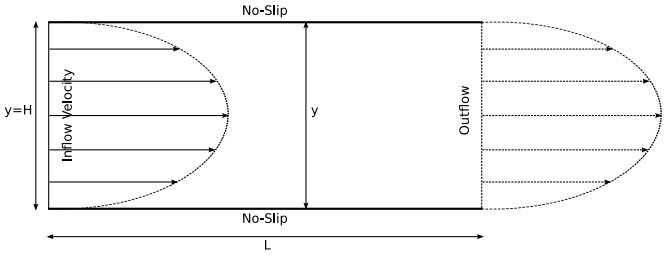

Figure 5.5: A Poiseuille flow in a channel or between two parallel plates. The flow is driven by a body force acting as a constant pressure gradient along the channel.

force. Poiseuille flow in a rectangular channel domain $[0, L] \times [0, H]$ with a parabolic inflow boundary condition:

$$u_x = \frac{-4\,y^2}{H^2} + \frac{4\,y}{H} \tag{5.23}$$

$$u_y = 0 \tag{5.24}$$

and natural outflow condition was simulated where the length of the channel $L = 5$, width $H = 1$ and the viscosity coefficient $\mu = 1.0$. The plot of the velocity vectors and pressure contours are shown in Figure (5.6). In Figure (5.7), the velocity profile at the middle of the channel is plotted as a function of y and is compared with the analytical

velocity u_x given by Equation (5.23).

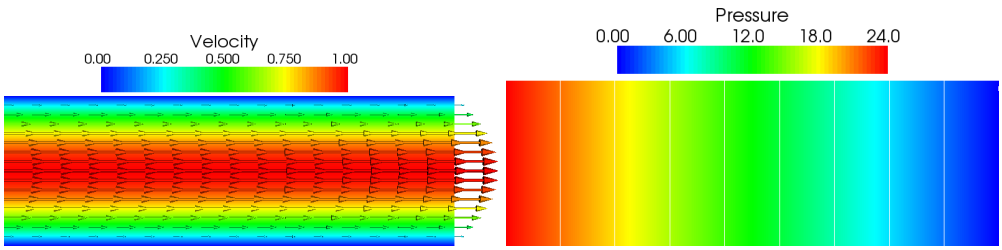

(a) Velocity Vectors (b) Pressure Contours

Figure. 5.6. Velocity and pressure field for the channel problem.

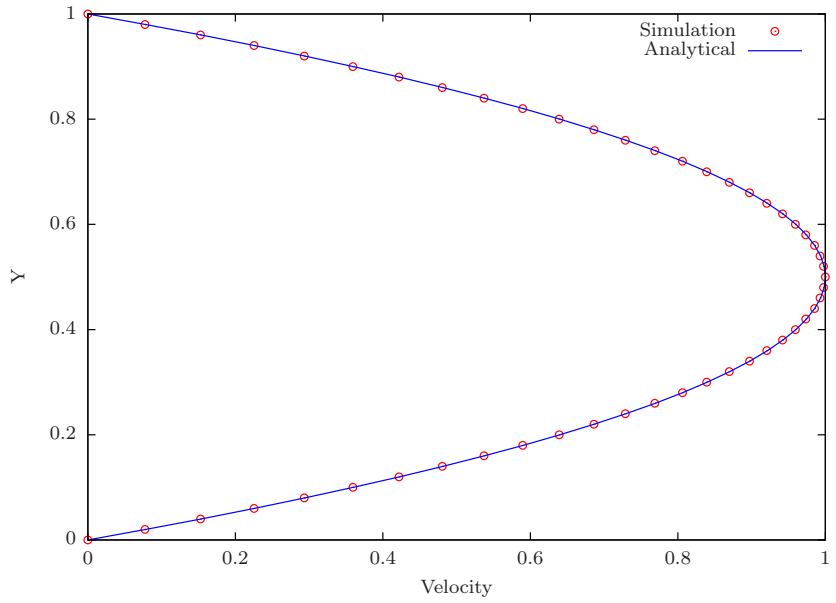

Figure. 5.7. Channel velocity profile as a function of y. The computed solution is shown by symbols and the analytical solution is shown by solid line.

5.7.5.4 Driven Cavity Problem

The third problem considered is the driven cavity problem in 2D, in which fluid is enclosed in a square cavity with an unit velocity imposed in the horizontal direction on the top boundary and no-slip condition on the remaining walls. This problem has been widely used as test case for validating incompressible fluid dynamic algorithms. Let u and v be the velocity in the x and y directions respectively. The upper wall (at $y = 1$) moves in the positive x direction at a constant velocity of 1, while the remaining three walls are stationary. At the two upper corners the horizontal velocity is discontinuous and generate strong singularity in the pressure solution. This adds an extra difficulty to the problem. These corner singularities are of great physical interest and therefore

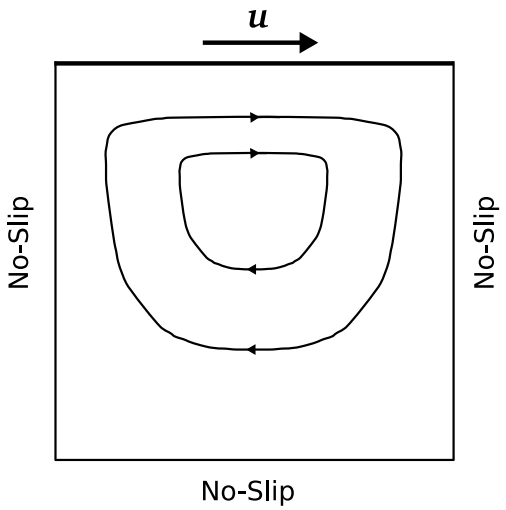

Figure 5.8: Geometry and boundary conditions for driven cavity problem: : The two-dimensional square cavity has no slip boundary conditions on all walls, the flow being driven by the top wall sliding across the cavity whilst the side and bottom walls are static.

driven cavity problem is regarded as a stringent test case. Steady solution evolves with recirculating vortex within cavity, as speed of upper lid is increased secondary vortices form in lower corners. The domain and boundary conditions of this problem are shown in the Figure (5.8).

The stokes flow in the driven cavity was simulated and the pressure contours and velocity field for the cavity flow are shown in Figure (5.9). The results show the symmetric characteristic of the Stokes flow. The primary vortex lies vertically symmetrical and close to the top lid and small eddies are formed in the lower corners. The singularity in the pressure field at the two upper corners also shown in the Figure (5.9). As the Reynolds number increases, the main vortex moves to the centre and slightly to right and lower vortices appear to grow in size. The Reynolds number in this case was 1. The behaviour of the horizontal and vertical component of the velocity is shown in Figure (5.10) where the mid-plane velocity profiles in the driven cavity are plotted. In Figure (5.10(a)) horizontal velocity along the vertical centre line is compared with the values given in Donea and Huerta (2003).

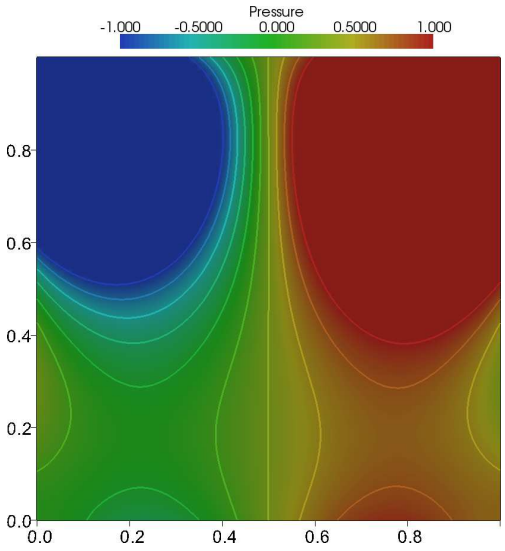

(a) Pressure isobars

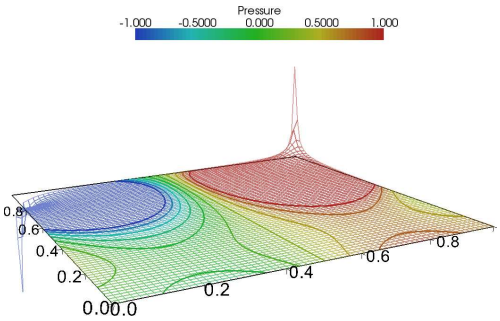

(b) Pressure singularities in the upper corners

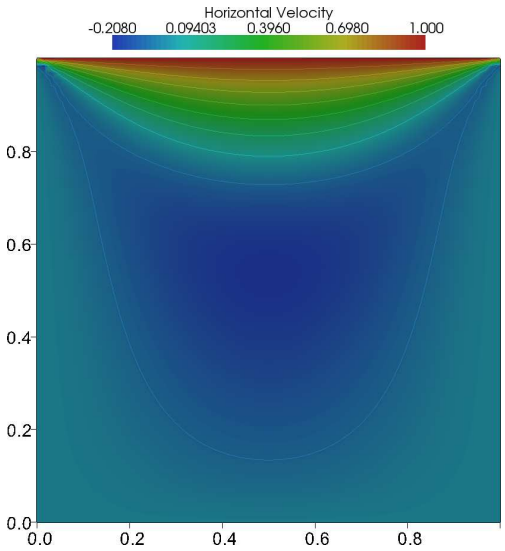

(c) Horizontal velocity

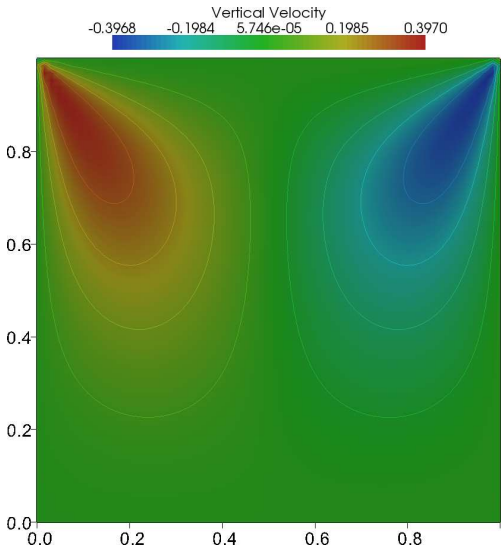

(d) Vertical velocity

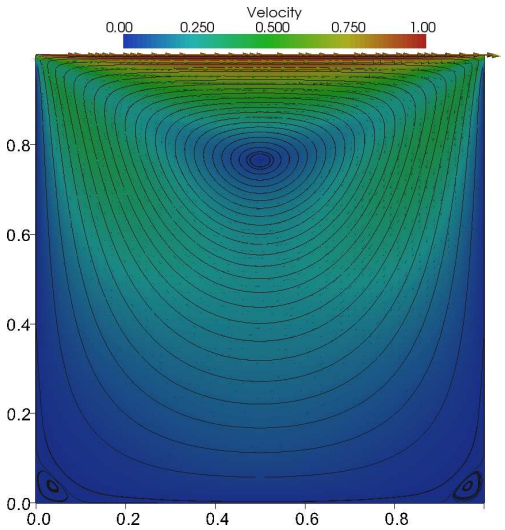

(e) Velocity streamlines

Figure. 5.9. Pressure iso-lines, velocity field and streamlines for the Stokes flow in the driven cavity. The contours show the symmetric characteristic of Stokes flow.

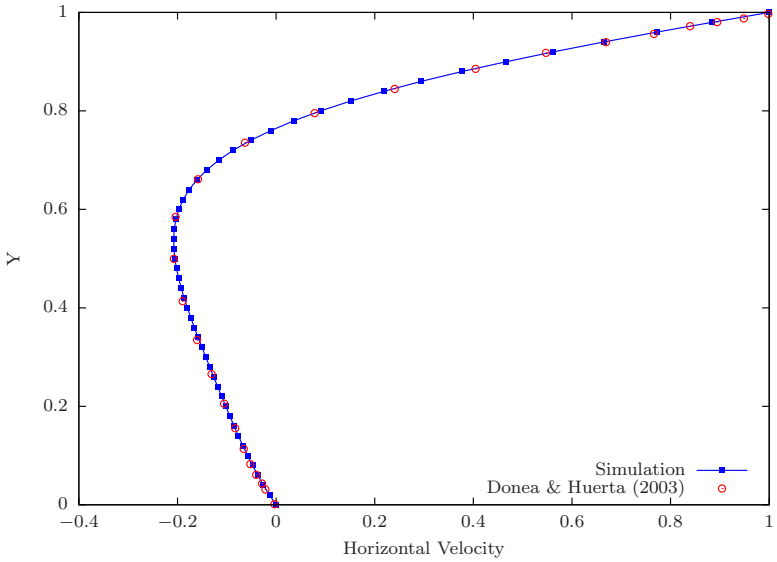

(a) Horizontal velocity profile. Comparison of horizontal velocity along the vertical line through the centre of cavity with the values given in Donea and Huerta (2003).

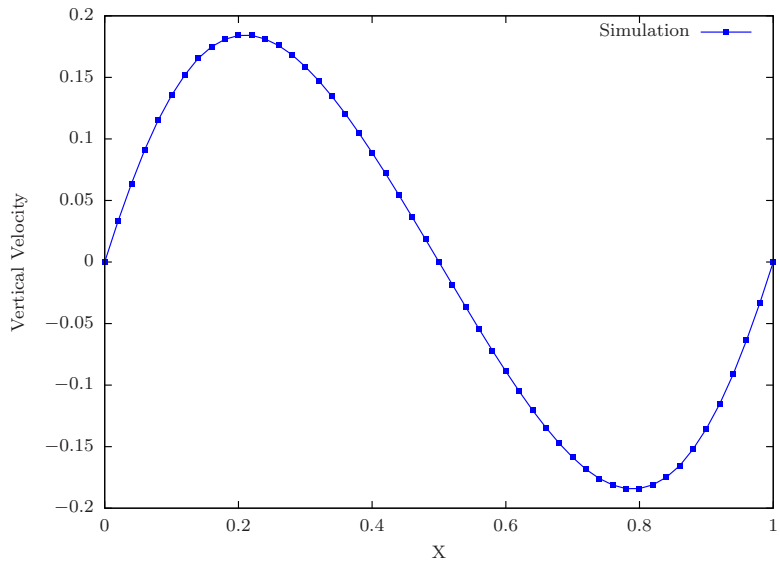

(b) Vertical velocity profile

Figure. 5.10. Mid-plane velocity profiles for the Stokes flow in driven cavity

In this Chapter, discontinuous Galerkin discretisation of the Stokes problem was presented in detail and some benchmark problems were solved to verify the implementation of the method.

6 Numerical Methods for Simulations on Complex Domain

6.1 Introduction

Classical numerical methods such as finite element and finite volume require a grid resolving the complicated boundaries of the domain. Generating such boundary fitted or conforming grid is a highly involved process especially if coarse grids (to reduce the number of unknowns) and high quality solution are required. Even though the mesh generation for complex geometries has advanced significantly over the last few years, even now it is considered as a time consuming and cumbersome task especially when solving realistic problems in three dimensions. Mesh generation is more complicated in cases which involve moving or evolving boundaries where it is required to fit the evolving surfaces. Several numerical methods have been developed in the past few years to address these difficulties by avoiding the meshing of complex domains. The main attraction of these methods lies in the fact that they do not require a conforming grid of the complex domain. Examples are immersed boundary method, fictitious domain method and cut-cell methods. These methods are generally known as Cartesian (or structured) grid based methods. There are other approaches like mesh-less (particle based) methods that are being used as well for handling complex domains. Recently, Engwer and Bastian (2005) introduced a new approach for the solution of partial differential equations on complex domains. Their approach is based on the discontinuous Galerkin discretisation of the governing partial differential equations on structured computational grid. The focus of this thesis is on simulating flow and transport through porous media at the pore-scale and it requires simulations on complex domains because of the complex nature of the pore spaces. Hence methods based on structured grids are most appealing as they provide an alternative by avoiding the meshing of complex domains. The new discontinuous Galerkin based approach of Engwer and Bastian (2005) is chosen for pore-scale simulations in this research. This Chapter gives a short overview of various methods for solving PDEs in complex domain including finite element and structured grid based methods. In particular, the new approach called Unfitted Discontinuous Galerkin (UDG) introduced by Engwer and Bastian (2005), which is based on the discontinuous Galerkin finite element technique is emphasised. Few examples simulations are given to demonstrate the working of the new approach

for pore-scale simulations.

6.2 Finite Element Methods

The standard finite element method (FEM) continues to dominate the numerical simulation of complex problems, not only due to its applicability to solve a variety of physical problems but also due to its ability to handle complex geometry and boundary conditions. Since the basis of every finite element method is the subdivision (often called triangulation) of the physical domain, the approximation quality is determined by the element attributes (such as maximal element size, presence of cusp elements) of the triangulation, while the computational effort is determined by its number of elements. The FEM can handle complex geometries by meshing the domain with sufficient accuracy. However, if the physical domain is very complicated and contains a lot of geometric details, then the minimal number of elements that are necessary to resolve the domain can be enormous and substantially increases the computational effort. The Figure (6.1(a)) is taken from (Zienkiewicz and Taylor 2001) shows a finite element mesh for an aerofoil. As the fluid dynamics and boundary layer around the aerofoil is considerably complex, the mesh is refined very much near the boundary to account for such behaviour. Away from boundaries one could use relatively coarser grid. We can see that the finite element method requires lots of elements near the aerofoil to get a reasonable solution. Hence resolving the shape of a complex boundary would require a very fine grid, resulting in a large number of degrees of freedom and hence increase in the computational effort. Moreover, creating a satisfactory mesh that conforms to the boundaries of the domain still requires significant efforts. Meshing itself is a complex process and is an active area of research. Mesh generation algorithms for three dimensional domains may produce poor or distorted elements in some regions that can lead to large error in the solution. The approximation error of the finite element method and the convergence behaviour of iterative linear solvers depend on the mesh quality. In addition to that, in finite element methods the domain can only be subdivided into shape regular elements (e.g. triangles, quadrilaterals, hexahedron, tetrahedron etc.) because the finite element basis functions depend on the shape of the elements (hence called shape functions). This restricts the use of arbitrary shaped elements in standard finite elements. Although the hanging nodes are allowed they require special treatment which is not straight forward in finite element methods.

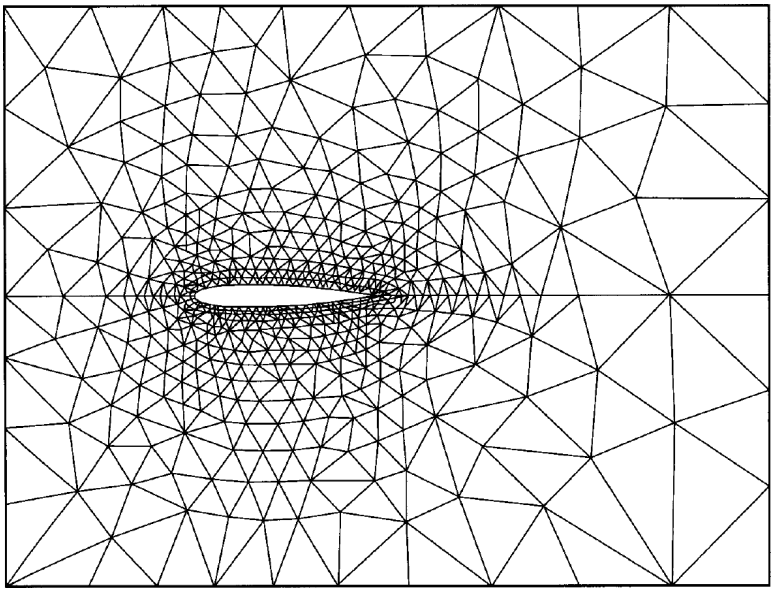

(a) Typical triangulation of an aerofoil. We can see that the grid is refined very much near the aerofoil to get a reasonable solution (taken from Figure 1.5, page 22 of Zienkiewicz and Taylor (2001)).

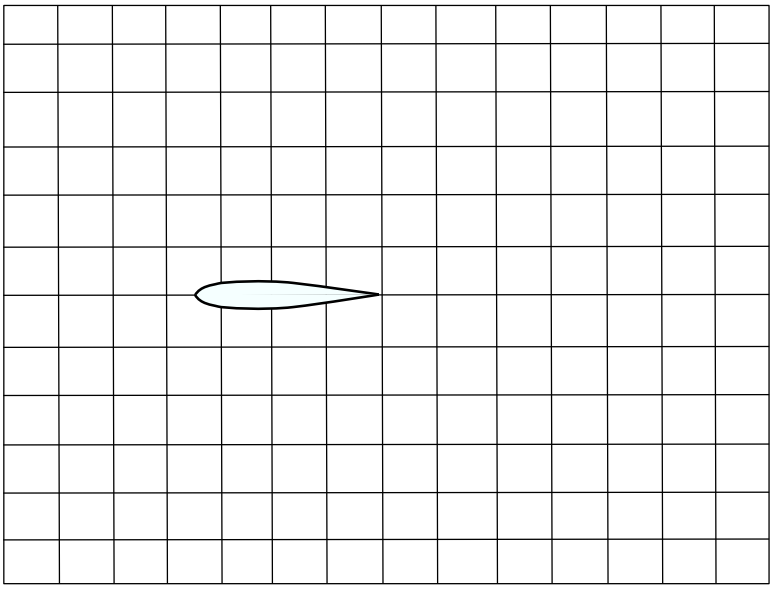

(b) A possible structured grid for the same aerofoil. The structured grid is much easier to generate than the unstructured grid.

Figure. 6.1. Unstructured and structured triangulation of an aerofoil

6.3 Structured Grid Based Methods

The structured grid based methods are an alternative to the finite element methods for simulations on complex domains. The main idea has been to use non-boundary fitting mesh, often a structured grid, for the simulation. The geometry of the domain is often represented using implicit equations and is therefore independent of the grid used. As

previously mentioned, the traditional numerical methods require a boundary conforming mesh and the mesh generation is considered time consuming and cumbersome task especially for large three dimensional mesh in realistic geometries. They add further difficulties when the domain is complex and evolving. The Structured grid based methods provide a very attractive alternative by avoiding the meshing of complex geometries and are preferred for problems with free boundaries. A possible non-conforming structured grid for the same aerofoil is given in Figure (6.1(b)). It can be seen that a structured grid is much easier to generate than an unstructured mesh and all the elements in the grid can have regular geometry (squares/rectangles/cubes). However, since the edges or faces in the grid are not guaranteed to be on the boundary, the traditional way of applying boundary conditions used in FEM or FVM cannot be used. This requires special approaches for introducing the boundary conditions. The last two decades saw various approaches being developed to handle complex geometries based on structured grids. They essentially differ in the way the boundary conditions are applied. In the next Section, some of these methods are briefly mentioned.

6.3.1 Immersed Boundary Methods

The immersed boundary method was first introduced by Peskin (1972) for studying the flow of blood in the human heart. In this method, the computational domain covers the physical domain without following the boundaries. This method requires enforcing the boundary conditions indirectly through the use of some forcing functions. Numerous approximation techniques have been proposed such as Fictitious domain or Embedded domain methods which work on the same principle. The essential difference between each other lies in the way in which the boundary conditions are imposed. For instance, in Fictitious Domain approach, boundary conditions are imposed as constraints on the partial differential equation. The PDEs with constraints are then solved using the technique of Lagrange multipliers. But the disadvantage is that it results in a saddle point problem and introduce additional unknowns. The advantage of course is that mesh generation is much easier.

6.3.2 Composite Finite Element Method

The composite finite element method, as introduced in (Hackbusch and Sauter 1991), was developed to improve geometric multigrid methods on domains with complicated structures and micro structures. This approach was primarily intended as a fast iterative solver, not as a discretisation scheme. The composite finite element method constructs piecewise linear basis functions on the fine background mesh and truncates them at the true boundary. Meshing is easy as structured grid can be used and computation can be performed efficiently because multigrid methods can be used as solvers. However,

computing the matrix entries are more difficult as basis functions contain complexity of structure and this method need more degrees of freedom.

6.4 Mesh-free Methods

Another type of methods for solving PDEs in complex domains are the so called mesh-free or mesh-less methods such as smoothed particle hydrodynamics (SPH) (Liu and Liu 2003). Most mesh-free methods are pure Lagrangian in character. They use a set of arbitrarily distributed nodes (or particles) which has a mass and velocity. These particles are put into the flow which are influenced by other particles that are within a certain distance from each other. SPH uses smoothed particles as interpolation points rather than a grid and hence considered suitable for problems involving free surface and moving boundaries. The main difference to standard finite element method is that the domain of interest is discretised only with nodes called particles. These particles interact via mesh-free shape functions in a continuum framework similar to finite element methods although particle connectivity's can change over the course of a simulation.

6.5 Discontinuous Galerkin Methods for Complex Geometry

The finite element discretisation is considered to be most suitable for problems with complex geometries, while a finite volume discretisation is well known for its conservation properties. The discontinuous Galerkin methods combine the advantages of both these methods into a single discretisation scheme and hence considered very suitable for simulations on complex domains. The compactness of DG discretisation, which only requires neighbouring information to construct inter-element numerical fluxes to evaluate the integrals is that makes it different from finite element and finite volume methods. One of the nice features of discontinuous Galerkin methods for numerical simulation in complex domains is that the grid can be arbitrary. The non-conforming grids with hanging nodes are allowed without much restriction and their treatment is straightforward in this approach. This method allows both spatial and polynomial adaptation. These properties make discontinuous Galerkin methods particularly suitable for numerical simulation in complex domains with non-boundary fitting framework. Furthermore, the shape functions can be independent of the shape of the elements hence the use of irregular elements are possible, at least theoretically. However, in practise there are certain difficulties when using irregular elements. For instance, the integral evaluations when assembling the stiffness matrix require the use of numerical quadrature rules which are defined only for shape-regular elements such as triangles, quadrilaterals etc. Thus imposing difficulties in using arbitrary elements in a straightforward manner. With special means, Engwer and Bastian (2005) introduced a way

to use arbitrary elements within the DG framework. Their approach is called unfitted discontinuous Galerkin (UDG). In the following Section a short description of the UDG approach is given. For a detailed understanding, we refer to Engwer and Bastian (2005; 2008), Engwer *et al.* (2008).

6.5.1 Unfitted Discontinuous Galerkin Method

A numerical method to approximate partial differential equations on meshes that do not conform to the domain boundaries was developed by Engwer and Bastian (2005). The method is conceptually simple and effectively exploits the nice features of discontinuous Galerkin schemes. It is called Unfitted Discontinuous Galerkin (UDG) method and offer a new approach for solving PDEs in complex domains, combining the idea of unfitted finite elements with a discontinuous Galerkin finite element discretisation. It is based on the observation that in discontinuous Galerkin approaches, the elements can have arbitrary shapes. Thus the elements can be taken as the intersection of a structured background mesh with complicated geometry. This freedom has been used to construct a grid by intersecting structured mesh (fundamental mesh) with the complex structure. In this framework, the boundary representation can be implicit, defined by an implicit function (such as level set function). This method allows more efficient computations than standard finite element methods, while still offering the benefits of the finite element method (Engwer and Bastian 2008). Moreover, this method is locally mass conservative and allows higher order computations.

6.5.1.1 Working Principle of UDG

Consider schematic representation of a pore-space as shown in Figure (6.2). A computational structured grid covering the given pore-space geometry is defined which is called the *fundamental grid*. Since the computation is performed on this fundamental grid (or background mesh), it is defined according to the desired results and generally, one would like to use a course fundamental grid to reduce the number of unknowns. As we can see in the Figure (6.3), the pore-space is covered by a fixed fundamental grid and the complex geometry cuts through the Cartesian grid cells resulting in elements of arbitrary shapes (see Figure 6.4). The support of the finite element shape functions are then restricted to these arbitrary forms within each element. The finite element computational procedure involves assembling of the stiffness matrix where certain integral terms are evaluated. This requires the integration over the interior and boundary of those irregular elements. Since the standard quadrature rules cannot be applied directly on such elements, a special approach is developed to handle this situation. This is accomplished by constructing a local triangulation within each irregular element by subdividing them into easily integrable sub-elements of standard shapes using a specially designed local triangulation (Engwer and Bastian 2008) algorithm. This procedure is

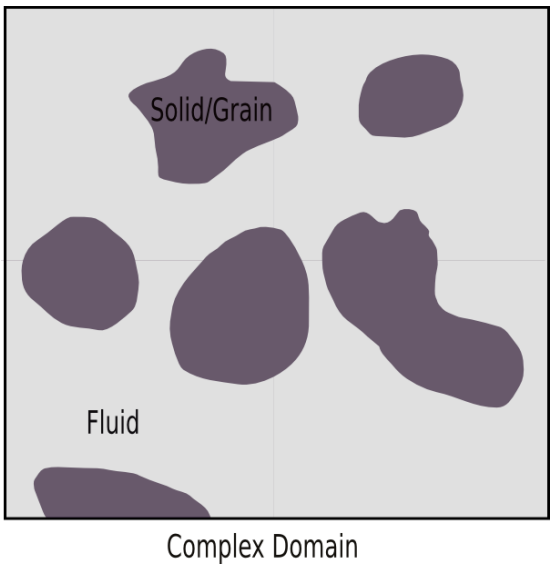

Figure. 6.2. Schematic representation of a pore-space showing the complex domain. The figure modified from Fahlke (2008).

called a *sub-triangulation*. The standard quadrature rules are then used for integrating over these regular sub-elements. Extended marching cube algorithm has been implemented in the UDG framework to provide local surface and volume triangulation. A schematic representation of the sub-triangulation is given in the Figure (6.5).

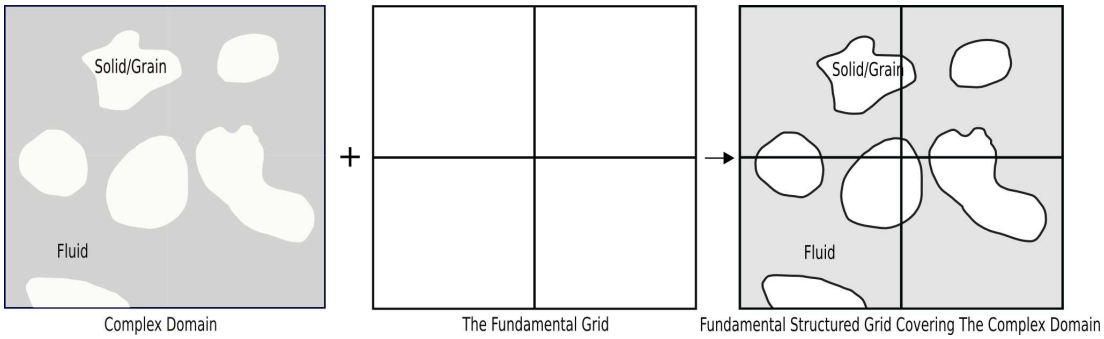

Figure. 6.3. In the UDG approach, a fundamental grid is defined to cover the complex domain.

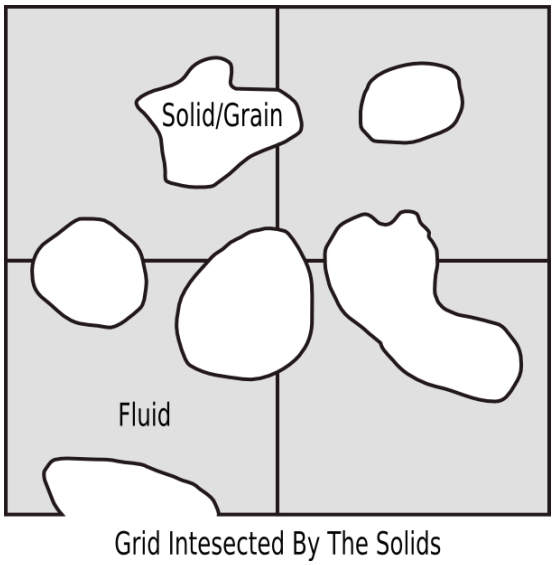

Figure. 6.4. In UDG, the intersection of the physical domain with underlying Cartesian grid leads to arbitrary shaped elements.

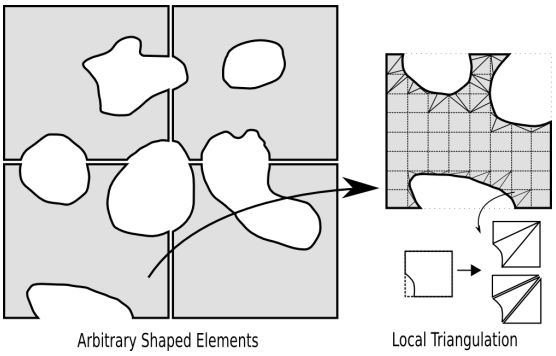

Figure. 6.5. A schematic illustration of the sub-triangulation in UDG. The integration over the boundary and over the non-standard elements are done by specially designed local triangulation (Engwer and Bastian 2008).

6.6 Implicit Representation of Complex Geometry

Simulations on complex domains and in particular pore-scale simulations require accurate methods to extract surfaces without expense and loss in geometric detail for instance from an image data. The implicit boundary representation provides a general and flexible way to represent complex geometries as image data (scalar function). This enables the surface extraction from CAD and image data (e.g. porous media and medical images using CT, NMR etc.) and the surface is then represented on a Cartesian grid with implicit functions. Most appealing thing about implicit geometry representation is that it facilitates direct simulation in irregular pore-scale geometries with structured grid based methods. Within the UDG implementation, the idea of implicit geometric representation via level set functions is used to represent complex geometries. In this

approach, a complex domain is given by

$$\Omega = \{x : \phi(x) > 0\}$$

and domain boundary by

$$\partial\Omega = \{x : \phi(x) = 0\}(\text{zero level set}).$$

Here the boundary $\partial\Omega$ is given as an iso-surface of a scalar function. The UDG approach to complex geometry is very well compatible with the techniques for surface and volume extraction from image data. The level set methods are used to obtain the complex boundaries and the surface is then represented on a Cartesian grid with implicit functions. The UDG implementation uses Extended Marching cube (and Marching tetrahedron) algorithms, which is a well known algorithm for polygonising a scalar field. Using this polygonisation routine, a two-dimensional and three-dimensional mesh description of the implicit surface can be obtained. The implicit surface generation in the UDG implementation consists of the following steps:

1. Input an implicit function, $I(x, y, z) = 0$
2. Apply marching cube/tetrahedron method
3. Marching cube algorithm solves equation $I(x, y, z) = 0$ to provide mesh description of the unknown surface
4. Generate 2D/3D mesh description

The Figure (6.6(a)) shows an artificial porous medium created using the implicit geometry representation. The centres and radii of randomly packed spheres in a given domain are generated using an open-source program by Skoge *et al.* (2006). In this program, one can specify the extend of the domain and the number of spheres to be packed. The implicit function to represent such a sphere packing is

$$\phi(x) = \min_k(|x - x_k|^2 - r_k^2)$$

where x_k and r_k are the centre and radius of k^{th} sphere respectively. Now,

$$x\colon \phi(x) = 0$$

gives the boundary (surface of spheres) of the sphere packing. Another example showing a packing of cylindrical objects to represent an industrial porous medium like a porous diffusion layer (PDL) (see Figure (2.1(b))) of PEM fuel cells is given in Figure (6.6(b)). Such idealised porous medium has been used for numerical studies of flow and transport through PDL of PEM fuel cells (Van Doormaal and Pharoah 2008).

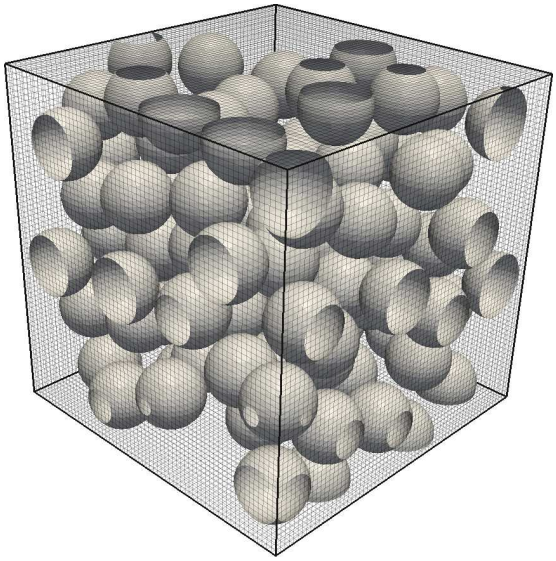

(a) An artificial porous medium made of 100 spheres packed randomly in a unit cube.

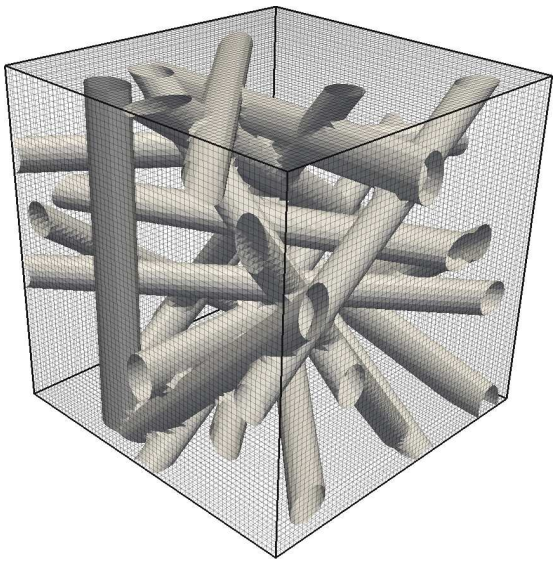

(b) Idealised representation of PDL of a PEM fuel cell made by randomly packed cylindrical objects. Such idealised porous medium has been used for numerical simulation of flow and transport through PDL of PEM fuel cells (Van Doormaal and Pharoah 2008).

Figure. 6.6. Examples of Implicit representation of complex (irregular) geometries on a Cartesian grid.

6.7 Results of Numerical Experiments Using UDG

The unfitted discontinuous Galerkin (UDG) scheme which is realised as a separate module in DUNE (Engwer and Bastian 2008) has been used in this thesis for handling complex pore-space geometry. The discontinuous Galerkin discretisation of the Stokes

equation was implemented within the UDG scheme in DUNE and used for the solution of pore-scale flow problems where Stokes equation is solved to obtain the pore-scale velocity field. In this Section, results of numerical experiments using UDG are presented.

6.7.1 Flow Around a Cylinder

Consider the Stokes flow around a cylinder in 2D where the domain is a unit square. The geometry of cylinder (in 2D it is a circle) is represented by a level set function as explained before (6.6). The geometry is represented on a grid level (*geometry level*), where mesh size is denoted by h_g. Here $h_g = 1/64$, that is, the unit square is refined globally 6 times and level set is defined on the finest level. The grid level on which the computation is done is denoted by *simulation level*. The Figure 6.7(a) shows the cylinder geometry in 2D and the corresponding grid where the circle in red colour is the boundary of the geometry. The Figure 6.7(b) shows the simulation grid (in blue) along with the grid where geometry is defined. A zoomed picture showing the cylinder boundary and the triangulation from the marching cube algorithm is shown in the Figure 6.7(c). The Figures (6.8) and (6.9) show the solution for the successive refinement of the grid starting from a course level of 1 to a fine level of 6. As we can see from the Figures, the solution converges and gets smoother as the grid is refined. It should be noted that the UDG approach gives reasonable solution even when the computational grid is coarse. In this way, sufficiently accurate solution can be obtained with lesser number of unknowns. This is an advantage especially when pore-scale simulations are to be carried out because sufficiently accurate solution can be obtained with less number of degrees of freedom. In traditional methods like standard finite element and finite volume, the number of degrees of freedom depends on the accuracy of geometrical approximation because finer mesh and consequently more unknowns are required for good approximation of the complex boundaries. However, with the UDG approach, the number of unknowns in a way is independent of the geometrical approximation.

6.7.2 Numerical Up-scaling Using UDG

The numerical simulations of fluid flow and transport in porous media at the continuum scale require the knowledge of effective parameters such as permeability, dispersion coefficients and capillary pressure/saturation relationships. The knowledge and reliable prediction of these effective properties are of great interest in contaminant transport and oil recovery processes. These macroscopic parameters are usually obtained by laboratory or field scale experiments, which are often difficult to conduct or time consuming. Nowadays detailed measurements of the pore-scale structures are possible, thanks to the advances made in the experimental imaging of porous media. As the governing equations on the pore-scale are well known, macroscopic parameters can be obtained directly from the pore-scale geometry by numerical upscaling. In this

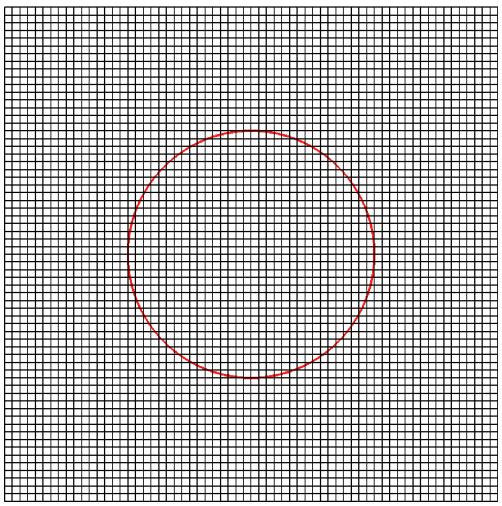

(a) Geometry of cylinder (in red) in 2D and the grid on which the geometry is defined.

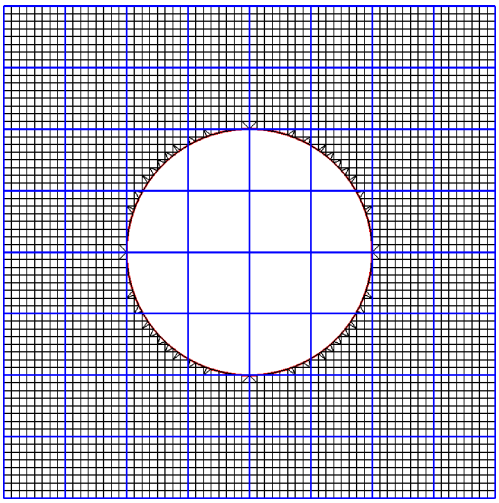

(b) The simulation (blue) and geometry (black) grid for the flow around cylinder.

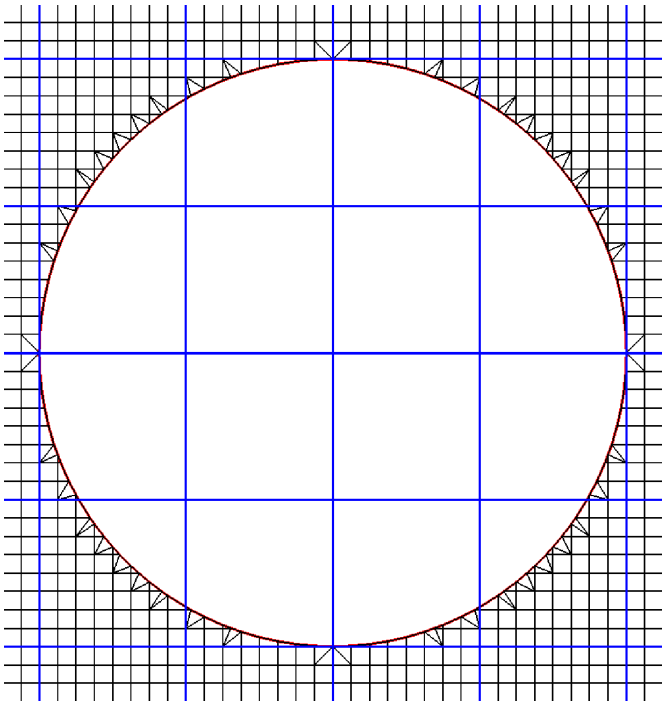

(c) Zoomed picture around the cylinder (red) showing the local triangulation.

Figure. 6.7. Simulation and geometry grids for the Stokes flow around a cylinder.

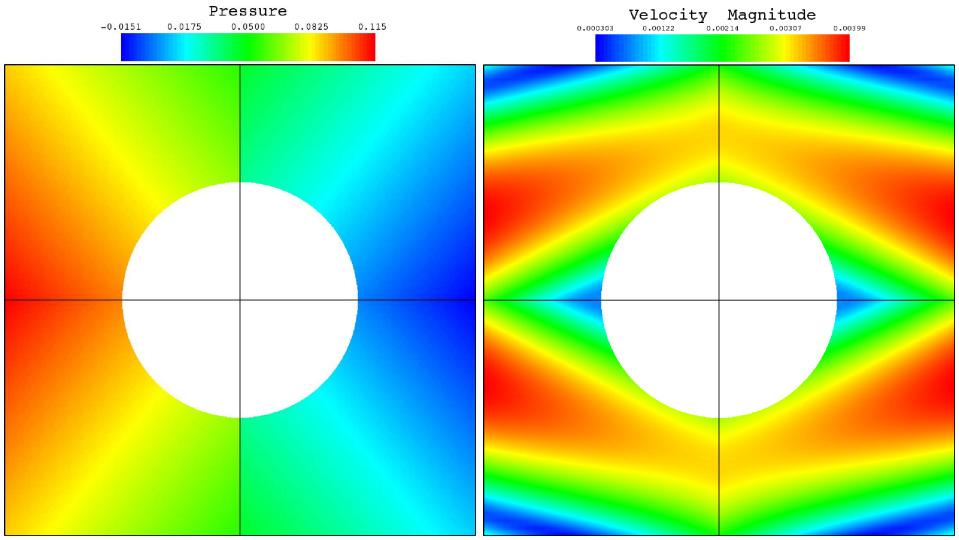

(a) Level 1

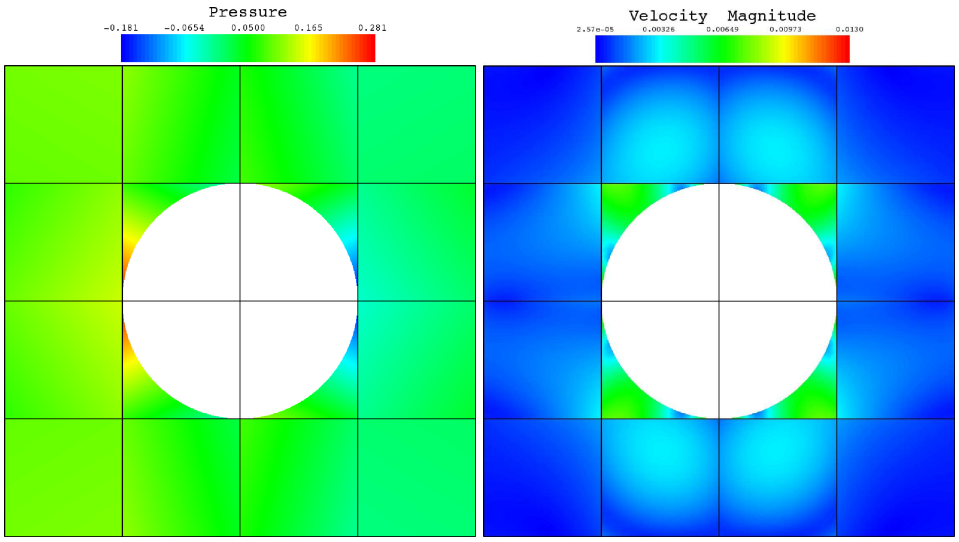

(b) Level 2

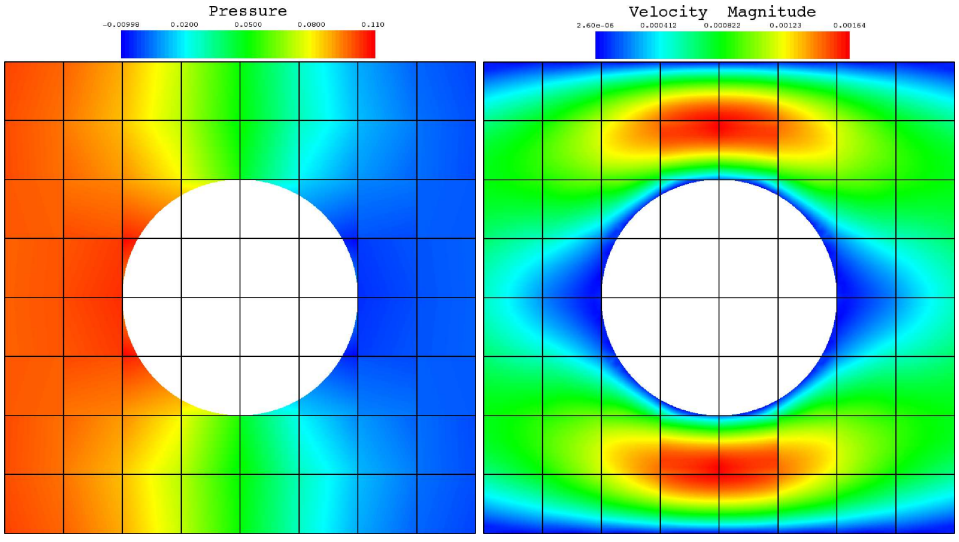

(c) Level 3

Figure. 6.8. Grid convergence test for flow around a cylinder (Level 1 to 3)

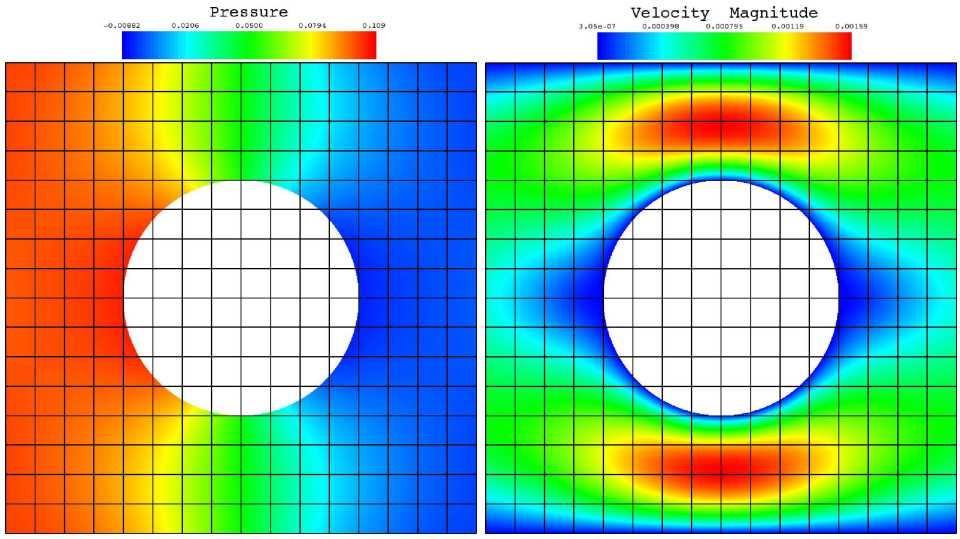

(a) Level 4

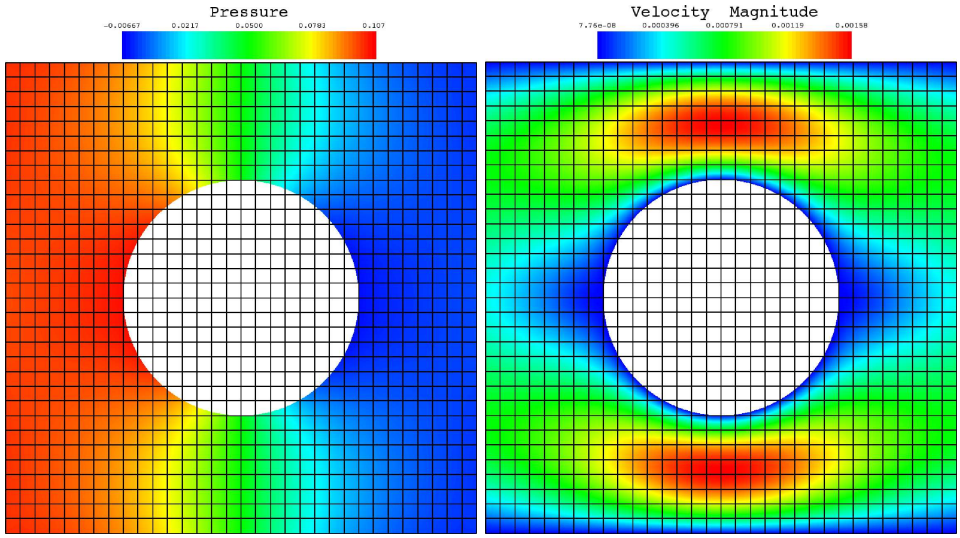

(b) Level 5

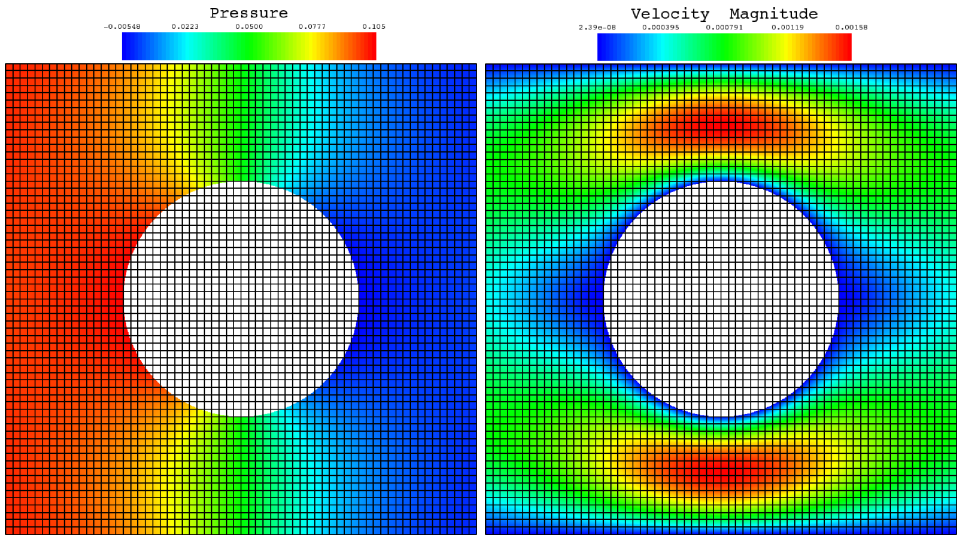

(c) Level 6

Figure. 6.9. Grid convergence test for flow around a cylinder (Level 4 to 6)

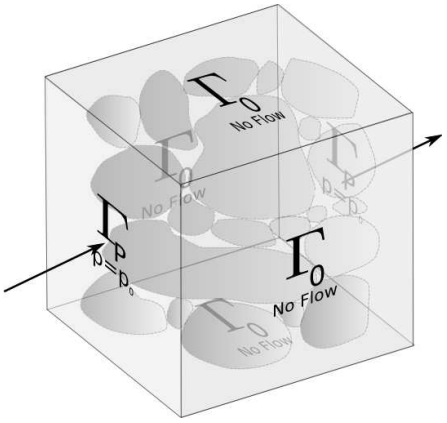

Figure 6.10: Boundary conditions for the numerical upscaling problem: pressure is prescribed at the inlet and outlet and No-flow condition on other sides of the domain. No-slip condition was given on the grains.

section, numerical upscaling examples are considered to show how UDG together with the DG implementation of the Stokes equation can be used for simulation on complex geometries. For more details we refer to Engwer *et al.* (2008).

Let $\mathbb{M}$ be a porous medium consisting of pore phase $\mathbb{P}$ and a solid phase $\mathbb{S}$. Now consider a single phase fluid flow through $\mathbb{M}$. At the pore-scale, the problem to be solved is that of slow laminar flow described by steady state Stokes equation in the pore space $\mathbb{P}$ with appropriate boundary conditions to obtain the permeability of the medium. On the pore-solid interface $\partial\mathbb{P}$, the no-flow or no-slip boundary conditions are applied. A schematic representation of the computational domain showing the boundary conditions is given in Figure (6.10). A macroscopic pressure gradient is imposed along the x axis by prescribing the pressure at the inlet and outlet of the domain. The no-flow boundary conditions are applied on other external boundaries of the domain. As usually done, the no-slip condition is given on the grain (spheres) surfaces. Then the Stokes equation is solved on the pore-scale to obtain the pore-scale velocity field and pressure within the pore-spaces. Finally using Darcy's law the macroscopic permeability tensor can be computed from the pore-scale velocity field for a given pressure gradient. Recalling the Darcy's law from Section (2.2.3):

$$\langle \mathbf{u}_d \rangle = -\frac{\underline{\boldsymbol{\kappa}}}{\mu} \nabla P \tag{6.1}$$

where ∇P is the applied pressure gradient, $\mathbf{u}_d$ is the Darcy velocity, μ is the dynamic fluid viscosity (for instance the coefficient of viscosity of water at room temperature is taken as $1 \cdot 10^{-3} Pa.s$) and $\underline{\boldsymbol{\kappa}}$ is the permeability tensor.

The permeability tensor is given as

$$\kappa = \begin{bmatrix} \kappa_{xx} & \kappa_{xy} & \kappa_{xz} \\ \kappa_{yx} & \kappa_{yy} & \kappa_{yz} \\ \kappa_{zx} & \kappa_{zy} & \kappa_{zz} \end{bmatrix}$$

The Darcy velocity $\mathbf{u}_d$ is obtained as the volume averaged velocity over the system,

$$\mathbf{u}_d = \frac{1}{|\Omega|} \int \mathbf{u} \, dx$$

where $|\Omega|$ is the volume of the porous medium. $\mathbf{u}_d$, the Darcy velocity (or often referred to as the Darcy flux), is not the pore-velocity (pore velocity is the one which fluid experiences when flowing through the pores). The Darcy velocity $\mathbf{u}_d$ is related to the pore-scale velocity $\mathbf{u}$ by the porosity (ϕ) as

$$\mathbf{u}_d = \mathbf{u} \, \phi.$$

The porosity ϕ is given by

$$\phi = \frac{|\Omega^p|}{|\Omega|}$$

where $|\Omega^p|$ is the volume of the pore-space. The average pore-velocity $\bar{\mathbf{u}}$ is obtained as

$$\bar{\mathbf{u}} = \frac{1}{|\Omega^p|} \int \mathbf{u} \, dx$$

Now, assuming the permeability tensor to be an isotropic diagonal tensor, the component xx in the main flow direction is computed using the Equation (6.2)

$$\kappa_{xx} = -\mu \frac{\bar{\mathbf{u}}\phi}{\nabla p} \tag{6.2}$$

6.7.2.1 Permeability for Simple Cubic (SC) Sphere Packing

In this section numerical results for the permeability of cubic array of spheres are compared with analytical results. We first considered the case of flow through a simple porous medium, i.e., a periodic simple cubic (SC) array of spheres of equal radii as depicted in the Figure (6.11(a)). The theoretical or analytical fluid permeability for such periodic array of spheres was given by Sangani and Acrovos (1982). For periodic array of spheres, they determined solutions of the Stokes equations in series formulation, whose coefficients are determined numerically. We computed the flow field through the SC sphere packing using the the prescribed pressure formulation (Equation (5.17)) of the Stokes equation as explained in the Section (5.6). At the inlet and outlet, pressures were prescribed and the imposed pressure difference caused the flow. On all other macroscopic boundaries, no flow boundary conditions were given. Also on the sphere surfaces, no flow condition was imposed. The Figure (6.12) shows the velocity field through the simple cubic sphere packing where red colour shows the high velocity magnitude. Once the pore-scale velocity field was obtained, the permeability in the main flow direction was computed using the equation (6.2). The simulation results

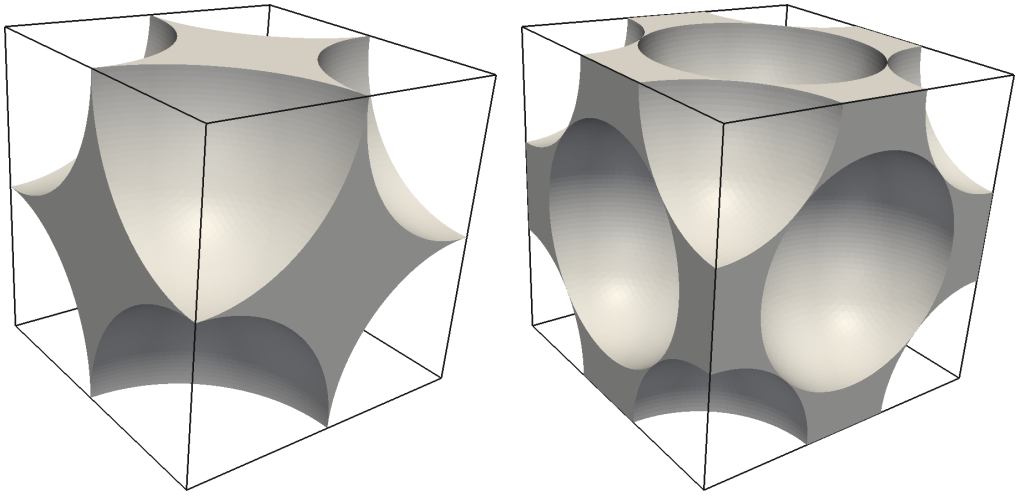

(a) Simple Cubic Packing (SC) (b) Face Centred Cubic Packing (FCC)

Figure. 6.11. Typical pore geometry of cubic array of spheres where Grey and White area represent fluid and solid regions respectively.

were compared with the analytical results given by Sangani and Acrovos (1982) for different ordered sphere packing (SC and FCC) and good agreement was obtained. In particular, permeability values were computed for various volume fraction of SC packing and errors were estimated. Analytical and computed permeabilities are listed in Table (6.1) for various values of $\psi = \frac{c}{c_{max}}$, which is a scaled sphere volume fraction where $c = \left(\frac{4\pi r^3}{3}\right)/L^3$ (r is the radius and $L = 1$ is the dimension of cube) and $c_{max} = \pi/6$ corresponds to the case when the spheres are touching each other. A corresponding plot is given in Figure (6.13). The Table (6.2) shows the theoretical and simulated values of permeability for SC and FCC packing for the case of closed packing (where spheres are just touching each other). We note that the values are in good agreement with those obtained analytically by Sangani and Acrovos (1982).

Volume fraction (ψ)	Porosity	κ_{eff} (Sangani and Acrovos 1982)	κ_{eff} (Computed)	Relative Error (%)
0.1	0.99951	9.1107e-1	1.0169	11.61
0.2	0.99587	3.8219e-1	4.0158e-1	5.07
0.4	0.96661	1.2327e-1	1.2578e-1	2.03
0.6	0.88709	4.4501e-2	4.4882e-2	0.85
0.8	0.73	1.3197e-2	1.3208e-2	0.08
1.0	0.478	2.5203e-3	2.5159e-3	0.17

Table 6.1. Comparison of permeability computed for a simple cubic sphere packing with analytical results.

A grid refinement study was also done for the FCC packing and we observed that the

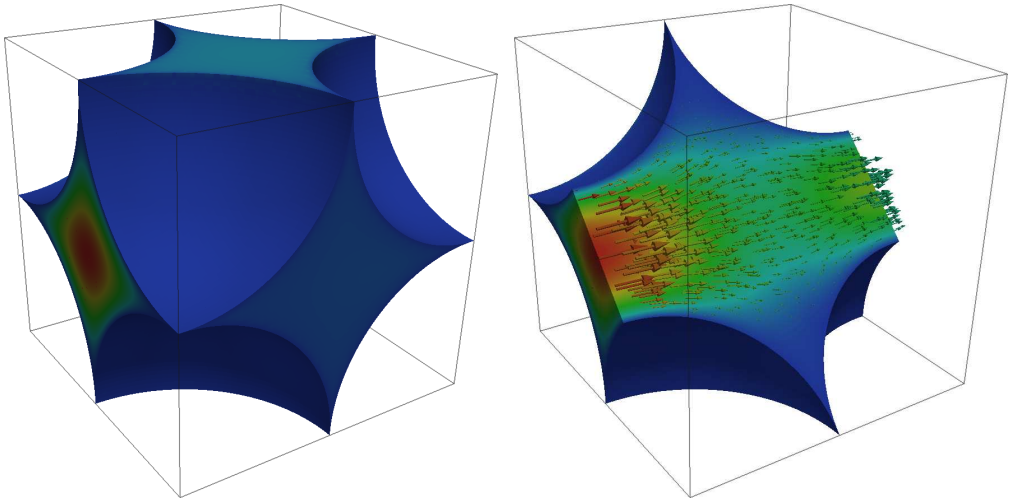

(a) Velocity variation at the inlet (b) A clipped section showing velocity field

Figure. 6.12. Velocity field through simple cubic sphere packing. The red and blue colour shows high and low velocity region.

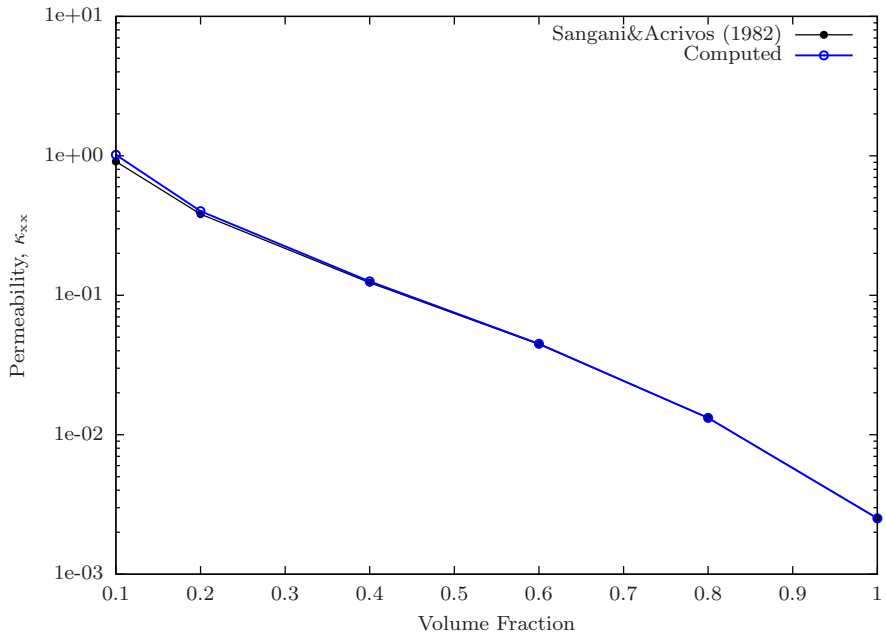

Figure. 6.13. Permeability computed for a periodic cubic sphere packing packing for various volume fraction compared with analytical solution given by Sangani and Acrovos (1982).

Type	ϕ	$\kappa_{analytical}$	$\kappa_{simulated}$
FCC	0.259	8.68e-05	8.69e-05
SC	0.476	2.52e-03	2.51e-03

Table 6.2. Comparison of theoretical and simulated permeability for cubic sphere packings

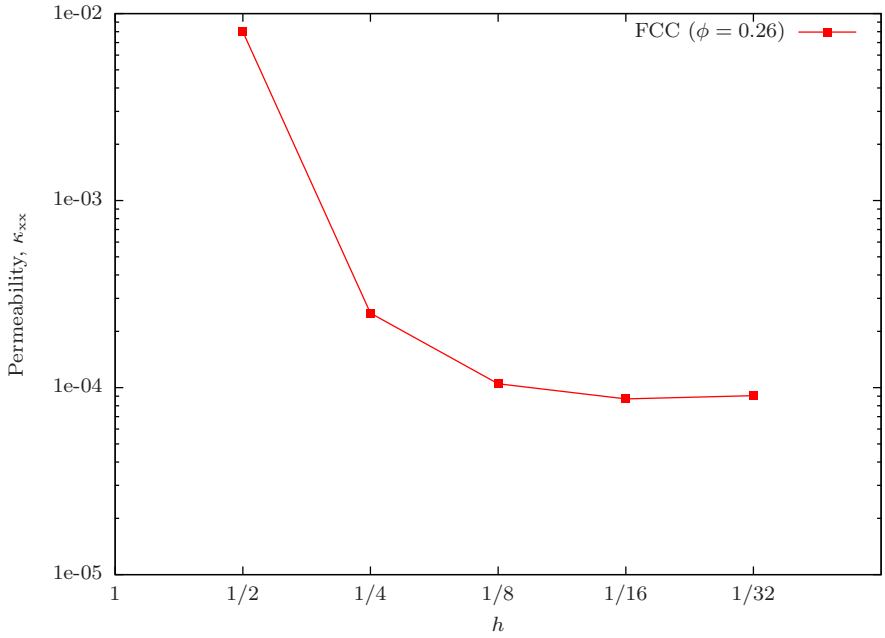

Figure. 6.14. Permeability computed for a FCC packing converging to the analytical value on a relatively coarser grid. The mesh size is represented by h.

permeability value is converging to the theoretical value even on a relatively courser grid. The plot is given in the Figure (6.14).

6.7.2.2 Permeability for a Random Sphere Packing

A more complex problem of finding permeability of an artificial porous medium (where the geometry is much more complex than the simple cubic array of spheres) by numerical upscaling is considered next. The artificial porous medium was generated by randomly packing 100 spheres in a cubic box (Figure 6.15) where the sphere packing data (centre and radius of each sphere) was obtained by an open source code by Skoge *et al.* (2006). The geometry of this porous medium is then generated using the idea of implicit geometric representation as discussed before. The packing geometry (100 Spheres of radii $r = 0.106$ randomly placed inside a unit cube) is given as a scalar function on mesh with mesh size $h_g = 1/64$. The space between the spheres is the pore-space $\mathbb{P}$ and the spheres constitute the solid phase $\mathbb{S}$. The permeability in the main flow direction has been computed and a grid refinement was carried out to learn how the permeability value converges as the mesh is refined. Indeed the permeability converges as the grid is refined and we can observe (see Figure 6.16) that even with coarser grid the permeability was obtained with sufficient accuracy. This is an advantage of using UDG where even with coarser computational grid the complex geometry problem can be solved with sufficient accuracy. Finally, the porosity's of the medium were changed by shrinking or expanding the spheres (see Table (6.3) for the values) and permeabilities

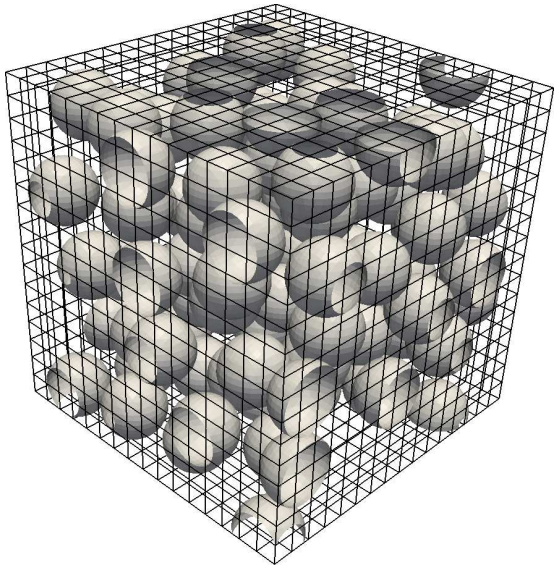

Figure. 6.15. Artificial porous medium made of randomly packed spheres where 100 spheres of equal radii are placed randomly in a unit cube. In this setup, the spheres are shrinked such that they are not touching each other.

were computed for different porosity values of the artificial medium. The simulation results on two successive course grid levels are shown in (Figure 6.17) and it can be seen that qualitatively the difference is very small and the nature of variation in the two levels is similar.

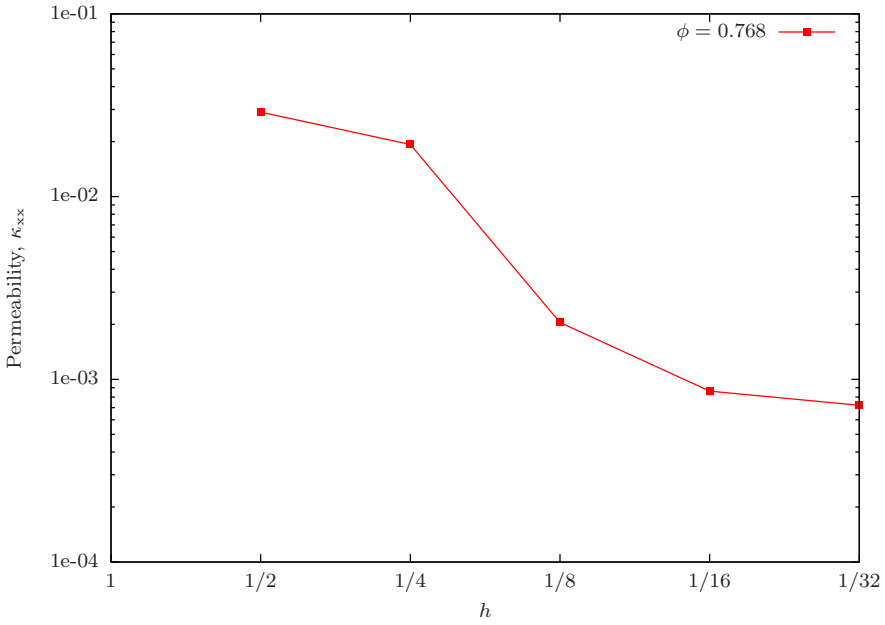

Figure. 6.16. Permeability for the artificial porous medium computed on various grid levels.

r	0.0318	0.0530	0.0742	0.0954	0.1060	0.1166
Φ	0.9886	0.9432	0.8437	0.6732	0.5534	0.4161

Table 6.3. The radii of spheres and corresponding porosity for the random sphere packing.

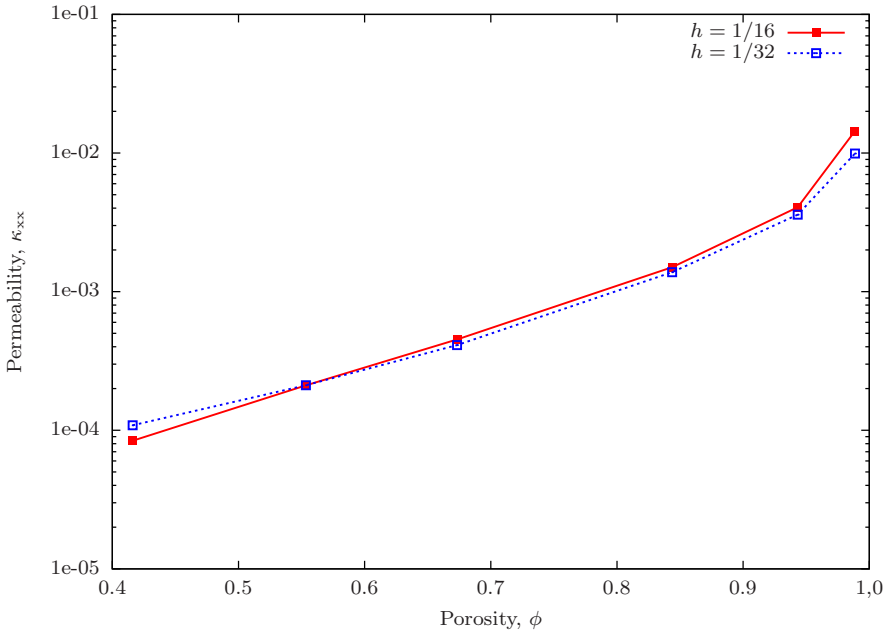

Figure. 6.17. Permeability computed for different porosities of random sphere packing on two successive grid levels. The porosity (ϕ) values were changed by varying the sphere radii (r).

It has been proven mathematically that (see Bear (1972)) Darcy's law for flow in porous media has analytical foundation where it can be derived from Stokes equations. With the recent advancements in porous media imaging and numerical discretisation schemes such as UDG, it is now possible to derive macroscopic parameters such as permeability by simulating fluid flow at the pore-scale modelled by the Stokes or Navier–Stokes equations. In this Chapter, it has been shown through examples that indeed it is possible to compute permeability by simulation on the pore-scale where UDG has been used to solve Stokes equation in artificial porous media like random sphere packing.

7 Numerical Simulation of Transport Through Porous Media

7.1 Introduction

The partial differential equation (PDE) describing the non-reactive or passive solute transport in porous media can be solved analytically or numerically. Since analytical solutions are available only for simple problems, the PDEs have to be approximated numerically for the solution of realistic problems. However, the solute transport equation offers some difficulties to solve numerically because of its dual (hyperbolic and parabolic) character. The mathematical properties of the transport equation (so called advection–dispersion equation (ADE)) change according to the terms in the equation which are dominant: when solute transport is dominated by advective transport, as is common in many field problems, then the ADE approximates to a hyperbolic type (e.g. in high permeability zones the velocity may be very high and the transport processes will be advection dominated). But if a system is dominated by dispersive fluxes such as in areas where fluid velocities are relatively low (e.g. in low permeability zones or near stagnation points, the velocity may be close to zero and the transport processes will be dominated by dispersion processes) the equation becomes parabolic in nature . Hence for the same system the governing equation may have hyperbolic nature in one area at a time and more parabolic in another area. This mixed character causes difficulties for the solution of the advection–dispersion equation.

Numerical solution of the advection–dispersion equation has been an active area of research for past three or four decades. Most numerical methods for solving the advection–dispersion equation can be classified into Eulerian, Lagrangian and mixed Eulerian–Lagrangian methods (Zheng and Bennett 2002). The common solution techniques based on Eulerian approach are finite difference, finite element and finite volume methods. They are well suited for solving parabolic equations like the flow equation or the diffusion equation. However, for advection-dominated problems grid-based methods suffer from numerical dispersion and numerical oscillations (Zheng and Bennett 2002). These problems can be avoided by imposing stability constraints such as restricting the grid spacing and size of time steps. Alternatively, Lagrangian methods can be used to avoid numerical problems of grid-based methods to solve the transport equation. Lagrangian methods offer interesting solution alternative to Eulerian methods mainly

due to their grid-free approach and their appealing physical interpretation. In contrast to Eulerian methods, the transport equation is not solved on a fixed grid but using a large number of moving particles. The random walk particle tracking (RWPT) is a pure Lagrangian based approach for numerically solving the ADE, and is used in this thesis. RWPT is well suited for transport processes where advection is dominant because it does not introduce spurious numerical diffusion. This Chapter gives a detailed description of the random walk particle tracking (RWPT) method.

7.2 Eulerian and Lagrangian Methods

A brief overview of Eulerian and Lagrangian methods is given next. The Eulerian methods such as finite difference, finite element and finite volume methods consist of solving the transport equation in a fixed spatial grid. They are generally mass conservative and handle dispersion dominated problems efficiently. However, for advection dominated problems that exist in many practical situations, an Eulerian method is susceptible to excessive numerical dispersion or artificial oscillations (Zheng and Bennett 2002). If the discretisation is too coarse, oscillations and numerical diffusion may yield poor or even incorrect solutions. These types of errors may be controlled by using a sufficiently fine spatial discretisation of the computational domain and small time steps. Consequently, the computational effort required may become prohibitive.

In Lagrangian methods such as RWPT, the partial differential equation governing solute transport is not solved directly. Instead, a large number of moving particles are used to approximate both advection and dispersion. They provide an efficient solution to advection dominated problems by essentially eliminating numerical dispersion (Kinzelbach 1990, Tompson and Gelhar 1990, Delay *et al.* 2005, Salamon *et al.* 2006). Since the RWPT method is not a direct numerical solution to the governing differential equation, it does not suffer from numerical dispersion (LaBolle *et al.* 1996). However, the lack of a grid may lead to computational difficulties. The velocity interpolation needed in particle tracking may also result in local mass balance errors and incorrect solutions (LaBolle *et al.* 1996). In addition, the concentration solution obtained by a Lagrangian method generally is not smooth compared to Eulerian solutions. The advantages and disadvantages of Lagrangian methods (RWPT) compared with Eulerian methods are as follows (LaBolle *et al.* 1996; 1998, Hassan and Mohamed 2003, Delay *et al.* 2005, Salamon *et al.* 2006):

Advantages

- Advection dominated transport can be simulated without introducing numerical dispersion and is easy to implement in a simulation code.
- By definition, the particle tracking procedure is perfectly mass conservative

- In principle, they do not require a space discretisation (grid), if velocities are known everywhere. Hence problems associated with the grid based methods are not present.
- The random walk procedure also has the advantage of being an intuitive representation of the physical dispersion process.
- Because of their intuitive and parallel nature, the algorithm is very suitable for parallel computing.

Limitations or Disadvantages:

- The main problem with particle tracking methods is the random fluctuations in the computed concentration. Although these fluctuations can be minimised by using large number of particles, improvements in the results are not of the same order as the increase in the computational costs (Hassan and Mohamed 2003, Salamon *et al.* 2006) because fluctuations are proportional to the square root of the number of particles.
- The random walk methods become less efficient computationally and require more computer memory and storage.
- Numerical accuracy is also affected when relatively large time steps are used because with large time steps, a particle may fail to consider local flow characteristics. Hence the time step must be chosen such that each particle is able to correctly sample the flow properties of each cell. It should also be noted that very small time steps lead to cumbersome calculations.

Another promising approach for transport modelling is the mixed Eulerian–Lagrangian methods. The mixed Eulerian–Lagrangian methods (e.g. Method of characteristics, Eulerian–Lagrangian Localised Adjoint Method (ELLAM) (Celia *et al.* 1990)) attempt to combine the advantages of the Eulerian and Lagrangian methods by solving the advection term (hyperbolic part) with a Lagrangian approach such as particle tracking and the dispersion term (parabolic part) with an Eulerian approach such as finite elements.

In this thesis, we use a random walk particle tracking, a pure Lagrangian based method for solving the advection-dispersion equation. The next Section discusses the principle of this method in detail.

7.3 Random Walk Particle Tracking Methods

The random walk particle tracking (RWPT) method is a typical example of a Lagrangian approach and has been used for the last few decades for the solution of transport problems not only to applications in porous media but also in other disciplines such as atmospheric sciences. Plenty of literature (Kinzelbach 1990, LaBolle *et al.* 1996, Roth and Hammel 1996, LaBolle *et al.* 1998, Delay *et al.* 2005) are available on this subject

and recently Salamon *et al.* (2006) provided a detailed overview of RWPT methods. In such methods, instead of solving the transport equation directly, the transport of solute mass by a large number of moving particles is considered. As mentioned previously, traditional Eulerian approaches present a number of problems when applied to advection dominated flow regimes. They generally require very fine discretisation of the transport domain to overcome problems of unstable numerical solutions and/or artificial diffusion. If the discretisation is too coarse, oscillations and numerical diffusion may produce poor or even incorrect solutions. The main attraction of RWPT methods is that they are found to be free of numerical dispersion and particularly effective and efficient for handling advection dominated transport problems. Hence at high Péclet numbers, numerical dispersion does not cause any convergence issues. Moreover, they are physically intuitive methods.

7.3.1 Basic Concepts

The basic idea of RWPT is that the mass transport in porous media may be considered as an average result of the movements of a large number of solute particles. A large number of passive or non-reactive particles are introduced into the flow field and move them by an advective motion along the streamlines and subsequent random diffusive motion. The random displacements allow to incorporate the effect of diffusion which make fluid particles to jump between different streamlines. In this way, each particle is engaged in two kinds of movements: one is advection (represented by the movement of the solute particle with an average velocity in the flow field) ; the other is dispersion, which may be seen as a random fluctuations around the average movement. The movement of the solute particles are then traced using appropriate methods. As long as the number of solute particles is large enough, mass transport in porous media can be correctly described (Zheng and Bennett 2002). These particles correspond to the mass concentration in an Eulerian method and since particles in the random walk method are not lost nor destroyed in the process, the method is mass conservative. Finally from the spatial equilibrium distribution of the particle ensemble, one can reconstruct common Euler concentration profiles. In principle, a grid is not necessary for the RWPT method. However, in practise, a grid may be employed for obtaining the velocity at random particle locations (for the interpolation of velocity at vertices to arbitrary particle locations). In addition, interpretation of the particle distribution as a concentration field may require a grid or some other means for converting the spatial distribution of particles to concentration values.

The well known macroscopic transport equation of a conservative solute in a porous media at the REV scale is given by the advection–dispersion Equation (2.21). Recalling

the equation as

$$\frac{\partial C}{\partial t} + \nabla \cdot (\mathbf{u}C) = \nabla \cdot (\underline{\boldsymbol{D}} \cdot \nabla C)$$

where $\underline{\boldsymbol{D}}$ is the dispersion coefficient tensor, C is the concentration, t is the time, $\mathbf{u}$ is the velocity vector obtained from the steady state flow equation. This represents a second order partial differential equation, which can be solved using RWPT method where each particle is moved according to the following stochastic differential equation (Zheng and Bennett 2002)

$$\boldsymbol{X}_i(t + \Delta t) = \boldsymbol{X}_i(t) + \boldsymbol{S}(t) + \boldsymbol{Z}(t)$$

where $\boldsymbol{X}_i(t)$ is the position vector of the i^{th} particle at time t, $\boldsymbol{S}(t)$ is the advective displacement and $\boldsymbol{Z}(t)$ is the random displacement associated with dispersion. In this process, between time t and $t + \Delta t$, a particle i moves from position $\boldsymbol{X}_i(t)$ to $\boldsymbol{X}_i(t + \Delta t)$ by advection and diffusion. The advective displacement is given by

$$\boldsymbol{S}(t) = \boldsymbol{u}(t) \cdot \Delta t$$

where $\boldsymbol{u}(t)$ is the local velocity at t. The diffusive displacement is given by

$$\boldsymbol{Z}(t) = \sqrt{2 \cdot D_m \cdot \Delta t} \cdot \boldsymbol{\xi} \tag{7.1}$$

where $\boldsymbol{\xi}$ is a a vector of length $\sqrt{dim}$ with a random direction. The *dim* is the space dimension. The $\boldsymbol{\xi}$ contains dim component random numbers drawn from a Gaussian distribution of *zero mean* and *unit variance* (Maier *et al.* 2000, Jimenez-Hornero *et al.* 2005).

7.3.1.1 Advective Displacement

Since the velocity field is known, a numerical integration scheme can be used to move particles from one position to another to approximate the advection of the solute particles where the movement is described by an ordinary differential equation (ODE) of the form

$$\frac{d\boldsymbol{x}}{dt} = \boldsymbol{u}(x, t).$$

This can be solved using simple integration schemes such as the simplest Euler's integration step:

$$\boldsymbol{x}(t + \Delta t) = \boldsymbol{x}(t) + \boldsymbol{u}(x, t) \cdot \Delta t.$$

For particles located in areas of relatively uniform velocity, the first order Euler algorithm have sufficient accuracy. However, for particles located in areas of strongly converging or diverging flows, the first order algorithm many not be sufficient unless Δt is very small. In such cases, a higher order schemes like Heun's method (2^{nd} order Runge–Kutta) may be used. Heun's scheme:

$$\boldsymbol{x}^*(t+\Delta t) = \boldsymbol{x}(t) + \boldsymbol{u}(x,t)\cdot\Delta t$$
$$\boldsymbol{x}(t+\Delta t) = \boldsymbol{x}(t) + \frac{1}{2}\{\boldsymbol{u}(x,t) + \boldsymbol{u}(x^*,t)\}\cdot\Delta t$$

7.3.1.2 Dispersive Movement

Since the spreading of the solute mass caused by dispersion can be described by a Gaussian or normal distribution (Bear 1972, Zheng and Bennett 2002, Roth 2007), a particle displacement is considered as a normally distributed random variable whose mean is the advective movement and standard deviation is the dispersive movement. The dispersive component, $\boldsymbol{Z}(t)$, corresponds to the vector whose module is constant and equal to $\sqrt{dim}$ where dim is the number of dimensions. For a given time step Δt, the random direction of $\boldsymbol{Z}(t)$ follows a Gaussian probability distribution function with a mean value of $zero$ and a variance of $2D_m\Delta t$. The dispersive displacement $\boldsymbol{Z}(t)$ is then given by

$$\boldsymbol{Z}(t) = N(0,\sigma^2)$$

where $N(0,\sigma^2)$ is a normally distributed random number with *zero* mean and $\sqrt{2D_m\Delta t}$ as standard deviation. The values for $N(0,\sigma^2)$ can be generated through random number generator (e.g. Press *et al.* (1993)). Hence for each time step, we assume that a particle i first moves a distance of $\mathbf{u}\Delta t$ according to the advection and makes a random walk along an arbitrary direction. The distance of the walk is $\sqrt{2D_m\Delta t}\ \boldsymbol{\xi}$. Thus the total displacement of the particle i is

$$\mathbf{u}\Delta t + \sqrt{2D_m\Delta t}\ \boldsymbol{\xi}. \tag{7.2}$$

The procedure is schematically shown in Figure (7.1). The total displacement of a particle i, in a given time step Δt is thus given by

$$\boldsymbol{X}_i(t+\Delta t) = \boldsymbol{X}_i(t) + \boldsymbol{u}(t)\cdot\Delta t + \sqrt{2D_m\Delta t}\ \boldsymbol{\xi} \tag{7.3}$$

This procedure is repeated for a large number of solute particles. Their displacements are different because the second term of the equation (7.2) is stochastic. Finally from the equilibrium distribution of particle ensemble, the dispersion coefficients can be determined using the method of moments as described in the next Section.

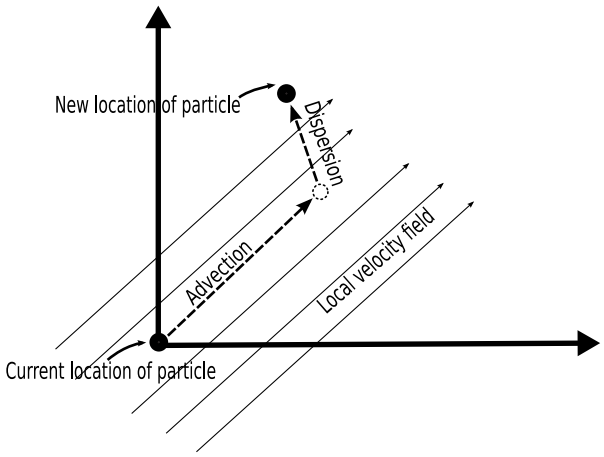

Figure 7.1: Two-dimensional random walk of a solute particle. The position of the particle vary due to advection and dispersion in a given time step. Dispersion step allows particles to cross different streamlines.

7.3.2 Method of Moments

The spatial moments serve as a simple physically meaningful description of overall solute concentration behaviour. The method of moments can be used to study the temporal behaviour of dispersion coefficients (both longitudinal and transverse) and to evaluate their asymptotic value when time becomes infinite (or for very longer duration) (Kitanidis 1988, Roth 2007). Usually only the first three moments are considered: the *zeroth* moment represents the total solute mass for the concentration profile, the *first moment* corresponds to the location of the centre of mass of the solute and the *second moment* corresponds to the spreading of the solute concentration around the centre of mass. Let $\boldsymbol{x}$ be the coordinates of the computed trajectory of a particle and let N_p be the number of particles. As long as the particles are in the computational domain, the total mass is constant. The centre of mass of the solute distribution in the longitudinal direction is approximated by the first moment as

$$\langle \boldsymbol{x}(t) \rangle = \frac{1}{N_p} \sum_{i=1}^{N_p} \boldsymbol{x}_i(t)$$

and the average velocity of the centre of the solute mass is determined by

$$\langle \boldsymbol{u} \rangle = \langle \boldsymbol{x}(t) \rangle / t. \tag{7.4}$$

The spread of mass (spatial variance) around $\langle \boldsymbol{x}(t) \rangle$ is approximated by the second moment as

$$var(\boldsymbol{x}(t)) = \frac{1}{N_p} \sum_{i=1}^{N_p} \boldsymbol{x}_i(t)^2 - \langle \boldsymbol{x}(t) \rangle^2.$$

The variance is usually represented by σ^2, where σ is the standard deviation. Now using the central limit theorem (Roth 2007), one can estimate the average displacement of

the solute particles (Jimenez-Hornero *et al.* 2005) as

$$\langle \boldsymbol{x}(t) - \boldsymbol{x}(t_0) \rangle = 0$$

and the square average displacement

$$\langle [\boldsymbol{x}(t) - \boldsymbol{x}(t_0)]^2 \rangle = 2D_m(t - t_0)$$

where t_0 is the initial time and $\langle \cdot \rangle$ represents the average operator. When both advection and diffusion processes are considered together, the dispersion coefficient D_{eff} replaces the diffusion coefficient D_m. The calculated second spatial moment of the solute about the centre of mass (i.e. spatial variance) over time allows estimation of the effective dispersion coefficient, D_{eff}. The temporal longitudinal (and transverse) dispersion coefficient is then defined by

$$D_{\text{eff}}(t) = \frac{1}{2}\frac{d\sigma^2}{dt} \tag{7.5}$$

where σ^2 is the spatial variance with time t. Using the RWPT, the second moment σ^2 can be estimated easily from particle displacements and the time derivative of the spatial variance (where variance is approximately proportional to time) yields the dispersion coefficient. The variance is computed according to

$$\sigma^2(t) = \sum_{i=1}^{N_p} (\Delta \boldsymbol{x}_i - \langle \boldsymbol{x}_i \rangle)^2$$

and

$$\Delta \boldsymbol{x} = \boldsymbol{x}(t) - \boldsymbol{x}(t_0)$$

where $\boldsymbol{x}(t)$ is the solute particle coordinates at time t. If $\frac{d\sigma^2}{dt}$ is constant, Fick's law is a valid model for the dispersion process.

7.3.3 Evaluation of Concentration

The solution of the advection–dispersion equation by the random walk method provides the discrete particle displacements (or positions) and not the concentration values. The concentration is represented by the density of moving particles at any particular time and usually it is evaluated on the underlying computational grid (finite element or finite difference) from which the flow solution is obtained. Even though no grid is needed for the RWPT method, interpretation of the particle distribution as a concentration field may require a grid or some other means for converting the spatial distribution of particles to concentration values. Hence it is necessary to locate the cell indices of

any particle in the computational domain. If the grid is regular it is straightforward to convert particle coordinates to cell indices. When unstructured grid is used, locating a particle and getting the cell index would turn out to be a complicated procedure. Since we are using the new UDG approach based on the structured grid to obtain the flow field, locating the particle position and corresponding element index is much easier. The concentration associated with a computational cell can be calculated from arithmetic averaging. Assuming the number of particles in the cell or element e at time t is N_e, the concentration for the cell at time t can be estimated as

$$C_e(t) = \frac{1}{V_e} \sum_{p=1}^{N_e} m_p$$

where m_p is the mass of the p^{th} particle within the cell e and V_e is the volume of the cell.

It should be noted that the number of particles used in the model has a great influence on the computation of concentration values. Since spreading of the solute is affected by the random component, two particles at the same initial location will most likely follow different paths. Hence a small number of particles may not model the spreading of the solute appropriately resulting in incorrect estimates of the concentration. Therefore a a large number of particles is required for a particle tracking model to give a better solution and as a result this considerably increases the computational costs.

7.3.4 Velocity Interpolation

The numerical implementation of random walk particle tracking is relatively very easy with one exception that it requires the velocity to be known everywhere in the computational domain. Due to the random steps needed to represent the dispersion behaviour, the particle may jump to anywhere in the domain and for the subsequent movement the velocity at the current arbitrary position is required. Usually when solving the flow equation using numerical methods, the resulting velocity field is given as a discrete point information, i.e. velocity is known only at some grid points (vertices) and some kind of interpolation is needed to obtain the velocity values at these arbitrary locations. Since this interpolated velocity should fulfil the local fluid mass balance at any location and the local solute mass conservation at any grid cell interface, the interpolation should be done carefully. The interpolation of the velocity from the known points to particle position is widely done using the linear and bilinear interpolation schemes. Furthermore, when the particle tracking is done on non-uniform or unstructured grids (usual finite element or finite volume grids) locating the grid cell containing the particle and interpolation of velocity are not an easy procedure (Chen and Pereira 1999, V. and C. 1999, Chordá *et al.* 2002, Pokrajac and Lazic 2002). In this case, there should be a special way to identify the current location of the particle and is a time consuming factor, which is necessary after each integation step. This procedure turns out be easy when a structured grid is

used, but for irregular grids a non-local cell search is needed for every evaluation. In fact, one advantage of the discontinuous Galerkin based method (UDG) used in this thesis is that it is based on a structured grid. Moreover, since the solution is represented within each element as a polynomial approximation the velocity field at any point inside an element can be found easily. Another advantage is that the DG based scheme is locally and globally mass conservative.

7.3.5 Boundary Conditions

When solving the advection–dispersion equation in complex porous media, the solid boundaries have to be dealt properly. This is in particular crucial when using RWPT method as improper boundary condition can significantly reduce the accuracy of the simulation. On the solid boundaries, it is natural to apply the no-flux boundary conditions for the solute particles, implying that no mass is able to pass through the solid surfaces of the porous medium. However, implementing the no-flux boundary condition is not easy and can affect the quality of the solution (Salles *et al.* 1993, Maier *et al.* 2000, Freund *et al.* 2005). Although the random walk approach has been used for the simulation of transport processes for a long time, there is no proper agreement on the correct implementation of no-flux boundary conditions when using particle based methods. Several approaches have been used in the literature to handle a particle hitting a solid boundary. The following are some of the major approaches (Szymczak and Ladd 2003):

1. Specular reflection

   The trajectory $\mathbf{X}(t)$ of a solute particle undergoing specular reflection on a plane defined by the unit normal vector $\hat{\mathbf{n}}$ is given by

   $$\mathbf{X}(t+\Delta t) = \mathbf{R}.[\mathbf{X}(t) + \mathbf{S}(t) + \mathbf{Z}(t)], \quad (\mathbf{X}(t) + \mathbf{S}(t) + \mathbf{Z}(t)) \notin \Omega$$

   where $\mathbf{R} = 1 - 2\hat{\mathbf{n}}\hat{\mathbf{n}}$ is the mirror reflection operator and Ω is the domain. Basically, if a particle hit the boundary $\partial\Omega$ with a velocity vector $\boldsymbol{L}$ then the reflected vector $\boldsymbol{L'}$ is given by

   $$\boldsymbol{L'} = 2 * (\boldsymbol{L} \cdot \hat{\mathbf{n}}) * \hat{\mathbf{n}} - \boldsymbol{L}$$

   where $\hat{\mathbf{n}}$ is the normalised normal vector on the boundary/plane, $*$ is the scalar multiplication operator and $\cdot$ is the dot product of two vectors.

2. Rejection

   In this approach, a move is rejected when the particle hits the boundary and the particle remains at its previous position for that time step. The problem with this approach is that the particles near the solid surfaces move much slower than those

in the bulk and would result in the *tailing* in the breakthrough curve. When the pore space is narrower more number of particles hit the boundary and moves get rejected. Hence they tend to remain near the surface and may accumulate time delays.

3. Multiple rejection

   As for the rejection condition, a move is rejected when a particle crosses the solid boundary and new moves are tried until a move is within the pore-space (that do not cross the solid boundary). The problem arises when particles are in a narrow region of pore-space where almost every move has a chance to hit the boundary.

4. Interruption (Salles *et al.* 1993)

   In this procedure, the particle stops at the boundary and its clock is incremented by $\gamma\Delta t$ with γ given by

   $$\mathbf{X}(t+\gamma\Delta t) = \mathbf{X}(t) + \gamma(\mathbf{S}(t) + \mathbf{Z}(t)) \in \partial\Omega$$

   For the remainder of the time step, $\Delta t' = (1-\gamma)\Delta t$, the particle moves away from boundary in a new randomly chosen direction using a sole diffusion step. In this condition, in fact the movement is the results of more random components which increases the variance of particle's displacement and overall displacement.

Rage (1996) used the rejection approach while Salles *et al.* (1993) and Maier *et al.* (2000) used the interruption method. Freund *et al.* (2005) used a combination of step by step movement with a simple reflection in which if a particle would end up in a solid, it is moved to the surface first and then using a sole diffusive step into the bulk fluid. Szymczak and Ladd (2003) has investigated different boundary conditions and reported that the specular reflection implementation seems to implement the no-flux boundary condition. They also showed that specular reflection condition is able to preserve an initially uniform particle distribution in the presence of reflective boundaries. Hence in the current work, the specular reflection boundary condition has been used to implement no-flux boundary condition for the transport simulation. This boundary condition has been tested with the Taylor-Aris dispersion (see Section (7.4.1)) between two parallel plates and results were obtained with smaller errors. It should be noted that in cases where more solid boundaries are near to each other, a particle lying between the surfaces might undergo multiple reflection in a given time step. This is particulary true for pore-scale problems where particles may undergo multiple reflections in narrow pore channels.

7.4 Implementation and Testing

The present implementation of random walk particle tracking algorithm is based on Roth and Hammel (1996) in which the movement of a single particle is considered and the movement is broken into a series of steps with duration Δt. At each step the particle is advected to represent the movement due to the average flow field, and then randomly displace it to represent diffusion or dispersion. This two step process moves the particle to a new location (see Figure (7.1)), where the velocity is recalculated and the process is repeated over and over again monitoring the particle's location as a function of time until the desired time is reached or particle reached the outlet of the domain. For a cloud of particles, the process is repeated for each particle. The simplest advection step is the Euler method. However, in the current implementation the higher-order Heun's predictor corrector algorithm was used as it is more accurate (Szymczak and Ladd 2003). Heun's method is a two-stage Runge-Kutta method where the advective displacement is given by

$$\boldsymbol{S}(t) = \frac{1}{2}\{\mathbf{u}(\mathbf{X}(t)) + \mathbf{u}(\boldsymbol{X}^p(t+\Delta t))\}\Delta t$$

where superscript p denote a predictor step. The predictor step for $\mathbf{X}^p$ is an Euler step. The Heun's method is weakly second order convergent when diffusion coefficient is independent of spatial position. The total displacement for a single time step is then constructed according to

$$\boldsymbol{X}_i(t+\Delta t) = \boldsymbol{X}_i(t) + \frac{1}{2}\{\mathbf{u}(\mathbf{X}(t)) + \mathbf{u}(\mathbf{X}^p(t+\Delta t))\}\Delta t + \sqrt{2D_m\Delta t}\,\boldsymbol{\xi}. \tag{7.6}$$

where the last term represents the random displacement component. The random displacement component requires a model of diffusion or dispersion and it is very easy to implement the random walk for molecular diffusion because the diffusion coefficient is typically both isotropic and homogeneous; that is, it is simply a constant scalar. At the pore-scale, one only have to consider random movement due to molecular diffusion. The random displacements Z are generally based on a Fickian model which yields Gaussian distributed random displacements. For that one require a random number generator that will generate the Gaussian random numbers given the mean and variance (standard deviation squared). In the present implementation we have used a random number generator from Press *et al.* (1993).

In this work, the RWPT was carried out using the Heun's method with variable or adaptive time step. Adaptive time steps were implemented to avoid unnecessary smaller steps by adjusting the time step according to the magnitude of the local velocity during the simulation. The time step is also constrained by the grid size h such that the largest possible particle displacement in one time step is always less than $h/2$. In this way, one can make sure that a particle would sample the local velocity field without jumping

over to longer distance. The velocity required by the particle tracking procedure was obtained by the new UDG approach as explained in the Section (6.5.1). Since the DG schemes can provide solutions on element level, there was no need for interpolating the velocities to arbitrary locations, instead, the velocities at the arbitrary locations inside elements can be directly computed from the DG solution coefficients.

7.4.1 Taylor-Aris Dispersion Between Parallel Plates

In this section the process of Taylor-Aris dispersion often known as Taylor dispersion (Taylor 1953; 1954, Aris 1956) between two parallel plates is simulated which is considered as the simplest dispersion benchmark problem (Jimenez-Hornero *et al.* 2005, Roth 2007) to verify the transport models. Taylor dispersion consists of the dispersion of a passive solute along a stationary flow in a channel or a tube with small transverse dimensions. A channel (or two parallel plates) geometry of the Taylor dispersion problem is shown in the figure (7.2). This problem was first treated experimentally and theoretically by Taylor (1953; 1954) and subsequently generalised by Aris (1956). It is an effect in which a shear flow increases the effective dispersion of solute particles by smearing out the concentration distribution in the direction of the flow and enhancing the rate at which it spreads in that direction. Taylor dispersion has fundamental importance in hydrodynamics and has many applications in various fields such as biological perfusion, chemical reactors, soil remediation and oil recovery. Though the problem is simple, it involves the effect of dispersion resulting from both velocity gradients and diffusion and is considered as a good test for code verification (Byron Bird *et al.* 1960, Baudet *et al.* 1989). In addition, it has been solved analytically (van Genuchten and Alves 1982) which allows one to make comparisons.

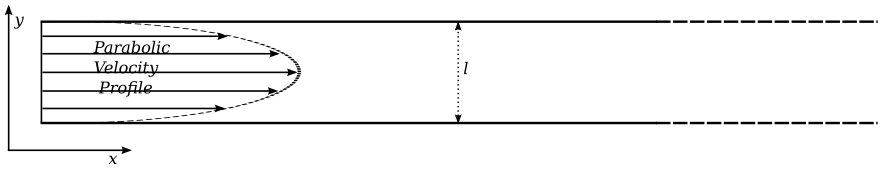

Figure. 7.2. The geometry of the Taylor-Aris dispersion problem. The flow is along the x axis between two parallel planes of infinite length separated by a distance of l with a parabolic velocity profile (Poiseuille flow). When a slug of solute is injected at the inlet, the solute spreads as it travels and the projection of the concentration on to the x axis eventually becomes a Gaussian.

7.4.1.1 Theory

The theory of Taylor-Aris dispersion is briefly covered here. Consider an established Poiseuille flow along x direction confined between two parallel plates separated by a distance of l. The plates are kept at $y = 0$ and $y = l$ as shown in the Figure (7.2).

The flow takes place along the x axis between two plates with a parabolic velocity profile (because the Poiseuille flow is characterised by a parabolic velocity profile) that is dependent only on the transverse coordinate y. Let the velocity profile be $\mathbf{u} = (u_x(y), 0)$ and u_m be the mean flow velocity in the flow direction, defined as

$$u_m = \frac{1}{l}\int_0^l u_x(y)\, dy \tag{7.7}$$

$$= \frac{2}{3}u_0 \tag{7.8}$$

where u_0 is the maximum velocity in the plane $y = \frac{l}{2}$, half-way between the plates. At time $t = 0$, a slug of solute is introduced (as an abrupt variation in the concentration) into the flow across the plane $x = 0$ perpendicular to the flow direction. Since the fluid is flowing slowly with flow gradients transverse to the flow direction, the solute particles are carried away by the flow in such a way that the particles close to the plates move much slower than those in the middle because of the parabolic velocity profile. In addition to that, the solute particles jump between fast and slow streamlines randomly due to transverse diffusion and disperses them along the direction of flow. In this regime, the spreading of the concentration front is purely due to advection and width of the spreading Δx increases linearly with time as $\Delta x = u_m t$. However, as the front moves downstream, the distribution of the solute particles between the plates becomes more uniform because of the transverse molecular diffusion across the flow. Aris (1956) showed that the characteristic time for this transverse diffusion $t_c \approx l^2/D_m$, where D_m is the molecular diffusion coefficient. He also showed that at times large enough compared to t_c, the variation of the mean concentration $C(x,t)$ over the flow section between parallel plates is governed by the convection-diffusion equation,

$$\frac{\partial C(x,t)}{\partial t} + u_m \frac{\partial C(x,t)}{\partial x} = D_{\text{eff}} \frac{\partial^2 C(x,t)}{\partial x^2}$$

where D_{eff} is the effective longitudinal dispersion coefficient. Furthermore it has been shown that for flow between parallel plates, after the characteristic time, the projection of the solute distribution onto the x-axis is nearly Gaussian. That is, the probability distribution of displacements in the long time regime is expected to become a Gaussian and its dynamics are given by the convection-diffusion equation giving rise to a Gaussian distribution whose centre moves at the average velocity u_m, and whose mean square displacement σ^2 is given by the effective dispersion coefficient $D_{\text{eff}} = \sigma^2/2t$ (Baudet *et al.* 1989).

For Poiseuille flow in a circular tube, Taylor (1953) showed that the dispersion coefficient could be explicitly calculated from the known properties of the flow field and the diffusivity of the solute. He provided a relationship between the dispersion coefficient and Péclet number for a circular tube where the dispersion coefficient D_{eff} is

given by

$$\frac{D_{\text{eff}}}{D_m} = 1 + \frac{Pe^2}{48} \tag{7.9}$$

and Aris (1956) further generalised this relationship. For a channel or flow between parallel plates it is given by

$$\frac{D_{\text{eff}}}{D_m} = 1 + \frac{Pe^2}{210} \tag{7.10}$$

where the Pe is the Péclet number (see Section (2.3.4.1)). Here Pe is defined as

$$Pe = \frac{u_m l}{D_m} \tag{7.11}$$

where u_m is the average velocity across the channel and l is the transverse dimension. In most dispersion processes, the relative magnitude of the convective and diffusive effects is given by the Péclet number Pe (Roth 2007). The Equation (7.10) can be written in general form considering the shape of the cross-section of the geometry as

$$D_{\text{eff}} = D_m(1 + \zeta Pe^2) \tag{7.12}$$

where ζ is a coefficient that depends on the shape of the cross-section of the geometry. In the case of a channel or parallel plates $\zeta = 1/210$ and for a capillary tube with circular cross-section $\zeta = 1/48$. From above equation (7.12) one can observe that, except at extremely low velocities where diffusion becomes dominant, molecular diffusion reduces the longitudinal dispersion by homogenising the solute concentration across the flow section. Additionally it can be observed from the Equation (7.12) that the effective dispersion coefficient at high velocities increases proportionally with the square of the velocity of the flow. This is the result obtained by Taylor and Aris. We can note that within the characteristic time given by Taylor and Aris, the particle had the time to explore the whole cross-section of the channel by a random process in which the particle randomly visits different streamlines characterised by distinct velocities, which tends to take it far from its original position. Particles are thus rapidly dispersed along the channel. At short times (times shorter than l^2/D_m), however, the solute mass follows the streamlines and hence it is stretched out linearly with time until diffusion acts to homogenise along the cross-section.

Recall the one dimensional transport equation (Equation (2.23)) from Chapter (2). Taylor (1953; 1954) studied shear flow dispersion in a tube and gave a model analogous to the one dimensional transport process of a solute concentration downstream of a continuous point source. The analytical expression is

$$C(x,t) = \frac{C_0}{2} erfc\left(\frac{x - u_m t}{\sqrt{2}\sigma}\right) \tag{7.13}$$

where $\sigma = \sqrt{2D_x t}$ is the square root of the variance of the solute concentration and C_0 is the concentration at $(x, t) = 0$ at the source. The above mathematical solution is valid only when the solute is fully mixed across the cross-section of the flow. This occurs at a downstream location $x \gg l^2/D_x$ which is called the far field. The Equation (7.13) is an expression for the breakthrough curve from the normal density function and it is often used to make verification studies (both for experimental and numerical simulations). The cumulative breakthrough curves can be computed for a porous medium sample at a distance of x and compared to the approximate theoretical solution (van Genuchten and Alves 1982) given as

$$\frac{C}{C_0} = \frac{1}{2} erfc \left[\frac{x - u_m t}{2(D_{\text{eff}} \cdot t)^{1/2}} \right] \tag{7.14}$$

where x is the distance at which the concentration of the solute is computed and *erfc* is the complementary error function.

7.4.1.2 Calculation of Effective Dispersion Coefficients

We have seen that the parabolic velocity profile causes the so called Taylor-Aris dispersion in simple geometries and the process can be described by an effective diffusion/dispersion coefficient D_{eff}. Now given the velocity profile, using the Taylor-Aris approach, one can determine the effective dispersion coefficient in the axial direction analytically using the Equation (7.10). Writing Equation (7.10) in terms of the average flow velocity, we get the analytical expression for the effective dispersion coefficient as

$$D_{\text{eff}} = D_m + \frac{l^2 u_m^2}{210\ D_m}$$

where D_m is the molecular diffusion coefficient. The quantity $\frac{D_{\text{eff}}}{D_m}$ can be calculated from numerical simulations by the method of moments as described in the Section (7.3.2). For instance, particles are released at time $t = 0$ and at $x = 0$ uniformly over the entire cross-section and are tracked as they travel through the domain. After the characteristic time, the first three moments of particle displacements are computed and these moments are used to determine the dispersion coefficients.

7.4.1.3 Simulation Results

The implementation of our random-walk particle tracking model was verified by comparing the longitudinal dispersion coefficient with Taylor-Aris analytical solutions for dispersion between parallel plates. According to Taylor-Aris dispersion theory when a solute cloud is dispersed between two parallel plates kept at l apart, after a characteristic time $t_c = l^2/D_m$, the projection of its concentration on the flow direction may be fitted with a Gaussian probability distribution with a variance $\sigma^2 = D_{\text{eff}} t$, where D_{eff} is the

effective longitudinal dispersion coefficient. D_{eff} can be calculated analytically using the Equation (7.10) and can be compared with numerical solutions obtained using the method of moments.

Consider two parallel plates of length 3600 units kept at a distance of 30 units apart. The parabolic velocity profile is imposed at the inlet and at the outlet a natural boundary condition was applied. On the plates, no-slip conditions were imposed for velocity. Then the Stokes equation was solved in this geometry and velocity and pressure field were computed for various inflow conditions. The mean velocities were calculated using the equation (7.7). After the computation of the Poiseuille flow in the channel, Taylor simulation was simulated using the random walk particle tracking approach with no-flow boundary condition on the plates. The particles are introduced into the flow field at the inlet ($x = 0$) and tracked as described in Section (7.3). The characteristic time to reach Taylor-Aris dispersion condition is calculated by

$$t_c = \frac{l^2}{D_m}$$

where l is the distance between parallel plates and D_m is the coefficient of molecular diffusion. The Figure (7.3) shows the concentration snap shots from a Taylor-Aris dispersion with $D_m = 0.35$, $u_m = 0.8326$ and $Pe = 71.365$. Here $tc = 2571.42$. Péclet numbers for the flow setup were calculated taking the separation of plates as the characteristic length.

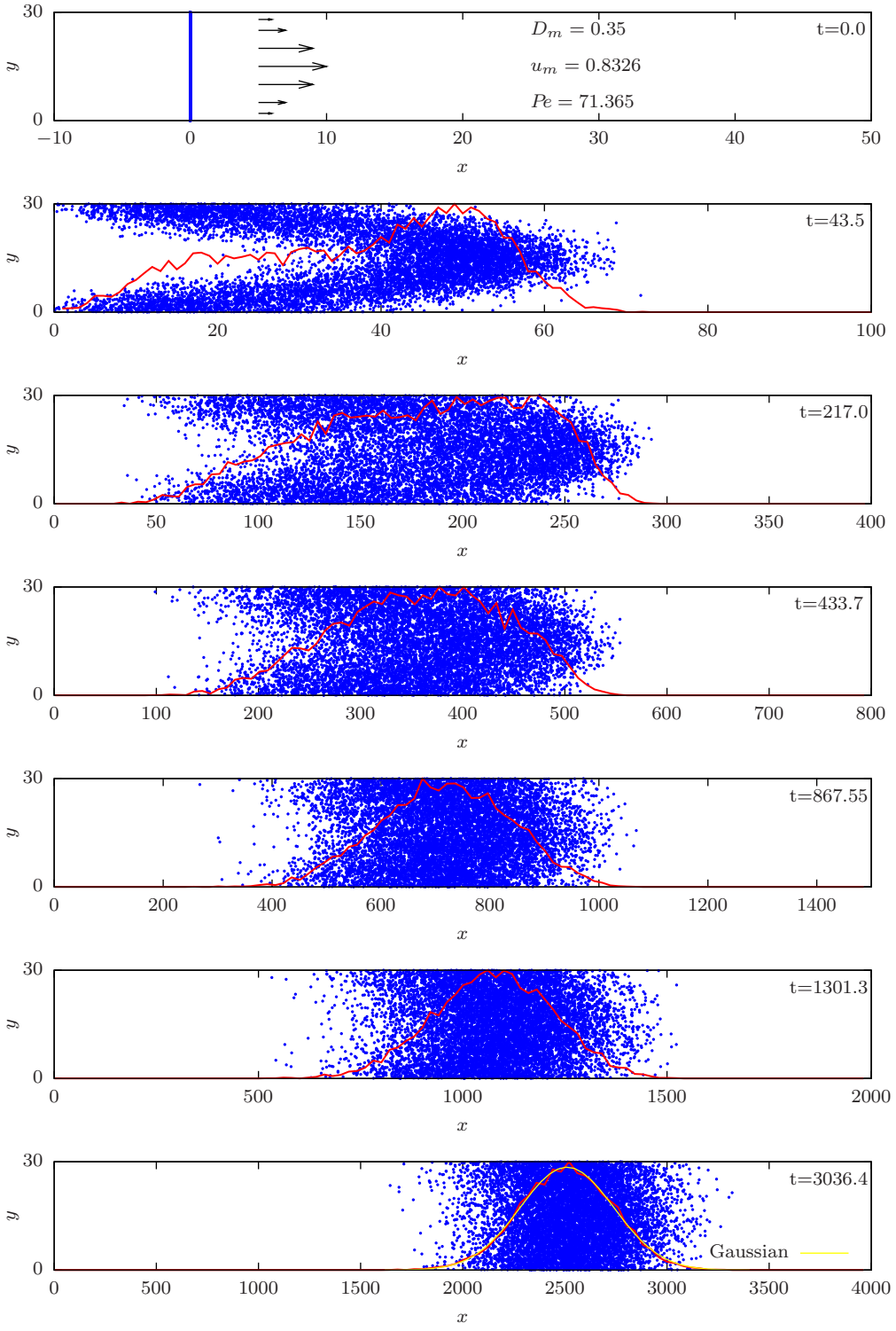

Figure. 7.3. Evolution of the concentration distribution in Taylor-Aris dispersion between parallel plates ($D_m = 0.35$, $u_m = 0.8326$, $Pe = 71.365$). At time t=0, particles are uniformly distributed over the cross-section at x=0. Their initial, intermediate and equilibrium positions are shown here. Initially when the effect of diffusion is small, particle distribution still has a parabolic shape. When the effect of diffusion starts to act upon in transitional stages particles are more spreading out and finally after a characteristic time, the projection of the concentration (red lines) on to the x axis (flow direction) approaches a Gaussian distribution (yellow) according to the central limit theorem.

The breakthrough curves from numerical experiments were computed as the amount of particles passing through the outlet of the domain (or the point of measurement) and compared with the approximate theoretical solution given by the Equation (7.14). Rewriting the Equation (7.14) as

$$\frac{C}{C_0} = \frac{1}{2}\text{erfc}\left[\frac{x - u_m t}{2(D_{\text{eff}} \cdot t)^{1/2}}\right] \tag{7.15}$$

where x is the distance at which the concentration of solute is computed and $erfc$ is the complementary error functions (van Genuchten and Alves 1982). The concentration measured is normalised with respect to the initial concentration and plotted with the normalised time $T^* = t\ u_m/x$ where t is the time and u_m is the mean flow velocity and x is the breakthrough distance. The flow was computed by solving the Stokes equation in the channel using the unfitted discontinuous Galerkin method as described in the Section (6.5.1). Taylor–Aris dispersion was simulated by taking $D_m = 0.25$ and the

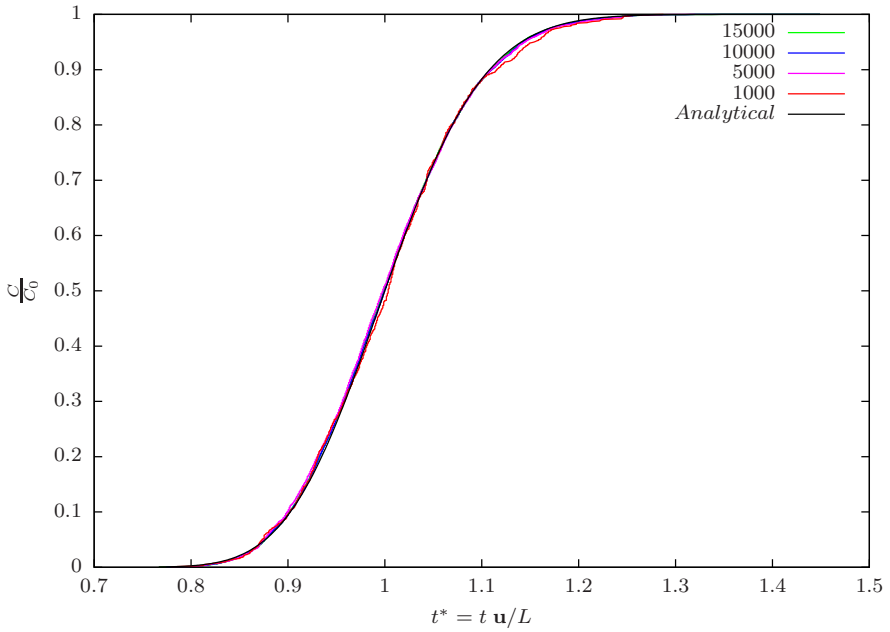

Figure. 7.4. Cumulative breakthrough curve for the Taylor-Aris dispersion. Simulated result is compared with analytical solution (7.15) and plotted for different number of particles. It can be seen that as the particles are increased the simulated result converges to analytical solution.

Figure (7.4) shows the normalised solute concentration C/C_0 as a function of normalised time. The breakthrough curves were plotted by varying the number of particles and found that there is no visible difference when the particles are increased above 5000. Hence for subsequent computations, we have chosen 10000 particles. In Figure (7.5), the time variation of the centre of mass of the particle concentration ($\langle x \rangle$) or first moment for different values of the mean velocities ($u_1 = 0.666502, u_2 = 0.333428, u_3 = 0.0832609$) are plotted. The Péclet numbers corresponding to the flow are 79.98, 40.01 and 9.99

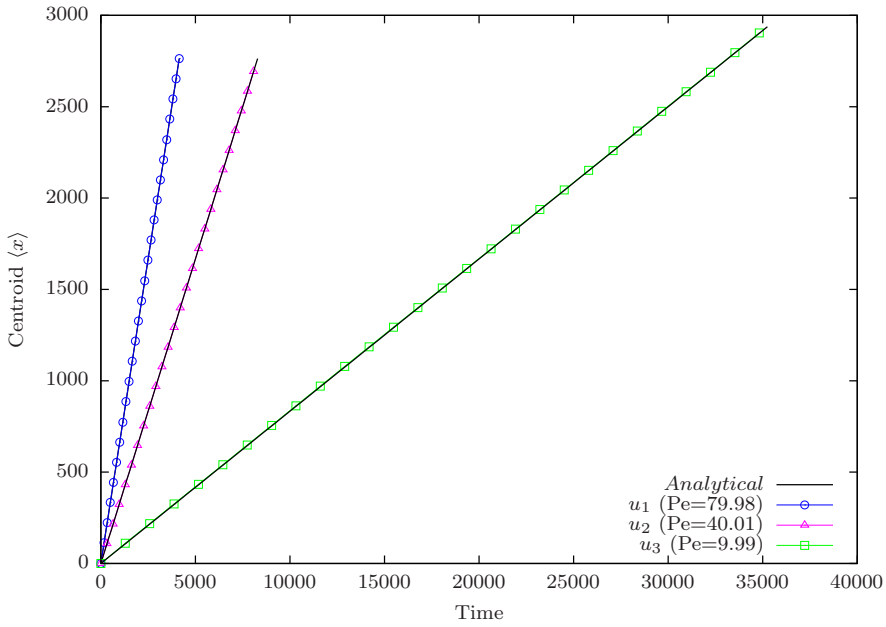

Figure. 7.5. Time variation of the centre ($\langle x \rangle$) of particle concentration obtained by computing the first moment in the flow direction as a function of time and the analytical solution corresponds to $u_m t$.

respectively by treating the width of the channel as the characteristic length. The values (first moments) were calculated by subtracting the first moment at time $t = 0$ from those at time t. It can be observed that the centre of solute mass is moving at constant velocity in each case and matches the analytical solution corresponds to $u_m t$. At long times, we observe that a linear variation of these two parameters as expected from the theoretical laws:

$$\langle x \rangle = u_m \, t \quad \text{(advection)}$$
$$\sigma = \sqrt{2 \, D_{\text{eff}} \, t} \quad \text{(dispersive spreading)}$$

The Figure (7.6) shows the time variation of variance (σ^2) for three different values of the mean velocity. It shows the mean square deviation $\langle x^2 \rangle - \langle x \rangle^2$ from $\langle x \rangle$ and shows that in each case solute spreading about its centre grows linearly. The analytical solution corresponds to $\sigma^2 = 2 D_{\text{eff}} t$ where D_{eff} was computed analytically using Equation 7.12. The convergence of the system towards the Gaussian Taylor dispersion regime was studied by plotting the time variations of $\sigma^2(t)/2t$ and $\langle x \rangle / t$ in Figures (7.7) and (7.8) respectively. From Equations 7.5) and (7.4, we know that these ratios should converge to D_{eff} and u_m respectively. In both plots, we can see that the simulated values are converging towards its theoretical solution. Finally the variation of $\frac{D_{\text{eff}}}{D_m}$ with Pe is also studied. The dispersion coefficients were calculated at varying fluid velocities (i.e. for different Pe) and the Figure (7.9) shows the computed dispersion coefficient versus Péclet number where the line corresponds to the theoretical Taylor-Aris solution.

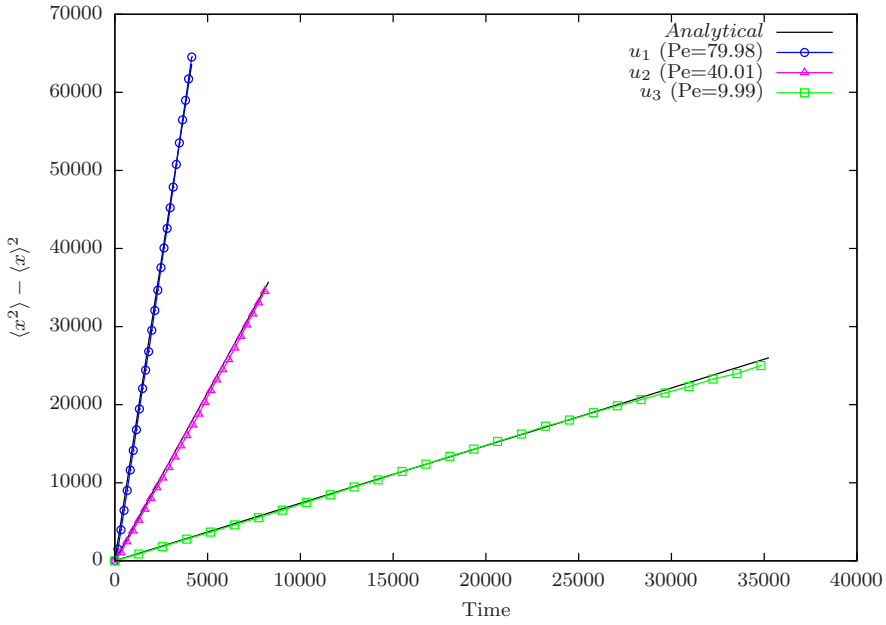

Figure. 7.6. Time variation of the centred second moment of solute concentration in the flow direction obtained by computing the mean square deviation $\langle x^2 \rangle - \langle x \rangle^2$ from $\langle x \rangle$. The analytical solution corresponds to $\sigma^2 = 2D_{\text{eff}}t$ where D_{eff} was computed analytically using Equation (7.12).

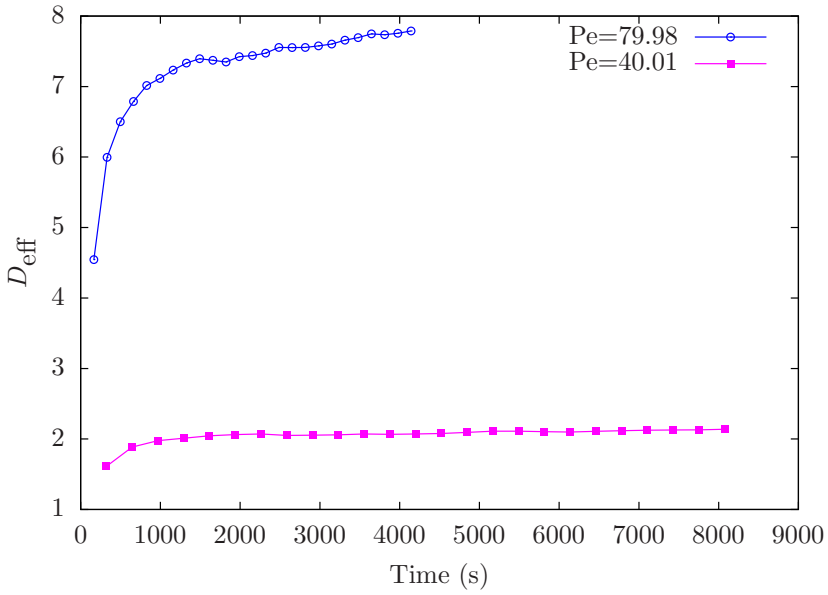

Figure. 7.7. Time variation of the dispersion coefficient ($D_{\text{eff}} = \sigma^2(t)/2t$) where convergence of the system towards the Taylor-Aris analytical solution (Equation 7.12) can be observed.

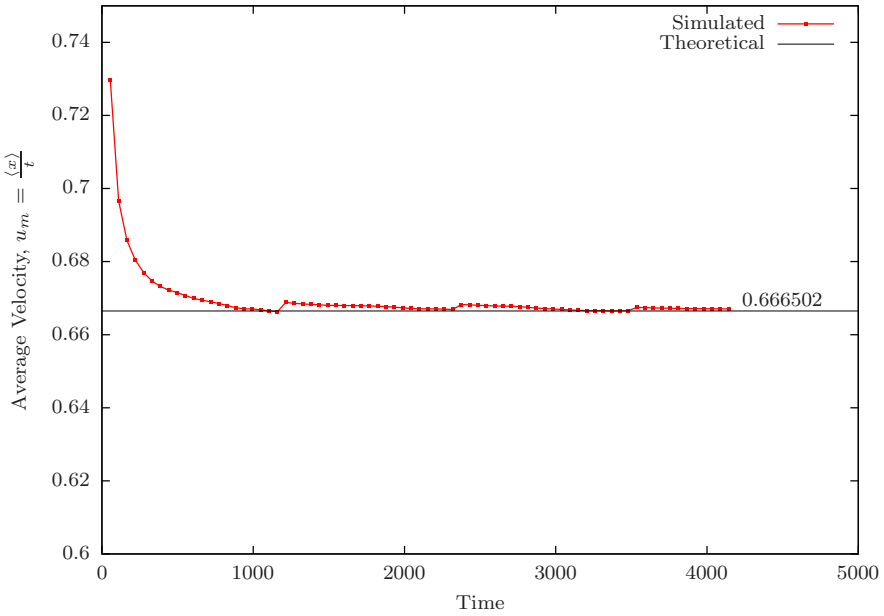

(a) Mean flow velocity = 0.6665, Pe = 79.98

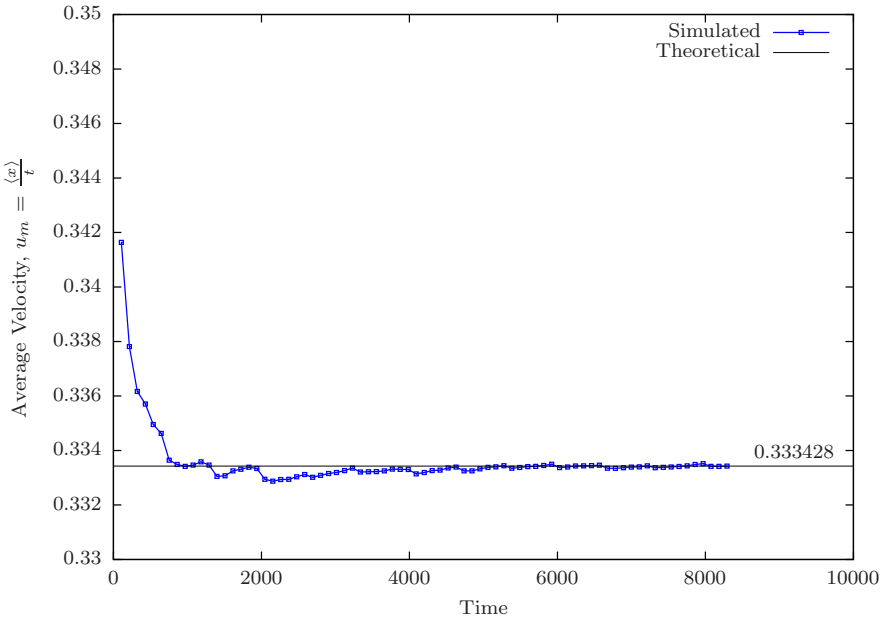

(b) Mean flow velocity = 0.3334, Pe = 40.01

Figure. 7.8. Average velocity of the centre of mass of the particle concentration. It can be seen that time variations of $\langle x \rangle / t$ converge towards the theoretical mean velocity given by Equation (7.4).

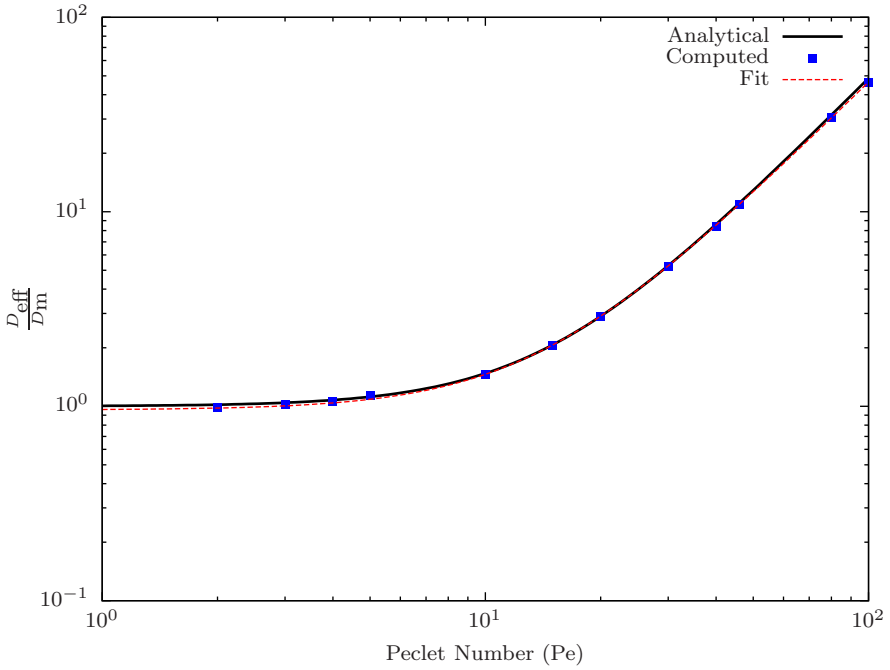

Figure. 7.9. Variation of the longitudinal dispersion coefficient D_{eff} with the Péclet Number for the Taylor-Aris dispersion. The simulated values and its fit are shown together with the analytical solution.

In this Chapter, we have applied our particle tracking code to the well known Taylor-Aris dispersion between two parallel plates in an attempt to verify and validate the code and found that the results are in good agreement with the theoretical predictions. The particle tracking implementation can now be used for more complex problems like simulation of dispersion in porous media.

8 Pore-scale Simulation of Dispersion

One of the most important transport processes that is responsible for spreading of solute particles in a porous medium is the hydrodynamic dispersion. Dispersion has high practical significance as it is an essential phenomenon in quantifying contaminant migration in soils and aquifers. Dispersion which is conceptually a simple process however has a complex macroscopic behaviour. Although dispersion coefficient D can be defined by $\sigma^2 = 2Dt$ where σ^2 is the variance of the solute position, breakthrough curves observed in numerous field and laboratory scale experiments typically exhibit long tails that cannot be explained using a fixed value of D (Bijeljic and Blunt 2006, Anwar *et al.* 2008). Solute particles must be transported through the porous medium for sufficiently long time so that a full sampling of complex flow field occurs before the dispersion coefficient can reach an asymptotic value and the spreading becomes a Gaussian. When these conditions are not met, solute particles undergo spreading in a non-Fickian manner and at this pre-asymptotic regime, the dispersion coefficient increases with time and distance travelled. This behaviour is known in literature in various names such as anomalous, non-Fickian, pre-asymptotic and non-Gaussian dispersion (Berkowitz *et al.* 2000, Delay *et al.* 2005, Salamon *et al.* 2006, Anwar *et al.* 2008). An illustration of concentration breakthrough curves exhibiting Gaussian and non-Gaussian behaviour is shown in Figure (8.1). This non-Fickian behaviour is mainly attributed to two generic mechanisms: the complex flow field and presence of mobile and immobile zones (Berkowitz *et al.* 2008). Berkowitz *et al.* (2006) reported that even in small scale homogeneous porous media, pore-scale disorder effects can lead to non-Fickian transport. Hence to understand and predict these non-Fickian or anomalous transport behaviours more fundamental approach is needed, which can provide useful insights into pore-scale effects.

8.1 Limitation of Advection-Dispersion Approach

Solute transport through natural porous media has generally been modelled by advection-dispersion equation (ADE) (see Section 2.4), which is based on the assumption of Fickian type dispersion. This basic assumption assumes that dispersion follows Fickian behaviour and hence breakthrough curves of solute input follow a Gaussian distribution and has been used widely for predicting and quantifying solute transport. However, many numerical and experimental studies have shown that solute spreading does not follow a

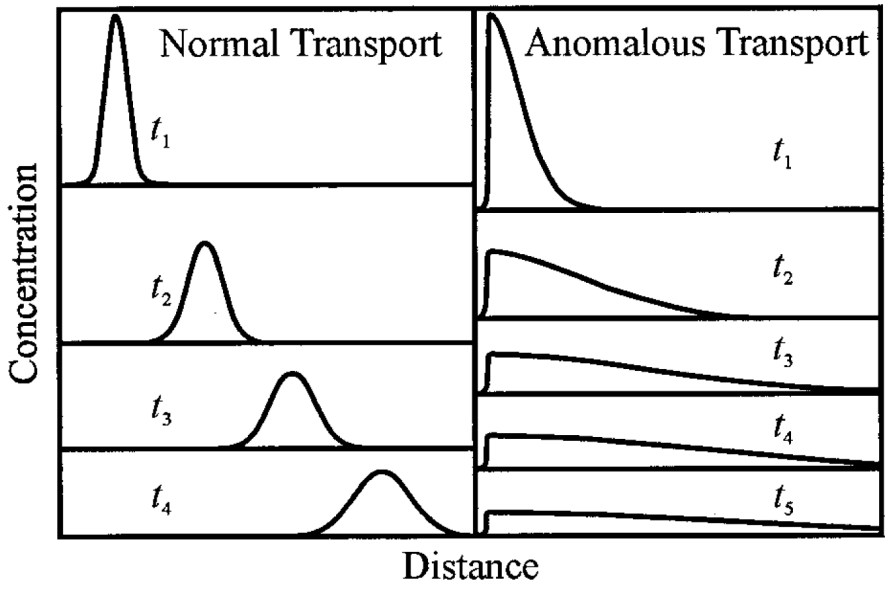

Figure. 8.1. Schematic illustration of concentration breakthrough curves exhibiting Gaussian and Non-Gaussian or Anomalous Transport (From Berkowitz *et al.* (2000)).

Gaussian distribution, i.e. solute spreads at rates different than that predicted by Fick's law. Consequently the concentration profiles obtained are highly skewed with heavy tails. Hence it is generally accepted that traditional advection-dispersion models can not predict the anomalous behaviours like sudden breakthrough and long tailing. The main reasons for the non-Fickian behaviour are thought to be the presence of heterogeneity at various scales and the trapping of solute particles in microscopic dead ends or stagnant pores. The variations in medium properties affect the velocity and path travelled by solute particles and consequently time of travel varies with heterogeneity of the medium. Since traditional models fail to describe non-Fickian behaviour, a more fundamental approach is required to understand and predict such anomalous transport behaviours. Furthermore when simulating macroscopic transport in a porous medium using the advection-dispersion equation, the parameters that quantify the solute dispersion are the longitudinal and transverse dispersion coefficients. From a continuum modelling perspective, which is the widely practised modelling approach, accurate values of these dispersion coefficients have to be used in the models to predict the results in a reliable way (for instance in risk assessment studies and remediation designs).

Despite numerous experimental and theoretical studies, still there is a lack of fundamental understanding of how pore structure controls dispersion and in particular behaviour of dispersion coefficients for various Péclet number regimes (Bijeljic and Blunt 2006). Pore-scale simulation is considered as a viable approach to study the basic mechanisms of solute transport at the pore level, which is essential for understanding the phenomenon of dispersion on a larger scales. Hence pore-scale modelling and simulation have became the preferred approach to quantify the influence of microscopic

properties on macroscopic behaviour. In this Chapter, pore-scale simulation of solute transport in porous media is presented and studied in detail.

8.2 Pore-scale Simulation of Transport

Many flow and transport phenomena are influenced by the pore scale characteristics and it is important to understand the processes at this scale to improve theory and models at larger scales. Although the only effective processes at the pore-scale are advection and molecular diffusion, the differential velocity distribution causes further mixing and spreading of concentration at the pore-scale. The parabolic velocity profile within the pores (creates velocity differences inside) and different pore sizes (cause mean velocities to differ from pore to pore) are the main reasons for such non-uniform velocity distribution (see Figure (2.5)). Since pore-scale velocity fluctuations and diffusion contribute to the hydrodynamic dispersion behaviours, numerical simulations that explicitly account for pore-scale properties can provide more information about macroscopic dispersion mechanisms. Furthermore, pore-scale simulations of flow and transport offer the possibility of modelling laboratory-scale experiments without averaging the properties of the porous medium. Hence modelling transport behaviour at the pore-scale is highly desirable.

In order to simulate the dispersion processes at the pore-scale, a velocity field within the pore space is required. This velocity field in turn is used for solving the advection-dispersion equation posed at the pore-scale either by Eulerian methods or by a random walk particle tracking method. However, as mentioned in the Chapter (3), one of the difficulties for pore-scale simulation is the presence of highly complex pore structure, which must be accounted when solving for pore-scale velocity field.

The most direct approach to model dispersion is to simulate transport directly on a three-dimensional representation of a porous medium (Bijeljic *et al.* 2004). Coelho *et al.* (1997) simulated dispersion through random packings of grains of arbitrary shape in which the flow field was computed numerically using finite difference method. Their study showed a good agreement with experiments in unconsolidated bead packs and sand for $Pe < 1000$. Maier *et al.* (2000) simulated dispersion in a 3D representation of a random pack of spheres. They were able to predict successfully the dispersion coefficient as a function of Péclet number in the range $1 < Pe < 5000$. Bijeljic *et al.* (2004) studied dispersion using pore-scale network simulation. Their model was able to quantitatively predict the asymptotic macroscopic dispersion coefficient over a broad range of Péclet numbers $0 < Pe < 10^5$. Further, Bijeljic and Blunt (2006) studied the complex macroscopic behaviour of dispersion in porous media as a function of Péclet number using a continuous time random walk (CTRW) approach for simulating transport. Several numerical methods have been used for pore-scale simulation of flow

(solving Stokes or Navier-Stokes equations). Magnico (2003) used a collocated finite volume approach to solve Navier-Stokes equations in 3D to study hydrodynamic and transport properties of packed beds in sphere packing. Martys *et al.* (1994) used a finite difference method to solve Stokes equation through random packings of non-overlapping and overlapping spheres while studying the permeability of different classes of random three-dimensional porous media via direct numerical simulation of Stokes flow. The Lattice-Boltzmann method has been used by several authors (Maier *et al.* 1998; 2000; 2002) for computing flow field at the pore-scale. Inamuro *et al.* (1999) carried out direct Navier-Stokes simulations using LBM in a three dimensional porous structure for high Reynolds numbers as well as for low Reynolds numbers. The porous structure consists of spherical bodies in a rectangular domain. Manwart *et al.* (2002) used both finite difference and Lattice-Boltzmann approaches for determining the permeabilities of porous media samples by solving the Stokes equations on the pore spaces of the samples.

In addition to numerical studies, various experimental techniques also have been applied to investigate the flow and transport in porous media. For example, we mention the work of Stöhr (2003) where a transparent porous medium with refractive index matching fluids and solids was used to study the dispersion of a tracer dye. A planar laser-induced fluorescence (PLIF) technique with higher spatial and temporal resolution was used to visualise and measure the 3D pore-scale flow and transport.

In this study, a new approach recently introduced by Engwer and Bastian (2005) is used for obtaining the microscopic flow field in the pore spaces of a porous medium. This is a direct numerical simulation approach in which the partial differential equations describing the flow through the pore-spaces are directly discretised and solved to obtain the velocity field. Subsequently a Lagrangian particle tracking method is used for the simulation of transport. The following Section gives the details of our approach.

8.2.1 Present Approach

We have learnt that solute transport at the macroscopic scale is the result of several physical processes such as advection, diffusion, boundary layer and holdup dispersion etc. acting at the pore-scale as described in the Section (2.3). Hence the macroscopic dispersion tensor can be related to pore-structure and pore-scale properties by solving problems at the pore-scale. In the present work, the solute transport processes are studied by simulating flow and transport at the pore-scale where the temporal evolution of the solute concentration $C(x,t)$ through a porous medium is obtained by solving advection-dispersion equation at the pore-scale subjected to a pore-scale velocity field given by the Stokes equation. The following steps are involved:

Pore-scale Flow Computation: The spatial distribution of fluid velocities within pore spaces is needed in order to solve the advection-diffusion equation at the pore-

scale. The Stokes equations, which represent the slow, laminar and incompressible flow of a fluid in a porous medium are solved to obtain the stationary velocity field. The UDG method is used to find the solution of the Stokes problem in the complex pore geometries.

Simulation of Transport: Transport is simulated by random walk particle tracking, where advection and diffusion is applied at the pore-scale. Particles are introduced into the computed Stokes velocity field and transported by advection and diffusion. The solute particles are followed through the pore-spaces and their positions are noted. Within each computational cell, particle velocities are obtained directly from the DG Stokes solution. At the free outflow boundary, particles are allowed to naturally flow out of the domain. The hydrodynamic dispersion coefficients are calculated from the particle distribution by method of moments.

8.3 Results of Two-Dimensional Simulations

In this Section, results of pore-scale simulation of transport carried out in a simple two-dimensional porous medium are presented. The 2D porous medium considered consists of a rectangular domain with randomly placed circular obstacles used in the work of Fahlke (2008) where he simulated transport at the pore-scale using a discontinuous Galerkin discretisation of the advection-dispersion equation. He had used the Stokes implementation described in this thesis together with unfitted discontinuous Galerkin approach to obtain the pore-scale velocity field. He obtained the concentration breakthrough curves and they showed non-Gaussian behaviour.

The two-dimensional setup consisted of a rectangular domain of 1.5×1.0 units with circular obstacles of radii 0.1 unit each. These obstacles were placed such that there is a small offset in the left side, which is free of internal obstacles (see Figure (8.2)). The flow is driven from left to right by an imposed pressure difference in that direction. The no-slip condition was applied on all internal obstacles and on the top and bottom sides of the domain. For the transport, no-flux condition was given on the surfaces of the obstacles and on the top and bottom sides. A rectangular solute pulse of size 0.25×0.5 with unit initial concentration as shown in Figure (8.2(a)) was used. The value of molecular diffusion coefficient is chosen as 0.001. Transport was simulated using a total number of 50000 particles. The computed Stokes velocity field and streamlines are shown in Figure (8.3). The concentration snap shots from the simulation are shown in Figure (8.4) together with the snap shots from Fahlke (2008) for comparison. We have observed that even after the main pulse has passed, there are concentrations trapped in some regions especially around the obstacles and low velocity region, which contribute to the observed tailing in the breakthrough curve. Figure (8.5) shows the distribution of solute particles for different Pe and clearly shows the spreading behaviour as the Pe is

changed. We can observe more mixing at low Pe and less mixing when Pe increases. In Figure (8.6) the concentration breakthrough curve plotted for different number of particles are shown and compared with breakthrough curve obtained by Fahlke (2008).

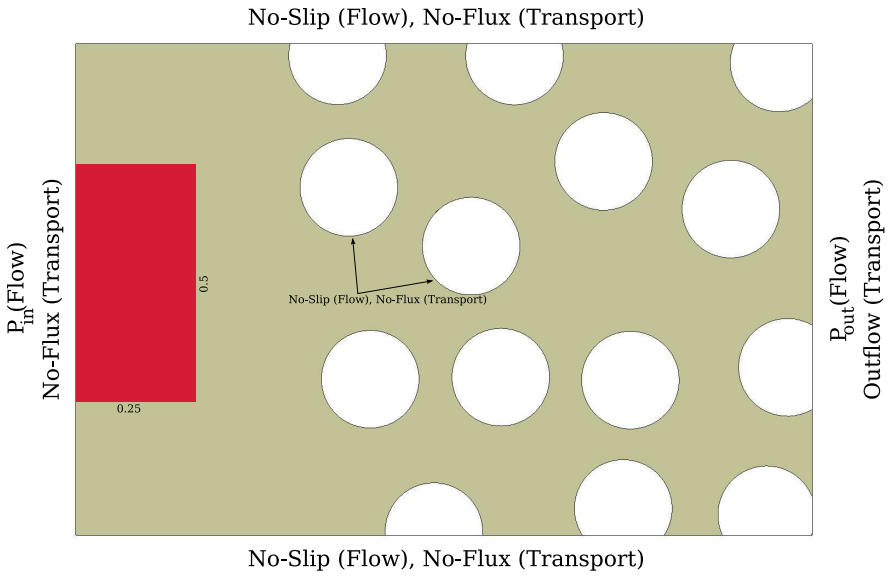

(a) Problem geometry with boundary conditions

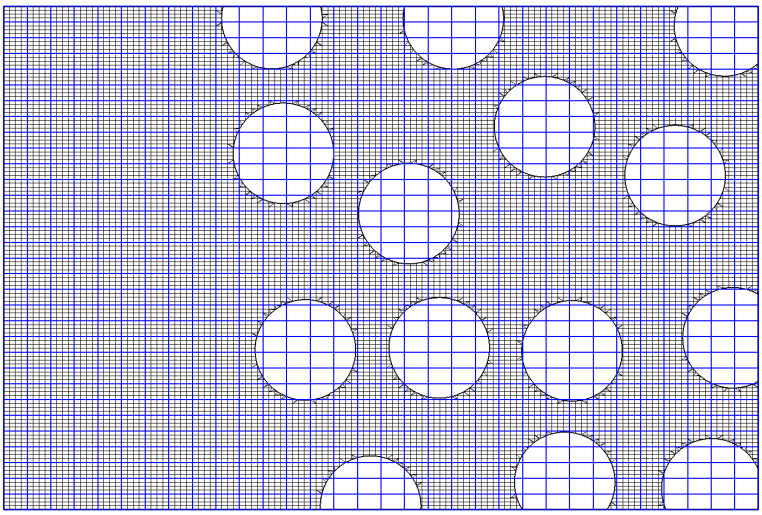

(b) Geometry with triangulation: Simulation grid is shown in blue and geometry grid is in black

Figure. 8.2. [Two-dimensional porous medium geometry and triangulation. The problem setup consists of a rectangular domain of 1.5 x 1.0 units with obstacles of circular discs of radii 0.1 unit each. These circular obstacles were placed such that there is a small offset near the inlet (left side), which is free of internal obstacles. The flow is driven from left to right by an imposed pressure difference.

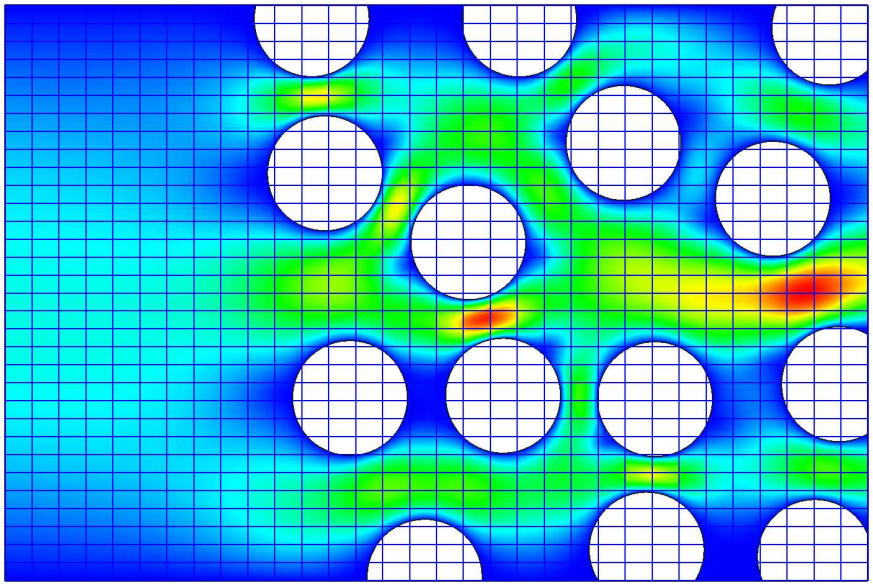

(a) Pore-scale velocity field

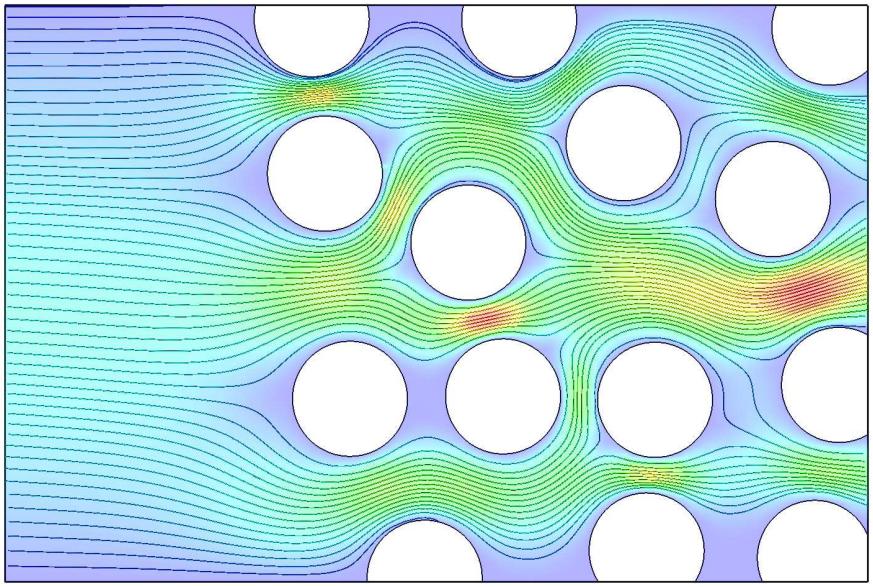

(b) Streamlines

Figure. 8.3. Pore-scale velocity field and streamlines for the two dimensional problem. Red colour shows high velocity and blue represents low velocity region. Low velocity regions around the obstacles and boundary layers are assumed to contribute to anomalous dispersion behaviour.

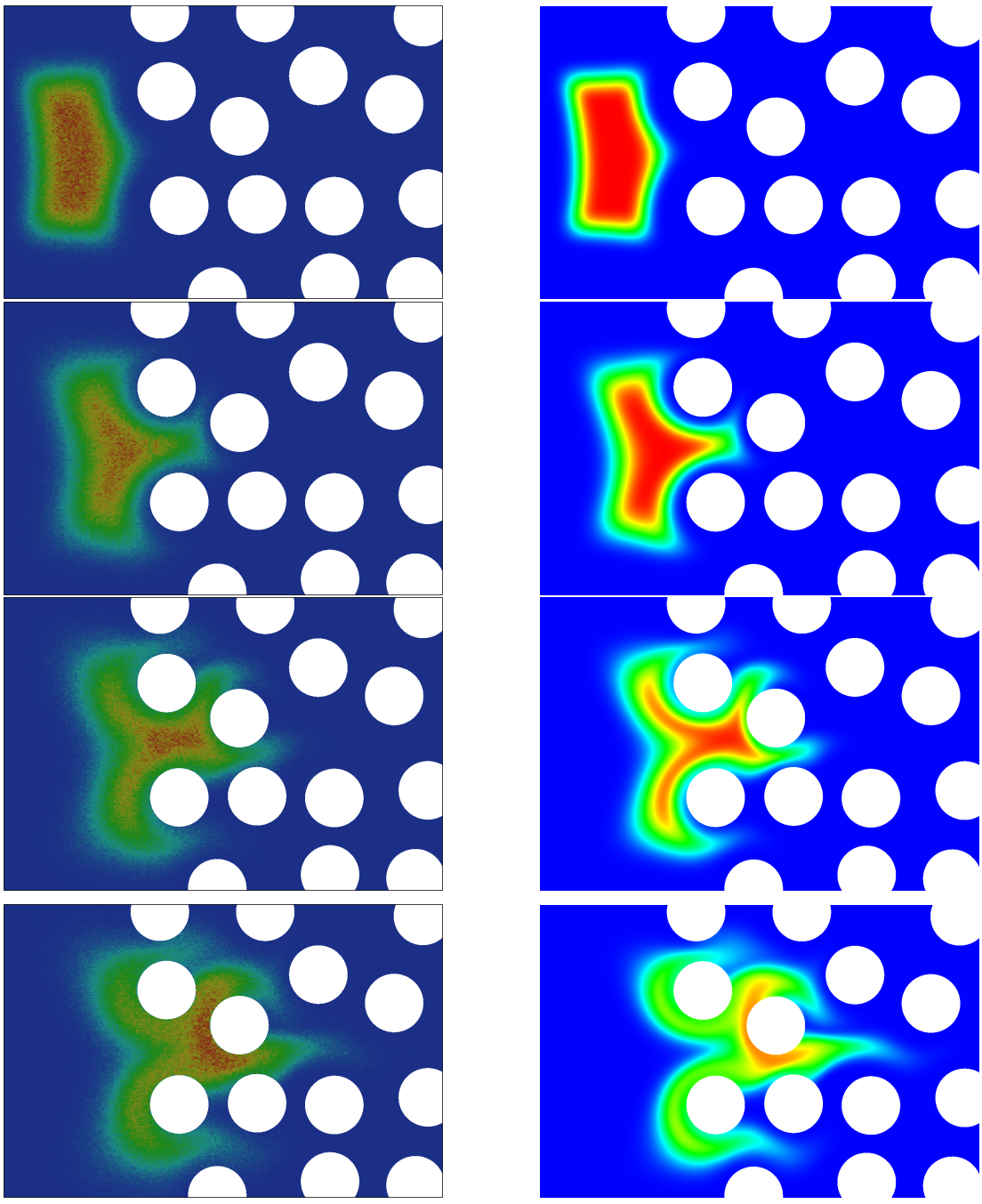

(a) Results from RWPT simulation

(b) Result from DG simulation (Fahlke 2008)

Figure. 8.4. Snap shots of solute concentration profiles for in a 2D irregular packing. The discrete nature of the concentration profile is typical to particle based methods. In this case, the transport is simulated with 100,000 particles. Concentration profiles obtained by an Eulerian method (DG FEM) by Fahlke (2008) are shown for comparison.

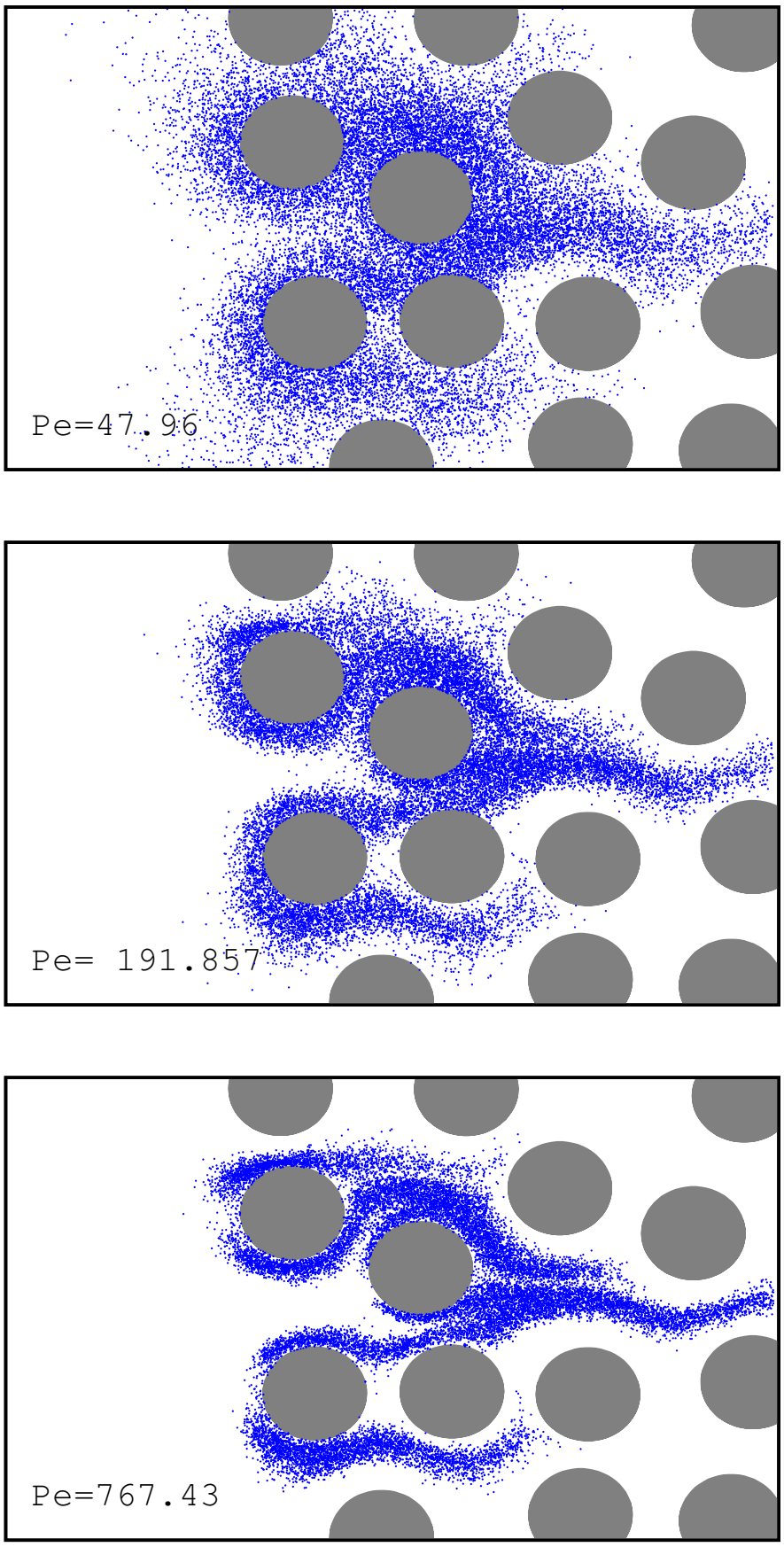

Figure. 8.5. Concentration snap shots during the evolution of a solute pulse for different Pe in a 2D irregular packing showing the effect of Pe on dispersion (spreading) behaviour. We can observe more mixing at low Pe and less mixing when Pe increases.

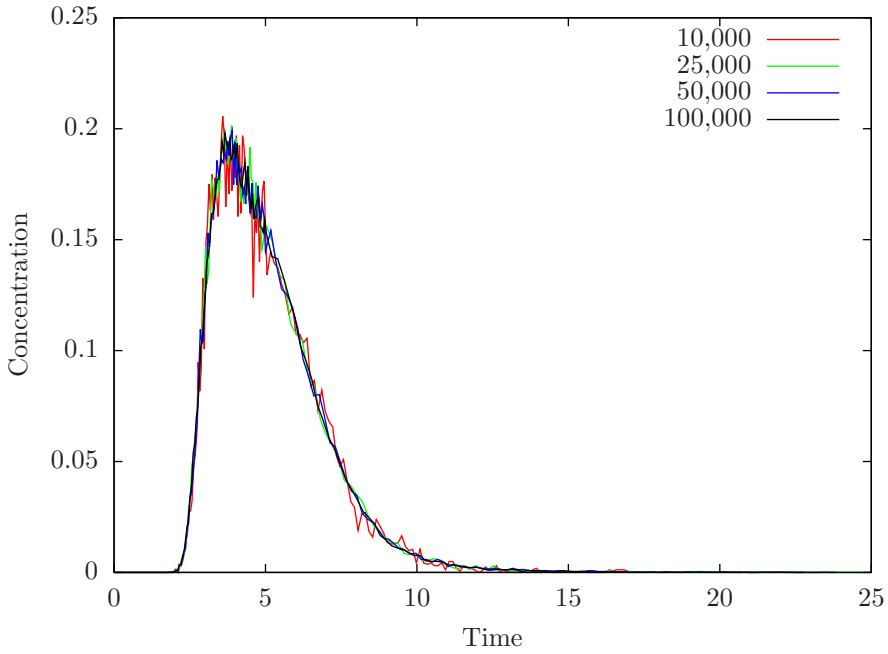

(a) Breakthrough curve plotted for different number of solute particles

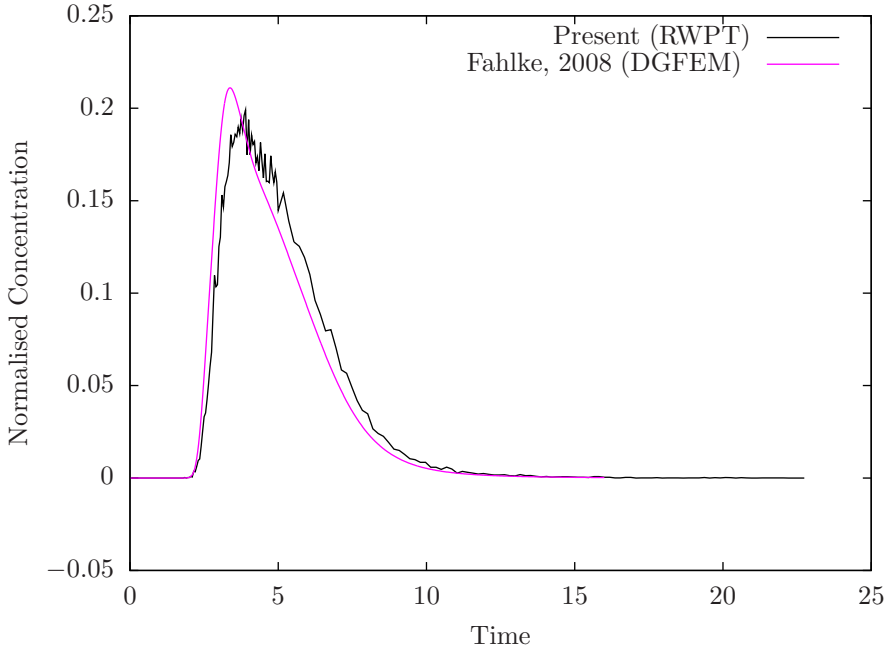

(b) Breakthrough curve compared with that of Fahlke (2008)

Figure. 8.6. Breakthrough curve obtained for a solute slug in an irregular packing in 2D. The curve is non-Gaussian because of the pore-scale heterogeneity, boundary layer and hold up dispersion effects acting at pore-scale.

8.4 Results of Three-Dimensional Simulations

In this Section, the transport behaviours in three dimensional artificial porous media made using randomly packed spheres are studied. Detailed flow simulations in such model porous media are carried out using the Unfitted discontinuous Galerkin method (UDG) described in Section (6.5.1) to obtain the 3D pore-scale velocity field and it is subsequently used as input to the Lagrangian random walk method for investigations of the transport behaviour.

8.4.1 3D Flow Simulation

In Figure (8.7) we show an artificial porous medium made using 500 spheres of uniform size (diameter =0.12407) randomly packed in to a cubic domain. In the simulation, a domain of size $1.2 \times 1 \times 1$ with an offset of 0.15 near the inlet is taken. The offset which is free of obstacles near the inlet is taken to stabilise the flow before entering into the porous medium. The porosity of the artificial porous medium is 0.503899. The flow was forced from left to right with a pressure drop boundary condition. The 3D calculations are carried out on a computational grid with 262144 elements obtained by globally refining the grid up to a level of 6 and is shown in the Figure (8.7(b)). With a quadratic velocity and linear pressure basis function, the DG Stokes system in 3D has 34 degrees of freedom (dof) in each element and hence a total of 8912896 dofs in the computation.

The computations were performed on machines available at IWR, University of Heidelberg with following configurations:

1. 4 x Dual Core Opteron 8222 3.0 GHz, 128 GB RAM
2. 4 x Quad Xeon 2.4 GHz, 128 GB RAM

The assembling of the stiffness matrix took about 4.8 hrs. The Bi-Conjugate Gradient Stabilised (BiCGSTAB) solver with ILU preconditioner was used for solving the linear system and took about 11.2 hrs. Hence approx. 16 hrs for a complete flow simulation.

The local velocity field in three axial planes is shown in Figure (8.8(a)) where one can clearly observe the non-uniform velocity variations within the planes, which are due to the random geometric arrangement of the spheres. Within the grains and on surface, the velocity is zero whereas inside the pores, velocity vary many order of magnitudes. A close-up view of the local velocity field is shown in the Figure (8.8(c)).

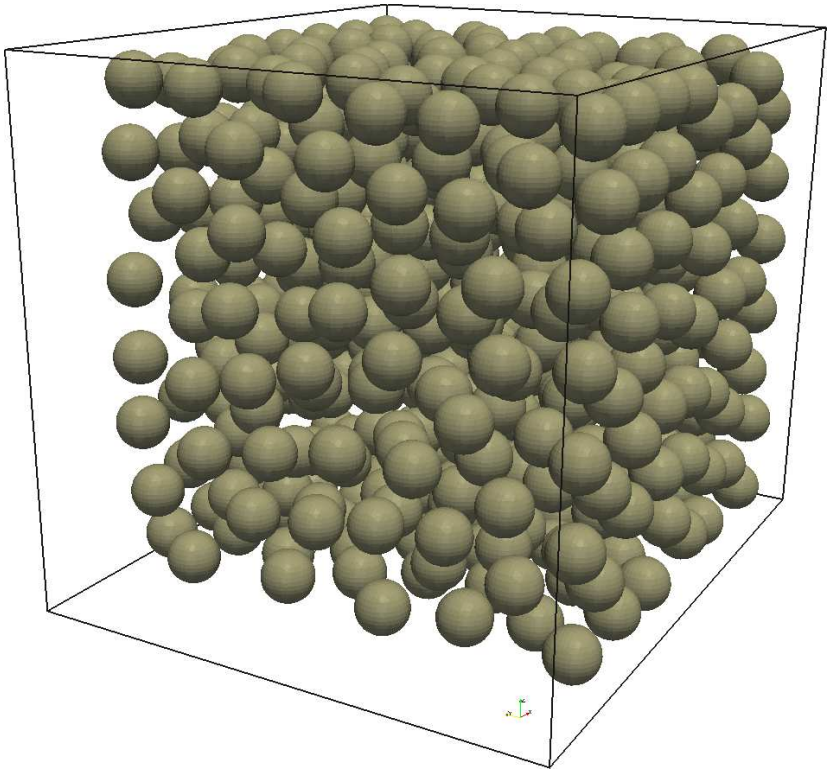

(a) Geometry of the artificial porous medium

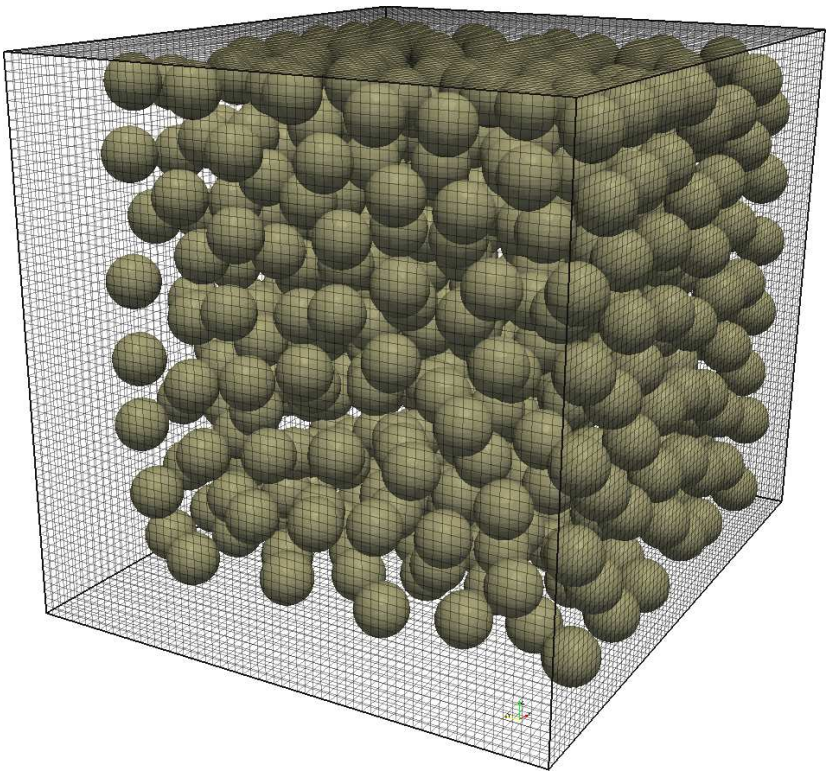

(b) The computational grid used for simulating Stokes flow

Figure. 8.7. Geometry of randomly packed spheres in a cubic domain. The porous medium was generated by packing 500 spheres of uniform size in a cubic domain with slight offset at the inlet to stabilise the flow. The spheres represent solid grains of the porous medium. Grid with 262144 elements are used for the computation.

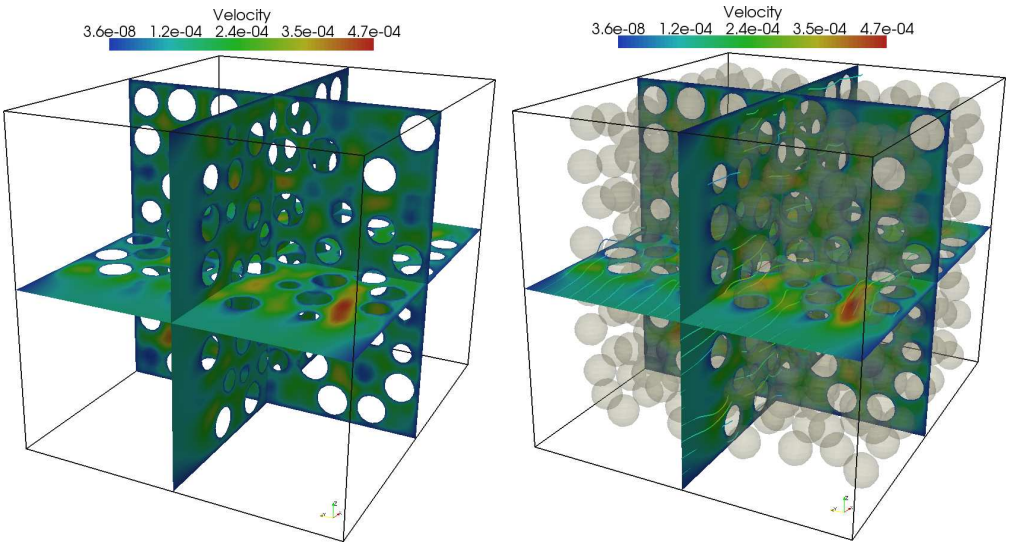

(a) Local velocity field in three axial planes of a random sphere packing

(b) Streamlines of the flow field

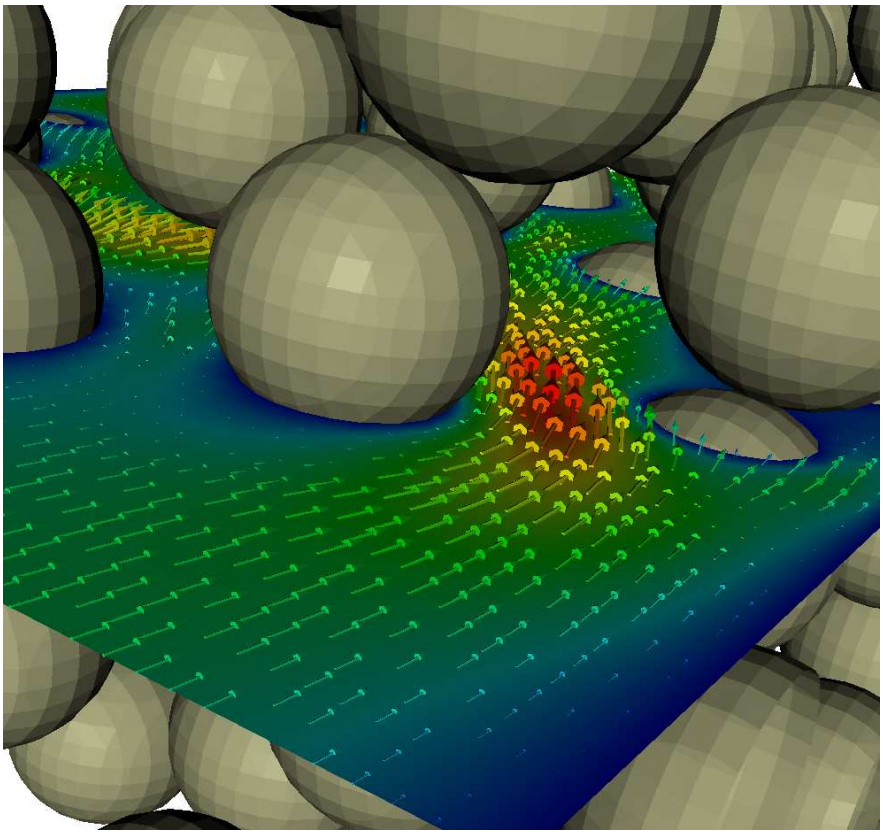

(c) Close-up view of computed velocity field through random sphere packing. Velocity vectors are shown in a 2D plane parallel to main flow direction. The red indicates high velocity and blue for very low velocity region.

Figure. 8.8. Computed pore-scale flow field through the random sphere packing medium and a close-up view of the velocity field. The pore-scale velocity field was computed by solving Stokes equation using UDG method.

8.4.2 3D Transport Simulation

Using the results of the flow field simulation presented in Section (8.4.1), the simulation of solute transport through the medium was performed using the random-walk particle tracking method. In Figure (8.9) we show the effect of diffusion by plotting the trajectories of particles from a point source. The thick black trajectory corresponds to the streamline when diffusion is absent. The coloured lines corresponds to the case when diffusion is present. We can see that in the presence of diffusion two particles released from the same initial location follow different paths. If only advection is considered, two particles at the same initial location will follow the same path as they just follow the same stream lines. The Figure (8.10) shows the temporal evolution of concentration

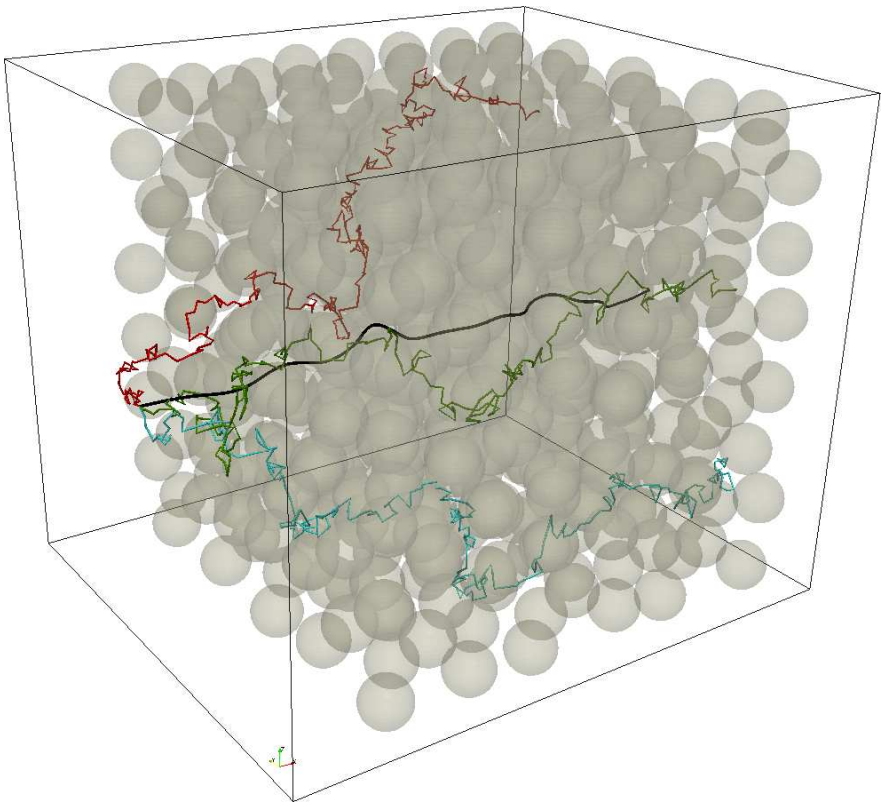

Figure. 8.9. Advective and dispersive particle trajectories through the sphere packing. The thick black line corresponds to the trajectory when diffusion is absent. In this case, when only advection is considered particles released from the same point just follow the same stream lines. On the other hand, when diffusion is present, movement of the particles is affected by the random component and two particles at the same initial location will most likely follow different paths. The coloured lines corresponds to the particle paths when diffusion is present.

at various sections along the main flow direction. The presence of low velocity regions around the spheres cause slower decay of the solute concentration even after the main pulse has passed because solute particles can enter and leave these region only by diffusion. It clearly shows the influence of pore structure on the transport behaviour.

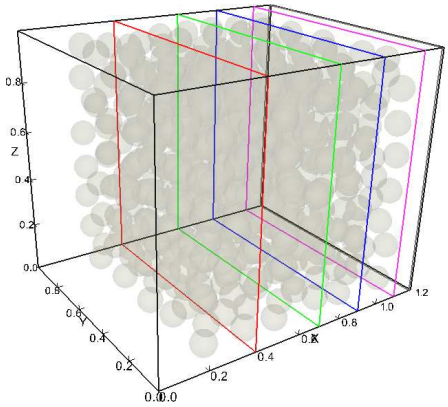

(a) Different sections in the porous medium along the flow direction where concentration profiles are computed.

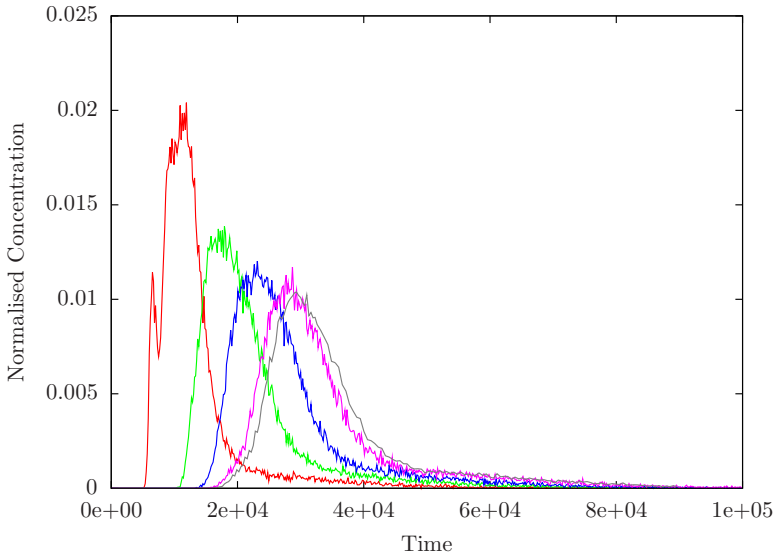

(b) Pe=309.3, D_m=1e-8

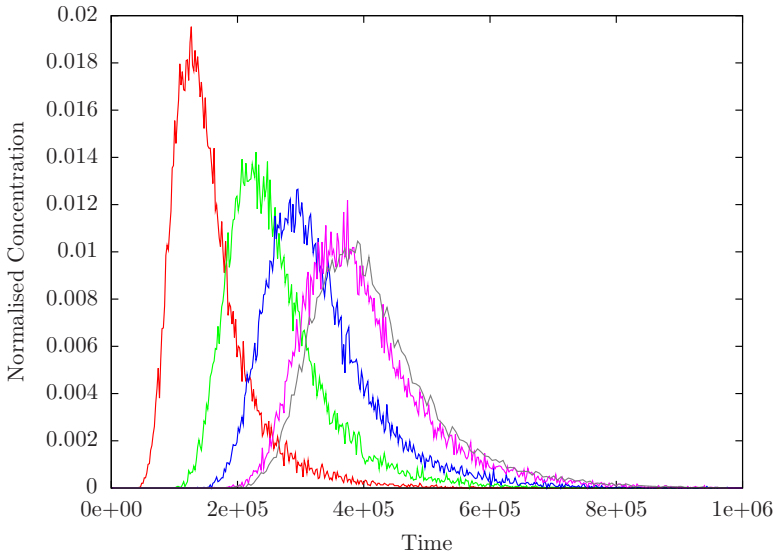

(c) Pe=25.67, D_m=1e-8

Figure. 8.10. Solute concentration profiles computed at different sections shown in Figure (8.10(a)). The presence of low velocity regions around the spheres cause slower decay of the solute concentration even after the main pulse has passed because solute particles can enter and leave these region only by diffusion. The observed tails in the concentration profiles are result of such boundary layer and hold up dispersion behaviour acting at the pore-scale.

8.4.3 Dispersion Coefficients: Comparison With Literature Data

In Section (2.5), the dependence of dispersion coefficients on Péclet number was described in detail. The asymptotic values of dispersion coefficients found to depend on various mechanisms such as molecular diffusion, mechanical dispersion, boundary layer and hold up dispersion. According to the contribution of these mechanisms on the dispersion behaviour, researchers categorised the dispersion into different Pe regimes. A standard way of describing longitudinal dispersion coefficient as a function of Pe in the laminar flow condition is by using Equation (2.35) and is recalled here:

$$\frac{D_L}{D_m} = \frac{1}{F\phi} + \alpha Pe + \beta Pe^{\delta} + \gamma Pe^2$$

In this Section, hydrodynamic dispersion coefficients obtained from the pore-scale simulation are compared with numerical and experimental results from literature. It should be noted that comparisons between simulation and experiment are complicated because of the difficulty of reproducing the exact geometry of the experimental porous medium in a simulation. In literature, the dispersion data are most frequently presented in logarithmic plots of D_L/D_m and D_T/D_m versus Pe and this custom is followed here too.

In order to determine the dependence of dispersion coefficients on the Péclet number, number of simulations were carried out by varying mean flow velocity and keeping D_m fixed, thereby changing the Pe. A value of D_m=1e-8 has been taken through out the simulations. The simulation results for longitudinal dispersion as a function of Péclet number are plotted in Figure (8.11) together with previously reported numerical and experimental results. The data are plotted as longitudinal dispersion coefficient divided by the molecular diffusion coefficient (D_L/D_m) versus Péclet number where Péclet number was defined with the mean fluid velocity and a characteristic length. The characteristic length for the artificial porous medium considered in this work is taken as the size (diameter) of the spheres. The data from our simulations are plotted together with the experimental results of Pfannkuch (1963), Seymour and Callaghan (1997), Kandhai *et al.* (2002), Khrapitchev and Callaghan (2003) and Stöhr (2003) and numerical results of Maier *et al.* (2000), Freund *et al.* (2005) and Bijeljic *et al.* (2004). As we can see results are in very good agreement over the range of Pe studied. We can observe from the graph (8.11) that at low Péclet number regime, molecular diffusion is the main mechanism causing dispersion. In this regime, the ratio D_L/D_m is close to unity. At higher Pe, ($3 < Pe < 300$) advection starts to have much more pronounced contribution to dispersive mixing. In this regime, even though the particles are moving faster, they still have time to sample low velocity region near obstacles. Here the spreading is caused by the interplay of mechanical dispersion and molecular diffusion. A power law relationship of the form given by Equation (2.31) is often used to describe dispersion in this regime. Power law exponent $\delta \approx 1.2$ is generally found in the

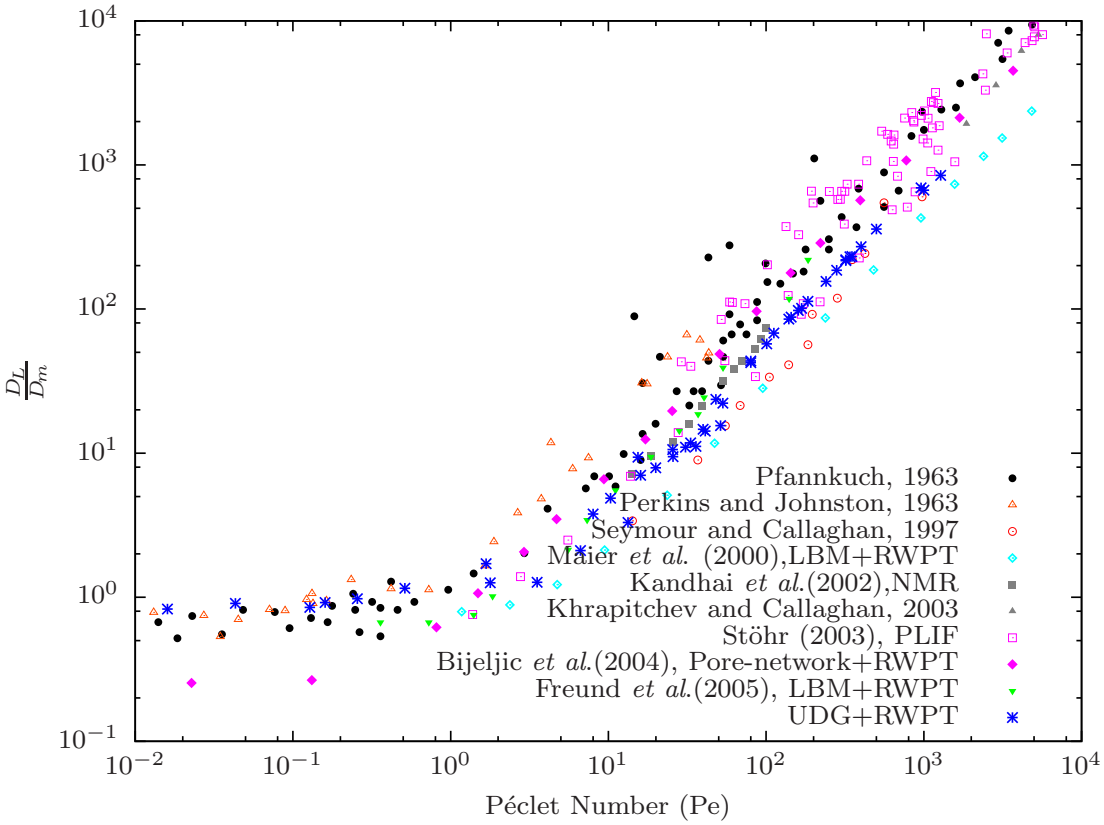

Figure. 8.11. Longitudinal dispersion coefficients in a random sphere packing from the pore-scale simulation compared to data reported in literature. The increase of longitudinal dispersion with Pe can be observed showing that the dispersion coefficient tends to the molecular diffusion coefficient for small velocities and becomes proportional to Pe at higher velocities. The pore-scale simulation results (UDG+RWPT) are compared with (1) experimental data on unconsolidated bead packs by Pfannkuch (1963) (2) data obtained by magnetic resonance imaging by Seymour and Callaghan (1997), Kandhai *et al.* (2002) and Khrapitchev and Callaghan (2003) (3) results obtained by planar laser induced fluorescence method by Stöhr (2003) (4) data obtained on random packing of spheres in a tubular container by Lattice-Boltzmann and particle tracking by Maier *et al.* (2000) and Freund *et al.* (2005) (5) results by Bijeljic *et al.* (2004) obtained using pore-network simulations.

literature. The best fit (see Figure (8.12)) of our results to Equation (2.31) in the regime $3 < Pe < 300$ is with $\beta = 0.214$ and power law coefficient $\delta = 1.203$. In Table (8.1), value of β and δ found in this work by pore-scale simulation is listed together with values from literature for comparison. The value of δ found by our pore-scale simulation agree well with that of Freund *et al.* (2005), Bijeljic *et al.* (2004) and Stöhr (2003).

In the mechanical dispersion regime ($Pe > 300$), a linear relation between dispersion coefficient and Pe is assumed. This is mostly advective dominated dispersion regime in which molecular diffusion effects are negligible because the particles are moving faster and their response to molecular diffusion have nearly no effect. Consequently for large Péclet number, we get a linear dependence of dimensionless dispersion coefficient on pore scale Pe. However, it should be noted that the particles once trapped in stagnant

zones and dead end pores can escape to main flow by diffusion only. Although this is very slow process compared to strong advective transport, holding of particles might occur in such conditions. Hence at moderately high Pe, diffusion is important and should not be neglected.

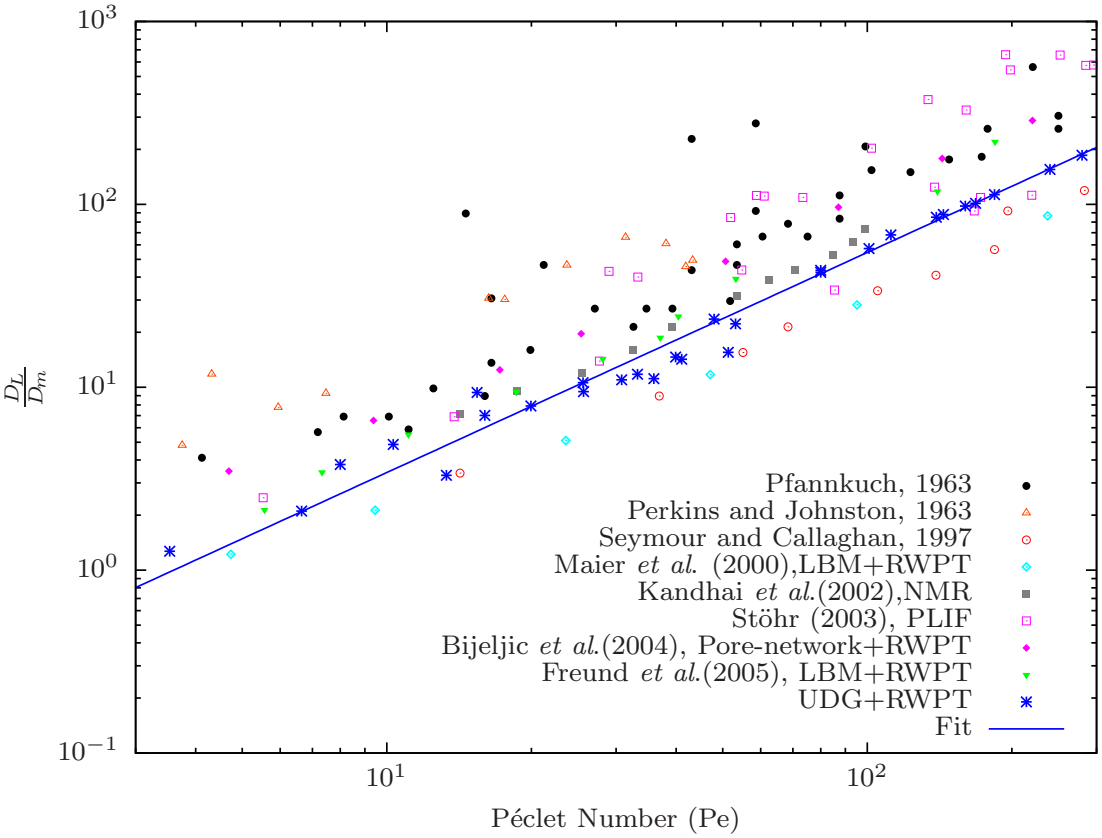

Figure. 8.12. Simulated longitudinal dispersion coefficients in a random sphere packing compared to data reported in literature in the power law regime ($3 < Pe < 300$). The line corresponds to the fit of the data to $\frac{D_L}{D_m} = \beta Pe^{\delta}$ with β=0.214003 and δ=1.20331.

Reference	β	δ
Pfannkuch (1963)	-	1.2
Gist *et al.* (1990)	0.46 – 3.9	0.93 –1.2
Dullien (1992)	-	1.2
Coelho *et al.* (1997)	0.26	1.29
Manz *et al.* (1999)	-	1.12
Stöhr (2003)	0.77	1.18
Bijeljic *et al.* (2004)	0.45	1.19
Freund *et al.* (2005)	0.303	1.21
This work	0.214	1.2033

Table 8.1. Comparison of the power law coefficient δ obtained by fitting data to Equation (2.31) with previously reported values.

A least squares fit of the longitudinal dispersion coefficient data to the Equation (2.35) for the full range of Péclet number studied is shown in Figure (8.13). The values of the parameters obtained are $\tau = \frac{1}{F\phi}$=0.79, β= 0.214, δ=1.203 and γ=1.241e-5. The value of γ which accounts for the hold up dispersion differs from Stöhr (2003) (3.0e-5) and Kandhai *et al.* (2002) (1.7e-3) most probably due to difference in the arrangement of grains in the porous medium. Maier *et al.* (2000), Bijeljic *et al.* (2004) and Freund *et al.* (2005) did not consider the effect of hold-up dispersion.

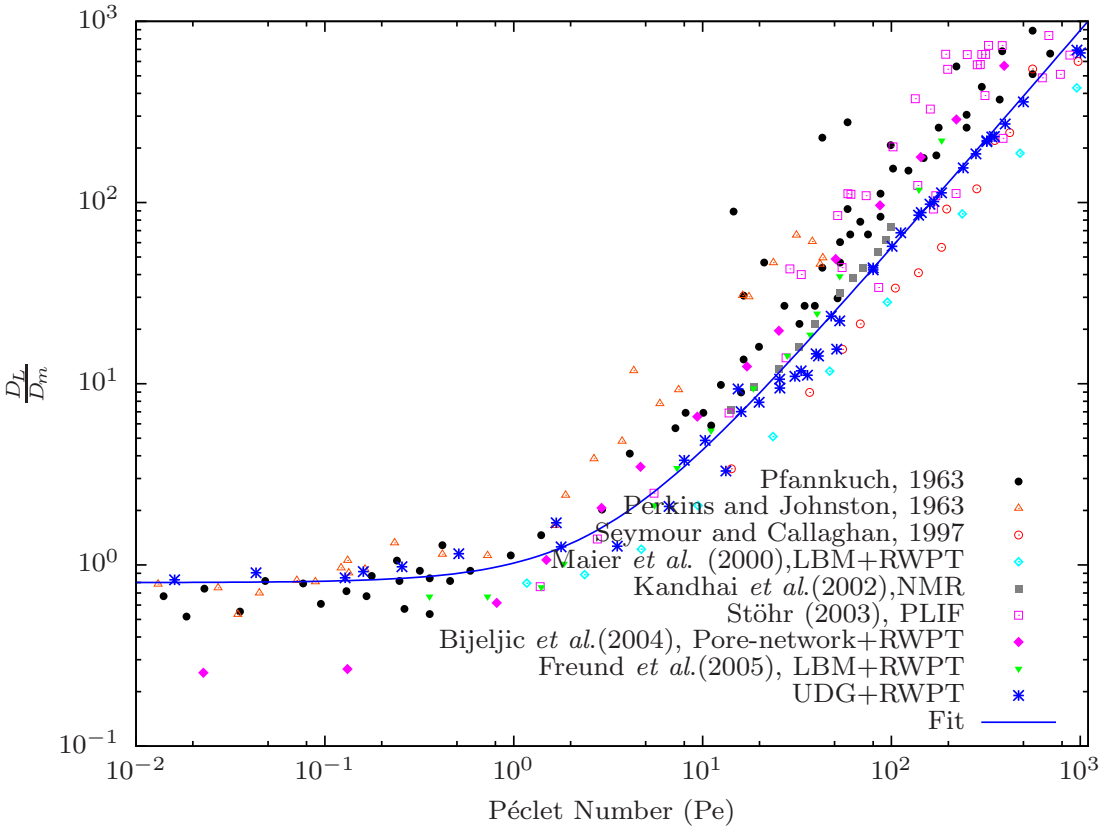

Figure. 8.13. Least squares fit of the simulated longitudinal dispersion coefficients to Equation (2.35) in a random sphere packing. The values of the parameters obtained by fitting are $\tau = \frac{1}{F\phi}$=0.79, β= 0.214, δ=1.203 and γ=1.241e-5.

Next we considered the transverse dispersion behaviour with Péclet number. The transverse dispersion causes spreading of the solute plume in the direction perpendicular to the direction of flow. It is considered important in solute transport as transverse mixing contribute to lateral spreading and smoothing of solute concentration in porous media. Although its effects are smaller compared to longitudinal dispersion, several studies have demonstrated its effects on overall solute dispersion behaviour and mentioned that the knowledge of transverse dispersion is essential in accurate prediction of solute transport behaviour. The dependence of D_T on Pe is still not understood clearly as evident from the large deviations in the experimental and numerical results (Sahimi

1993, Maier *et al.* 2000, Bruderer and Bernabé 2001, Freund *et al.* 2005, Bijeljic and Blunt 2007).

The Figure (8.14) shows the variation of transverse dispersion coefficients with Pe. As we can see, although the data for transverse dispersion coefficients are more scattered, it captures the trend and as expected increases with increase in Pe. However, in the power law regime, the best fit for the data yields a power law coefficient $\delta \approx 0.3$ which is lower than the experimental results (0.9 by Sahimi (1993) and 0.87 by Stöhr (2003)). Our data is more in the range of that predicted by Maier *et al.* (2000). It should be noted that even a value as low as 0.2 was suggested by Bruderer and Bernabé (2001) from their work on transverse dispersion in heterogeneous network and mentioned that the experimental results usually over estimate the transverse dispersion. Comparing D_L and D_T, we can confirm that the values of D_T in all Pe ranges are always lower than D_L.

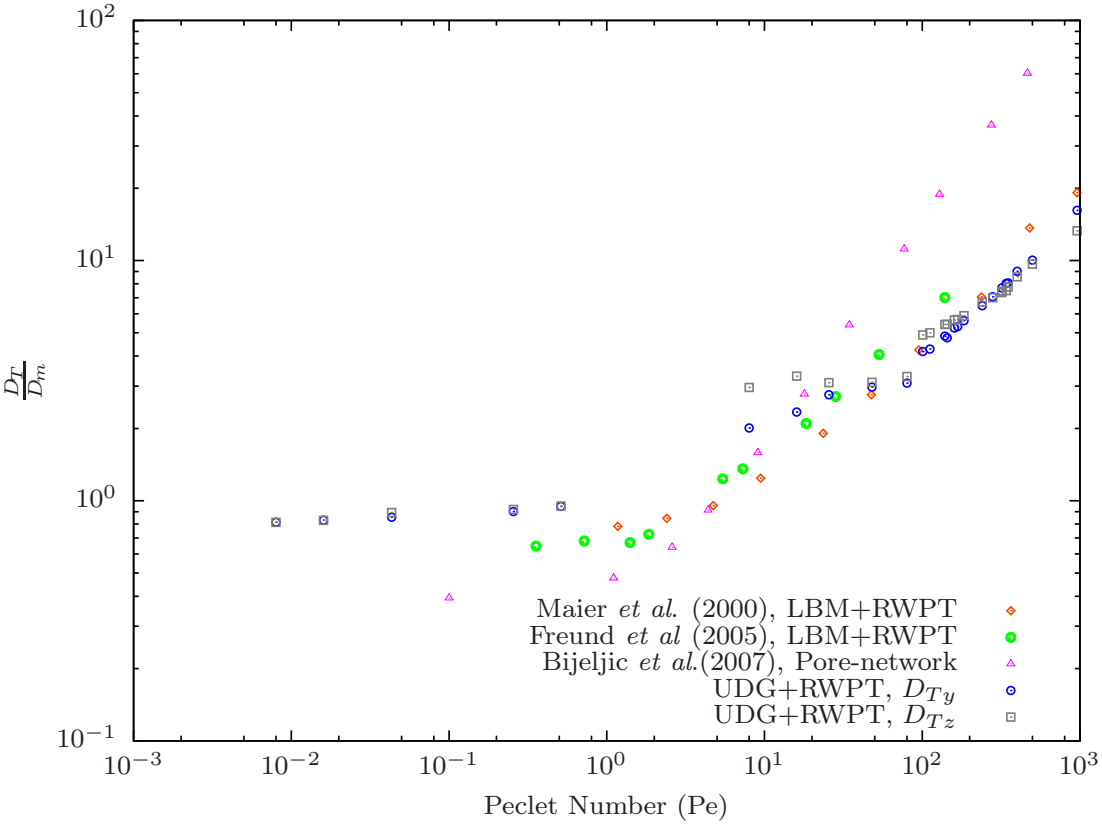

Figure. 8.14. Simulated transverse dispersion coefficients in a random sphere packing compared to data reported in literature. Even though the data is more scattered, it captures the trend of variation. In the power law regime, data is more in close to that of Maier *et al.* (2000). The predicted power law coefficient $\delta \approx 0.3$ is lower than the experimentally found values. It should be noted that even a low value of 0.2 has been suggested by Bruderer and Bernabé (2001).

In this Chapter, pore-scale simulations of flow and transport in porous media in which the pore spaces and geometries are explicitly accounted were used to demonstrate links

between microscopic and macroscopic phenomena. Using UDG, the Stokes equation which governs the slow flow in porous media was solved to obtain the detailed 3D pore-scale flow field, which was characterised by uneven velocity distribution due to the random arrangements of impermeable spheres. Using the results of the flow field simulation, transport of non-reactive solute particles was simulated by a random-walk particle tracking approach to obtain the 3D concentration field. From the 3D concentration field (particle distribution in particle based methods), we have estimated longitudinal and transverse dispersion coefficients. In this way, we have studied the influence of pore-scale properties on large-scale behaviour in which macroscopic properties are estimated from pore-scale numerical simulations. Further, a study was carried out for a range of Pe to know the relationship between Pe and dispersion coefficients. The longitudinal and transverse dispersion coefficients have been computed for different Péclet numbers in random sphere packing and results were compared to various experimental and numerical results from literature. In the boundary layer regime ($3 < Pe < 300$), a power law dependence of D_L on Pe is confirmed with power law coefficient δ=1.203. It is observed that pore-scale heterogeneity and the low velocity regions near the grains of the porous medium (spheres) give rise to anomalous or non-Fickian dispersion. This happens when a solute particle in the boundary layer near the solid grains cannot move due to convection. Diffusion is required to be able to get out of the boundary layer. Therefore, diffusion even though small in magnitude, influences the dispersion behaviour at moderate Pe. The comparison between the pore-scale simulation results and results from literature show that pore-scale simulation is able to predict the dispersion coefficient for a wide range of Pe. It is shown that the approach chosen here for the pore-scale simulation of flow and transport in random sphere packing works very well and can be used for the determination of dispersion coefficients in more realistic porous media.

9 Summary and Conclusions

This work is a numerical contribution to the study of fluid flow and transport through porous media. The research presented in this dissertation has focused on improving the understanding of flow and transport in porous media with the goal of linking pore-scale properties to macroscopic parameters and flow and transport behaviours at large scale using a direct numerical simulation approach. While Lattice-Boltzmann and pore-network methods have become the choice for solving pore-scale flow and transport problems in complex porous media, efficient direct numerical solution algorithms have advantages in certain situations, for instance, easy incorporation of complex geometries obtained using imaging techniques. The analysis of pore-scale simulation results has enabled us to investigate the dependence of macroscopic parameters such as permeability and dispersion coefficients on pore-scale properties and compare the results with those reported in literature.

A new discontinuous Galerkin based numerical method called Unfitted Discontinuous Galerkin (UDG) has been used for simulating fluid flow at the pore-scale by solving the Stokes equations directly on the complex pore geometry. The computed flow field was used in a random-walk particle tracking model to simulate the transport at the pore-scale. UDG is a Cartesian grid based approach and does not require a grid resolving the complex boundary thereby avoiding the generation of a conforming grid even in complex geometries. The efficiency of Cartesian grid is exploited in this approach and found to be highly suitable for direct numerical simulations. In structured grid based approaches, the difficulty arises when the grid intersects the domain boundaries and UDG has special way of handling such complications. The resolution of the structured grid can be chosen based on the required accuracy of the simulation and in general it does not depend on the complexities of domain boundaries. Since it is a direct numerical simulation approach, simplified geometries like that used in pore-network models are not necessary. In comparison to standard finite element methods, it can handle complex geometries with sufficient accuracy yet with lesser number of mesh elements. Moreover, since the method is based on the discontinuous Galerkin discretisation of the governing PDEs it is locally and globally mass conservative, a highly desirable property for flow and transport simulation.

Using the UDG method, we first implemented the DG discretisation of the Stokes equations and presented benchmark computations for simulation of Stokes flow. Pore-scale simulations through simple three-dimensional geometries such as cubic packing of

spheres were presented and compared our results with analytical solutions aiming to validate the method. Additionally, we presented results on computation of permeability from pore-scale simulation where convergence of permeability as a function of grid resolution for cubic and random arrays of spheres were shown. We showed that both the pore-scale flow features and the permeability could be computed at a reasonable computational cost and results were matching well with analytical and literature data.

We then studied the pore-scale dispersion by simulating flow and transport in two and three dimensional porous media. A particle tracking model was developed to simulate transport of non-reactive solute particles subjected to a velocity field computed on the pore-scale using UDG, where transport includes the effect of both molecular diffusion and advection. Our particle tracking implementation has been verified and validated by simulating Taylor-Aris dispersion phenomena between two parallel plates and results were in close agreement with analytical solutions. When simulating pore-scale transport, particle positions were recorded and the dispersion coefficients were calculated from the variance of particle distribution using the method of moments. The result of the two-dimensional transport simulation in a channel with circular obstacles was compared with the result obtained by a DG discretisation of convection-dispersion equation. We further carried out pore-scale simulations for a wide range of the characteristic Péclet number, Pe and computed the dispersion coefficients. The simulated results agree well with the data reported in the literature, which indicates that our method can successfully simulate dispersion behaviour.

The UDG method is found to be well suited for simulating fluid flow through complex porous media. Since the method is based on the discontinuous Galerkin discretisation of the governing partial differential equations, it has all the advantages of DG methods and additionally it can easily handle the complex boundaries. This makes it an elegant approach to solving flow problems at the pore-scale. UDG is flexible and convenient tool for pore-scale simulation and in general for simulation in complex geometries. As we have shown in this work, it can successfully simulate Stokes flow in complex porous media. Among its benefits are the simplicity of a uniform structured grid and easy incorporation of complex geometry via implicit function or level set methods. These features are advantageous for fluid-flow problems in complex geometries. The UDG method is also well suited for parallel computing because of the underlying DG discretisation of the partial differential equations where DG is highly parallel in nature.

In conclusion, the pore-scale simulations using UDG in model porous media (random sphere packing) carried out in this work have indeed given us new insights into the flow and transport in porous media. In particular, the dependence of permeability and dispersion coefficients on pore structure and pore-scale properties were investigated.

Outlook

The Unfitted Discontinuous Galerkin is a powerful and promising direct numerical simulation technique for pore-scale simulation, though there are scope for improvements. It is computationally demanding because the DG discretisation introduces more unknowns than a standard finite element discretisation. As a consequence, at present it requires long computational time when used in serial computers and a parallel implementation is must for a better performance. On the implementation side, assembling of the stiffness matrix can be improved (speed up) further where parallelisation could be effectively used. Additionally, introducing local adaptive refinement of the fundamental grid would make the method much more flexible to use.

The method has been applied successfully to single phase flow and transport through ideal porous media represented by random sphere packing. Next step would be to apply to more realistic geometries obtained from tomography images and make qualitative and quantitative comparisons with experimental results. Moreover, quantitative comparisons with other well known pore-scale modelling approaches such as pore-network and LBM would be very interesting as well. Finally, it can be extended to study multiphase flow problem at pore-scale, which is more challenging as it results in new problems and issues due to the presence of fluid interfaces and contact lines.

Bibliography

Aarnes, J. E., Kippe, V., Lie, K.-A. and Rustad, A., 2007. Modelling of multiscale structures in flow simulations for petroleum reservoirs., *Geometrical Modeling, Numerical Simulation, and Optimization*, Springer Verlag, S. 307–360.

Acharya, R. C. 2004. *Upscaling of Nonlinear Reactive Transport: from Pore to Core*, Phd thesis, Wageningen University.

Anwar, S., Cortis, A. and Sukop, M. C., 2008. Lattice Boltzmann simulation of solute transport in heterogeneous porous media with conduits to estimate macroscopic continuous time random walk model parameters, *Progress in Computational Fluid Dynamics* **8**:213 – 221.

Aris, R. 1956. On the dispersion of a solute in a fluid flowing through a tube, *Proceedings of the Royal Society of London. Series A, Mathematical and Physical Sciences* **235**:67–77.

Arnold, D. N. 1982. An interior penalty finite element method with discontinuous elements, *SIAM J. Numer. Anal.* **19**:742–760.

Arnold, D. N., Brezzi, F., Cockburn, B. and Marini, L. D., 2000. Discontinuous Galerkin methods for elliptic problems, *In* B. Cockburn, Karniadakis, G. E. and Shu, C.-W., (ed.) *Discontinuous Galerkin Methods: Theory, Computation and Applications*, Lecture Notes in Computational Science and Engineering, Vol. 11, Springer Verlag, Berlin, Heidelberg, New York, S. 89–101.

Arnold, D. N., Brezzi, F., Cockburn, B. and Marini, L. D., 2001. Unified analysis of discontinuous Galerkin methods for elliptic problems, *SIAM J. Numer. Anal.* **39**:1749–1779 (electronic).

Babuška, I. and Zlamal, M., 1973. Nonconforming elements in the finite element method with penalty, *SIAM Journal on Numerical Analysis* **10**:863–875.

Babuška, I., Baumann, C. E. and Oden, J. T., 1999. A discontinuous hp finite element method for diffusion problems: $1 - D$ analysis, *Comput. Math. Appl.* **37**:103–122.

Baker, G. A., Jureidini, W. N. and Karakashian, O. A., 1990. Piecewise solenoidal vector fields and the Stokes problem, *SIAM J. Numer. Anal.* **27**:1466–1485.

Bassi, F. and Rebay, S., 1997. A high-order accurate discontinuous finite element method for the numerical solution of the compressible Navier–Stokes equations, *Journal of Computational Physics* **131**:267–279.

Bastian, P. 2003. Higher order discontinuous Galerkin methods for flow and transport in porous media, *In* E. Bänsch (ed.) *Challenges in Scientific Computing – CISC 2002*, number 35 in *LNCSE*, S. 1–22.

Bastian, P. and Reichenberger, V., 2000. Multigrid for higher order discontinuous Galerkin finite elements applied to groundwater flow, *Technical Report 2000-37*, SFB 359.

Bastian, P. and Rivière, B., 2003. Superconvergence and H(div)-projection for discontinuous Galerkin methods, *Int. J. Numer. Meth. Fluids.* **42**:1043–1057.

Bastian, P. and Rivière, B., 2004. Discontinuous Galerkin methods for two-phase flow in porous media, *Technical Report 2004–28*, IWR (SFB 359), Universität Heidelberg.

Bastian, P., Blatt, M., Dedner, A., Engwer, C., Klöfkorn, R., Kornhuber, R., Ohlberger, M. and Sander, O., 2008a. A generic grid interface for parallel and adaptive scientific computing. Part II: Implementation and tests in DUNE, *Computing*. accepted.

Bastian, P., Blatt, M., Dedner, A., Engwer, C., Klöfkorn, R., Ohlberger, M. and Sander, O., 2008b. A generic grid interface for parallel and adaptive scientific computing. Part I: Abstract framework, *Computing*. accepted.

Bastian, P., Droske, M., Engwer, C., Klöfkorn, R., Neubauer, T., Ohlberger, M. and Rumpf, M., 2004. Towards a unified framework for scientific computing, *In* R. Kornhuber, Hoppe, R., Keyes, D., Périaux, J., Pironneau, O. and Xu, J., (ed.) *Proceedings of the 15th Conference on Domain Decomposition Methods*, LNCSE, Springer-Verlag. accepted for publication.

Batchelor, G. K. 1970. *An introduction in fluid dynamics*, Cambridge University Press.

Batu, V. 2006. *Applied Flow and Solute Transport Modeling in Aquifers: Fundamental Principles and Analytical and Numerical Methods*, CRC Press, Taylor & Francis.

Baudet, C., Hulin, J. P., Lallemand, P. and dH́umieres, D., 1989. Lattice-gas automata: A model for the simulation of dispersion phenomena, *Physics of Fluids A: Fluid Dynamics* **1**:507–512.

Baumann, C. E. 1997. *An hp-adaptive discontinuous Galerkin method for computational fluid dynamics*, Phd thesis, The University of Texas at Austin.

Baumann, C. E. and Oden, J. T., 1999a. A discontinuous hp finite element method for convection–diffusion problems, *Computational Methods in Applied Mechanics and Engineering* **175**:311–341.

Baumann, C. E. and Oden, J. T., 1999b. A discontinuous hp finite element method for the Euler and Navier–Stokes equations, *International Journal for Numerical Methods in Fluids* **31**:79–95.

Baumann, C. E. and Oden, J. T., 2000. An adaptive–order discontinuous Galerkin method for the solution of the Euler equations of gas dynamics, *International Journal for Numerical Methods in Engineering* **47**:61–73.

Bear, J. 1972. *Dynamics of fluids in porous media*, Elsevier, New York.

Berkowitz, B., Emmanuel, S. and Scher, H., 2006. Non-Fickian Transport: Quantifying Tracer Transport Measurements, *AGU Fall Meeting Abstracts* S. F3+.

Berkowitz, B., Emmanuel, S. and Scher, H., 2008. Non-Fickian transport and multiple-rate mass transfer in porous media, *Water Resources Research* **44**:3402–+.

Berkowitz, B., Scher, H. and Silliman, S. E., 2000. Anomalous transport in laboratory-scale, heterogeneous porous media, *Water Resources Research* **36**:149–158.

Bijeljic, B. and Blunt, M. J., 2006. Pore-scale modeling and continuous time random walk analysis of dispersion in porous media, *Water Resources Research* **42**:1202–+.

Bijeljic, B. and Blunt, M. J., 2007. Pore-scale modeling of transverse dispersion in porous media, *Water Resources Research* **43**:12–+.

Bijeljic, B., Muggeridge, A. H. and Blunt, M. J., 2004. Pore-scale modeling of longitudinal dispersion, *Water Resources Research* **40**:11501–+.

Blatt, M. and Bastian, P., 2007. The iterative solver template library, *In* B. Køagström, Elmroth, E., Dongarra, J. and Wasniewski, J., (ed.) *Applied Parallel Computing – State of the Art in Scientific Computing*, Vol. 4699 of *Lecture Notes in Scientific Computing*, Springer, S. 666–675.

Braess, D. and Schumaker, L. L., 2007. *Finite Elements: Theory, Fast Solvers, and Applications in Solid Mechanics*, Cambridge University Press, Cambridge. Third Edition.

Brenner, S. C. and Scott, L. R., 2002. *The Mathematical Theory of Finite Element Methods*, second, Springer Verlag, Berlin, Heidelberg, New York.

Bruderer, C. and Bernabé, Y., 2001. Network Modeling of Dispersion: Transition from Taylor Dispersion in Homogeneous Networks to Mechanical Dispersion in Very Heterogeneous Ones, *Water Resources Research* **37**:897–908.

Byron Bird, R., Steward, W. E. and Lightfoot, E. N., 1960. *Transport phenomena*, John Wiley & Sons, New York.

Castillo, P. 2002. Performance of discontinuous Galerkin methods for elliptic pdes, *SIAM Journal on Scientific Computing* **24**:524–547.

Celia, M., Russell, T., Herrera, I. and Ewing, R., 1990. An eulerian-lagrangian localized adjoint method for the advection-diffusion equation, *Advances in Water Resources* **13**:187–206.

Chen, X. Q. and Pereira, J. C. F., 1999. A new particle-locating method accounting for source distribution and particle-field interpolation for hybrid modeling of strongly coupled two-phase flows in arbitrary coordinates, *Numerical Heat Transfer, Part B: Fundamentals* **35**:41 – 63.

Chordá, R., Blasco, J. A. and Fueyo, N., 2002. An efficient particle-locating algorithm for application in arbitrary 2d and 3d grids, *International Journal of Multiphase Flow* **28**:1565 – 1580.

Ciarlet, P. and Lions, J., 1991. *Handbook of Numerical Analysis – Volume II Finite Element Methods (Part 1)*, North-Holland.

Cockburn, B. and Shu, C.-W., 1998. The local discontinuous Galerkin method for time-dependent convection-diffusion systems, *SIAM J. Numer. Anal.* **35**:2440–2463.

Cockburn, B. and Shu, C.-W., 2001. Runge–Kutta discontinuous Galerkin methods for convection-dominated problems, *J. Sci. Comput.* **16**:173–261.

Cockburn, B., Kanschat, G., Schötzau, D. and Schwab, C., 2002. Local discontinuous Galerkin methods for the Stokes system, *SIAM J. Numer. Anal.* **40**:319–343.

Cockburn, B., Karniadakis, G. E. and Shu, C.-W., 2000. *Discontinuous Galerkin Methods: Theory, Computation and Applications*, Lecture Notes in Computational Science and Engineering, Vol. 11, Springer Verlag, Berlin, Heidelberg, New York.

Coelho, D., Thovert, J.-F. and Adler, P. M., 1997. Geometrical and transport properties of random packings of spheres and aspherical particles, *Phys. Rev. E* **55**:1959–1978.

Darcy, H. 1856. *Les Fontaines de la Ville de Dijon*, Dalmont, Paris.

Dawson, C. N. 2006. Foreword for the special issue on discontinuous Galerkin method, *Computer Methods in Applied Mechanics and Engineering* **195**:3183.

Dawson, C. N., Sun, S. and Wheeler, M. F., 2004. Compatible algorithms for coupled flow and transport, *Computer Methods in Applied Mechanics and Engineering* **193**:2565–2580.

Delay, F., Ackerer, P. and Danquigny, C., 2005. Simulating Solute Transport in Porous or Fractured Formations Using Random Walk Particle Tracking: A Review, *Vadose Zone J* **4**:360–379.

Deville, M. O., Fischer, P. F. and Mund, E. H., 2002. *High-Order Methods for Incompressible Fluid Flow*, Cambridge University Press.

Donea, J. and Huerta, A., 2003. *Finite Element Methods for Flow Problems*, Wiley.

Dullien, F. A. 1992. *Porous Media: Fluid Transport and Pore Structure*, Academic Press, California.

Elman, H., Silvester, D. and Wathen, A., 2005. *Finite Elements and Fast Iterative Solvers with Applications in incompressible fluid dynamics*, Numerical Mathematics and Scientific Computation, Oxford University Press, Oxford, New York.

Engwer, C. and Bastian, P., 2005. A discontinuous Galerkin method for simulations in complex domains, *Technical Report 5707, IWR , Universität Heidelberg* S. http://www.ub.uni–heidelberg.de/archiv/5707/.

Engwer, C. and Bastian, P., 2008. An unfitted finite element method using discontinuous Galerkin, in preparation.

Engwer, C., Bastian, P. and Kuttanikkad, S. P., 2008. An unfitted discontinuous Galerkin finite element method for pore scale simulations, *PARA 2008, 9th International Workshop on State-of-the-Art in Scientific and Parallel Computing, May 13-16, NTNU, Trondheim, Norway*.

Fahlke, J. 2008. *Pore scale simulation of transport in porous media*, Diploma thesis, The Faculty of Physics and Astronomy, University of Heidelberg, Germany.

Filippini, L. and Toselli, A., 2002. hp finite element approximations on non-matching grids for the Stokes problem, *Technical Report 2002-22*, Seminar for Applied Mathematics, ETHZ.

Freund, H., Bauer, J., Zeiser, T. and Emig, G., 2005. Detailed simulation of transport processes in fixed-beds, *Industrial & Engineering Chemistry Research* **44**:6423–6434.

Geller, S., Krafczyk, M., Tölke, J., Turek, S. and Hron, J., 2006. Benchmark computations based on lattice–Boltzmann, finite element and finite volume methods for laminar flows, *Computers & Fluids* **35**:888–897.

Girault, V. and Raviart, P.-A., 1979. *Finite Element Approximation of the Navier-Stokes Equations (Lecture Notes in Mathematics)*, Springer.

Girault, V. and Wheeler, M., 2008. Discontinuous Galerkin methods, *In* R. Glowinski and Neittaanmäki, P., (ed.) *Partial Differential Equations: Modelling and Numerical Simulation*, Computational Methods in Applied Sciences, Vol. 16, Springer Verlag, Berlin, Heidelberg, New York, S. 3–26.

Girault, V., Rivière, B. and Wheeler, M. F., 2005a. A discontinuous Galerkin method with nonoverlapping domain decomposition for the Stokes and Navier-Stokes problems, *Math. Comp.* **74**:53–84.

Girault, V., Rivière, B. and Wheeler, M. F., 2005b. A splitting method using discontinuous Galerkin for the transient incompressible Navier-Stokes equations, *Mathematical Modelling and Numerical Analysis* **39**:1115–1148.

Gist, G. A., Thompson, A. H., Katz, A. J. and Higgins, R. L., 1990. Hydrodynamic dispersion and pore geometry in consolidated rock, *Physics of Fluids A: Fluid Dynamics* **2**:1533–1544.

Grossmann, C., Roos, H. G. and Stynes, M., 2007. *Numerical Treatment of Partial Differential Equations*, Universitext, Springer–Verlag, Berlin.

Hackbusch, W. and Sauter, S. A., 1991. Composite Finite Elements for the Approximation of PDEs on Domains with complicated Micro-Structures, *Preprint*.

Hansbo, P. and Larson, M. G., 2002. Discontinuous Galerkin methods for incompressible and nearly incompressible elasticity by nitsche's method, *Computer Methods in Applied Mechanics and Engineering* **191**:1895–1908.

Hassan, A. E. and Mohamed, M. M., 2003. On using particle tracking methods to simulate transport in single-continuum and dual continua porous media, *Journal of Hydrology* **275**:242–260.

Hendersen, A. 2007. *The Paraview Guide*, Kitware, Inc.

Heywood, J., Rannacher, R. and Turek, S., 1996. Artificial boundaries and flux and pressure conditions for the incompressible Navier–Stokes equations, *International Journal for Numerical Methods in Fluids* **22**:325–352.

Inamuro, T., Yoshino, M. and Ogino, F., 1999. Lattice-Boltzmann simulation of flows in a three-dimensional porous structure, *International Journal for Numerical Methods in Fluids* **29**:737–748.

Jimenez-Hornero, F. J., Giraldez, J. V. and Laguna, A., 2005. Simulation of Tracer Dispersion in Porous Media Using Lattice Boltzmann and Random Walk Models, *Vadose Zone J* **4**:310–316.

Kaestner, A., Lehmann, E. and Stampanoni, M., 2008. Imaging and image processing in porous media research, *Advances in Water Resources* **31**:1174–1187.

Kandhai, D., Hlushkou, D., Hoekstra, A. G., Sloot, P. M. A., Van As, H. and Tallarek, U., 2002. Influence of stagnant zones on transient and asymptotic dispersion in macroscopically homogeneous porous media, *Phys. Rev. Lett.* **88**:234501.

Karakashian, O. A. and Jureidini, W. N., 1998. A nonconforming finite element method for the stationary Navier–Stokes equations, *SIAM J. Numer. Anal.* **35**:93–120.

Karakashian, O. A. and Katsaounis, T., 2006. Numerical simulation of incompressible fluid flow using locally solenoidal elements, *Computers & Mathematics with Applications* **51**:1551–1570.

Khrapitchev, A. A. and Callaghan, P. T., 2003. Reversible and irreversible dispersion in a porous medium, *Phys. Fluids* **15**:2649–2660.

Kinzelbach, W. 1990. Simulation of pollutant transport in groundwater with the random walk method, *Groundwater Monitoring and Management*, number 173 in *Proceedings of the Dresden Symposium*, IAHS.

Kitanidis, P. K. 1988. Prediction by the method of moments of transport in a heterogeneous formation, *Journal of Hydrology* **102**:453–473.

Knabner, P. and Angerman, L., 2003. *Numerical Methods for Elliptic and Parabolic Partial Differential Equations*, Texts in Applied Mathematics, Springer Verlag, Berlin, Heidelberg, New-York.

LaBolle, E. M., Fogg, G. E. and Tompson, A. F. B., 1996. Random-walk simulation of transport in heterogeneous porous media: Local mass-conservation problem and implementation methods, *Water Resources Research* **32**:583–593.

LaBolle, E. M., Quastel, J. and Fogg, G. E., 1998. Diffusion theory for transport in porous media: Transition-probability densities of diffusion processes corresponding to advection-dispersion equations, *Water Resources Research* **34**:1685–1694.

Lazarov, R. and Ye, X., 2007. Stabilized discontinuous finite element approximations for Stokes equations, *Journal of Computational and Applied Mathematics J. Comput. Appl. Math.* **198**:236–252.

LeSaint, P. and Raviart, P. A., 1974. On a finite element method for solving the neutron transport equation, *In C. de Boor, editor, Mathematical Aspects of finite elements in partial differential equations* S. 89–145.

Liu, G. R. and Liu, M. B., 2003. *Smoothed Particle Hydrodynamics: A Meshfree Particle Method*, World Scientific Publishing Company.

Magnico, P. 2003. Hydrodynamic and transport properties of packed beds in small tube-to-sphere diameter ratio: pore scale simulation using an Eulerian and a Lagrangian approach, *Chemical Engineering Science* **58**:5005–5024.

Maier, R. S., Kroll, D. M., Bernard, R. S., Howington, S. E., Peters, J. F. and Davis, H. T., 2000. Pore-scale simulation of dispersion, *Physics of Fluids* **12**:2065–2079.

Maier, R. S., Kroll, D. M., Bernard, R. S., Howington, S. E., Peters, J. F. and Davis, H. T., 2002. Enhanced dispersion in cylindrical packed beds, *Philosophical Transactions: Mathematical, Physical and Engineering Sciences* **360**:497–506.

Maier, R. S., Kroll, D. M., Kutsovsky, Y. E., Davis, H. T. and Bernard, R. S., 1998. Simulation of flow through bead packs using the lattice-Boltzmann method, *Physics of Fluids* **10**:60–74.

Manwart, C., Aaltosalmi, U., Koponen, A., Hilfer, R. and Timonen, J., 2002. Lattice-Boltzmann and finite-difference simulations for the permeability for three-dimensional porous media, *Phys. Rev. E* **66**:016702.

Manz, B., Gladden, L. F. and Warren, P. B., 1999. Flow and dispersion in porous media: Lattice-Boltzmann and nmr studies, *AIChE Journal* **45**:1845–1854.

Martys, N. S., Torquato, S. and Bentz, D. P., 1994. Universal scaling of fluid permeability for sphere packings, *Phys. Rev. E* **50**:403–408.

Morton, K. W. and Mayers, D. F., 2005. *Numerical Solution of Partial Differential Equations: An Introduction*, Cambridge University Press.

Nitsche, J. A. 1971. Über ein Variationsprinzip zur Lösung von Dirichlet-Problemen bei Verwendung von Teilräumen, die keinen Randbedingungen unterworfen sind, *Abh. Math. Sem. Univ. Hamburg* **36**:9–15.

Oden, J. and Baumann, C., 2000. A conservative dgm for convection-diffusion and Navier-Stokes problems, *In* B. Cockburn, Karniadakis, G. E. and Shu, C.-W., (ed.) *Discontinuous Galerkin Methods: Theory, Computation and Applications*, Lecture Notes in Computational Science and Engineering, Vol. 11, Springer Verlag, Berlin, Heidelberg, New York, S. 179–196.

Oden, J. T., I.Babuška and Baumann, C. E., 1998. A discontinuous hp finite element method for diffusion problems, *Journal of Computational Physics* **146**:491–519.

Øren, P. E. and Bakke, S., 2003. Reconstruction of berea sandstone and pore-scale modelling of wettability effects, *Journal of Petroleum Science & Engineering*.

Pan, C., Hilpert, M. and Miller, C. T., 2001. Pore-scale modeling of saturated permeabilities in random sphere packings, *Phys. Rev. E* **64**:066702.

Pan, C., Luo, L.-S. and Miller, C. T., 2006. An evaluation of lattice Boltzmann schemes for porous medium flow simulation, *Computers & Fluids* **35**:898–909.

Pan, C., Prins, J. F. and Miller, C. T., 2004. A high-performance lattice Boltzmann implementation to model flow in porous media, *Computer Physics Communications* **158**:89–105.

Peskin, C. S. 1972. Flow patterns around heart valves: A numerical method, *Journal of Computational Physics* **10**:252–271.

Pfannkuch, H. 1963. Contribution à l'étude des déplacements de fluides miscibles dans un milieu poreux. (contribution to the study of the displacement of miscible fluids in a porous medium), *Rev. Inst. Fr. Petrol.* **18**:215–270.

Pokrajac, D. and Lazic, R., 2002. An efficient algorithm for high accuracy particle tracking in finite elements, *Advances in Water Resources* **25**:353 – 369.

Press, W. H., Teukolsky, S. A., Vetterling, W. T. and Flannery, B. P., 1993. *Numerical Recipes in FORTRAN; The Art of Scientific Computing*, Cambridge University Press, New York, NY, USA.

Rage, T. 1996. *Studies of Tracer Dispersion and Fluid Flow in Porous Media*, Phd thesis, University of Oslo.

Reed, W. H. and Hill, T. R., 1973. Triangular mesh methods for the neutron transport equation, *Technical Report LA–UR–73–479*, Los Alamos Scientific Laboratory.

Rivière, B. 2000. *Discontinuous Galerkin methods for solving the miscible displacement problem in porous media*, Phd thesis, University of Texas at Austin.

Rivière, B. and Girault, V., 2006. Discontinuous finite element methods for incompressible flows on subdomains with non-matching interfaces, *Computer Methods in Applied Mechanics and Engineering* **195**:3274–3292.

Rivière, B., Wheeler, M. F. and Banas, K., 2000. Discontinuous Galerkin method applied to a single-phase flow in porous media, *Computational Geosciences* **4**:337–349.

Rivière, B., Wheeler, M. F. and Girault, V., 1999. Improved energy estimates for interior penalty constrained and discontinuous Galerkin methods for elliptic problems. part i, *Computational Geosciences* **3**:337–360.

Romkes, A., Prudhomme, S. and Oden, J. T., 2006. Convergence analysis of a discontinuous finite element formulation based on second order derivatives, *Computer Methods in Applied Mechanics and Engineering* **195**:3461–3482.

Roth, K. 2007. *Soil Physics. Lecture Notes*, Institute of Environmental physics, University of Heidelberg, http://www.iup.uni-heidelberg.de/institut/forschung/groups/ts/students.

Roth, K. and Hammel, K., 1996. Transport of conservative chemical through an unsaturated two-dimensional miller-similar medium with steady state flow, *Water Resources Research* **32**:1653–1663.

Sahimi, M. 1993. Flow phenomena in rocks: from continuum models to fractals, percolation, cellular automata, and simulated annealing, *Rev. Mod. Phys.* **65**:1393–1534.

Salamon, P., Fernandez-Garcia, D. and Gomez-Hernandez, J., 2006. A review and numerical assessment of the random walk particle tracking method, *Journal of Contaminant Hydrology* **87**:277–305.

Salles, J., Thovert, J.-F., Delannay, R., Prevors, L., Auriault, J.-L. and Adler, P. M., 1993. Taylor dispersion in porous media. determination of the dispersion tensor, *Physics of Fluids A: Fluid Dynamics* **5**:2348–2376.

Sangani, A. S. and Acrovos, A., 1982. Slow flow through a periodic array of spheres, *International Journal of Multiphase Flow* **8**:343–360.

Schäfer, M. 2006. *Computational Engineering – Introduction to Numerical Methods*, Springer-Verlag New York, Inc., Secaucus, NJ, USA.

Schötzau, D., Schwab, C. and Toselli, A., 2003. Mixed hp-dgfem for incompressible flows, *SIAM J. Numer. Anal.* **40**:2171–2194.

Seymour, J. D. and Callaghan, P. T., 1997. Generalized approach to nmr analysis of flow and dispersion in porous media, *AIChE J.* **43**:2096.

Shahbazi, K. 2005. An explicit expression for the penalty parameter of the interior penalty method, *Journal of Compuational Physics* **205**:401–407.

Shahbazi, K., Fischer, P. F. and Ethier, C. R., 2007. A high-order discontinuous Galerkin method for the unsteady incompressible Navier-Stokes equations, *J. Comput. Phys.* **222**:391–407.

Skoge, M., Donev, A., Stillinger, F. H. and Torquato, S., 2006. Packing hyperspheres in high-dimensional Euclidean spaces, *Physical Review E (Statistical, Nonlinear, and Soft Matter Physics)* **74**:041127.

Spaid, M. A. A. and Phelan, F. R., 1997. Lattice Boltzmann methods for modeling microscale flow in fibrous porous media, *Physics of Fluids* **9**:2468–2474.

Stöhr, M. 2003. *Analysis of flow and transport in refractive index matched porous media*, Phd thesis, University of Heidelberg.

Sun, S. 2003. *Discontinuous Galerkin Methods for Reactive Transport in Porous Media*, Phd thesis, The University of Texas at Austin.

Szymczak, P. and Ladd, A. J. C., 2003. Boundary conditions for stochastic solutions of the convection-diffusion equation, *Physical Review E* **68**:036704+.

Tartakovsky, A. M., Meakin, P., Scheibe, T. D. and West, R. M. E., 2007. Simulations of reactive transport and precipitation with smoothed particle hydrodynamics, *J. Comput. Phys.* **222**:654–672.

Taylor, G. I. 1953. Dispersion of soluble matter in solvent flowing slowly through a tube, *Proceedings of the Royal Society of London. Series A, Mathematical and Physical Sciences (1934-1990)* **219**:186–203.

Taylor, G. I. 1954. Conditions under which dispersion of a solute in a stream of solvent can be used to measure molecular diffusion, *Proceedings of the Royal Society of London. Series A, Mathematical and Physical Sciences (1934-1990)* **225**:473–477.

Thomée, V. 2001. From finite differences to finite elements. a short history of numerical analysis of partial differential equations, *J. Comp. Appl. Math* **128**:1–54.

Tompson, A. F. B. and Gelhar, L. W., 1990. Numerical simulation of solute transport in three-dimensional, randomly heterogeneous porous media, *Water Resources Research* **26**:2541–2562.

Toselli, A. 2002. hp discontinuous Galerkin approximations for the Stokes problem, *Mathematical Models & Methods in Applied Sciences (Math. Models Methods Appl. Sci.)* **12**:1565–1597.

V., P. S. and C., K. K., 1999. Calculation of particle trajectories in complex meshes, *Numerical Heat Transfer Part B: Fundamentals* **35**:431–437.

Van Doormaal, M. A. and Pharoah, J. G., 2008. Determination of permeability in fibrous porous media using the lattice Boltzmann method with application to pem fuel cells, *International Journal for Numerical Methods in Fluids* **9999**:n/a+.

van Genuchten, M. T. and Alves, W. J., 1982. Analytical solutions of the one-dimensional convective-dispersive solute transport equation, *Technical Report 1661*, U.S. Department of Agriculture, Technical Bulletin.

Versteeg, H. K. and Malalasekera, W., 2007. *An Introduction to Computational Fluid Dynamics: The Finite Volume Method*, Prentice Hall.

Vogel, H.-J., Tolke, J., Schulz, V. P., Krafczyk, M. and Roth, K., 2005. Comparison of a Lattice-Boltzmann Model, a Full-Morphology Model, and a Pore Network Model for Determining Capillary Pressure-Saturation Relationships, *Vadose Zone J* **4**:380–388.

Wheeler, M. F. 1978. An elliptic collocation-finite element method with interior penalties, *SIAM J. Numer. Anal.* **15**:152–161.

Wildenschild, D., Hopmans, J. W., Rivers, M. L. and Kent, A. J. R., 2005. Quantitative Analysis of Flow Processes in a Sand Using Synchrotron-Based X-ray Microtomography, *Vadose Zone J.* **4**:112–126.

Zhang, X. and Lv, M., 2007. Persistence of anomalous dispersion in uniform porous media demonstrated by pore-scale simulations, *Water Resources Research* **43**:7437–+.

Zheng, C. and Bennett, G. D., 2002. *Applied Contaminant Transport Modeling*, John Wiley & Sons. Second Edition.

Zhu, Y. and Fox, P. J., 2002. Simulation of pore-scale dispersion in periodic porous media using smoothed particle hydrodynamics, *J. Comput. Phys.* **182**:622–645.

Zienkiewicz, O. C. and Taylor, R. L., 2001. *The Finite Element Method, Fluid Dynamics*, 6, Butterworth Heinemann, Oxford.

Zunino, P. 2008. Mortar and discontinuous Galerkin methods based on weighted interior penalties, *In* U. Langer, Discacciati, M., Keyes, D., Widlund, O. and Zulehner, W., (ed.) *Domain Decomposition Methods in Science and Engineering XVII*, Vol. 60 of *Lecture Notes in Computational Science and Engineering*, Springer, Heidelberg, S. 155–164. Proceedings of the 17th International Conference on Domain Decomposition Methods held at St. Wolfgang / Strobl, Austria, July 3–7, 2006.